



HAL
open science

Development and advanced characterization of high performance hard magnetic materials

Svetlana Ponomareva

► **To cite this version:**

Svetlana Ponomareva. Development and advanced characterization of high performance hard magnetic materials. Materials Science [cond-mat.mtrl-sci]. Université Grenoble Alpes; Université polytechnique de Tomsk (Russie), 2017. English. NNT : 2017GREAY035 . tel-01699598

HAL Id: tel-01699598

<https://theses.hal.science/tel-01699598>

Submitted on 2 Feb 2018

HAL is a multi-disciplinary open access archive for the deposit and dissemination of scientific research documents, whether they are published or not. The documents may come from teaching and research institutions in France or abroad, or from public or private research centers.

L'archive ouverte pluridisciplinaire **HAL**, est destinée au dépôt et à la diffusion de documents scientifiques de niveau recherche, publiés ou non, émanant des établissements d'enseignement et de recherche français ou étrangers, des laboratoires publics ou privés.

THÈSE

Pour obtenir le grade de

**DOCTEUR DE LA COMMUNAUTÉ UNIVERSITÉ
GRENOBLE ALPES**

**préparée dans le cadre d'une cotutelle entre *la
Communauté Université Grenoble Alpes et
l'Université Polytechnique de Tomsk***

Spécialité : **Nanophysique**

Arrêté ministériel : le 6 janvier 2005 - 7 août 2006

Présentée par

Svetlana PONOMAREVA

Thèse dirigée par **Florence MARCHI** et **Oleg KHASANOV**
codirigée par **Vladimir AN**

préparée au sein de **l'Institut Néel, CNRS/UGA**
et de **l'Institut de la physique des hautes technologies, TPU**

dans **l'École Doctorale de Physique**

Développement et caractérisation avancée de matériaux magnétiques durs de haute performance

Thèse soutenue publiquement le **30 mai 2017**

devant le jury composé de :

Olga, KAZAKOVA

Principle Research Scientist, National Physics Laboratory, Londres,
Royaume-Uni, Rapporteur

Michael, GAUTHIER

Directeur de recherche, Institut FEMTO-ST, Besançon, France, Rapporteur,

Nora, DEMPSEY

Directrice de recherche, Institut Néel, CNRS/UGA UPR2940, Grenoble,
France, Membre

Rostislav, GRECHISHKIN

Professeur, Tver State University, Tver, Russia, Membre

Herve, COURTOIS

Professeur, Institut Néel, CNRS/UGA UPR2940, Grenoble, France, Président



Abstract

Nowadays in medicine and biotechnology a wide range of applications involves magnetic micro/nano-object manipulation including remote control of magnetic beads, trapping of drug vectors, magnetic separation of labelled cells and so on. Handling and positioning magnetic particles and elements functionalized with these particles has greatly benefited from advances in microfabrication. Indeed reduction in size of the magnet while maintaining its field strength increases the field gradient. In this context, arrays made of permanent micromagnets are good candidates for magnetic handling devices. They are autonomous, suitable for integration into complex systems and their magnetic action is restricted to the region of interest.

In this thesis we have elaborated an original approach based on AFM¹ and MFM² for quantitative study of the magnetic force and associated force gradients induced by TMP³ micromagnet array on an individual magnetic micro/nano-object. For this purpose, we have fabricated smart MFM probes where a single magnetic (sub)micronic sphere was fixed at the tip apex of a non-magnetic probe thanks to a dual beam FIB/SEM⁴ machine equipped with a micromanipulator.

Scanning Force Microscopy conducted with such probes, the so-called *Magnetic Particle Scanning Force Microscopy (MPSFM)* was employed for 3D mapping of TMP micromagnets. This procedure involves two main aspects: (i) the quantification of magnetic interaction between micromagnet array and attached microsphere according to the distance between them and (ii) the complementary information about micromagnet array structure. The main advantage of MPSFM is the use of a probe with known magnetization and magnetic volume that in combination with modelling allows interpreting the results ably.

We conducted MPSFM on TMP sample with two types of microparticle probes: with superparamagnetic and NdFeB microspheres. The measurements carried out with superparamagnetic microsphere probes reveal attractive forces (up to few tens of nN) while MFM maps obtained with NdFeB microsphere probes reveal attractive and repulsive forces (up to one hundred of nN) for which the nature of interaction is defined by superposition of microsphere and micromagnet array magnetizations. The derived force and its gradient from MFM measurements are in agreement with experiments on microparticle trapping confirming that the strongest magnetic interaction is observed above the TMP sample interfaces, between the areas with opposite magnetization. Thanks to 3D MFM maps, we demonstrated that intensity of magnetic signal decays fast with the distance and depends on micromagnet array and microsphere properties.

Besides the magnetic interaction quantification, we obtained new information relevant to TMP sample structure: we observed and quantified the local magnetic roughness and associated fluctuations, in particular in zones of reversed magnetization. The variation of detected signal can reach the same order of magnitude as the signal above the micromagnet interfaces. These results complete the experiments on particle trapping explaining why magnetic microparticles are captured not only above the interfaces, but also inside the zones of reversed magnetization.

Quantitative measurements of the force acting on a single (sub)microsphere associated to the modelling approach improve the understanding of processes involved in handling of magnetic objects in microfluidic devices. This could be employed to optimize the parameters of sorting devices and to define the quantity of magnetic nanoparticles required for labelling of biological cells according to their size. More generally these experimental and modelling approaches of magnetic interaction can meet a high interest in all sorts of applications where a well-known and controlled non-contact interaction is required at micro and nano-scale.

Key words: permanent micromagnet array, Atomic and Magnetic Force Microscopy (AFM and MFM), microparticle probe fabrication, nano-scale interaction quantification and mapping, micromagnetic modelling, micromagnetism.

¹ Atomic Force Microscopy

² Magnetic Force Microscopy

³ Thermo Magnetic Patterning

⁴ Focused Ion Beam / Scanning Electron Microscope

Résumé

Actuellement, de plus en plus d'applications en médecine et en biotechnologie impliquent de manipuler des micro/nano-objets magnétiques telles que le piégeage de vecteurs de médicaments ou la séparation magnétique de cellules. La manipulation et le positionnement de nanoparticules magnétiques (NPM) ou d'éléments fonctionnalisés avec ces particules ont profité des progrès en microfabrication. En effet, la diminution de la taille de l'aimant tout en maintenant son champ magnétique augmente son gradient. Dans ce contexte, les réseaux de micro-aimants permanents sont des bons candidats en tant qu'éléments clés pour des dispositifs de manipulation magnétique. Ils sont autonomes, adaptés à l'intégration dans les systèmes complexes et leur action magnétique est limitée à la région d'intérêt.

Cette thèse vise à l'élaboration d'une approche originale basée sur la microscopie à force atomique et magnétique (AFM, MFM) pour une étude quantitative de la force magnétique et des gradients associés induits sur un micro/nano-objet magnétique par un réseau de micro-aimants obtenus via la lithographie thermomagnétique (TMP). Pour cela, on a développé des sondes spécifiques où une seule sphère magnétique (sub)micronique a été fixée à l'apex de la pointe AFM grâce à un micromanipulateur disponible au sein d'un microscope MEB équipé d'une colonne FIB (Focus Ion Beam). La microscopie à sonde locale réalisée avec ces sondes, a permis de cartographie 3D en topographie et en force du réseau de micro-aimants. Grâce à cette procédure deux aspects principaux ont été obtenu: (1) la quantification de l'interaction magnétique entre le réseau de micro-aimants et la microsphère et (2) des informations complémentaires sur la structure magnétique des réseaux de micro-aimants TMP. L'avantage de la MPSFM (Magnetic Particle Scanning Force Microscopy) repose sur une sonde à aimantation et à volume magnétique connus qui combiné avec la modélisation a conduit à une meilleure compréhension de l'action magnétique de ce type de réseaux de micro-aimants.

Pour étudier l'action des réseaux de micro-aimants, deux types de sondes ont été employées : des microsphères superparamagnétiques et de NdFeB. Les mesures effectuées avec une sonde de microsphère superparamagnétique révèlent des forces d'attraction (jusqu'à quelques dizaines de nN) alors que les cartes MFM obtenues avec une sonde de microsphère de NdFeB révèlent des forces attractives et répulsives (jusqu'à 100 nN). Pour ces dernières, la nature de l'interaction est définie par la superposition des aimantations de la microsphère et du micro-aimant. Grâce aux courbes force-distance obtenues avec ces sondes, on a validé expérimentalement que l'intensité du signal magnétique diminue rapidement avec la distance et dépend des propriétés du micro-aimant et de la microsphère.

Outre la quantification spatiale de l'interaction magnétique, on a obtenu de nouvelles informations relatives à la structure magnétique du réseaux de micro-aimants: on a observé et quantifié la présence de fluctuations magnétiques locales conduisant à une rugosité magnétique en particulier dans les zones d'aimantation opposée. La variation de cette rugosité détectée peut atteindre ponctuellement le même ordre de grandeur que le signal au-dessus des interfaces de micro-aimants. Ces résultats permettent de mieux comprendre le piégeage des particules hors des interfaces magnétiques imposées par le motif du réseau.

Les mesures quantitatives de la force agissant sur une microsphère unique améliorent la compréhension des processus impliqués dans des dispositifs microfluidiques. Ainsi les résultats obtenus ont validé et amélioré les modèles utilisés pour décrire la procédure de piégeage, pour ajuster les paramètres de dispositifs de tri ou encore pour optimiser la quantité de nanoparticules magnétiques nécessaire pour le marquage des cellules biologiques en fonction de leur taille.

Plus généralement, ces approches expérimentales et numériques de l'interaction magnétique peuvent rencontrer un grand intérêt dans toutes sortes d'applications où une interaction sans contact bien connue et contrôlée est requise aux micro- et nano-échelles.

Mots clés: réseau de micro-aimants permanentes, microscopie à force atomique et à force magnétique (AFM et MFM), fabrication de la sonde à microparticule, quantification et cartographie d'interaction à nano-échelle, modélisation micromagnétique, micromagnétisme.

Table of content

Abstract	3
Résumé	4
Table of content	6
List of abbreviations	9
List of tables	10
Working Context	12
References	17
Chapter I: Introduction	20
I. Introduction	21
I.1 Characteristics and classification of magnetic materials: dia-, para- and ferro-magnetism	22
I.2 <i>Hard</i> and <i>soft</i> magnetic materials	24
I.3 Magnetic flux sources	27
I.4 Description of magnetic particles	28
I.5 Short review on (sub)microparticle manipulation	31
References	35
Chapter II: Description and applications of micromagnet array	39
II. Description and applications of micromagnet array	40
II.1 Micromagnet array fabrication	40
II.1.1 Hard magnetic film preparation - Triode Sputtering	40
II.1.2 Thermo Magnetic Patterning (TMP)	43
II.1.3 Topographic patterning (TOPO).....	45
II.1.4 Micro Magnetic Imprinting (μ MI)	46
II.2 Micromagnet array properties	48
II.2.1 Modelling of TMP micromagnet array properties.....	48
II.2.2 Micromagnet array for particles trapping.....	54
II.2.3 Localization and identification of magnetic pattern.....	55
II.2.4 Reverse depth determination of TMP sample.....	57
II.2.5 Direct measurements of stray field produced by micromagnet array.....	58
II.2.6 Nano-scale characterization of TMP sample surface morphology and magnetic properties.....	61
II.2.7 Micromagnet array properties. Summary.....	64
II.3 Microfluidic devices for micro-objects handling	66
II.3.1 Static capture and positioning.....	66
II.3.2 Dynamic capture and separation.....	69
II.3.3 Continuous guiding.....	70
References	72

Chapter III: Microsphere Scanning Force Microscopy for quantitative magnetic interaction studies	75
III. Microsphere Scanning Force Microscopy for quantitative magnetic interaction studies	76
III.1 Scanning Force Microscopy	76
III.1.1 Atomic Force Microscopy probe	78
III.1.2 Tip-sample interaction	80
III.1.3 Force spectroscopy mode	82
III.1.4 Imaging in Static Mode (DC)	85
III.1.5 Imaging in Dynamic Mode (AC)	86
III.2 Magnetic Force Microscopy (MFM)	89
III.2.1 General Operating Mode	89
III.2.2 Our Working conditions	89
III.2.3 Magnetic Force or Force Gradient mapping	90
III.2.4 MFM on micromagnet array using standard MFM probes	91
III.3 Microsphere Scanning Force Microscopy	94
III.3.1 Microsphere probe fabrication using AFM manipulation	95
III.3.2 Force gradient mapping between micromagnet array and a single microsphere ..	96
III.3.3 Toward quantitative mapping: Microsphere probe fabrication by Focused Ion Beam	97
References	101
Chapter IV: Quantitative study of TMP sample action on a single magnetic (sub)micronic object.....	105
IV. Quantitative study of TMP sample action on a single magnetic (sub)micronic object	106
IV.1 Definition of micromagnet array – magnetic microsphere system.....	106
IV.2 Simulations of magnetic interaction using CADES framework.....	109
IV.2.1 Modelling of micromagnet array	109
IV.2.2 Modelling of hard magnetic microsphere.....	110
IV.2.3 Modelling of superparamagnetic microsphere	110
IV.3 Micromagnet array mapping with Superparamagnetic Microsphere Probe.....	111
IV.3.1 Quantification of Force Gradient variation in <i>lateral</i> direction	113
IV.3.2 Quantification of Force Gradient variation in <i>vertical</i> direction.....	115
IV.3.3 Quantification of Force variation in <i>lateral</i> direction	117
IV.3.4 Quantification of Force variation in <i>vertical</i> direction.....	119
IV.3.5 Magnetic force density variation	122
IV.4 Micromagnet array mapping with Hard Magnetic Microsphere probe	124
IV.4.1 Effect of probe magnetization orientation	127
IV.4.2 Experimental prospective to explore non-symmetrical behaviour of MJ	129
IV.4.3 <i>Vertical</i> variation of force intensity above a symmetric MJ	131

IV.4.4 Magnetic force density variation	132
IV.5 Summary.....	134
References	136
Chapter V: Conclusions and prospects.....	138
V. Conclusions and prospects	139
V.1 Conclusions.....	139
V.2 Prospects	141
References	143
Annex II.1. TMP mask fabrication procedure.....	144
Annex II.2. Main approaches to magnetic field calculations	145
Annex II.3 Magnetic field and field gradient simulations for TMP magnets	147
Annex II.4. Simulation of magnetic field and magnetic force acting on a superparamagnetic microsphere above the “stripes-like” TMP sample with CADES framework.....	149
Annex II.5. Simulation of magnetic field and magnetic force acting on a NdFeB microsphere above the “stripes-like” TMP sample with CADES framework.....	152
Annex III.1. Calculation of the forces arising between the probe and the sample at micro/nano-scale distance	155
Annex III.2 Calculations of the cantilever frequency shift due to added mass	158
Annex III.3 Superparamagnetic microspheres (microParticles GmbH)	160
Annex III.4. List of the non-magnetic AFM probes with attached magnetic microspheres	162
Annex IV.1 Influence of topographic features on MFM imaging: protocol and data treatment for quantitative measurements.....	165
Annex IV.2. Calculation of magnetic force acting on a single magnetic micro/nano particle.....	167
Annex IV.3 Effect of sphere diameter and magnetic volume on the width of magnetic junction and force intensity	168
List of figures	171
List of scientific papers	179
Acknowledgements.....	181

List of abbreviations

AFM	Atomic Force Microscopy
AM-AFM	Amplitude Modulation Atomic Force Microscopy
CMP	Chemical Mechanical Planarization
DRIE	Deep reactive Ion Etching
EDX	Energy Dispersive X-ray (analysis)
FIB	Focused Ion Beam
FM-AFM	Frequency Modulation Atomic Force Microscopy
FMF	Force Modulation Microscopy
IACVD	Ion Assisted Chemical Vapour Deposition
IP	In Plane
LFM	Lateral Force Microscopy
LSH	Lift Scan Height
MEMS	Micro-Electro-Mechanical System
MFM	Magnetic Force Microscopy
MJ	Magnetic Junction
μMI	Micro Magnetic Imprinting
MOIF	Magneto Optical Indicator Film
MoM	Method of Moments
MPFM	Micro Particle Force Microscopy
MSFM	Microparticle Scanning Force Microscopy
NP	Nano Particle
NRZ	Non Reversed Zone
NSOM	Near-field Scanning Optical Microscopy
OOP	Out of Plane
PDMS	PolyDiMethylSiloxane
PID	Proportional Integral Derivative (controller)
PVD	Physical Vapour Deposition
RZ	Reversed Zone
SCM	Scanning Capacitance Mode
SEM	Scanning Electron Microscopy
SFM	Scanning Force Microscopy
SHPM	Scanning Hall Probe Microscopy
SPM	Scanning Probe Microscopy
SSRM	Scanning Spreading Resistance Mode
STM	Scanning Tunnelling Microscopy
TMP	Thermo Magnetic Patterning
TOPO	Topographical patterning
VSM	Vibrating Sample Magnetometer

List of tables

Table 1.1. Rare Earth Elements: World Production and Reserves in 2011.....	14
Table 1.2. The comparison of ferromagnetic, paramagnetic and diamagnetic materials.	24
Table 1.3. Magnetic properties of several <i>hard</i> magnetic materials.....	27
Table 1.4. Traditional and recently developed approaches for manipulation of micro/nano-objects....	34
Table 2.1. Deposition and annealing parameters with measured magnetic properties for SmCo and NdFeB hard magnetic films. *Results for SmCo films deposited at 350°C.....	42
Table 2.2. General parameters of TMP, TOPO and μ MI magnetic flux sources.....	65
Table 3.1. Comparison between traditional Optical and Electron microscopies, MOIF and SPM.	77
Table 3.2. Main advantages and disadvantages of Contact, Tapping and Non-Contact modes.	88
Table 3.3. Comparison of MFM probes characteristics used for experiments.....	91
Table 3.4. Information about superparamagnetic microspheres used for MPFM probes fabrication. Data marked with * is provided by microParticles GmbH. The weight (volume) of magnetic NPs wt.% (vol.%) was calculated as a ratio between weight (volume) of all magnetic inclusions inside a microsphere and microsphere total weight (volume).	98
Table 3.5. Information about NdFeB microspheres used for MPFM probes fabrication provided by Molycorp Magnequench.....	99
Table 4.1. List of superparamagnetic microsphere probes.....	111
Table 4.2. Characteristics of a TMP sample mapped with 2.85 μ m, 1.5 μ m and 3.5 μ m superparamagnetic microsphere probes at $LHS = 600$ nm.....	113
Table 4.3. Force gradient measurements with 2.85 μ m and 0.29 μ m superparamagnetic microsphere probes.....	117
Table 4.4. Width of MJs at the half height measured with superparamagnetic microsphere probes in static and dynamic mode for $LSH = 700$ nm.....	118
Table 4.5. List of NdFeB microparticle probes used for Microsphere Scanning Force Microscopy. .	124
Table 4.6. Characteristics of a TMP sample mapped with 1.3 μ m and 1.7 μ m NdFeB microsphere probes at $LHS = 600$ nm.....	125

Working Context

This PhD project took place between Néel Institute (Grenoble, France) and Tomsk Polytechnic University (TPU, Tomsk, Russia) in a frame of a Cotutelle agreement. At TPU, the study was dedicated to the development of a new fabrication process for SmFeN-based magnets and investigation of their material properties (chemical composition, crystalline structure...) while examination of their magnetic properties was conducted mainly at Néel Institute. In parallel, the work dedicated to study of interaction between magnetic (sub)microsphere and NdFeB micromagnet array was conducted at Néel Institute. These twofold works are been undertaken in the context of the development and characterization of high performance magnetic materials.

Nowadays, high performance magnetic materials are playing a crucial role in clean energy technologies (hybrid electric vehicles, wind turbines) and have great potential for micro-devices dedicated to biology and healthcare applications [1,2]. For efficient employment of magnetic material in such areas, detailed studies of their properties are required. The analysis of magnetic structure serves for a better understanding of the material itself, and contributes to the improvement of extrinsic magnetic properties through an optimization of the fabrication process. The stray magnetic field analysis is of particular interest for the development of magnets for applications in micro-systems in biology, medicine and beyond, when the interaction between a magnet and an object of interest plays a crucial role. Magnetic materials have been employed for remote control of magnetic micro/nano-objects [3,4], trapping of drug vectors [5], sorting of magnetic and non-magnetic objects [6], magnetic resonance imaging (MRI) [7], application of highly local mechanical strain in living organisms [8] and so on. The experiments on manipulations of magnetic micro/nano-objects based on magnetic interaction known as the magnetophoretic force are of particular interest for medicine and biotechnology where micrometre sized magnets seem to be very attractive for such applications. Indeed they produce high field (typically around few hundreds of mT, comparable to magnetic field of bulk magnets) and field gradient (up to 10^6 T/m), but the range of strong magnetic interaction is limited to few tens of micrometres (Figure 1.1).

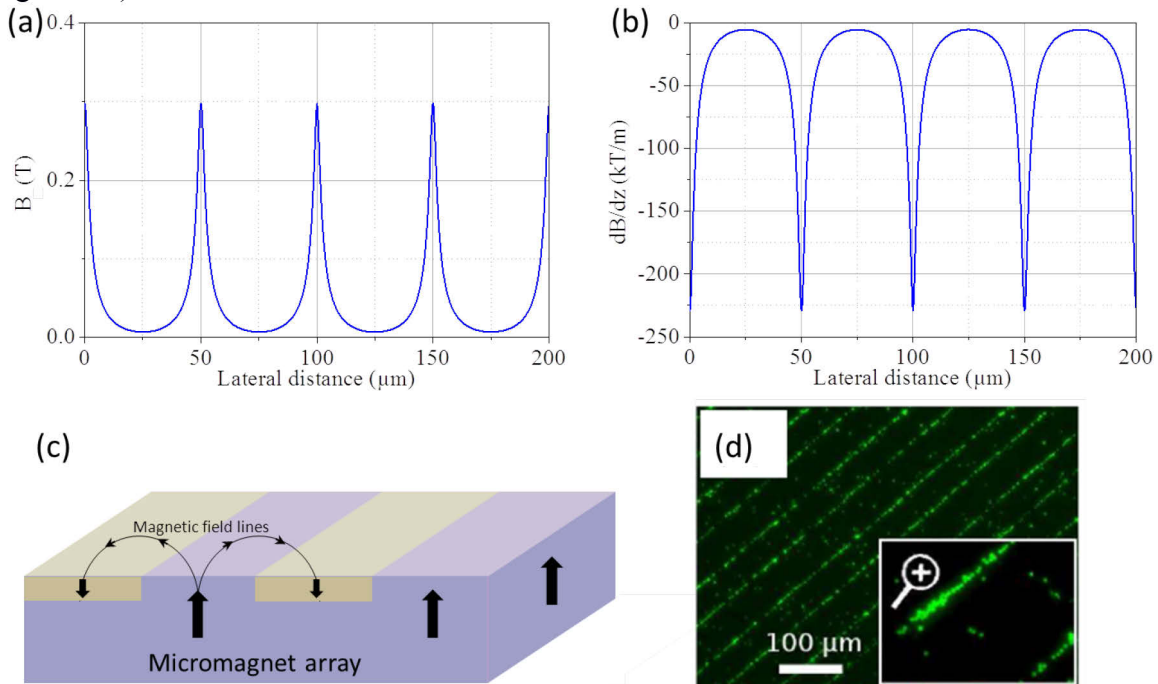


Figure 1.1. (a) Magnetic field B and (b) field gradient $\partial B/\partial z$ calculated for out-of-plane (oop) magnetized NdFeB micromagnet array with stripes of $50 \mu\text{m}$ width (c) at distance of $1 \mu\text{m}$ from the surface with Model 2 (Section II.2.1). (d) Fluorescence image of superparamagnetic particles of $1.4 \mu\text{m}$ diameter trapped by oop magnetized NdFeB micromagnet [9].

At the Néel Institute in the Micro and Nano Magnetism (MNM) group, three different approaches for micro-scale magnet array fabrication have recently been developed:

- (2009) Topographic Patterning (TOPO): formation of a physical magnetic pattern on the film surface by modulating its morphological structure [10];
- (2010) Thermo Magnetic Patterning (TMP): production of high field gradient magnetic structure by reorientation of magnetization at certain zones of the film using laser irradiation combined with an application of an opposite magnetic field [11];
- (2012) Micro Magnetic Imprinting (μ MI): formation of magnetic structure by positioning of magnetic particles in a transparent (flexible or rigid) polymer matrix under magnetic field [12,13].

Mainly NdFeB thick films with out-of-plane magnetization and SmCo thick films with in-plane magnetization were fabricated by first two approaches (TOPO and TMP); NdFeB microparticles were used for fixation in polymer matrix for μ MI samples fabrication. A number of experiments have been conducted to demonstrate the potential of these micromagnet arrays for handling of magnetically labelled micro/nano-objects and for their integration in microfluidic⁵ devices [9,10,11,13].

Till now sensitive method to measure directly this magnetic interaction and to distinguish it from different forces has not been developed. A quantitative study of the magnetic forces induced by micromagnet arrays on magnetic micro/nano-objects is of great interest from both, the fundamental and applied points of view. Indeed it will be relevant to validate and to improve the models employed until now to describe the trapping process taking place in microfluidic devices based on micromagnet array. In addition, comparison of the magnetic forces with surface forces (Van der Waals, capillary, electrostatic) is essential in micro-scaled devices, where these latter forces may become dominant.

Thus, the first goal of this work is to find a reliable and reproducible approach to measure and to distinguish magnetic force from the others. During this PhD period thanks to the expertise of Nano-Optics and Force Group of Néel Institute, we have developed smart probes where a single hard magnetic or superparamagnetic microsphere is glued to the tip apex of an AFM cantilever and we have conducted interaction measurements at micro- and nano-scale. With these smart probes, qualitative and quantitative direct measurement of magnetic forces between specific (sub)micro-objects (superparamagnetic/ferromagnetic spheres) and micromagnets in gaseous and liquid environments were performed. The Scanning Force Microscopy conducted with such probes, the so-called *Magnetic Particle Scanning Force Microscopy (MPSFM)* [14] is complimentary to standard methods for characterization of magnetic samples, such as Magnetic Force Microscopy, Scanning Hall Probe Microscopy, Vibrating Sample Magnetometry, Magneto Optical Indicator Films and so on. MPSFM is a non-destructive technique that provides direct force or force gradient measurements with high resolution. In parallel to this experimental work, modelling of magnetic forces and force gradients acting on superparamagnetic or hard magnetic microsphere flying above a micromagnet array has been carried out. These two approaches have been combined to analyse the results. Consequently, we have conducted not only quantitative force/force gradient measurements that can be employed for optimization of microfluidic devices, but also deduced an additional information about micromagnet array structure and proposed explanations for unexpected particle trapping behaviour observed in magnetic microfluidic devices.

The second aim of this PhD project concerns the fabrication of SmFeN-based bulk magnetic materials. This choice has been done in order to meet the recent demand for high efficiency and cost effective magnets for hybrid/electric vehicles and other areas where high magnetic properties and high working temperatures are required. Nowadays Nd₂Fe₁₄B (2:14:1

⁵ Microfluidic system is a system that processes small amounts of fluids (10^{-9} to 10^{-8} litres), using channels with lateral dimensions of tens to hundreds of micrometres.

phase) magnets exhibit the highest maximum energy product [15,16,17]. The main drawbacks of this material are relatively low operating temperature (below 200°C) and coercivity (10 kOe). Up to now, the most effective solution is to partially substitute Nd by some heavy rare earth elements such as Dy and Tb to improve magnetocrystalline anisotropy (generally, about 30% of Nd is replaced by Dy in the NdFeB magnets for the electric vehicles motors applications) [18]. Based on the calculated substitution energies, it was shown that Dy/Tb doping elements prefer to enter the 2:14:1 phase rather than the Nd-rich phase (NdO). The selective occupation of Dy and Tb in the 2:14:1 structure enhances the magnetic anisotropy field. Such approach results in substantially increased coercivity. However, it leads to decrease in the magnetization due to the antiparallel coupling of Fe and Dy/Tb magnetic moments and increase in cost due to high price⁶ of Dy and Tb (Figure 1.2) since China holds the near-monopoly position of rare earth production in the world (Table 1.1).

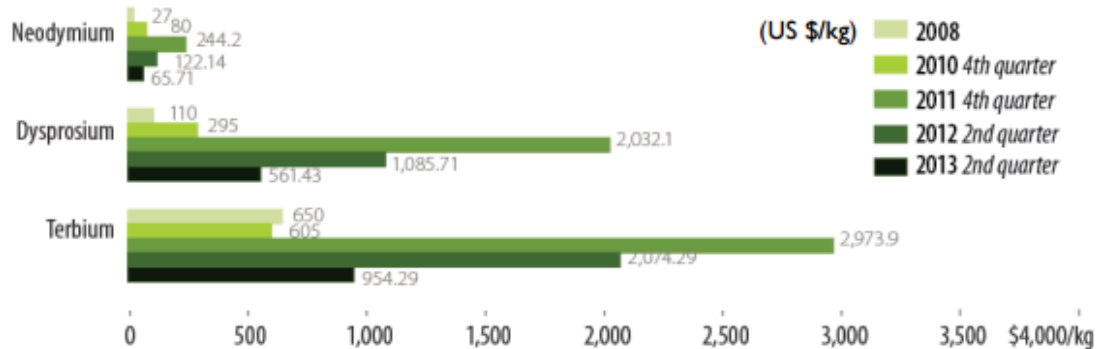


Figure 1.2. Selected Rare Earth Oxide Prices, 2008-2013 (US \$/kg) (adapted from [19]).

Country	Mine Production (metric tons)	% of total	Reserves (million metric tons)	% of total	Reserve Base (million metric tons)	% of total
United States	none		13.0	13	14.0	9.3
China	105,000	95	55.0	50	89.0	59.3
Russia	NA		19.0	17	21.0	14
Other	---		---	---	---	---
Total	111,000		110.0		154	

Table 1.1. Rare Earth Elements: World Production and Reserves in 2011(adapted from [19]).

Thus, the reduction of Dy/Tb content in neodymium magnets with high operating temperatures is a high priority. Till now several solutions have been developed like two-alloy sintering route and the grain boundary diffusion method [20,21,22,23]. An alternative solution could rely on another material with high magnetic properties and no need of high-cost heavy rare earth additives such as Dy and Tb to improve coercivity and thermal stability: SmFeN intermetallic compound meets all these requirements. Intrinsic magnetic properties of Sm₂Fe₁₇N_x (x~3) are comparable with these of NdFeB magnets: high Curie temperature (476°C and 265°C, respectively), high remanence (1226 emu/cm³ and 1280 emu/cm³, respectively) and large anisotropy field (anisotropy constant K₁, 8.6·10⁷ erg/cm³ and 4.9·10⁷ erg/cm³). However, since SmFeN magnets were reported for the first time in 1990 [24], no significant progress in their production was achieved because conventional sintering techniques cannot be applied due to decomposition of SmFeN compound into α-Fe and SmN phases at temperatures higher than 500°C. Nowadays non-conventional techniques such as

⁶ According to the Ministry of Economy Trade and Industry (METI) of Japan, prices for dysprosium and neodymium metals rose dramatically. The price for dysprosium metal rose from \$250/kg in April 2010 to \$2,840/kg by July 2011, while the price for neodymium metal rose from \$42/kg in April 2010 to \$334/kg in July 2011. 2011 prices taken from CRS Report R42510, China's Rare Earth Industry and Export Regime: Economic and Trade Implications for the United States, by Wayne M. Morrison and Rachel Y. Tang. Prices for 2012 (Q-2) and 2013 (Q-2) were obtained from the Lynas Corp. Ltd., Quarterly Report, June 2013.

Spark Plasma Sintering (SPS) [25], Shock Compression [26] and Explosion Sintering [27] are applied for SmFeN bulk samples fabrication. In this work, an original approach has been developed to fabricate bulk SmFeN-based magnets from commercially available powders. It relies on the specific technique of net-shaping bulk magnets from nano- and micro-metric powders using dry powder compaction [28]. The developed technology based on magnetic pre-alignment of the raw powder and following Spark Plasma Sintering, has shown the potential to fabricate highly dense compacts at low temperatures, which is very attractive for bulk magnet processing. The structural characterization of raw powders and as-sintered magnets has been carried out in Tomsk, while magnetic characterization has been conducted in Grenoble (macroscopic measurements with a range of magnetometers). The impact of the initial magnetic powder composition, the use of metallic binders, magnetic powder pre-alignment and sintering parameters on structural and magnetic properties of bulk samples has been studied. This work has been carried out in the context of a number of on-going projects dealing with hard magnetic materials (Nissan collaboration). The additional experiments on bulk magnets fabrication by a novel approach called High Voltage Electric Discharge Compaction Technique [29] have been carried out in collaboration with the National Research Nuclear University MEPhI, Moscow. The obtained results are promising, but require additional time for detailed study. The work on SmFeN-based magnets has already been presented in national (Russian) and international conferences [30,31], and the first experimental results can be found in [32]. The overall description of this work will be provided in another manuscript written according to the rules of the Russian Federation for PhD students; the defence is planned in 2017.

As a result, much effort is now going into developing original fabrication approaches and micro/nano scale magnetic characterization techniques. Both of these complementary aspects have been studied in the framework of the PhD project between Université Grenoble Alpes (UGA and Néel Institute Grenoble, France) and Tomsk Polytechnic University (TPU, Tomsk, Russia). A novel approach to bulk magnets fabrication based on dry powder compaction technique has been studied in Tomsk while the advanced magnetic characterization of these bulk magnets, as well as micromagnets developed at the Néel Institute has been carried out in Grenoble.

The manuscript is organized as follows:

- The first chapter provides a general introduction on magnetic materials where the main parameters characterizing dia-, para- and ferro-magnets are explained and a particular attention is paid to magnetic microspheres. Finally, a short review of the state of the art to handle spheres at micro/nano-scale concludes this introduction chapter.
- The second chapter is focused on the description and applications of micromagnet arrays. It includes an introduction on thick film preparation using the high deposition rate triode sputtering equipment of the Néel Institute. The first part of this chapter describes and compares procedures used to fabricate micromagnet arrays: Thermo Magnetic Patterning (TMP), Topographic Patterning (TOPO) and Micro Magnetic Imprinting (μ MI). The second part of the chapter provides a wide range of experiments demonstrating potential of such magnetic flux sources applications in biology and medicine to deviate species (e.g. cells, bacteria) functionalized with magnetic nanoparticles; to separate out magnetic microspheres from non-magnetic ones and to trap biological cells tagged with magnetic nanoparticles. For comparison of experimental results with the predicted ones, several models describing magnetic microsphere – micromagnet array system are presented. Most important in terms of personal involvement have been fabrication of μ MI samples, conduction of basic trapping experiments and adaptation of the models to describe conducted experiments.
- The third chapter is focused on experimental tools and techniques used in the context of this work. It presents the preliminary study on micromagnet arrays with Scanning Force Microscopy techniques such as Atomic and Magnetic Force Microscopy (AFM/MFM). Two original approaches developed during my PhD work to produce smart probes for Micro Particle Force Microscopy are described in details. Thanks to these magnetic microsphere probes, direct and quantitative measurements of the force acting on the microsphere above a micromagnet array are performed. Most important in terms of personal involvement have been qualitative and quantitative AFM/MFM characterization of micromagnet arrays and fabrication of smart MFM probes.
- The fourth chapter concerns detailed AFM/MFM analysis of the micromagnet array and its interaction with a single magnetic (sub)micro-object. It provides the comprehensive description of the model used for numerical simulation. The outcome of this analysis constitutes the first direct quantitative measurements of the interactions (magnetic force and force gradient) exerted by a micromagnet on a well-define magnetic micro-object.
- All the main results are summarized in conclusions and new directions for micromagnet arrays and smart probes applications are provided in prospects.

References

- 1 “The Role of Magnetic Forces in Biology and Medicine”, B.J. Roth, *Exp Biol Med* (Maywood) 236(2), pp. 132–137 (2011).
- 2 “The use and abuse of magnets in healthcare”, J. E. Upledger, *Journal of Bodywork and Movement Therapies*, Volume 3, Issue 2, pp. 67-73 (1999).
- 3 “Magnetism and microfluidics”, N. Pamme, *Lab Chip*. 6 (1), pp. 24-38 (2006).
- 4 “Microfluidic applications of magnetic particles for biological analysis and catalysis”, M.A.M. Gijs, F. Lacharme, U. Lehmann, *Chem. Rev.* 110, pp. 1518-1563 (2010).
- 5 “Magnetic nanoparticles for drug delivery”, M. Arruebo, R. Fernandez-Pacheco, M.R. Ibarra, J. Santamaria, *Nano Today* 2 (22) (2007).
- 6 “Local control of magnetic objects in microfluidic channels”, C. Derec, C. Wilhelm, J. Servais, et al. *Microfluid Nanofluid* 8, p. 123 (2010).
- 7 “Functional magnetic particles for medical application”, M. Shinkai, *Journal of Bioscience and Bioengineering*, Volume 94, Issue 6, pp. 606-613 (2002).
- 8 “Evolutionary conservation of early mesoderm specification by mechanotransduction in Bilateria”, T. Brunet, A. Bouclet, P. Ahmadi, D. Mitrossilis, B. Driquez, A.-C. Brunet, L. Henry, F. Serman, G. Béalle, C. Ménager, F. Dumas-Bouchiat, D. Givord, C. Yanicostas, D. Le Roy, N.M. Dempsey, A. Plessis, E. Farge, *Nat. Commun.* 4 (2821) (2013).
- 9 “Micromagnet structures for magnetic positioning and alignment”, L. F. Zanini et al, *J. Appl. Phys.* 111, 07B312(2012).
- 10 “Micro-patterning of NdFeB and SmCo magnet films for integration into micro-electro-mechanical-systems”, A. Walther et al, *Journal of Magnetism and Magnetic Materials*, Vol. 321, No. 6, pp. 590–594 (2009). *Current Perspectives: Perpendicular Recording*.
- 11 “Thermomagnetically patterned micromagnets”, F. Dumas-Bouchiat et al, *Applied Physics Letters*, Vol. 96, No. 10, 102511 (2010).
- 12 “Procédé de fabrication d’un film comprenant des microstructures magnétiques tridimensionnelles,” N. M. Dempsey and F. Dumas-Bouchiat, Patent FR1254667(2012).
- 13 “Micro-magnetic imprinting of high field gradient magnetic flux sources” N.M. Dempsey et al, *Appl. Phys. Lett.* 104, 262401 (2014).
- 14 “Magnetic particle imaging with a cantilever detector”, J. W. Alldredge and J. Moreland, *Journal of Applied Physics* 112, 023905 (2012).
- 15 “High-energy product neodymium-iron-boron permanent magnets”, J. J. Croat, J. F. Herbst, R. W. Lee, and F. E. Pinkerton, *J. Appl. Phys.* 55, p. 2078 (1984).
- 16 “New material for permanent magnets based on neodymium and iron”, M. Sagawa, S. Fujimura, M. Togawa, H. Yamamoto, and Y. Matsuura, *J. Appl. Phys.* 55, pp. 2083-2087 (1984).
- 17 “Magnetic Materials and Devices for the 21st Century: Stronger, Lighter, and More Energy Efficient”, O. Gutueisch, M. A. Willard, E. Bruck, C. H. Chen, S. G. Sankar, and J. P. Liu, *Adv. Mater.* 23, pp. 821-842 (2011).
- 18 “The partitioning of Dy and Tb in NdFeB magnets: A first-principles study”, X. B. Liu and Z. Altounian, *Journal of Applied Physics* 111, 07A701 (2012).
- 19 “Rare Earth Elements: The Global Supply Chain”, M. Humphries, CRS Report for Congress December 16 (2013).
- 20 “Microstructure analysis of sintered Nd-Fe-B magnets improved by Tb-vapor sorption”, N. Watanabe, M. Itakura, N. Kuwano, D. Li, S. Suzuki, and K. Machida, *Mater. Trans.* 48, pp. 915-918 (2007).
- 21 “Dysprosium-saving improvement of coercivity in Nd-Fe-B sintered magnets by Dy₂S₃ additions”, A. M. Gabay, M. Marinescu, W. F. Li, J. F. Liu, and G. C. Hadjipanayis, *J. Appl. Phys.* 109, 083916 (2011).
- 22 “Coercivity enhancement in Nd-Fe-B sintered permanent magnet by Dy nanoparticles doping”, W. Q. Liu, H. Sun, X. F. Yi, X. C. Liu, D. T. Zhang, M. Yue, and J. X. Zhang, *J. Alloys Compd.* 501, pp. 67-69 (2010).
- 23 “Tb nanoparticles doped Nd–Fe–B sintered permanent magnet with enhanced coercivity”, M. Yue, W. Q. Liu, D. T. Zhang, Z. G. Jian, A. L. Cao, and J. X. Zhang, *Appl. Phys. Lett.* 94, 092501 (2009).
- 24 “Improved magnetic properties by treatment of iron-based rare earth intermetallic compounds in ammonia”, J. M. D. Coey and H. Sun, *Journal of Magnetism and Magnetic Materials*, 87, pp. L251-

L254 (1990).

25 “Magnetic properties of anisotropic Sm–Fe–N bulk magnets produced by spark plasma sintering method”, T. Saito, *Journal of Magnetism and Magnetic Materials* 320 pp. 1893–1897 (2008).

26 “Magnetic properties of fully dense Sm₂Fe₁₇N_x magnets prepared by shock compression”, T. Mashimo, X. Huang, S. Hirose, K. Makita, Y. Kato, S. Mitsudo, M. Motokawa, *Journal of Magnetism and Magnetic Materials* 210 pp. 109-120 (2000).

27 “Magnetic properties of sintered Sm₂Fe₁₇N_y magnets”, B. Hu, X. Rao, J. Xu, G. Liu, Y. Wang and X. Dong, *J. Appl. Phys.* 74 (1), 1 (1993).

28 “Method for compacting powder materials into articles and a mold for implementing the method”, E. S. Dvilis, O. L. Khasanov, V. M. Sokolov, J. P. Pokholkov, US patent –No. 6919041 (2005). Euro patent application –No. EP 1459823 A1 (2004).

29 “High Voltage Electric Discharge Consolidation of Tungsten Carbide - Cobalt Powder, Nanocomposites with Unique Properties and Applications in Medicine and Industry”, E. Grigoryev, Dr. J. Cuppoletti (Ed.), ISBN: 978-953-307-351-4, InTech (2011).

30 “Fabrication of SmFeN-based magnets by spark-plasma sintering technology”, S.A. Ponomareva et al, VI Russian Conference of Young Scientists "Materials science, technology and the environment in the third millennium", Institute of Strength Physics and Materials Science of the Siberian Branch of the Russian Academy of Sciences (ISPMS SB RAS), Tomsk, Russia, 11-13 May 2016.

31 “Micro-structure and magnetic properties of Zn-doped SmFeN magnets produced by Spark Plasma Sintering”, J.P. Loison, S.A. Ponomareva, V.V. An and O.L. Khasanov, Proceeding of 7th International Conference “Nanoparticles, nanostructured coatings and microcontainers: technology, properties, applications”, p.45, Tomsk, Russia, 12-15 May 2016.

32 “Fabrication of SmFeN-based magnetic materials by Spark Plasma Sintering method”, S.A. Ponomareva, O.L. Khasanov, F. Marchi, N.M. Dempsey, V.V. An, A.O. Khasanov, *Fundamental research*, No. 10(3), pp. 548-554 (2016).

Chapter I: Introduction

- I. Introduction..... 21**
- I.1 Characteristics and classification of magnetic materials: dia-, para- and ferro-magnetism 22
- I.2 *Hard* and *soft* magnetic materials 24
- I.3 Magnetic flux sources 27
- I.4 Description of magnetic particles 28
- I.5 Short review on (sub)microparticle manipulation 31
- References 35

I. Introduction

First attempts to understand magnetic nature of materials have been done around 2500 years ago by philosophers of Greece, China and India [1,2,3]. Ancient people studied the lodestones, which are naturally magnetized pieces of iron ore. The first detailed description of their magnetic properties was introduced by Pliny the Elder [4].

In XII-XIII centuries magnetic materials became more and more employed for different applications. For example, the mariners of Europe and China were using compass with the floating magnetic needle for navigation. However, the explanation of the relation between the iron needle orientation and the Earth's magnetic field was proposed only three hundred years later by William Gilbert which carried out a number of experiments trying to explain magnetic properties of materials [5].

In XIX-XX centuries significant step in understanding of magnetism has been done. The discoveries of Oersted, Ampere, Arago and Faraday were unified by theory of electricity, magnetism and light of James Clerk Maxwell [6]. Deep comprehension of magnetism combined with variety of new technologies has led to a significant progress in elaboration of magnetic materials in the XX century [7].

The first noteworthy event was the transition from steel-based magnets to AlNiCo with high shape anisotropy. The main fabrication techniques were casting and powder technology. The energy product calculated from the response of magnetic material submitted to an external magnetic field (Figure 1.7), reaches 15 MGOe nowadays for AlNiCo [8].

The next important step in the development of permanent magnets was the discovery of ceramic magnets with hexagonal structure in the middle of XX century [9]. Unlike AlNiCo they provide high magneto crystalline anisotropy and therefore, high coercivity. However, low working temperatures (below 300°C) and magnetic induction limit the energy product up to 5 MGOe decreasing the number of possible applications.

The discovery of rare earth intermetallic compounds was one of the most important breakthroughs in the development of permanent magnets. SmCo magnets (SmCo₅ –1:5 type and Sm₂Co₁₇ –2:17 type) represent the first and the second generations of rare earth based permanent magnets providing high magneto crystalline anisotropy, magnetic induction and Curie temperature. The energy product for 1:5 type reaches 18-24 MGOe [10] and for 2:17 type is up to 34 MGOe [11].

Taking into account the high price of Co-based magnets research was then focused on the development of the third generation magnets that combine lower price with excellent magnetic properties. In 1984 two groups of researchers reported about discovery of NdFeB compounds [12,13,14,15]. Nowadays these magnets exhibit the best magnetic properties; their fabrication procedure is well developed and magnetic energy $(BH)_{max}$ (55 MGOe) has almost reached its theoretical maximum.

SmFeN intermetallic compound can be considered as an alternative to NdFeB magnets. They exhibit excellent intrinsic magnetic properties such as high Curie temperature (34% higher than for NdFeB), high saturation magnetization (10% higher than for NdFeB) and large anisotropy field (two times higher than for NdFeB). In the additional PhD manuscript written in Russian the study of structural and magnetic properties of SmFeN-based magnets fabricated by Spark Plasma Sintering and High Voltage Electric Discharge Compaction techniques will be presented.

The sketch demonstrating the main steps in the development of permanent magnets and their energy products $(BH)_{max}$ is presented in Figure 1.3

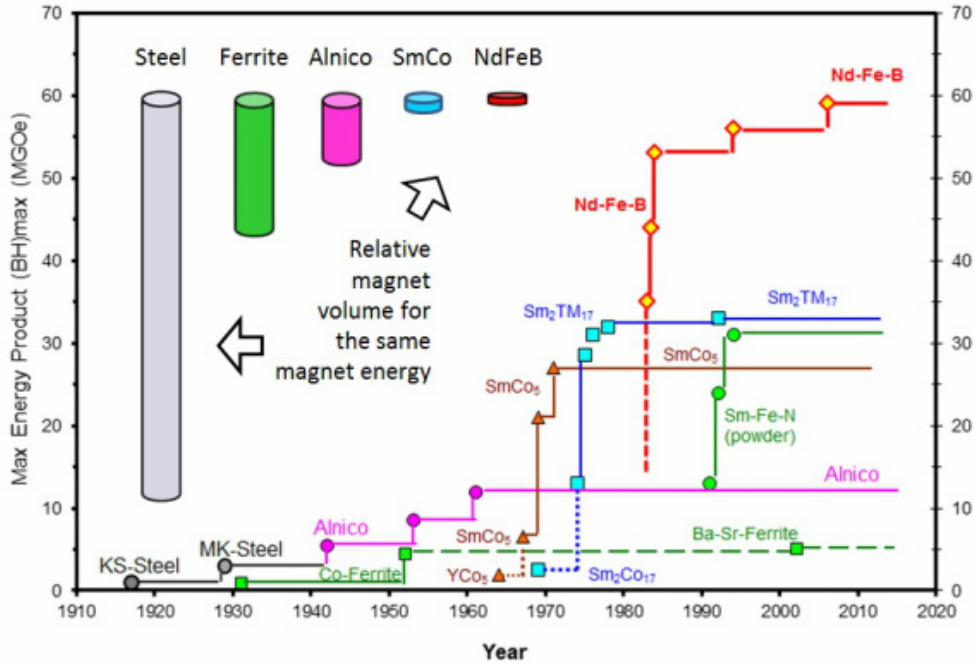


Figure 1.3. Development of permanent magnets [16].

To date, rare earth magnets are used in the automotive industry, for the production of wind turbines, most of electric appliances, in biology, and many other areas.

To characterize magnetic materials studied in this work the following concepts will be introduced: induction, susceptibility, permeability, remanence, coercivity and so on. Depends on the behaviour of material in presence/absence of magnetic field it can be classified as diamagnetic, paramagnetic or ferromagnetic. In the next sections magnetic properties will be discussed; main attention will be paid to the permanent magnets (in particular micromagnet arrays) and magnetic microparticles which have been studied in this work.

I.1 Characteristics and classification of magnetic materials: dia-, para- and ferromagnetism

Each material provides intrinsic response to the magnetic field H , which is called magnetization M . For isotropic materials both, magnetic field H and magnetization M are aligned along the same axis inside the material. Magnetic induction B takes into account both the magnetic field H and the magnetization M inside a magnetic material and expresses the relation between these two terms:

$$\vec{B} = \mu_0 \vec{H} + \mu_0 \vec{M}, \quad (1.1)$$

where $\mu_0 = 4\pi \cdot 10^{-7} \text{N/A}^2$ is the permeability of free space.

The ratio between magnetization M and magnetic field H describes the magnetic susceptibility:

$$\chi = M/H \quad (1.2)$$

Thus, the magnetic induction B can be expressed in terms of susceptibility χ :

$$\vec{B} = \mu_0 \vec{H} + \mu_0 \chi \vec{H} = \mu_0 (1 + \chi) \vec{H} = \mu_0 \mu_r \vec{H} = \mu \vec{H}, \quad (1.3)$$

where $\mu_r = \mu/\mu_0$ is the relative permeability and μ is the permeability of a specific medium (magnetic material).

Based on sign and magnitude of magnetic susceptibility χ providing the relation between magnetic field and magnetization, magnetic materials can be classified as diamagnetic, paramagnetic and ferromagnetic (phenomenological classification) (Figure 1.4). This approach ignores the nature of microscopic carriers of magnetism and does not consider their interaction, so magnetic states like antiferromagnetic and ferrimagnetic cannot be recognized.

Detailed description of all types of magnetism can be found in [17], here only diamagnetic, paramagnetic and ferromagnetic materials will be discussed.

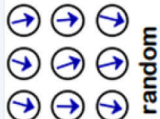
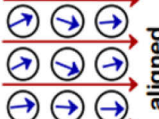
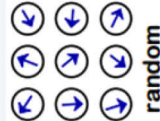
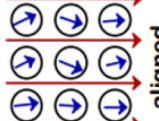
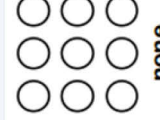
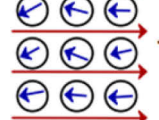
	No Applied Magnetic Field ($H = 0$)	Applied Magnetic Field (H)
Ferromagnetic material ($\mu \gg \mu_0$)	 random	 aligned
Paramagnetic material ($\mu > \mu_0$)	 random	 aligned
Diamagnetic material ($\mu < \mu_0$)	 none	 opposing

Figure 1.4. Magnetic moments behaviour for ferromagnetic, paramagnetic and diamagnetic materials with and without external magnetic field H .

Diamagnetic material

The susceptibility of diamagnetic materials is always negative (in the range from -10^{-6} to -10^{-4}) and usually does not depend on the temperature. In such materials (for example, carbon, copper, water, silicon) atoms and molecules do not have net magnetic moment⁷. The presence of magnetic field induces a weak opposite magnetization to the applied field direction (Figure 1.4). All the materials exhibit diamagnetic properties but often these effects are weak and can be neglected. Diamagnetic materials have applications in microsystems [18,19,20] and for actuated magnetic levitation [21,22].

Paramagnetic material

The susceptibility of paramagnetic materials is positive (in the range from 10^{-4} to 10^{-3}) and depends on the temperature. For such materials the magnetization decays with increase of the temperature. This dependence can be described by Langevin equation:

$$M = M_0 \left[\coth(x) - \frac{1}{x} \right], \quad x = \frac{\mu_0 m_0 H}{k_B T} \quad (1.4)$$

where M_0 is the saturation magnetization at 0 K, m_0 is the magnetic moment modulus, k_B is the Boltzmann constant and T is the temperature.

In paramagnetic materials atoms have a net magnetic moment. Without application of magnetic field they do not interact with each other and are free to rotate in any direction. When such material is submitted to external magnetic field the global moment is aligned in the direction parallel to the applied field creating net magnetization (Figure 1.4). After removal of the field it becomes zero again. This behaviour can explain lower magnetization of paramagnetic materials at higher temperatures: heating induces the thermal agitation of magnetic moments leading to lower alignment with an applied field.

⁷ Net magnetic moment is the sum of moments from all electrons.

Ferromagnetic material

The properties of ferromagnetic material are similar to paramagnetic ones: the susceptibility is positive (usually in the range from 10^4 to 10^5) and decays with increase of the temperature due to the thermal agitation of the moments. The temperature corresponding to the situation where the thermal agitation of magnetic moments overcomes coupling interaction is called the Curie temperature, T_c . Heating the magnetized ferromagnetic material above the Curie temperature is one of the ways to demagnetize it. Ferromagnets as well as paramagnets have net atomic moment, but the moments are strongly coupled together. When ferromagnetic material is submitted to an external field, the moments rotate in order to align parallel to the applied field direction until the material reaches saturation. When the field is removed, due to preferential orientation of individual magnetic moments the global moment of ferromagnet after magnetization is not equal to zero. At this point if the material is magnetized again but in opposite direction until the saturation and then magnetized along the initial direction, the magnetization as a function of the field exhibit hysteresis behaviour.

The comparison of ferromagnetic, paramagnetic and diamagnetic materials is provided in Table 1.2. The detailed analysis of the hysteresis loop (or magnetization curve, $M(H)$) of ferromagnetic material is presented in the next section and helps to classify the magnets according to their properties. This knowledge assists to choose the right magnetic material depending on the application.

	Diamagnetic material	Paramagnetic material	Ferromagnetic material
Permanent dipole moments	Do not have permanent dipole moments	Have permanent dipole moments	Have enormous permanent dipole moments
Spin alignment	No spin moment	All spins or magnetic moments are randomly oriented	All spin moments are parallel oriented
Interaction between dipoles	No interaction exist	The interaction between dipoles is either negligible or they do not interact among themselves	The interaction between dipoles results in a parallel orientation of all dipoles. A spontaneous magnetization exists in the material
Net intrinsic moment	The electrons of each pair have orbital motion and spin motion in opposite sense. Thus the resultant magnetic dipole moment is zero	The magnetic fields due to the orbiting and spinning electrons do not cancel out. A net intrinsic moment is induced	The magnetic fields due to the orbiting and spinning electrons do not cancel out. Thus there is a net intrinsic moment. A large number of unequal electron pairs induces large net intrinsic moment
Susceptibility	Negative; independent of temperature	Positive and small; inversely proportional to the absolute temperature	Positive and large; depends on the temperature

Table 1.2. The comparison of ferromagnetic, paramagnetic and diamagnetic materials (adapted from [23]).

1.2 Hard and soft magnetic materials

The total magnetization of ferromagnetic material can be equal to zero, when Weiss domains (regions where the coupled moments are spontaneously aligned together, Figure 1.5a) are oriented randomly with no preferential direction. However, the domains inside magnetic material have tendency to minimize the energy; the interface between them is the

transition zone, where magnetic moments orientation is gradually changed from one direction to another according to magnetization of neighbouring domains. These zones called Bloch walls⁸ provide a response to an applied magnetic field (Figure 1.5b). For high anisotropy materials the width of Bloch wall is about few nanometres (3 ± 2 nm for $\text{Nd}_2\text{Fe}_{14}\text{B}$, [24]).

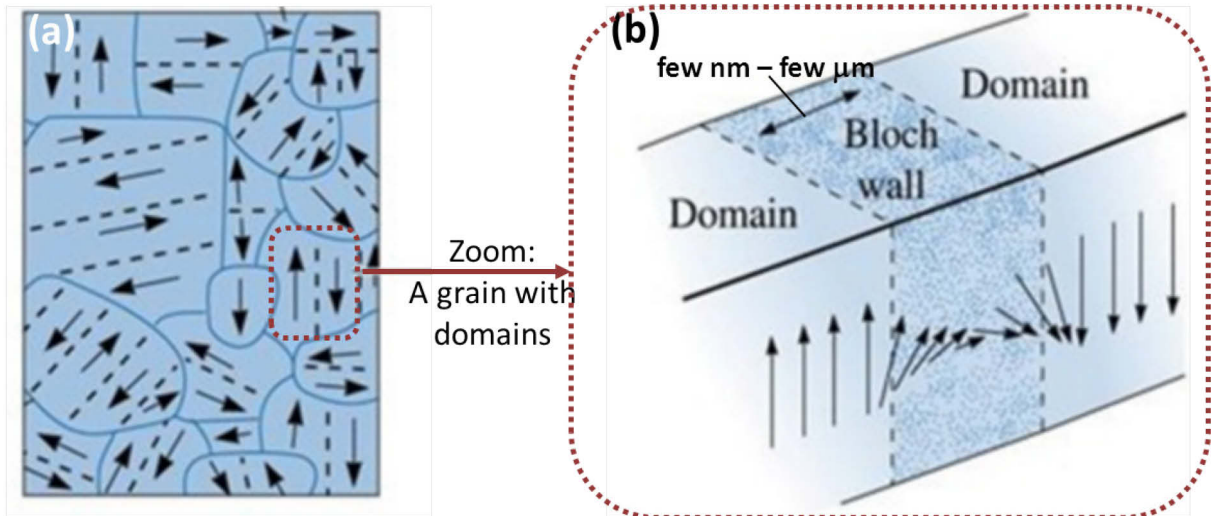


Figure 1.5. (a) A qualitative sketch of magnetic domains in a polycrystalline material. The dashed lines show demarcation between different magnetic domains; the dark blue curves show the grain boundaries. (b) The magnetic moment in adjoining atoms changes its direction continuously across the boundary between domains [25].

The magnetization M as a function of applied field H (*hysteresis loop or $M(H)$ curve*) for ferromagnetic material and the orientation of magnetic moments under external field are shown in Figure 1.6.

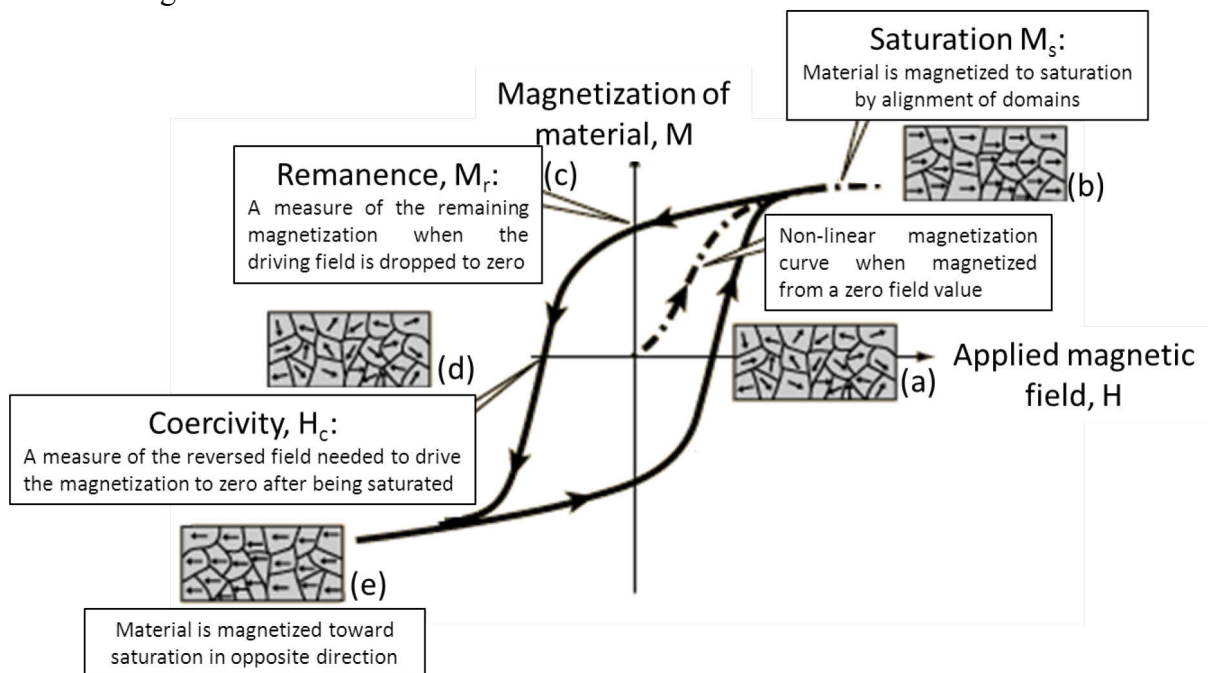


Figure 1.6. $M(H)$ hysteresis loop of ferromagnetic material.

⁸ Bloch wall is a narrow transition region at the boundary between magnetic domains, over which the magnetization changes from its value in one domain to that in the next. Bloch walls are usually preferable in bulk materials, i.e. when dimensions of magnetic material are considerably larger than domain wall width. Magnetic moments within Bloch wall rotate gradually along the axis perpendicular to the wall. In very thin film where the exchange length is very large compared to the thickness, Néel wall (narrow transition region between magnetic domains) is the common magnetic domain wall type. Magnetic moments within Néel wall rotate along direction parallel to the wall.

The main parameters to describe ferromagnetic material can be extracted from a hysteresis loop. For better understanding of magnetic properties of a chosen material, its structure, in particular Weiss domains behaviour under applied magnetic field should be discussed. Initially, a ferromagnetic material consists of magnetic domains with random orientation (Figure 1.6 (a)). Applied magnetic field leads to reorientation of magnetic moments towards its direction. Displacement of Bloch walls causes the growth of domains with magnetic moments parallel to applied field while reduction of other domains is observed. When all the moments are aligned with magnetic field the saturation state M_s is reached (Figure 1.6 (b)).

Removal of the field leads to decrease of magnetization: some magnetic moments are reoriented, some keep the magnetization parallel to the previously applied field (Figure 1.6 (c)). The magnetization remaining after magnetic field is dropped to zero is called remanent magnetization or remanence M_r .

If on previously saturated material an opposite magnetic field is applied, at a certain moment the global magnetization will drop to zero due to alignment of domains with preferential directions (Figure 1.6 (d)). The field inducing zero global magnetization of saturated magnetic material is called coercivity field or coercivity H_c . Following increase of an opposite magnetic field leads to magnetization toward saturation in opposite direction (Figure 1.6 (e)).

According to the coercivity value magnetic materials can be divided in two groups: *soft* and *hard* magnets. Magnetically *soft* materials are easier to demagnetize after the saturation state, the H_c value is low ($\mu_0 H_c$ is typically less than 10^{-3} T), while *hard* magnetic materials provide high coercivity ($\mu_0 H_c$ is usually in the range between 0.5 and 2 T). Typical hysteresis loops for *soft* and *hard* ferromagnetic materials are presented in Figure 1.7 (a, b).

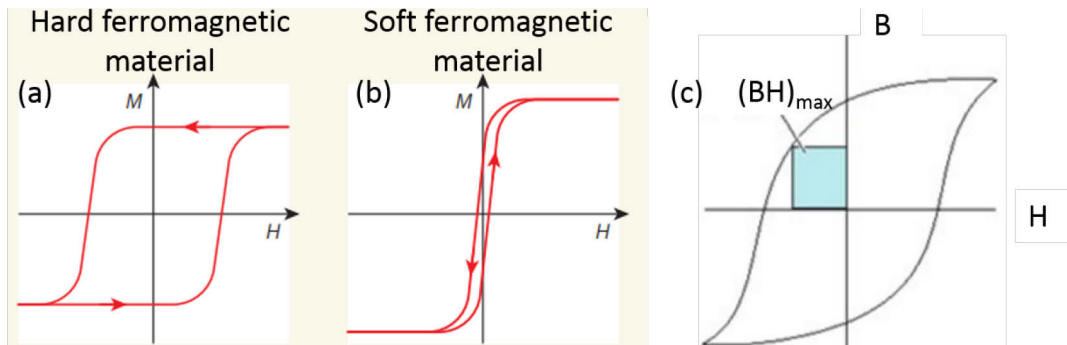


Figure 1.7. Typical $M(H)$ hysteresis loops of (a) *hard* and (b) *soft* ferromagnetic material (adapted from [26]). (c) $B(H)$ hysteresis loop with the energy product $(BH)_{max}$ related to the power or energy required to demagnetize the magnet.

The area inside the hysteresis loop is related to the amount of energy dissipation upon reversal of the field. Coercivity and remanence are the main extrinsic properties of a magnet that can be found from the hysteresis loop or so-called $M(H)$ or $B(H)$ plot. To convert $M(H)$ into $B(H)$ the equation (1.1) can be applied. $B(H)$ curve define the energy that a magnet can store: the so-called energy product $(BH)_{max}$ is calculated from the demagnetization curve (fourth quadrant of the hysteresis loop) and equal to the maximum of the B and H product (Figure 1.7 c).

Usually *soft* magnetic materials are employed for transformers and motor cores to minimize the energy dissipation with the alternating fields associated with AC electrical applications. Hard magnetic materials are applied for permanent magnets production and magnetic recording/memory devices.

The work described in this manuscript focuses mainly on study of micromagnet arrays made of permanent NdFeB magnets. The typical properties of bulk neodymium magnets in comparison with several *hard* magnetic materials (in chronological order) are presented in Table 1.3.

Material	Composition (wt%)	Remanence B_r (T)	Coercivity H_c (A/m)	$(BH)_{max}$ (kJ/m ³)	Curie temperature T_c (C)
Tungsten steel	92.8 Fe; 6 W; 0.5 Cr; 0.7 C	0.95	5900	2.6	760
Sintered AlNiCo	34 Fe; 7 Al; 15 Ni; 35 Co; 4 Cu; 5 Ti	0.76	125000	36	860
Sintered ferrite	BaO-6Fe ₂ O ₃	0.32	240000	20	450
Cobalt rare-earth	SmCo ₅	0.92	720000	170	725
Sintered NdFeB	Nd ₂ Fe ₁₄ B	1.16	848000	255	310

Table 1.3. Magnetic properties of several *hard* magnetic materials [27].

I.3 Magnetic flux sources

Depends on the structure and magnetic properties of materials, some of them can be considered as magnetic flux sources providing high magnetic field and field gradient. Three main types of magnetic flux sources are soft magnets, electromagnets and permanent magnets. One of the most developed areas is a production of *soft magnets* as sources of high field gradients for Micro-Electro-Mechanical Systems (MEMS). The attraction of soft magnets can be explained by no need of external power sources (the polarizing field is produced by a permanent magnet) and absence of Joule heating while generating a magnetic field. Soft magnets show a significant magnetization only when they are polarized by an external magnetic field; in absence of the polarizing field, these materials create virtually zero stray fields. Thus, they provide a possibility to switch “on” and “off” magnetic field easily.

Electromagnets can modulate a magnetic field locally and very precisely by adjusting the current they conduct. Today this technique is widely spread in such devices as Helmholtz coils used to act on microscopic bacteria and micro-coils built below microfluidic channels [28]. The main drawback of using electromagnets (especially in biological applications) is the Joule heating while generating a magnetic field.

Permanent magnets considered as sources of magnetic flux, have to be distinguished between macro-scale (or bulk) and micro-magnets. Despite the same physical phenomena behind, the fabrication techniques are very different. Bulk magnets were the first sources of magnetic field in microfluidic devices. Rare-earth permanent magnets of different size and shape produce high field at large distance, but their field gradient is restricted to the edges of the magnet. To generate a significant magnetic force on an object, both high magnetic field and field gradient are required.

Arrays made of permanent micromagnets are specifically attractive for such applications because they combine compact and autonomous character with high field gradient [29]. They are suitable for integration with lab-on-chip, microfluidic and other devices since the stray field created by these magnets is restricted to the region of interest and no need of external field is required. The drawback of permanent magnets is that they do not have “on/off” possibility and real-time modulation. Despite this disadvantage, permanent micromagnets are considered to be very promising for flow cell sorting devices. Such arrays have been used recently to separate out magnetic microspheres from non-magnetic ones, both flowing in a microfluidic channel [30] as well as to trap biological cells tagged with magnetic nanoparticles [31]. An example of microfluidic device based on micromagnet array consisted of oppositely magnetized micromagnets (“up” and “down”) is presented in Figure 1.8a. Figure 1.8b demonstrates zoom of transition between “up” and “down” neighbouring magnets, the so-called *magnetic junction* (MJ) where the highest magnetic field and field gradient are observed (Figure 1.8c).

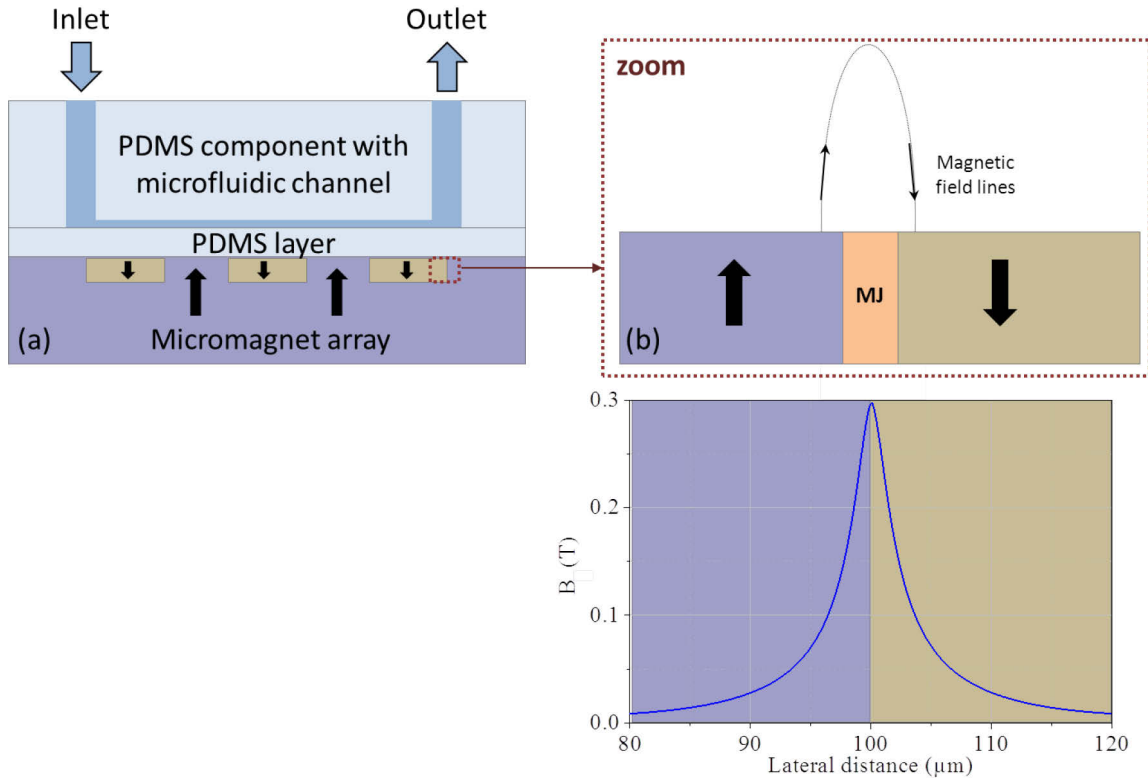


Figure 1.8. (a) Side-view schematic of microfluidic channel based on micromagnet array. (b) Zoom of transition area (magnetic junction, MJ) between two neighbouring oppositely magnetized magnets. (c) Numerical simulations of total magnetic field B above the magnetic junction.

In this work the arrays of permanent micromagnets (mainly NdFeB) used for micro- and nano-objects handling have been studied. They are the sources of high field gradients (magnetic flux sources) that can be exploited to deviate or trap species (e.g. cells, bacteria) functionalized with magnetic nanoparticles [30].

I.4 Description of magnetic particles

Nowadays magnetic particles are commonly involved in biotechnology and medicine applications where their particular properties are linked to their micro and nano-scale dimensions. For example, decrease of the sphere radius by a factor of 10^3 leads to decrease of its volume by 10^9 times, while surface-to-volume ratio increases by a factor of 10^3 . It means that such particles with small volume and large surface area thanks to attachment of specific functional components to their surface can be exploited for labelling, targeting and separation applications. Nowadays magnetic beads are commonly used for gene and drug delivery [32,33], magnetic resonance imaging (MRI) [34,35,36], hyperthermia [37,38] and so on. The applications of magnetic particles in microfluidic devices will be discussed in Chapter II.

Typical requirements for magnetic particles in such applications are the spherical shape and the narrow size distribution with an average diameter from few nanometres up to few microns (depends on the fabrication technique). Magnetic spheres can be formed by polymer matrix with embedded magnetic nanoinclusions, core-shell structures, solid magnetic spheres and etc. Manipulation of such microparticles with the field generated by permanent magnet or electromagnet, independent of normal microfluidic or biological processes is a big advantage compared to non-magnetic microparticles.

In our experiments two types of magnetic particles have been studied: *hard* (NdFeB) and superparamagnetic (iron oxide nanoparticles embedded in polystyrene matrix) microspheres. Detailed description of all the magnetic beads used in this work is presented in Chapter III, section III.3.2 (Tables 3.4 and 3.5) and in the Annex III.3. Here only basic information is provided.

Hard magnetic microspheres

NdFeB microspheres (MQP-S-11-9-20001-070, Molycorp Magnequench) have been produced by employing an atomization process followed heat treatment. Figure 1.9 presents the fourth quadrant of the hysteresis loop [39]. With their high remanence (730-760 mT) and intrinsic coercivity (670-750 kA/m), these particles are classified as *hard* magnetic material. A decrease of magnetic properties with increase of the temperature (typical for ferromagnetic materials) is observed: coercivity measured at room temperature is about two times higher than the one measured at 175°C (700 kA/m and 330 kA/m, respectively).

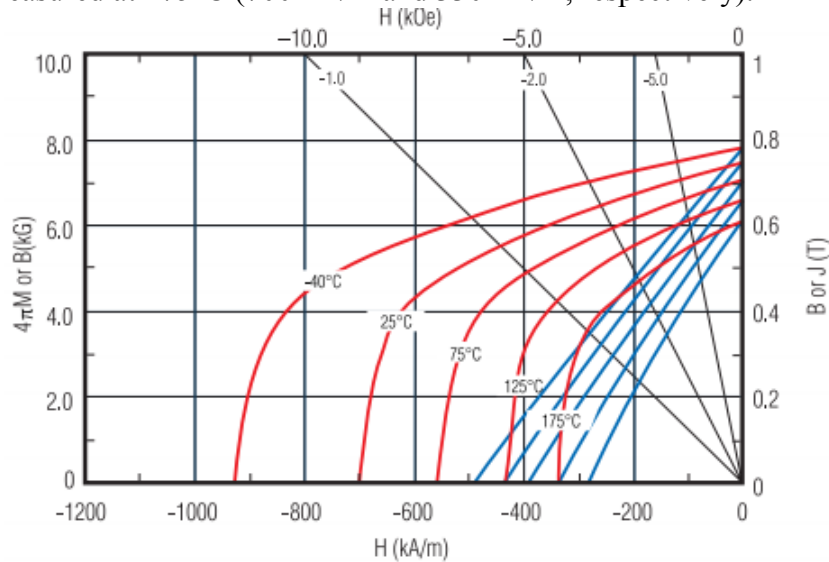


Figure 1.9. Fourth quadrant of $B(H)$ hysteresis loop for NdFeB microspheres at different temperatures (-40, 25, 75, 125, 175°C) (datasheet provided by Molycorp Magnequench, [39]).

Superparamagnetic microspheres

Superparamagnetic behaviour occurs in ferromagnetic (and ferrimagnetic⁹) single-domain particles, when their size is smaller than a particular threshold value D_{sp} (usually about 1-50 nm depends on the material). With increase of the particle dimensions the demagnetization field becomes too big to maintain a uniformly magnetized particle and the magnetization of the particle splits into multiple domains of uniformly magnetized spins (Figure 1.10).

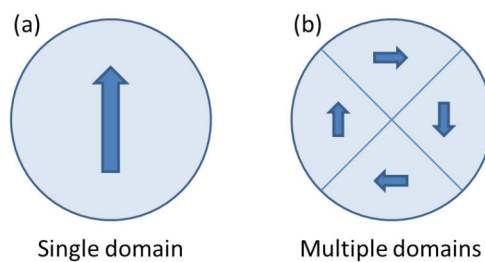


Figure 1.10. (a) A single domain particle has a net magnetic moment; (b) Net magnetic moment of multidomain particle is cancelled by the orientation of different domains.

Superparamagnetic materials behave as paramagnetic materials (hence the “paramagnetism” in the name). In presence of an external magnetic field superparamagnetic particles can be magnetized according to the applied field direction and in absence of magnetic field when the time used to measure the magnetization of the nanoparticles is much longer than the Néel relaxation time¹⁰, their magnetization appears to be in average zero.

⁹ Ferrimagnetic material is the material that has populations of atoms with opposing magnetic moments, which are unequal and a spontaneous magnetization remains.

¹⁰ In small nanoparticles, magnetization can randomly flip direction under the influence of temperature. The typical time between two flips is called the Néel relaxation time.

However, the susceptibility of superparamagnetic material is much higher than of paramagnetic one (hence the “super” in the name). In case of superparamagnetic particles used for biotechnological applications, usually they consist of polymer matrix with single-domain nanoinclusions of iron or iron oxide (such as magnetite (Fe_3O_4) or maghemite ($\gamma\text{-Fe}_2\text{O}_3$) which are stable against oxidation) that are biocompatible. To estimate the D_{sp} value in a single-domain magnetic particle (time-averaged magnetization without a magnetic field is zero) the following condition must be respect: magnetic energy of the particle should be about 10 times lower than the thermal energy $k_B T$, where k_B is the Boltzmann constant and T is the absolute temperature [40]. It should be noticed that superparamagnetic behaviour is observed below Curie temperature.

$M(H)$ magnetization curve of a collection of superparamagnetic particles used in our experiments (microParticles GmbH) is presented in Figure 1.11. Applied magnetic field aligns the particles, which results in a high net magnetic moment. Hysteresis-free behaviour ensures a fast decay of the net magnetic moment after removal of the magnetic field. It means that suspended superparamagnetic particles do not agglomerate after removal of the field (i.e. they stay suspended) while ferromagnetic particles exposed to an external magnetic field form chain-like structures along field direction (due to magnetic dipole interaction) which remain after removal of the field (Figure 1.12 a,b) [41]. This is a huge advantage of superparamagnetic particles for applications in biology and medicine, especially drug delivery: under influence of external magnetic field they can drag drug molecules to the target and when the field is switched off the probability of thrombosis or blockage of blood capillaries is minimal due to their colloidal stability. Superparamagnetic particles tagged to the biomaterial of interest can be removed from a matrix using magnetic field. The behaviour of superparamagnetic particles in comparison with ferromagnetic ones in presence of an external field is illustrated in Figure 1.12.

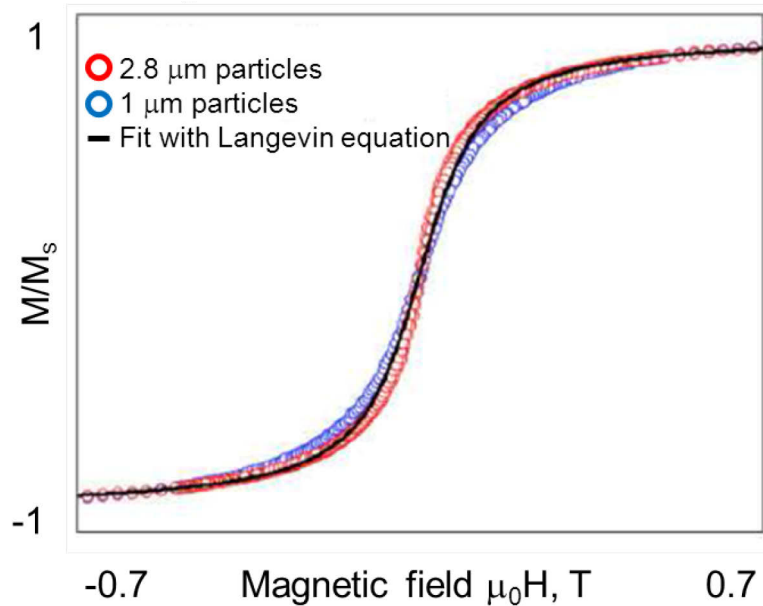


Figure 1.11. Experimental magnetization curves of superparamagnetic microspheres of 2.8 μm diameter (red) and 1 μm diameter (blue) and fitting with Langevin equation [42].

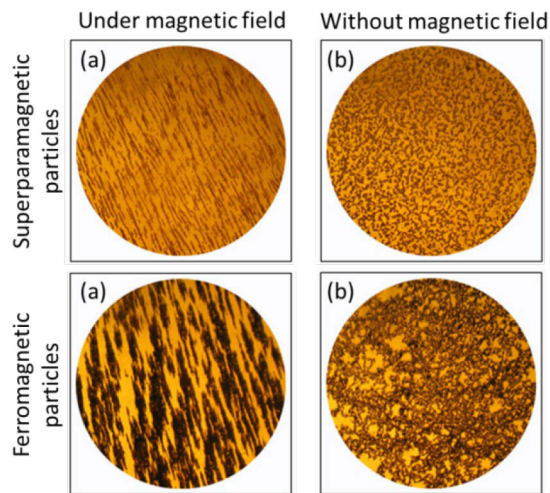


Figure 1.12. (a) Superparamagnetic particles under the influence of an external magnetic field form “chain” structure. (b) Superparamagnetic particles in absence of an external magnetic field with monodispersed particle distribution. (c) Ferromagnetic particles under the influence of an external magnetic field form “chain” structure. (d) Ferromagnetic particles in absence of an external magnetic field form aggregates [41].

I.5 Short review on (sub)microparticle manipulation

The handling of micro/nano-particles (for example, sieving, sorting or trapping) is becoming increasingly common with a range of medical and biological applications. Manipulation of cells or biomolecules is employed in various areas from in vitro fertilization to genetic engineering. Wide range of microparticles offers a highly convenient and flexible system for developing reagents for assays and bioseparations. Table 1.4 in the end of this section summarizes some traditional and recently developed approaches for manipulation of micro- and nano-objects [43].

There are several kinds of manipulations on micro/nano-particles: positioning, trapping, sorting, guiding and so on. These techniques can be based on the particles intrinsic properties, such as size, density, shape, and electrical polarizability (label-free methods) or on the extrinsic properties, such as magnetization to execute manipulation or separation from fluidic media.

This PhD work is mainly focused on measurements of the magnetic action exerted by micromagnet sample on the magnetic beads. Thus, the approaches for particle *trapping* and *positioning* will be discussed more in details. The techniques for particles *sorting* involving electric and magnetic fields, sound pressure, optical forces and gravity are summarized in [44].

The positioning and trapping of micro/nano-particles is aimed to arrange them in a particular place. The first experiments on micron-sized particles manipulations by optical forces were demonstrated in 1970 [45,46]. For the standard optical tweezers the tweezing zone is limited to the small region illuminated by the operating laser and simultaneous trap of a large number of particles is complicated due to the strong focusing requirement. The new achievement in this area (like holographic optical tweezers or plasmonic tweezers and their combination with photopolymerization) allows not only single micro/nano-particle positioning, but also formation of three dimensional structures of nanoparticles and their positioning on the substrate [47]. However, there are still some barriers that should be overcome to progress further in this area: low throughput, the accuracy of nanoparticles manipulation, heating of plasmonic structures (cooling schemes should be integrated) and so on.

Another approach to manipulate micro/nano-particles is to use the acoustic fields [48]. Transport and rotation of individual particles or agglomerates is possible and limited by

diffraction of acoustic waves (not efficient for single nanoparticles manipulations).

The particles can be trapped due to combination of physically patterned sample (usually by photolithography) and capillary forces: for example, template-assisted self-assembly (TASA) [49] (Figure 1.13). A dispersion containing colloidal polymer particles flows over the surface, the particles are trapped in the templates as the liquid drains away. The high throughput (several square millimetres in an area that contain more than 10^5 elements) and high flexibility make this method so attractive for particles positioning: depending on the geometrical shape of the template and beads dimensions, single particles positioning or formation of different assemblies (round, elongated, triangular, or hetero-aggregates) may be possible [50]. In each template hole, the beads are pushed to one particular side that tends to alignment of the assembled structures all in one direction. This is the crucial point for applications sensitive to anisotropic features (e.g., optical polarization). The TASA technique has been implemented for trapping of (sub)micron size particles (down to 50 nm). The main drawback of this method is that the capillary force decreases in effectiveness with reduction in particle size meanwhile the randomizing effects of thermal energy become more significant. Moreover, for positioning of nanometre size particles the physically patterned templates should be produced which is still difficult to accomplish routinely using e-beam lithography alone (block copolymer self-assembly and nanoimprint can be implemented [51]).

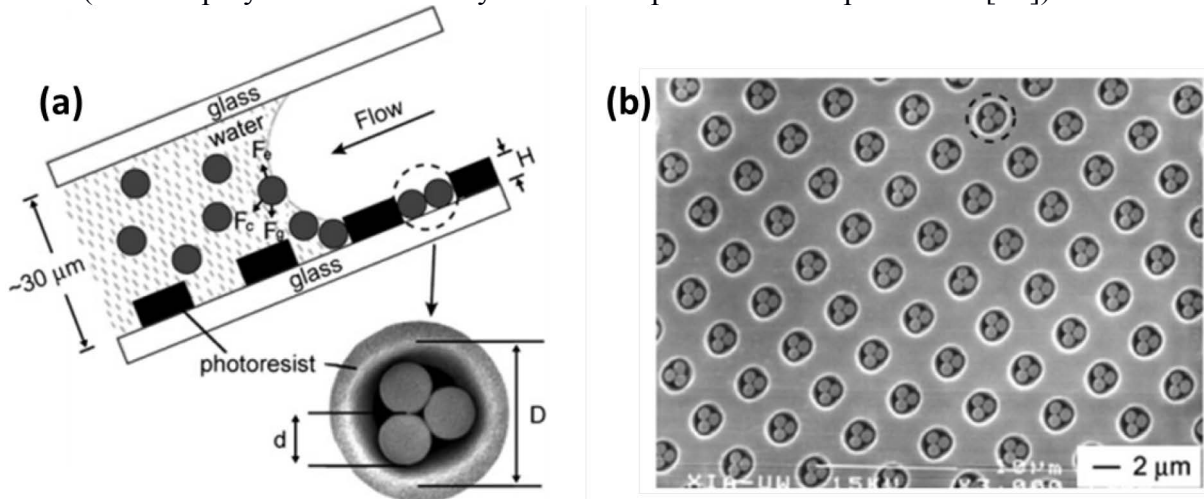


Figure 1.13. (a) A schematic illustrating the fluidic cell used in a TASA process. The template hole depth is indicated by H , the diameter of the template is D , and the diameter of the colloidal spheres is d . The possible forces that may be exerted on a colloidal sphere next to the rear edge of the liquid slug are the capillary force (F_c), gravitational force (F_g) and electrostatic force (F_e) and are illustrated above. (b) SEM image of an example of TASA where a two-dimensional array of trimmers was formed from 0.9 μm polystyrene beads [50].

Dielectrophoresis for particles manipulations was first introduced in 1978 [52]. Its principle is based on the fact that in a non-uniform electric field, the particle experiences a net dielectrophoretic force. Particle motion is determined by the magnitude and polarity of charges induced by an applied field: dielectrophoretic force will push the particle toward regions of higher electric field (if the suspended particle has polarizability higher than the medium) or toward regions of low field strength (if the medium has a higher polarizability than the suspended particle). Nowadays dielectrophoresis has reached an exciting stage including electrically-controllable trapping, focusing, translation, fractionation and characterization of particulate mineral, chemical, and biological analyses within a fluid suspending medium [53]. The main drawbacks of this approach are AC electroosmosis and possible cell damage or electroporation.

An alternative approach to trap the particles is based on application of electrostatic forces. (Nano)Xerography [54,55] demonstrates the use of trapped charge to pattern inorganic nanoparticles from a powder, gas phase (aerosol), and liquid phase (suspension) (Figure 1.14).

The charged regions are defined by a conductive stamp placed in contact with a polymer substrate that forms the electret (the charge-carrying plate used in xerography). Single particle manipulation, random particle deposition and parallel particle assembly in one, two or three dimensions structures is possible. The best achieved resolution is 100 nm (is limited by the smallest possible feature size that can be fabricated on the electrode structure) with the patterned area up to 1 cm². The main drawbacks are related to the lag in yield and speed, but they can be overcome by using self-assembly mechanisms. The implementation of Atomic Force Microscopy to generate strong local electric fields above the surface of electret thin films makes nanoxerography process simpler and faster (no need of clean room or vacuum equipment) [56].

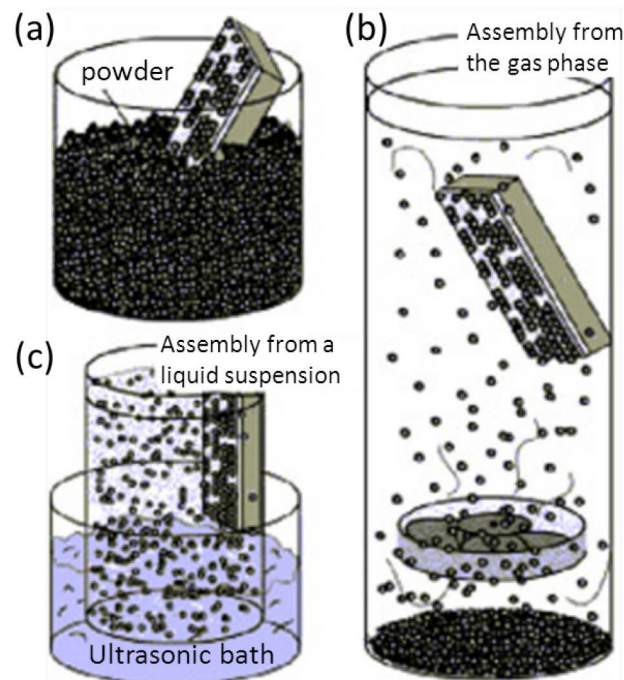


Figure 1.14. Three different methods for depositing nanoparticles on a surface patterned with electric charge: (a) The charged chip is immersed into nanoparticle powder. (b) The charged chip is exposed to nanoparticles that are suspended in the gas phase. (c) The silicon chip is immersed into a solution that contains nanoparticles that are agitated using an ultrasonic bath [54].

The use of magnetic fields is widely spread for trapping of magnetic particles or elements functionalized with these particles [31]. Bulk and micro- permanent magnets [57,58,59], electromagnets [60], soft magnets [61] are commonly used as magnetic flux sources for magnetic beads handling. Non-homogeneous magnetic field allows both, single particle or agglomerates positioning usually in liquid environment (magnetophoresis). An example of microfluidic device based on micromagnet array used for magnetically labelled bacteria trapping is presented in Figure 1.15. The main advantage of such an approach is that beads can be magnetically manipulated using magnetic fields, independently of normal microfluidic or biological processes. One, two or three dimensional structures can be formed. However, for magnetophoretic applications the non-magnetic objects should be magnetically labelled or the inverse ferrofluids (ferrofluids containing nonmagnetic particles) can be used. It was demonstrated (theoretically) that in such environment due to the presence of a non-uniform magnetic field non-magnetic particles are submitted to magnetophoretic force [62].

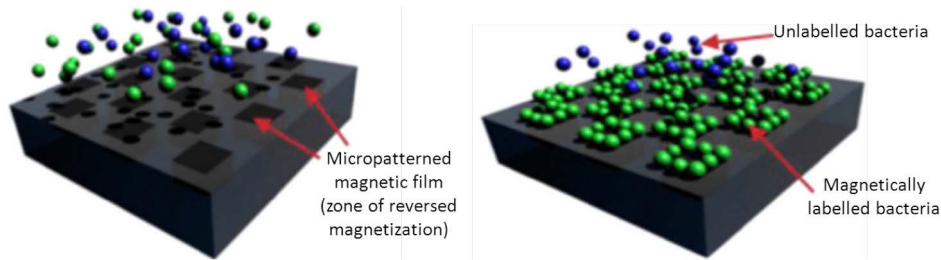


Figure 1.15. Schematic representation of a specific attraction of magnetically labelled bacteria onto a $100 \times 100 \mu\text{m}^2$ micromagnet arrays [63].

Technique	Features	Limitations
Optical manipulation	<ul style="list-style-type: none"> Optical waves generate optical forces Manipulation based on particle volume and permittivity of suspension and particles Optical wavelength and intensity are key parameters 	<ul style="list-style-type: none"> Heating during a long term process
Acoustophoresis	<ul style="list-style-type: none"> Acoustic waves generate acoustic forces Manipulation based on size, density and compressibility Amplitude and frequency of acoustic wave are key parameters 	<ul style="list-style-type: none"> Not efficient in nano-scale particle sizes Heating during a long term process
Electrophoresis	<ul style="list-style-type: none"> Uniform electric field generates electrophoretic force Electrophoretic force pushes the charged particles towards opposite charge Viscosity of media, particle sizes and permittivity of the particles are key parameters 	<ul style="list-style-type: none"> Limited to charged particles Slow particle migration times Limited to purification and separation applications
Dielectrophoresis	<ul style="list-style-type: none"> Non-uniform electric field generates the force Particles are neutral or semiconductor Motion depends on relative polarizability of the particle with respect to the suspension media Particles size, permittivity, and conductivity of particles and suspension media are key parameters 	<ul style="list-style-type: none"> Efficiency and precision of the process depends on electrodes fabrication and geometry Not recommended for bio applications because of high electric field gradients Dielectrophoretic force decreases extremely with particles size
Magnetophoresis	<ul style="list-style-type: none"> Magnetic field generates magnetic force Minimally invasive and generally safe for bio-particles The magnitude of magnetic field, particle size and magnetic susceptibilities of the particles and suspension media are key parameters 	<ul style="list-style-type: none"> Limited to the magnetic particles Magnetic tagging is required for non-magnetic particles Agglomeration of ferromagnetic particles in on/off magnetization sequence
Capillary forces for manipulation	<ul style="list-style-type: none"> Particles are trapped in the patterned templates due to capillary forces The geometry of the template, particle shape and dimensions, viscosity of media are key parameters 	<ul style="list-style-type: none"> Capillary force decreases in effectiveness with reduction in particle size Thermal energy takes place for small diameter particles

Table 1.4. Traditional and recently developed approaches for manipulation of micro/nano-objects.

References

- 1 “Historical Beginnings of Theories of Electricity and Magnetism”, M. Fowler (1997).
- 2 “Early Evolution of Power Engineering”, H. P. Vowles, *Isis* 17 (2), pp. 412–420 (1932).
- 3 “Origine de la Boussole II. Aimant et Boussole”, Li Shu-hua *Isis* 45 (2), p.175 (1954).
- 4 “The Natural History, Book XXXIV. The natural history of metals”, Pliny the Elder, “The metal called live iron”, Chap. 42.
- 5 “On the Magnet”, W. Gilbert, first English ed, London (1900). “The De Magnete of William Gilbert”, D. H. D. Roller, Amsterdam: Menno Hertzberger (1959).
- 6 “A treatise on electricity and magnetism”, J.C. Maxwell, Vol I, II Oxford : Clarendon Press (1873).
- 7 “Magnetic Materials and Devices for the 21st Century: Stronger, Lighter, and More Energy Efficient”, O. Gutfleisch , M. A. Willard , E. Brück , C. H. Chen , S. G. Sankar , and J. Ping Liu, *Adv. Mater.* 23, pp. 821–842 (2011).
- 8 “Recent Developments in High-Energy Alnico Alloys”, E.R. Cronk, *J. Appl. Phys.*, V. 37, No.3, pp. 1097-1100 (1966).
- 9 “Recent Ferrite Magnet Developments”, A. Cocharadt, *J. Appl. Phys.*, V. 37, p. 1112 (1966).
- 10 “Effect of hot deformation on texture and magnetic properties of Sm–Co and Pr–Co alloys”, A.M. Gabay, W.F. Li, G.C. Hadjipanayis, *Journal of Magnetism and Magnetic Materials*, V. 323, pp. 2470–2473 (2011).
- 11 “High (BH)max Permanent Magnets with Near-Zero Reversible Temperature Coefficient of Br”, Marinescu M. et al, *Proceedings of 20th International Workshop on Rare earth permanent magnets and their applications*, Crete (2008).
- 12 “New material for permanent magnets on a base of Nd and Fe”, M. Sagawa, S. Fujimura, N. Togawa, H. Yamamoto, and Y. Matsuura, *J. Appl. Phys.*, V. 55, p. 2083 (1984).
- 13 “Permanent magnet materials based on the rare earth-iron-boron tetragonal compounds”, M. Sagawa ; S. Fujimura ; H. Yamamoto ; Y. Matsuura ; K. Hiraga, *EEE Trans.Magn.MAG-20*, pp. 1584-1589 (1984).
- 14 “Praseodymium-iron- and neodymium-iron-based materials: a new class of high-performance permanent magnets”, J. J. Croat, J. F. Herbs, R. W. Lee, F. E. Pinkerton, *J. Appl. Phys.*, V. 55, pp. 2078-2082 (1984).
- 15 “High-energy product Nd-Fe-B permanent magnets”, J. J. Croat, J. F. Herbst, R. W. Lee, and F. E. Pinkerton, *Appl. Phys. Lett.*, V. 44, pp. 148-149 (1984).
- 16 “Advances in nanostructured permanent magnets research”, N. Poudyal, *Journal of Physics D: Applied Physics*, Vol. 46 (2013).
- 17 <http://www.birmingham.ac.uk/Documents/college-eps/metallurgy/research/Magnetic-Materials-Background/Magnetic-Materials-Background-4-Classification-of-Magnetic-Materials.pdf>
- 18 “Evaluation of Eddy-Current Effects on Diamagnetic Bearings for Microsystems”, Jie-Yu Chen, Jian-Bin Zhou, G. Meng, and Wen-Ming Zhang, *IEEE Transaction on industrial electronics*, Vol. 56, No. 4, (2009).
- 19 “Diamagnetic bearings for MEMS: Performance and stability analysis”, Jie-Yu Chen, Jian-Bin Zhou, Guang Meng, *Mechanics Research Communications*, Vol. 35, Iss. 8, pp. 546–552 (2008).
- 20 “Efficient modeling approach for optimization of a system based on passive diamagnetic levitation as a platform for bio-medical applications”, H. Chetouani, B. Delinchant, G. Reyne, *COMPEL - The international journal for computation and mathematics in electrical and electronic engineering*, Vol. 26 Iss. 2, pp.345 – 355 (2007).
- 21 “Magnetic levitation of large water droplets and mice”, L.Yuanming, Zh. Da-Ming, S. Donald M., I. Ulf, *Advances in Space Research*, No. 45 (1), pp. 208–213 (2010).
- 22 “Magnetic gravity trick grows perfect crystals”, K. Kurt, *New Scientist* (2011).
- 23 G. Vijayakumari, *Engineering Physics (GTU)*, S.Chand (G/L) & Company Ltd; Eighth edition (2014).
- 24 “Measurement of magnetic domain wall width using energy-filtered Fresnel images”, S. J. Lloyd, J. C. Loudon, P. A. Midgley, *Journal of Microscopy*, Vol. 207, pp. 118–128 (2002).
- 25 “The Science and Engineering of Materials, Sixth Edition”, D. R. Askeland, P. P. Fulay, W. J. Wright. Publisher, Global Engineering, pp. 777-784 (2010).
- 26 “Magnetic alloys break the rules”, R. D. James, *Nature*, Vol. 521 (2015).
- 27 <http://www.xraymachines.info/article/729188170/soft-and-hard-magnetic-materials/>

- 28 “Controlling Magnetotactic Bacteria through an Integrated Nanofabricated Metallic Island and Optical Microscope Approach”, L. M. González et al, *Scientific Reports* 4, Article number: 4104 (2014).
- 29 “Magnetic characterization of micropatterned Nd-Fe-B hard magnetic films using scanning Hall microscopy”, M. Kustov et al, *J. Appl. Phys.* 108, 063914 (2010).
- 30 “Autonomous micro-magnet based systems for highly efficient magnetic separation”, L. F. Zanini et al, *Appl. Phys. Lett.* 99, 232504 (2011).
- 31 “Microfluidic applications of magnetic particles for biological analysis and catalysis”, M.A.M. Gijs, F. Lacharme, U. Lehmann, *Chem. Rev.* 110, pp. 1518-1563 (2010).
- 32 “Magnetic nanoparticles for gene and drug delivery”, S. C. McBain, H.H.P. Yiu, J. Dobson, *Int J Nanomedicine*, No. 3(2), pp. 169–180 (2008).
- 33 “Magnetic microspheres as magical novel drug delivery system: A review”, S. Kakar et al, *Journal of Acute Disease*, Vol.2, Iss.1, pp. 1-12 (2013).
- 34 “Magnetic resonance imaging by using nano-magnetic particles”, H. Shokrollahi et al, *Journal of Magnetism and Magnetic Materials*, Vol. 369, pp. 176–183 (2014).
- 35 “In vivo magnetic resonance imaging of hyperpolarized silicon particles”, M. C. Cassidy, H.R. Chan, B. D. Ross, P. K. Bhattacharya and C. M. Marcus, *Nature Nanotechnology* 8, pp. 363–368 (2013).
- 36 “Magnetic Resonance Imaging: In-Vitro MPI-Guided Real Time Catheter Tracking and 4D Angioplasty Using a Road Map and Blood Pool Tracer Approach”, J. Salamon, M. Hofmann, C. Jung, M.G. Kaul, F. Werne, K. Them, et al, *Magnetic Particle*, PLoS ONE 11(6): e0156899 (2016).
- 37 “Magnetic particle hyperthermia — a promising tumour therapy?”, S. Dutz and R. Hergt, *Nanotechnology*, Vol.25, No. 45 (2014).
- 38 “The effect of field parameters, nanoparticle properties and immobilization on the specific heating power in magnetic particle hyperthermia”, Rudolf Hergt et al, *Journal of Physics: Condensed Matter*, Vol. 18, No. 38 (2006).
- 39 http://www.mqitechnology.com/downloads/powder_datasheet_PDF/MQP-S-11-9-20001-070-pds.pdf
- 40 “Magnetic properties of nanostructured materials”, L. Pelecky and R.D. Rieke, *Chemistry of Materials* 8 (8), pp. 1770–1783 (1996).
- 41 http://www.chemicell.com/products/magnetic_particles/magnetic_particle_separation.html
- 42 “Structures magnetiques et micro-systemes pour applications biologiques”, L. Zanini, PhD thesis, Université de Grenoble, France (2013) <NNT : 2013GRENT004>. <tel-00820317>.
- 43 “Acoustic Manipulation and Alignment of Particles for Applications in Separation, Micro-Templating, and Device Fabrication”, K. Moradi, FIU Electronic Theses and Dissertations, paper 1753 (2015).
- 44 “Continuous flow separations in microfluidic devices”, N. Pamme, *Lab Chip*, No. 7, pp. 1644–1659 (2007).
- 45 “Acceleration and trapping of particles by radiation pressure”, A. Ashkin, *Phys. Rev. Lett.* 24, pp. 156–159 (1970).
- 46 “Atomic-beam deflection by resonance-radiation pressure”, A. Ashkin, *Phys. Rev. Lett.* 25, pp. 1321–1324 (1970).
- 47 “Optical trapping and manipulation of nanostructures”, O. M. Marago et al, *Nature Nanotechnology* 8(11), pp. 807-819 (2013).
- 48 “Dynamic-field devices for the ultrasonic manipulation of microparticles”, B. W. Drinkwater, *Lab Chip*, Vol. 16, pp. 2360-2375 (2016).
- 49 “Template-Assisted Self-Assembly: A Practical Route to Complex Aggregates of Monodispersed Colloids with Well-Defined Sizes, Shapes, and Structures” Yadong Yin et al, *J. Am. Chem. Soc.*, Vol. 123, pp. 8718-8729 (2001).
- 50 “Template-assisted self-assembly: a versatile approach to complex micro- and nanostructures”, M. Rycenga et al, *Soft Matter*, Vol. 5, pp. 1129–1136 (2009).
- 51 “High throughput sub-10 nm metallic particles organization on templates made by block copolymer self-assembly and nanoimprint”, J. Arias-Zapata et al, *Microelectronic Engineering*, Vol. 141, pp. 155–159 (2015).
- 52 “Dielectrophoresis: The Behavior of Neutral Matter in Nonuniform Electric Fields (Cambridge Monographs on Physics)”, H.A. Pohl, Cambridge University Press (1978).

- 53 “Review Article—Dielectrophoresis: Status of the theory, technology, and applications”, R. Pethig, *Biomicrofluidics* Vol. 4, 022811 (2010).
- 54 “Approaching nanoxerography: the use of electrostatic forces to position nanoparticles with 100 nm scale resolution”, H.O. Jacobs, S.A. Campbell, M.G. Steward, *Adv. Mater.*, Vol. 14, No. 21 (2002).
- 55 “Printing nanoparticles from the liquid and gas phases using nanoxerography”, C. R Barry et al, *Nanotechnology*, Vol. 14, pp. 1057–1063 (2003).
- 56 “How to Control AFM Nanoxerography for the Templated Monolayered Assembly of 2 nm Colloidal Gold Nanoparticles”, L. Ressler et al, *IEEE Transaction on nanotechnology*, Vol. 8, No. 4 (2009).
- 57 “Micro-patterning of NdFeB and SmCo magnet films for integration into micro-electro-mechanical-systems”, A. Walther et al, *Journal of Magnetism and Magnetic Materials*, Vol. 321, No. 6, pp. 590–594 (2009). Current Perspectives: Perpendicular Recording.
- 58 “Thermomagnetically patterned micromagnets”, F. Dumas-Bouchiat et al, *Applied Physics Letters*, Vol. 96, No. 10, 102511 (2010).
- 59 “Microchip-based immunomagnetic detection of circulating tumor cells”, K. Hoshino, Y.-Y. Huang, N. Lane, M. Huebschman, J. W. Uhr, E. P. Frenkel, and X. Zhang, *Lab Chip*, Vol. 11 (2011).
- 60 “On-chip micro-electromagnets for magnetic-based bio-molecules separation”, Q. Ramadan, V. Samper, D. Poenar, and C. Yu, *Journal of Magnetism and Magnetic Materials*, Vol. 281, No. 2-3, pp. 150 – 172 (2004).
- 61 “Magnetic core shell nanoparticles trapping in a microdevice generating high magnetic gradient”, B. Teste, F. Malloggi, A.-L. Gassner, T. Georgelin, J.-M. Siaugue, A. Varenne, H. Girault, and S. Descroix, *Lab Chip*, Vol. 11, pp. 833–840 (2011).
- 62 “Magnetophoresis of Nonmagnetic Particles in Ferrofluids”, Y. Gao et al, *J. Phys. Chem. C*, Vol. 111, pp. 10785-10791 (2007).
- 63 “Development and applications of a DNA labeling method with magnetic nanoparticles to study the role of horizontal gene transfer events between bacteria in soil pollutant bioremediation processes”, J. Pivetal, M. Frénéa-Robin, N. Haddour et al, *Environ Sci. Pollut. Res.*, Vol. 22, pp. 20322–20327 (2015).

Chapter II: Description and applications of micromagnet array

II. Description and applications of micromagnet array	40
<u>II.1 Micromagnet array fabrication</u>	40
<u>II.1.1 Hard magnetic film preparation - Triode Sputtering</u>	40
<u>II.1.2 Thermo Magnetic Patterning (TMP)</u>	43
<u>II.1.3 Topographic patterning (TOPO)</u>	45
<u>II.1.4 Micro Magnetic Imprinting (μMI)</u>	46
<u>II.2 Micromagnet array properties</u>	48
<u>II.2.1 Modelling of TMP micromagnet array properties</u>	48
<u>II.2.2 Micromagnet array for particles trapping</u>	54
<u>II.2.3 Localization and identification of magnetic pattern</u>	55
<u>II.2.4 Reverse depth determination of TMP sample</u>	57
<u>II.2.5 Direct measurements of stray field produced by micromagnet array</u>	58
<u>II.2.6 Nano-scale characterization of TMP sample surface morphology and magnetic properties</u>	61
<u>II.2.7 Micromagnet array properties. Summary</u>	64
<u>II.3 Microfluidic devices for micro-objects handling</u>	66
<u>II.3.1 Static capture and positioning</u>	66
<u>II.3.2 Dynamic capture and separation</u>	69
<u>II.3.3 Continuous guiding</u>	70
<u>References</u>	72

II. Description and applications of micromagnet array

In this chapter three types of micromagnet arrays developed in the Micro and Nano Magnetism (MNM) group at the Néel Institute will be discussed. They are suitable for integration with lab-on-chip, microfluidic and other devices since the stray field created by these magnets is restricted to the region of interest and no need of external field is required. The aims of this chapter are:

- To present three different approaches for micromagnet array fabrication;
- To provide an adequate theoretical model to describe micromagnet array properties;
- To provide the first results of qualitative and quantitative characterization of micromagnet arrays;
- To demonstrate the suitability of micromagnet arrays for trapping and sorting of magnetic microspheres and biological species functionalized with magnetic nanoparticles;
- To compare experimental results with these predicted by modelling.

In this context we completed previously obtained results with additional experiments¹. Most of the studied samples were fabricated by MNM team and I was involved in this process. I followed the procedure of magnetic films patterning by TMP approach and fabricated a number of μ MI samples by embedding NdFeB and SmFeN microparticles in polymer matrix. To study the properties of produced samples we have employed various techniques.

In the next sections we discuss the possible size and shape of micromagnet arrays, their magnetic properties, limitations due to fabrication technique and adaptability to the potential applications for each method.

II.1 Micromagnet array fabrication

This section describes the three main types of micromagnet arrays and their associated fabrication processes that have been developed and optimized at Néel Institute in the Micro and Nano Magnetism (MNM) group:

- Thermo Magnetic Patterning (TMP): production of high magnetic field gradient structure by reorientation of magnetization at certain zones of the film using laser irradiation combined with an application of an opposite magnetic field [1];
- Topographic Patterning (TOPO): formation of a physical pattern on the film surface by modulating its morphological structure [2];
- Micro Magnetic Imprinting (μ MI): formation of magnetic structure by positioning of magnetic particles in a transparent (flexible or rigid) polymer matrix under magnetic field [3].

The two first methods require deposition of homogenous and flat hard magnetic films while the last one requires a master structure (for example, TMP or TOPO magnet) to produce modulated magnetic field to induce assembly of magnetic particles.

II.1.1 Hard magnetic film preparation - Triode Sputtering

Triode Sputtering is a physical vapour deposition (PVD) technique and its main advantage is the high deposition rate that can reach up to 20 $\mu\text{m}/\text{h}$, depends on the target material, size, voltage, target-substrate distance. The set-up of high deposition rate triode sputtering machine available at Neel Institute and dedicated to hard magnetic films preparation (NdFeB and SmCo) is presented in Figure 2.1.

The substrate and the target are positioned inside a vacuum chamber. The dimension of a target can be up to $10 \times 10 \text{ cm}^2$. A substrate diameter up to 8 inches is acceptable, but 4-inch

¹ In this Chapter all the experiments we have conducted in the framework of this thesis are marked with #.

silicon wafers are most commonly used (for following integration with microelectronic devices). The target holder can accommodate four targets. During the deposition the substrate holder can be rotated in order to increase the film composition homogeneity and thickness. The target-substrate distance can be adjusted as well. The working pressure is controlled by a flow of argon gas. The heating of a tungsten filament positioned close to both the target and the substrate leads to the electron emission. The collision between electrons and inert argon atoms generates plasma. By applying an electrical potential between the target and the substrate, positive argon ions Ar^+ are accelerated towards a negatively polarized target. To adjust the electrons trajectory and to confine the argon plasma two bulk permanent magnets are inserted. The target alloy is sputtered in all the directions including the substrate placed in front of the target.

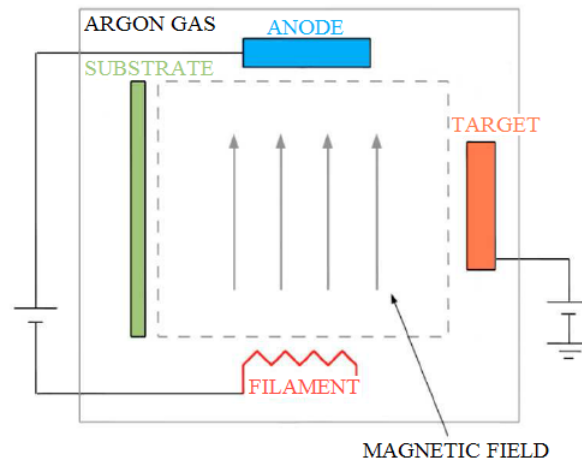


Figure 2.1. Schematic of the triode sputtering apparatus.

Magnetic properties of a deposited film depend on its structure: crystalline or amorphous. The deposition parameters were chosen to induce crystallographic texture and thus, to maximize the remanent magnetization and energy product of the hard magnetic material. In the case of NdFeB films a two-step process (deposition and annealing) leads to the crystallization of deposited film via heat treatment [4]. The grain size and shape of a crystalline film are strongly correlated with the deposition and annealing temperatures. The high quality films usually have equiaxed² or columnar grains. To obtain equiaxed grains the deposition temperature is set to $\leq 450^\circ\text{C}$, which causes a formation of an amorphous phase exhibiting magnetically soft behaviour. Following annealing at 750°C leads to growth of anisotropic, magnetically hard phase (Figure 2.2a).

An increase of a deposition temperature up to 500°C with following annealing at 750°C causes columnar grain formation; the grains can be as long as the film's thickness (few microns) (Figure 2.2b) [5,6,7]. The parameters for SmCo and NdFeB hard magnetic films deposition and measured magnetic properties are summarized in Table 2.1. As my work focused on NdFeB patterned films, their fabrication process will be discussed in more details.

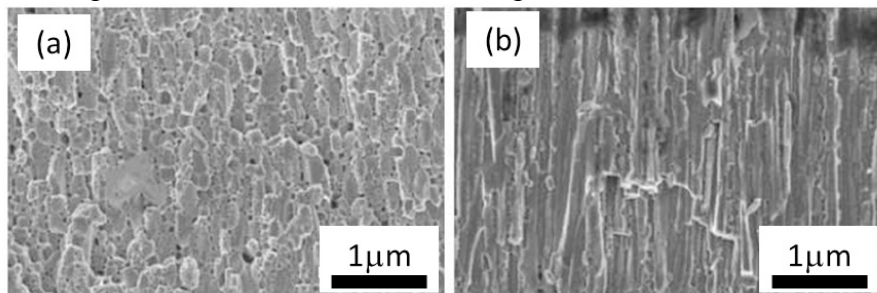


Figure 2.2. SEM fracture views of NdFeB films microstructure showing (a) equiaxed grains and (b) columnar grains [6].

² Equiaxed grains – grains with approximately equal dimensions.

The annealing temperature has strong influence on the film structure and its final magnetic properties. An increase of the temperature leads to formation of high anisotropy films with improved coercivity ($\mu_0 H_c = 0.3, 0.8$ and 1.2 T are obtained with depositions at 500 °C, 575 °C and 600 °C, respectively), but due to the extraction of Nd-rich liquid phase the peel-off and fractures on the film surface can happen.

	SmCo [8]	NdFeB [5]
Target material	$\text{Sm}_{23}\text{Co}_7$	$\text{Nd}_{16.8}\text{Fe}_{74.7}\text{B}_{8.5}$
Film thickness, (μm)	5	5-20
Deposition rate, ($\mu\text{m}/\text{hour}$)	3.6-18	18
Deposition temperature, ($^{\circ}\text{C}$)	≤ 600	≤ 500
Post-deposition annealing, ($^{\circ}\text{C}$)	750	750
Magnetic texture ³	In-plane	Out-of-plane
Coercivity, $\mu_0 H_c$, (T)	1.3*	up to 2.7
Remanence, B_r , (T)	0.8*	1.28
Notes	Optimal deposition temperature is $350\text{-}400^{\circ}\text{C}$: highest magnetic properties, no film peel-off.	Formation of equiaxed grains at 450°C deposition temperature, formation of columnar grains at 500°C .

Table 2.1. Deposition and annealing parameters with measured magnetic properties for SmCo and NdFeB hard magnetic films. *Results for SmCo films deposited at 350°C .

To minimize the fracturing of the film surface a tantalum buffer layer and a thermally oxidized silicon wafer are used for NdFeB films fabrication [9]. The sketch in Figure 2.3 (a) illustrates the final structure of NdFeB film prepared for TMP process. Buffer Ta layer is deposited to prevent interdiffusion between lower interface of NdFeB film and oxygen-based substrate material (SiO_2 layer on Figure 2.3a). A capping Ta layer is deposited to prevent oxidation of the NdFeB layer. Moreover, the extraction of Nd-rich liquid phase is restricted due to the presence of capping layer. This improves the coverage of individual $\text{Nd}_2\text{Fe}_{14}\text{B}$ grains by Nd-rich phase due to their magnetic decoupling leading to higher film coercivity [10,11]. Indeed with an increase of Nd content (up to a certain point) film coercivity can reach 2.7 T due to the excellent distribution of the Nd-rich grain boundary phase giving better isolation of the $\text{Nd}_2\text{Fe}_{14}\text{B}$ grains with respect to magnetic exchange interactions [10]. Therefore a Nd-rich target was used for triode sputtering. Silicon as a substrate provides potential of such films applications in magnetic Micro-Electro-Mechanical Systems (MEMS) and Microfluidic devices [12,13].

The sketch of high coercivity SmCo thick films fabricated by triode sputtering [8] is presented in Figure 2.3 (b). Usually Cr buffer and capping layers (50 nm) are used to prevent diffusion into Si substrate and oxidation, respectively.

Atomic force microscopy[#] (AFM) and scanning electron microscopy (SEM) images (Figure 2.4) reveal the topography of NdFeB film. These techniques together with Energy-dispersive X-ray spectroscopy (EDX) show features of bumpy shape containing Nd-rich material on the film surface [10]. These bumps, formed during the annealing step of the film fabrication are due to extrusion of Nd-rich material out of the film. According to the AFM analysis, height of these bumps is up to 1 μm .

High-performance NdFeB and SmCo magnetic films fabricated by high rate triode sputtering and annealing have been employed for micromagnet array fabrication.

²In-plane and out-of-plane hysteresis loops confirming a high out-of-plane texture on a NdFeB film and in-plane texture on a SmCo film.

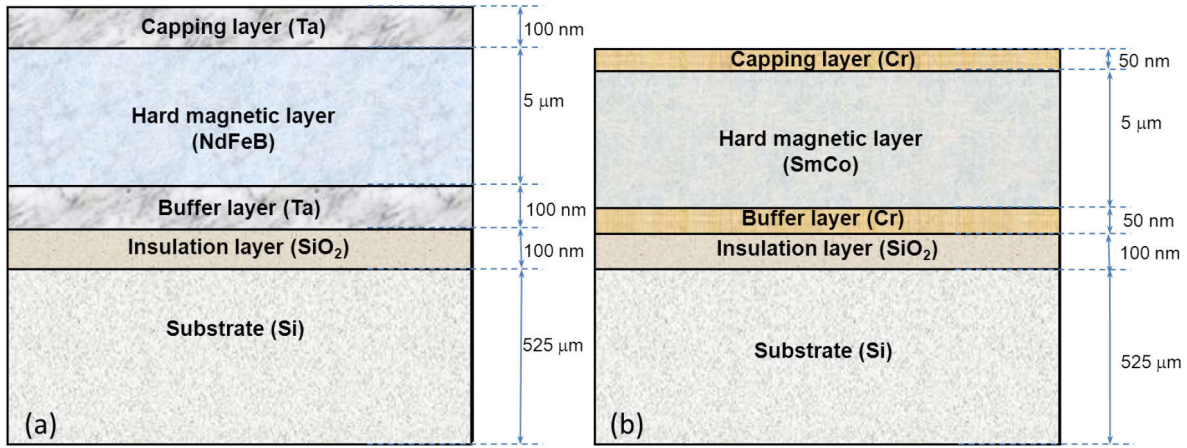


Figure 2.3. The structure of a hard magnetic film deposited on a silicon substrate: (a) NdFeB; (b) SmCo.

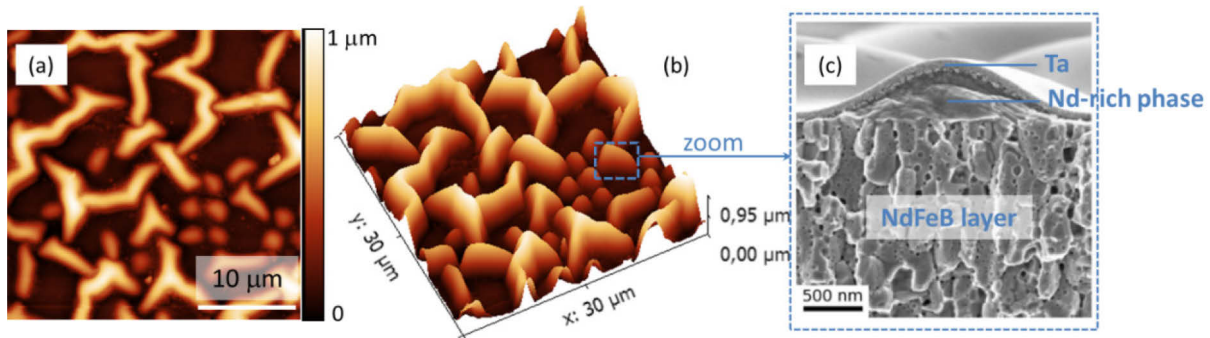


Figure 2.4. (a) [#] AFM image of NdFeB film surface with bumps. (b) [#] 3D AFM image of NdFeB film surface with bumps. (c) SEM image of a fracture cross-section of NdFeB film: Ta coating layer, Nd-rich bump and NdFeB film with columnar structure are observed [6].

II.1.2 Thermo Magnetic Patterning (TMP)

Thermo Magnetic Patterning (TMP) is a technique to modify locally the magnetization orientation of a magnetic film by simultaneous thermal and magnetic action, leading to a magnetic pattern formation. The main principle of this process is based on conversely proportional dependence of magnetization with temperature (when hard magnetic film is heated, its coercivity is reduced) combined with an application of a magnetic field in opposite direction to the initial film magnetization [1]. To form a micromagnet pattern on a magnetic film four main steps should be completed (Figure 2.5):

Step 1 (Figure 2.5a): Annealed magnetic film is saturated in the out-of-plane (oop) or in-plane (ip) direction by a magnetic field significantly exceeding the film's room temperature coercivity (7 T in our case) produced by superconducting coil.

Step 2 (Figure 2.5b): The film is placed above a bulk magnet that produces a field of around 0.5 T (should not exceed the film's room temperature coercivity) in the direction opposite to the initial film magnetization. The mask with desired pattern is positioned on the top of the film and the laser beam is focused on the mask.

Step 3 (Figure 2.5c): The laser beam passing through the mask apertures heats⁴ the film locally. Heat diffuses through the film lowering its coercivity in the irradiated zones.

Step 4 (Figure 2.5d): The regions of the film where the coercivity is overcome by the external field have reoriented magnetic moments.

⁴ Local heating leads to drop of coercivity. The temperature should not overcome Curie temperature to avoid film demagnetization.

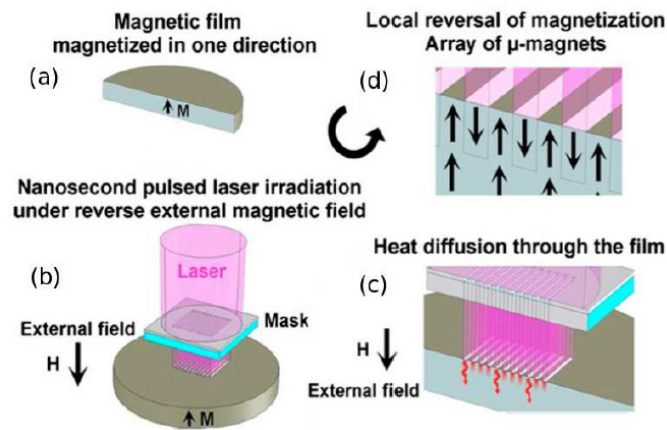


Figure 2.5. Schematic of Thermo Magnetic Patterning principle [1].

As a result of TMP process, non-reversed zones (NRZs) with initial magnetization and reversed zones (RZs) with opposite magnetization form the magnetic pattern (micromagnet array) on hard magnetic film. The difference in magnetization direction between NRZ and RZ leads to high field gradient at the interface between them, the so-called magnetic junction (MJ).

The main parameters that can be varied to obtain better quality pattern are the laser fluence (the energy per surface unit), the external field (should not overcome the film's room temperature coercivity) applied with a bulk magnet or an electromagnet, and the temperature of the sample by placing it above a heating plate with a precise temperature (increase of initial sample temperature improves magnetization reversal for a fixed laser fluence).

In practise, for TMP pattern fabrication on NdFeB films, High-Pulse-Energy Excimer Laser COMPexPro 102 with the wavelength of 248 nm and fluence of 240 mJ/cm^2 was used for 20-25 ns (1 Hz). With this fluence, reversal thickness of approximately $0.9\text{--}1.3 \text{ }\mu\text{m}$ was obtained (see sections II.2.4, II.2.5). This type of laser was chosen for its high homogeneity in space and high maximum fluence. However, the choice of a good laser is not enough to produce high quality micromagnet arrays on hard magnetic film. The key point to obtain homogeneous pattern is the quality of the mask.

In TMP process, the main requirement for a mask is to have two different zones: zone A of high transmittance and zone B of low transmittance for the laser beam. Two types of masks can be used for TMP: (i) home-made masks produced by microfabrication techniques and (ii) commercially available masks from different suppliers. Usually commercial masks are produced according to the required pattern and present a thin sheet of an opaque material (like copper or Si_3N_4) with holes inside. For the masks produced in the laboratory (home-made masks) quartz substrate with more than 85% of transmittance for a wavelength of 248 nm is used. Quartz-based mask costs less than the commercial one, but it takes more time and steps to fabricate it, especially when the pattern dimensions are less than $10 \text{ }\mu\text{m}$. One of the most important parameters for a mask is the thickness that should vary from tens up to few hundred micrometres. Thus, a small tilt in the mask during TMP fabrication can significantly affect the irradiation zones. The parallelism of upper and lower faces of the quartz-based mask is very important, because when they are not parallel, laser beam can be reflected multiple times inside the substrate, thus, creating fringe patterns of irradiation. Moreover in all mask, the edges of the patterns can diffract the laser beam, creating fringes of higher and lower intensity. In Figure 2.6[#] optical images of quartz mask and two TMP samples with trapped NdFeB microspheres of $5 \text{ }\mu\text{m}$ diameter are presented (particles are mainly trapped above the interface between NRZ and RZ revealing the pattern). Both TMP samples were produced using the same mask with the stripes pattern of $50 \text{ }\mu\text{m}$ width (Figure 2.6 a). In Figure 2.6b, the density of trapped microparticles is homogenous along each pattern line while in Figure 2.6c some parts of the lines are free of particles leading to an additional modulation in 45°

direction (blue dotted lines) to initial horizontal stripes pattern (dark green lines). Increase of trapped magnetic particles density with the period of about $200\ \mu\text{m}$ is observed. Since the same mask has been used for fabrication of both samples (without and with additional pattern) the effect of parallelism of upper and lower mask faces on the pattern quality is excluded. Additional modulation can be explained by “interference patterning”: the tilt between mask and sample leads to maximization of light intensity in certain regions and therefore higher heating causing magnetization reversal in these regions [1].

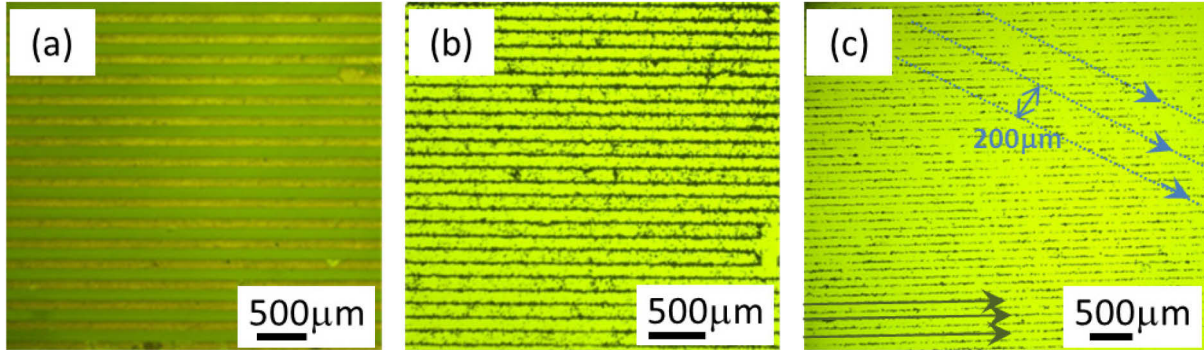


Figure 2.6[#]. Optical images of (a) Quartz mask for TMP fabrication: green lines are the apertures of the mask; (b) TMP sample with trapped $5\ \mu\text{m}$ NdFeB particles: horizontal stripes pattern is observed; (c) TMP sample with trapped $5\ \mu\text{m}$ NdFeB particles: horizontal stripes pattern (dark green arrows) and stripes pattern of 45° tilt to the initial one (blue dotted arrows) are observed.

In this work, mainly home-made quartz masks (mask production is described in Annex II.1) were used for TMP sample production: NdFeB films with 50 and $100\ \mu\text{m}$ stripes pattern were fabricated.

II.1.3 Topographic patterning (TOPO)

Topographic patterning is based on the photolithography (Al mask + wet etching) and the deep-reactive ion etching technique (DRIE) to create desired structure on a Si wafer before the magnetic film deposition. Using this method, patterns of different shape and size (squares, lines, rings and etc.) can be produced. For the small patterns (from 5 to $25\ \mu\text{m}$ as the smallest lateral dimension) the etching depth is about $20\ \mu\text{m}$; for the large patterns (50 to $200\ \mu\text{m}$ as the smallest lateral dimension) the etching depth⁵ is up to $100\ \mu\text{m}$.

Once the pattern is done, Ta layer and then magnetic film are deposited all over the substrate. After deposition process, the sample is magnetically saturated in one direction (out-of-plane or in-plane). The difference in height between magnetic layers creates a field gradient at the interfaces, which can be used for example for magnetic particles trapping. Topographic patterning technique step-by-step and final result are presented in Figure 2.7.

Substrate patterning:

Step 1: Deposition of $100\ \text{nm}$ Al layer on a Si wafer;

Step 2: Spin-coating of photoresist on the Al layer and pattern creation by soft lithography;

Step 3: Wet etching: Al layer covered by photoresist remains and will serve as a “hard mask” while etching the silicon substrate;

Step 4: Si substrate is etched by DRIE to create a desired topography;

Step 5: Removal of remained resist and Al layer; thermal oxidation of the substrate to produce a superficial SiO_2 layer (adhesion layer);

Magnetic layer deposition:

Step 6: Triode deposition of magnetic and buffer/capping layers;

⁵ Increase of the etching depth while maintaining lateral dimensions (high aspect ratio) might lead to the breakage of the features during further steps: film deposition and integration with microelectronic systems.

Planarization:

Step 7 (optional): Chemical-Mechanical-Planarization [14] (CMP) can be used to remove the topographical relief (the upper magnets).

The impact of the planarization step on the topographically patterned NdFeB films has been studied in [2]. It was shown that degradation in magnetic properties of thus patterned films, compared to continuous planar films, was prevented⁶ by the application of Ar ion etching of the film surface followed by the deposition of a Ta layer prior to film annealing.

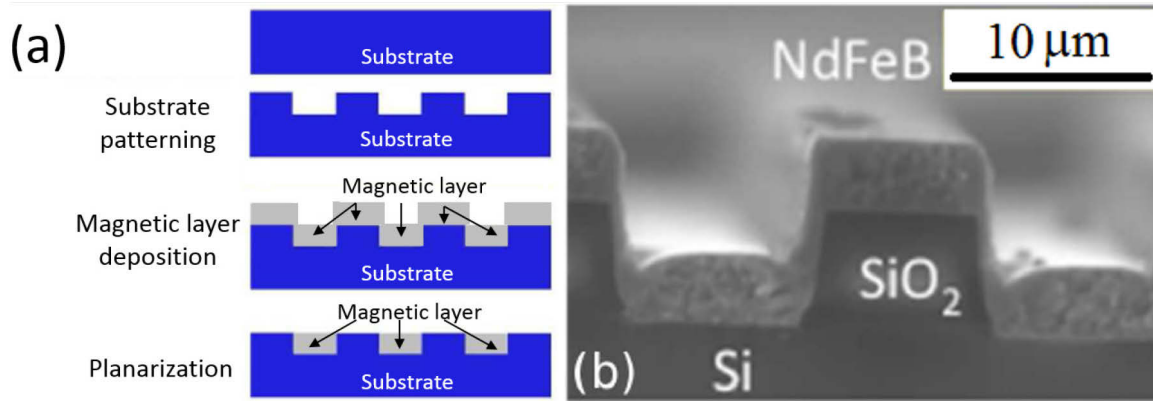


Figure 2.7. (a) Simplified steps to produce topographically patterned micromagnets: substrate patterning; deposition of a magnetic layer; planarization by removal of the upper magnets. The last step is optional, depending on the application. (b) SEM image (side-view) of a TOPO patterned magnet [2].

There are two main limitations for TOPO magnets fabrication: feature dimensions and aspect ratio. Creation of the pattern (step 2) by exposing a photoresist to UV light allows fabricating patterns with the size not less than one micron. To fabricate a smaller pattern slower and more expensive processes are required. DRIE technique allows production of high aspect ratio patterns; however the following fabrication steps and integration to a microsystem can lead to breakage of created pattern.

Another approach to TOPO technique is based on deposition of a magnetic film on a flat substrate and subsequently wet etching at certain zones. A schematic of the wet etching process for topographic magnet fabrication is shown in Figure 2.8. The detailed procedure is described in [2].

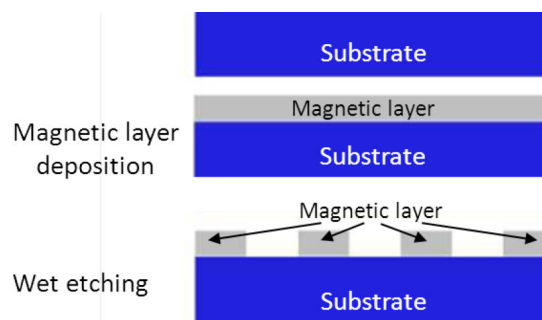


Figure 2.8. Schematic representation of topographic patterning by the wet etching method [2].

II.1.4 Micro Magnetic Imprinting (μ MI)

Another process developed by the MNM group (in 2012) called Micro Magnetic Imprinting (μ MI), is a low-cost and fast technique based on the positioning of magnetic particles in non-magnetic matrix to fabricate magnetic flux sources on flexible (or rigid) and transparent substrate [3]. The μ MI principle is based on magnetic powder positioning by a

⁶ Rare earth elements have a high affinity for oxygen and surface oxidation of RE-TM magnets leads to degradation in their magnetic properties

modulated magnetic field and subsequently embedding in a polymer matrix: the final sample is a magnetic pattern made of magnetic particles fixed in a polymer film. TMP and TOPO micromagnet arrays are ideal candidates for modulated field. The μ MI fabrication process consists of following steps (Figure 2.9):

Step 1: Magnetic particles spread in alcohol are sprinkled onto a TMP or TOPO magnet (the so-called master). Dry air or hot plate can be used for faster alcohol evaporation and non-trapped particles removal;

Step 2: Liquid polymer binder is poured on the master with trapped magnetic particles and hardened.

Step 3: The hardened polymer binder containing magnetic microparticles is peeled off from the master.

In Figure 2.9 pyramidal agglomerations of the particles above the interfaces between RZ and NRZ are observed. Such trapping behaviour can be explained by fast decay of magnetic field produced by master sample with increase of the distance between captured microsphere and source of magnetic field (master structure).

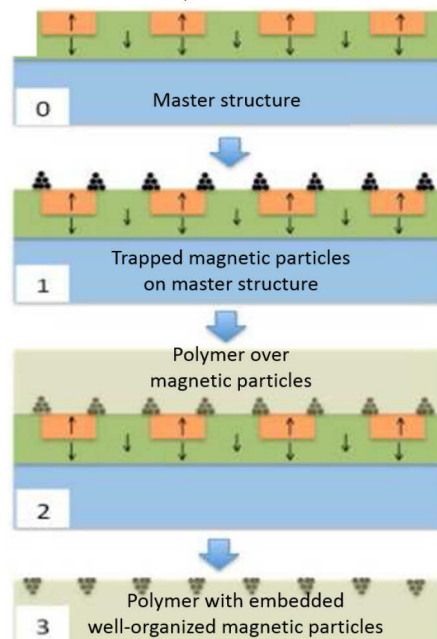


Figure 2.9. Schematic diagram of the micro magnetic imprinting process: (0) master structure; (1) hard magnetic particles sprinkled onto master structure and magnetophoretically concentrated at the interfaces between neighbouring micromagnets; (2) polymer binder poured over the trapped magnetic particles; (3) the solid composite is peeled off the master structure [3].

Figure 2.10a[#] and Figure 2.10b[#] illustrate μ MI samples with 5 μ m diameter NdFeB isotropic particles (MQFP-B, Magnequench International, Inc.) and 3 μ m diameter SmFeN anisotropic particles (Z12, Nichia Corporation) trapped in PDMS⁷ matrix using TMP magnet as a master structure.

The μ MI structures have demonstrated their efficiency as magnetic flux sources providing high field gradient (up to $5 \cdot 10^5$ T/m) [3]. In my work only TMP samples as master structures and PDMS as polymer binder were used for μ MI samples fabrication.

The μ MI fabrication process is simple, fast and inexpensive. A transparent matrix allows the observation of objects using transmission optical microscopy, while the rigidity and flexibility of the structure can be varied by modifying the type and thickness of matrix. μ MI structures can be cut into different shapes and sizes for diverse open surface trapping experiments (e.g., as base plates in Petri-dishes, as dip-sticks for plunging into sample tubes, for in-vivo bio-marker harvesting or targeted drug delivery). All these factors together make

⁷ PDMS – Polydimethylsiloxane, $(C_2H_6OSi)_n$.

μ MI magnetic flux sources very attractive for applications in biology. Biological cells functionalized with superparamagnetic beads have been trapped by μ MI structures [3].

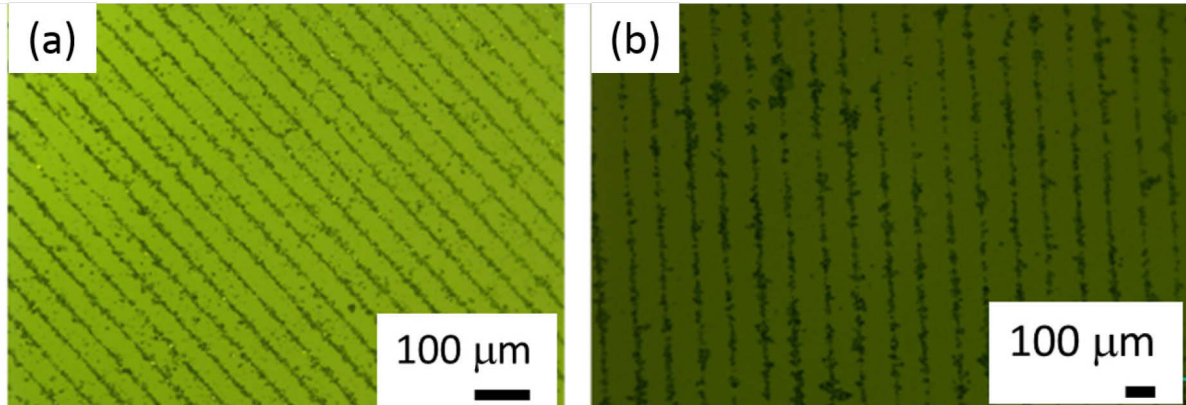


Figure 2.10[#]. (a) Optical plane-view for 5 μ m diameter NdFeB trapped particles. (b) Optical plane-view for 3 μ m diameter SmFeN trapped particles. Magnetic particles are separated by a pitch of about 50 μ m, which corresponds to the width of the micromagnets in the master TMP structure.

These three types of micromagnet flux sources present similar but specific magnetic properties impacting their magnetic field intensity and spatial distribution and by the way their trapping capabilities. For this reason, detailed study of micromagnet arrays properties is required.

II.2 Micromagnet array properties

Micromagnet arrays with high field gradients have been successfully used for magnetic particles trapping and more complicated biological and medical applications up to integration in microfluidic devices and MEMS. However, the preliminary experiments for static capturing and positioning of magnetic particles have demonstrated some discrepancy between the theoretical calculation results and experimental ones: a part of magnetic microparticles was captured out of magnetic junctions exhibiting the highest field gradient (Figure 2.10). This leads to the need of additional detailed study of magnetic flux sources. For this purpose, theoretical approach has been combined to several physical characterizations obtained with various techniques.

In the next sections the model developed for calculations of micromagnet arrays properties and simulations of possible magnetic particles handling will be briefly described. The results of basic experiments on magnetic microparticles trapping with the magnetic flux sources will be analysed. The difference between theoretical and experimental results will be underlined and discussed.

II.2.1 Modelling of TMP micromagnet array properties

Micromagnet array can be considered as a set of permanent magnets with well-known geometrical structure and fixed magnetization with alternate orientation. With the knowledge of magnetic pattern, spatial distribution of both vertical and horizontal magnetic field components can be calculated. The first attempts to model micromagnet structure and its interaction with single magnetic object (microsphere) were done during PhD work of Luiz Zanini (MNM group at the Institut Néel, 2010-2013) (Model 1). Then with the help of Andre Dias (PhD student from MNM group at the Institut Néel, 2013-2016) commercial software (CADES framework, G2Elab, Grenoble) was employed to develop adequate model for micromagnet array and its interaction with single magnetic object (Model 2). The main approaches to calculate a field from a magnet are detailed in Annex II.2.

In the model, TMP film is considered as a parallelepiped (of length L , width W and thickness t) with desired magnetic pattern. In the experimental work during my PhD mainly samples with stripes magnetic pattern were used, so only this pattern was modelled[#]. The

reversed zone is considered as a parallelepiped (of length l , width w and thickness h_r). Initial magnetization of patterned film is M_{up} and magnetization of reversed zone is M_d , number of stripes is N . The schematics of Model 1 and Model 2 with possible microsphere positions are presented in Figure 2.11.

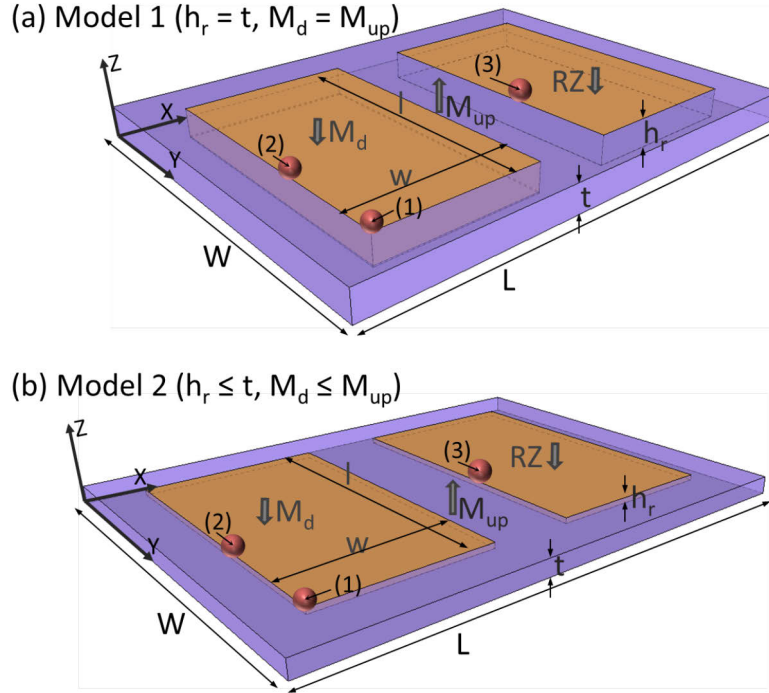


Figure 2.11. Schematic of Model 1 (a) and Model 2 (b). Points (1), (2) and (3) correspond to the different position of magnetic microsphere: (1) – the sphere is located at the edge of the pattern above the last stripe; (2) – the sphere is located above the last stripe in the middle; (3) – the sphere is located in the middle of the pattern (centre of the film).

The use of micromagnet arrays for micro-object handling applications leads to necessity of modelling not only the sample structure, but also its interaction with single magnetic object (for example, microsphere). The main parameters of the simulations based on Model 1 and Model 2 are presented below.

Model 1 (developed by L. Zanini):

Micromagnet array structure⁸ (Figure 2.11a):

- The magnetization of NRZ is equal to magnetization of RZ: $M_{up} = M_d$;
- The thickness of RZ is equal to the film thickness: $h_r = t$;

Magnetic microsphere:

- The microsphere is considered:
 - (a) as a point in which the whole magnetic mass is concentrated or
 - (b) as a number of points inside the sphere volume with fixed coordinates ;
- The distance between the sphere and magnetic film is the distance between sphere centre and top of magnetic layer;
- The superparamagnetic microsphere behaviour is described by Langevin function calculated in one point for case (a) and in a number of points for case (b);
- The hard magnetic microsphere can be modelled as a sphere divided into N^3 ($N = 20$) cubes in which the field and field gradient are considered to be constant;

⁸ Based on the number of tests and careful reading of the code we have concluded that despite the fact that magnetizations of NRZ and RZ (as well as the film thickness and RZ thickness) can be set independently, variation of RZ magnetization and RZ thickness does not change the field produced by micromagnet array. Indeed, according to the code RZ magnetization is equal to NRZ magnetization, but has the opposite direction; the film thickness is equal to the RZ thickness.

- The force acting on the sphere above the interface between NRZ and RZ is independent of the position above the whole pattern: the field above one interface does not affect the field above another neighbouring interface (interaction force for sphere located in position (1) is equal to these for positions (2) and (3) (Figure 2.11a): $F_1 = F_2 = F_3$).

Model 2 (CADES model):

Micromagnet array structure (Figure 2.11b):

- The magnetization of NRZ can be different from magnetization of RZ: $M_{up} \geq M_d$;
- The thickness of RZ can be adjusted $h_r : 0 < h_r \leq t$;

Magnetic microsphere (Figure 2.12):

- The microsphere is considered as a cube of equal volume⁹;
- In the model for superparamagnetic microsphere the sphere is discretized along the X, Y and Z axes, then the Method of Moments (MoM) is applied to compute a uniform induced magnetization in each elementary block. [15] (Figure 2.12a);
- NdFeB microsphere is modelled as a permanent magnet with magnetization M_{sph} that can be rotated by an angle Θ (Figure 2.12b);
- The force acting on the sphere above the patterned array depends on the sphere position above the sample (interaction force for sphere located in position (1) is not equal to these for positions (2) and (3) (Figure 2.11b): $F_1 \neq F_2 \neq F_3$).

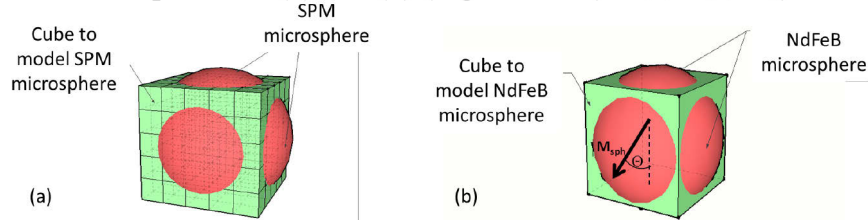


Figure 2.12. Magnetic microsphere (red) is modelled as a cube of equal volume (green) in Model 2: (a) Superparamagnetic (SPM) microsphere discretized along the X, Y and Z axes; (b) NdFeB microsphere modelled as a permanent magnet cube with magnetization M_{sph} that can be oriented with an angle Θ .

Magnetic induction¹⁰ B computed with Model 1 is presented in Figure 2.13[#]. The parameters of the simulations are:

- $W = 1$ cm – width of the film; $L = 3$ cm – length of the film;
- $t = 1.3$ μm – thickness of the film; $N = 20$ – number of stripes;
- $w = 50$ μm – width of the stripe; $w_0 = 50$ μm – distance between stripes;
- $l = 0.5$ cm – length of the stripe; $h_r = t = 1.3$ μm – thickness of the reversed zone;
- $M_{up} = M_d = 1.2$ T – magnetization of the reversed and non-reversed zone (RZ and NRZ).

The magnetic induction values were normalized (from 0 to 1): field at the surface above the magnetic junction (MJ) $B(z = 0) = 1$ and at the distance of 5 μm $B(z = 5 \mu\text{m}) = 0$. Fast decay of magnetic field along z and x axis is observed. Magnetic induction B at lateral distance (along x -axis) reaches its maximum above the MJ and drops almost to zero at distance of less than 1 μm from MJ. Along z -axis magnetic induction decays fast as well: at the distance of 100 nm from the surface above MJ, it decreases by a factor of 3.5: $B(z = 0)/B(z = 100 \text{ nm}) = 1/0.29 = 3.4$; at the distance of 4.95 μm the field is reduced by a factor of 12.5 compared to its value at the surface above MJ: $B(z = 0)/B(z = 4.95 \mu\text{m}) = 1/0.08 = 12.5$.

⁹ The sphere is modelled as a cube in order to use pure analytical formula for magnetic field calculations and to decrease the computation time.

¹⁰ Magnetic induction B is used here for the sake of simplicity to present the data in Tesla (or T/m for derivatives) and not in A/m (or A/m² for derivatives).

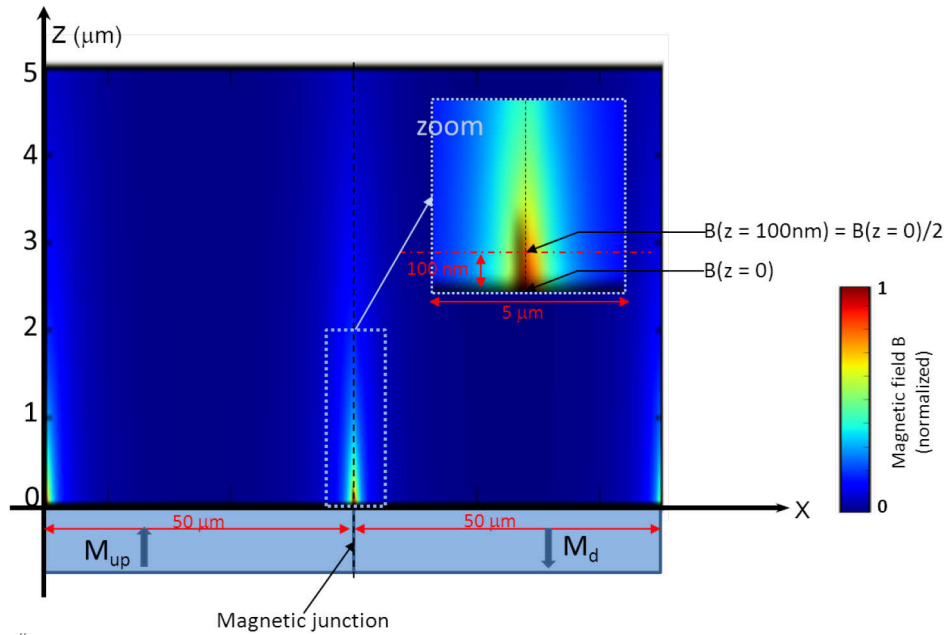


Figure 2.13#. Graphical representation in 2D of magnetic field B above the magnetic junction simulated with Model 1.

To complete this information the total magnetic field produced by TMP samples with stripes of different width ($w = 50, 100$ and $200 \mu\text{m}$) and corresponding field gradient profiles were calculated (Figure 2.14). The curves have been computed using Model 1, all the parameters apart of RZ width w and distance between the stripes $w_0 = w$ remained the same as for Figure 2.13. The magnetic field and field gradient were calculated at the distance of $1 \mu\text{m}$ from the surface. Red curves correspond to the sample with stripes width $w = 50 \mu\text{m}$, green curves to the one with $w = 100 \mu\text{m}$ and blue curves to the one with $w = 200 \mu\text{m}$. It should be noticed that red curves sometimes are partially covered by green and blue ones, and green curves are partially superposed by blue ones. Zero lateral position corresponds to the first magnetic junction for all three modelled samples.

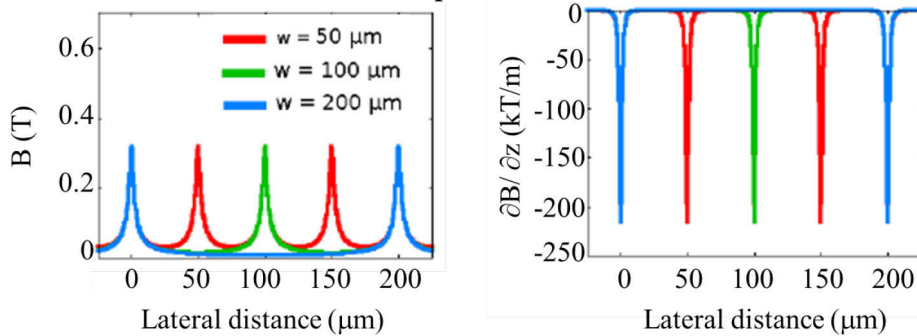


Figure 2.14. Magnetic field B and field gradient $\partial B/\partial z$ calculated with Model 1 for TMP magnet with stripes of 50 (red), 100 (green) and 200 (blue) μm widths at distance of $1 \mu\text{m}$ from the surface [6].

Both, magnetic field B and its field gradient $\partial B/\partial z$ reach the maximum above the interface between RZ and NRZ (magnetic junctions). Magnetic field gradient $\partial B/\partial z$ up to $2 \cdot 10^5 \text{ T/m}$ was estimated. This confirms that in trapping experiments magnetic particles should be captured above the magnetic junctions. It is also observed that the width of the pattern stripes does not affect strongly the magnetic field and field gradient intensity for a distance of $1 \mu\text{m}$ above the surface.

For the measurements at $10 \mu\text{m}$ from the surface above the magnetic junctions the stripes width has an impact on field/field gradient intensity. Slightly higher values (8.5%) observed for wide stripes pattern (200 and $100 \mu\text{m}$) than for narrow one ($50 \mu\text{m}$). However, above the centre of each stripe of 200 and $100 \mu\text{m}$ width magnetic field drops almost to zero (80% of

field intensity reduction: 0.01 T versus 0.047 T for maximum peak value), while for 50 μm lines the field remains positive (40% of field intensity reduction: 0.027 T versus 0.045 T for maximum peak value). Further discussions and results of simulations for magnetic field B and its gradient $\partial B/\partial z$ at distances of 10 and 50 μm are presented in Annex II.3.

Albeit Models 1 and 2 produce close results for the magnetic field in case of using the same parameters for micromagnet array structure (Figure 2.15a,b), the magnetic force between sample and magnetic micro-object calculated with Model 2 (Figure 2.15c illustrates the interface) is more relevant. It provides more accurate results thanks to possibility of (i) discretisation of magnetic volume distribution to model superparamagnetic microspheres and (ii) use of permanent magnet model for NdFeB microsphere simulations. The Model 2 has some additional advantages: the magnetization of NRZ can be different from magnetization of RZ, the depth of RZ can be adjusted, the sphere volume is distributed in space and the magnetization of hard magnetic sphere can be tilted. The main drawback of Model 2 is that additional blocks should be added to model not only magnetic field and force, but also their derivatives.

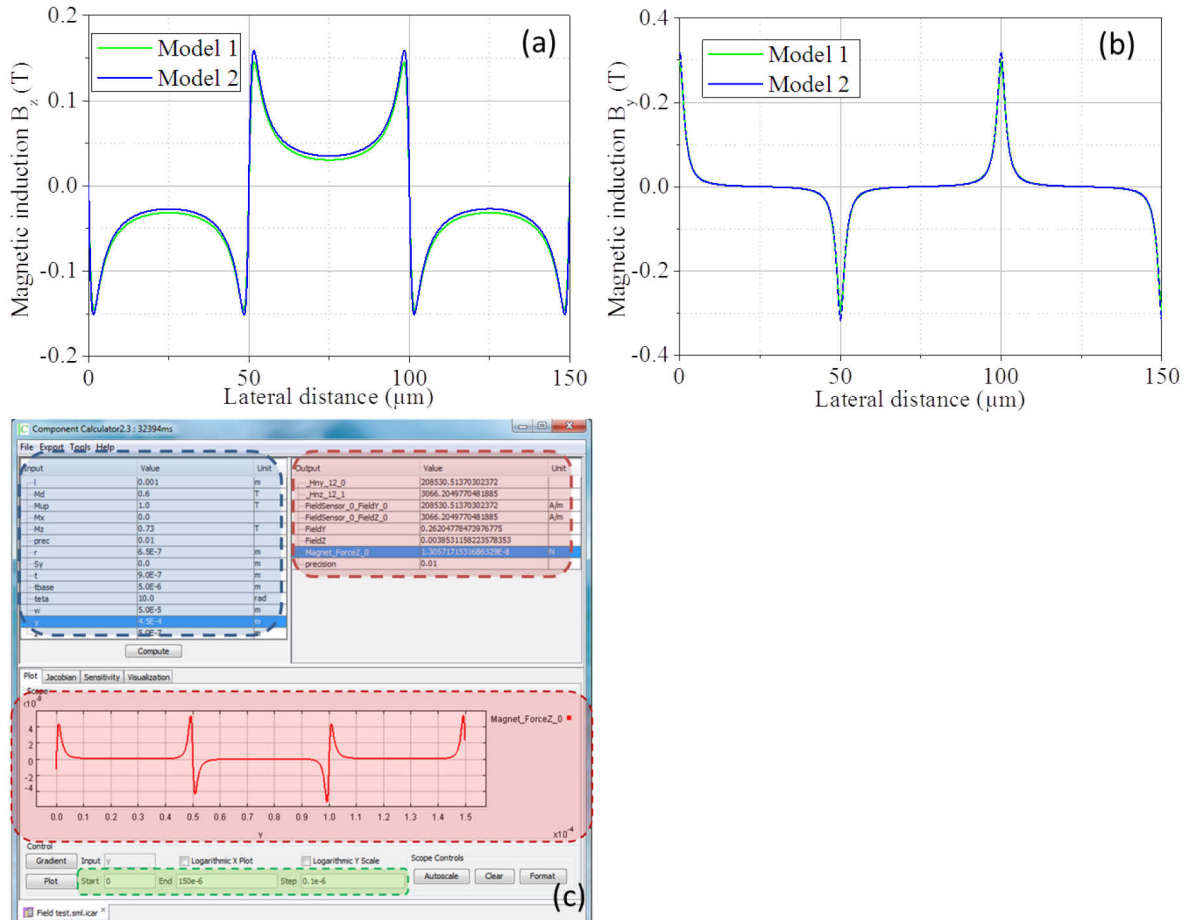


Figure 2.15. Results of magnetic field simulations with Model 1 and Model 2: (a) B_z component of magnetic induction; (b) B_y component of magnetic induction. (c) Interface of the program used for simulation of magnetic field and magnetic force acting on a NdFeB microsphere above the “stripe-like” TMP sample by CADES framework. Input area is marked by blue and output area is marked by red. Top: lateral positioning of microsphere y is chosen as an input. Magnetic force acting on it in z -direction $Magnet_ForceZ_0$ is chosen as an output. Bottom: Plot of magnetic force as a function of microsphere lateral positioning (red area) with the step of 0.1 μm (green area).

Detailed manual explaining the use of the program for simulation of systems with superparamagnetic and NdFeB microspheres above micromagnet array is presented in Annex II.4 and II.5.

The Model 2 (CADES framework) has been employed to study the impact of reversed depth thickness h_r and total magnetic film thickness t on the z -component of magnetic field

exerted by TMP sample (Figure 2.16)[#]. The calculations have been performed with following parameters:

- $W = 1$ cm – width of the film;
- $N = 20$ – number of stripes;
- $w = 50$ μm – width of the stripe;
- $M_{up} = 1.1$ T – magnetization of the non-reversed zone (NRZ);
- $M_d = 0.9$ T – magnetization of the reversed zone (RZ).
- $L = 1$ cm – length of the film;
- $l = 0.5$ cm – length of the stripe;
- $w_0 = 50$ μm – distance between stripes;

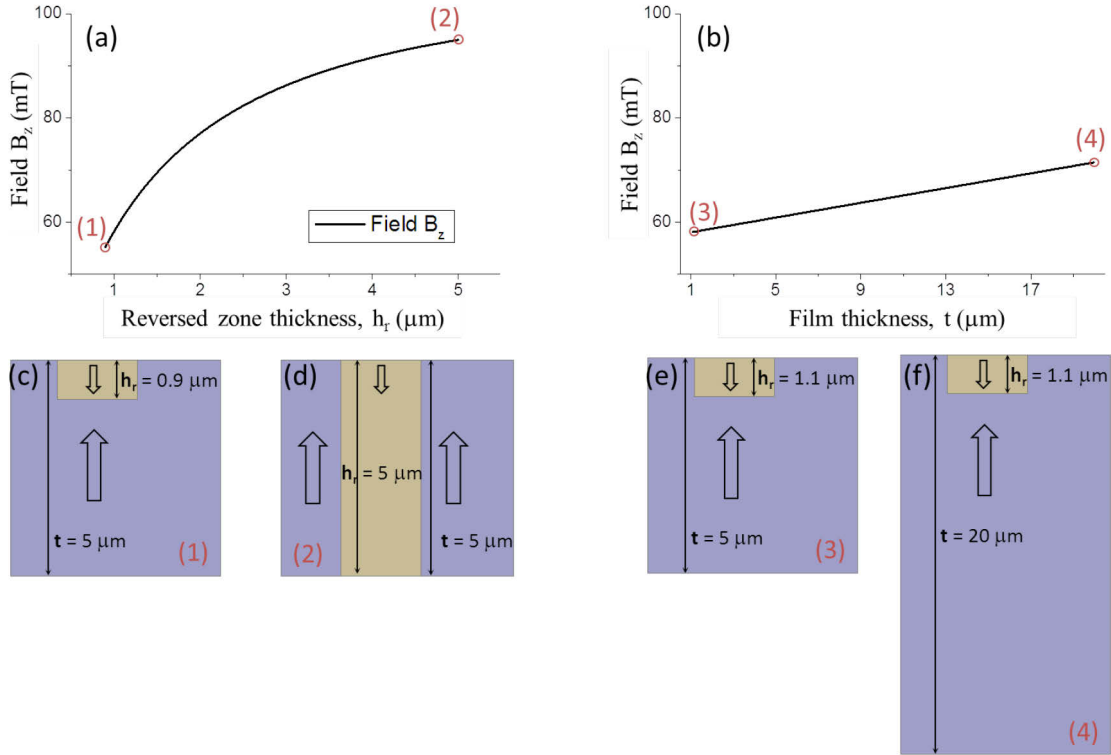


Figure 2.16[#]. Z-component of magnetic field for TMP sample with 50 μm stripes calculated at 1 μm above the MJ: (a) the effect of RZ depth for a fixed film thickness; (b) the effect of the total film thickness. (c), (d) Schematics of TMP configuration corresponding to positions (1) and (2) on the graph (a). (e), (f) Schematics of TMP configuration corresponding to positions (1) and (2) on the graph (b).

In Figure 2.16a the film thickness t was fixed ($t = 5$ μm) and the depth of RZ h_r was varying (0.9 $\mu\text{m} \leq h_r \leq 5$ μm), while in Figure 2.16b the depth of RZ h_r was fixed ($h_r = 1.1$ μm) and the total film thickness t was varying (1.1 $\mu\text{m} \leq t \leq 20$ μm). Magnetic field along z-axis was calculated at the distance of 1 μm above the top of magnetic layer.

We observed that the z-component of sample stray field varies significantly with the RZ thickness: from its minimal value $h_r = 0.9$ μm (position (1) in Figure 2.16a, corresponding sketch of the film structure is presented in Figure 2.16c) up to the total film thickness $h_r = t = 5$ μm (position (2) in Figure 2.16a, corresponding sketch of the film structure is presented in Figure 2.16d), B_z increases by a factor of 2 (55 mT and 95 mT, respectively).

The impact of the total film thickness t while depth of RZ $h_r = 1.1$ μm remains unchanged is not so strong. With enlargement of t from RZ thickness $t = h_r = 1.1$ μm (position (3) in Figure 2.16b, corresponding sketch of the film structure is presented in Figure 2.16e) up to $t = 20$ μm (position (4) in Figure 2.16b, corresponding sketch of the film structure is presented in Figure 2.16f) B_z increases by about 20% (58 mT and 71 mT, respectively).

The properties of RZ have strong impact on z-component of magnetic field arising from the sample; the variation of RZ thickness or magnetization (magnetic inhomogeneity) can

strongly affect the trapping process. Considering the theoretical model described above (where RZ and NRZ areas are parallelepipeds) the general trapping process of magnetic microparticles can be predicted. Since the strongest force/force gradient is observed above the interface between NRZ and RZ, the magnetic particles should be trapped along the magnetic junctions.

In the next sections basic experiments on static capture and positioning of magnetic particles will be compared with the expected results from a theoretical model.

II.2.2 Micromagnet array for particles trapping

The first basic experiments[#] on particles attraction by permanent micromagnet array were carried on with two kinds of magnetic microspheres (i) polymer microspheres with homogeneously dispersed magnetic nanoinclusions – *superparamagnetic* particles (SPM, microParticles GmbH) and (ii) *hard* magnetic microspheres of NdFeB (Magnequench International, Inc.). The choice of SPM particles relies on their similarities in shape and dimensions with certain cells. Moreover, the polymer (polystyrene) matrix density is close to the density of the aqueous medium used in experiments (usually about 1 g/cm³) and the amount of magnetic particles inside the bead can be selected according to the supplier. SPM particles serve as a fair model, for instance, for a cell labelled with a certain amount of magnetic nanoinclusions. Also in the biological and medical applications, the capture of functionalized particles itself is of foremost importance. The hard magnetic microparticles were chosen to extend the range of measurements and to sense both attractive and repulsive forces. Moreover, quantification of interaction between micromagnet array and hard magnetic microsphere provides additional information about the sample structure (Section IV.4).

The goal of preliminary capturing experiments is to estimate qualitatively the magnetic attraction and capturing properties of micromagnet arrays. For this study, ethanol¹¹ with 3 μm in diameter SPM particles in low concentration was poured on a NdFeB TMP films with chess-board and stripes patterns (Figure 2.17a and Figure 2.17b, respectively); the solution was left to settle for a few minutes. Similar experiment[#] was performed with 5 μm NdFeB particles on NdFeB TMP film with stripes pattern (Figure 2.17c). It is observed that for both types of particles (superparamagnetic and NdFeB) their distribution does not depend on the TMP pattern in the sense that for all the patterns the strongest attraction occurs above the magnetic junctions (between oppositely “up” and “down” magnetized neighbouring micromagnets) while the particles sediment above non-patterned zone is distributed randomly.

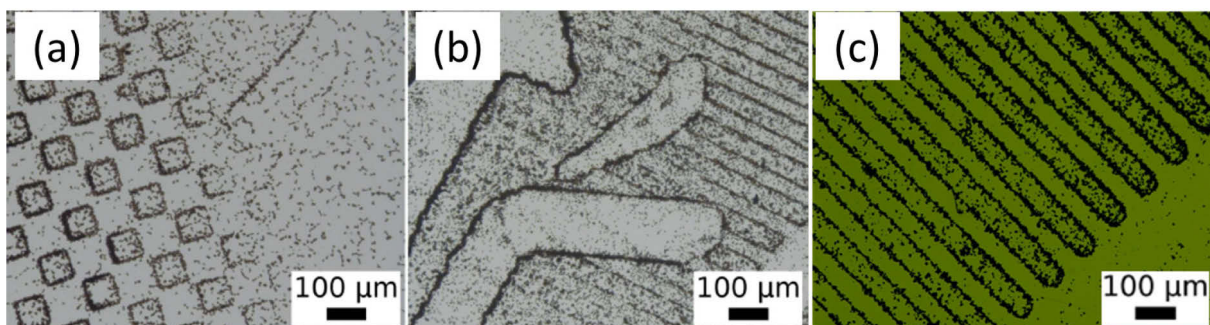


Figure 2.17. Magnetic microparticles trapped by NdFeB TMP film: (a) 3 μm in diameter SPM particles trapped by chess-board pattern; (b) 3 μm in diameter SPM particles trapped by stripes pattern [6]; (c) 5 μm in diameter NdFeB particles trapped by stripes pattern.

One can notice that there are some particles between the magnetic junctions and also out of the magnetic pattern; it should not be the case if real TMP samples are the same as it is described in theoretical model. The density of trapped particles is higher inside the RZs of magnetic film (inside squares in Figure 2.17a and inside stripes in Figure 2.17b).

¹¹ Ethanol was chosen to avoid the possible particles degradation/oxidation and due to its fast evaporation.

These observations are independent of the particle properties (size, magnetic moment and magnetic behaviour: superpara- or ferro-) and also of the pattern shape. It can be caused by magnetic properties of the pattern in general and by irregularities of the magnetic film: a variation in chemical composition, an oxidation spot, a non-magnetic or less-magnetic intergranular phase, topographical roughness, etc. As the number of particles trapped inside the RZs and NRZs is different, this leads to an additional signature of magnetic inhomogeneity of the film, in particular for RZs.

In order to qualitatively evaluate the intensity of these traps, experiments on fluid flow impact were carried out. Figure 2.18 shows trapped 3 μm in diameter SPM particles without (a) and with (b) fluid flow induced by agitation with a pipette. The drag force removes most of the particles and only strongly trapped particles remains (Figure 2.18b).

These results confirm that most of the particles are trapped at or in closed vicinity of the magnetic junctions thanks to the high magnetic interaction. However, after induction of strong fluid flow some microspheres remain captured inside RZs (red circles in Figure 2.18b) and very few spheres are captured in NRZs (blue circles in Figure 2.18b). This indicates one more time that RZs of patterned magnetic films exhibit magnetic inhomogeneity.

A detailed experimental study of structural and magnetic properties of patterned magnetic films at micro and nano-scale is required to understand better the interaction between micromagnet array and magnetic particles.

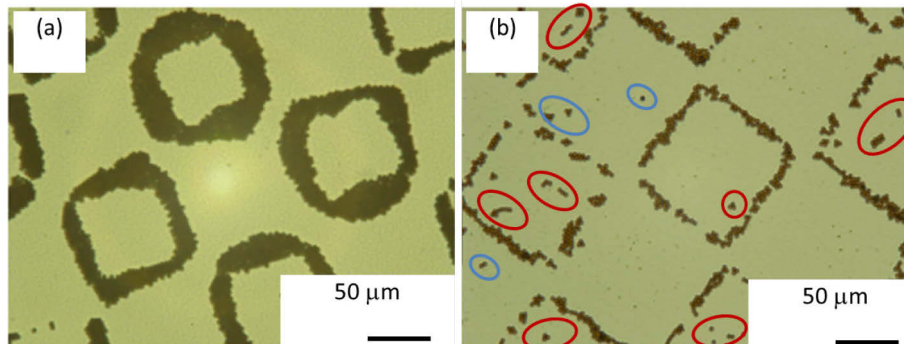


Figure 2.18. (a) A large amount of 3 μm in diameter SPM particles is captured above an array of magnetic squares. (b) The drag force removed most of the particles once a strong fluid flow is induced [6]. Particles that remain trapped inside RZ are marked with red circles and inside NRZ are marked with blue circles.

II.2.3 Localization and identification of magnetic pattern

Thanks to Magneto-Optic Imaging Films (MOIFs) allowing direct visualization of magnetic stray field distribution [16], the micromagnet patterns were localized and their lateral dimensions were measured[#].

A MOIF is composed of two layers: aluminium layer with ferrite garnet film above. The main principle of MOIF is based on the interaction between polarized light and magnetic material. When the polarized light passes through the garnet, its plane of polarization is rotated proportionally to the magnetic component, which is parallel to its direction of incidence. This Faraday rotation occurs twice, since the light is reflected by the aluminium layer and passes through the garnet a second time before visualization (Figure 2.19). The double rotation improves the contrast obtained with the MOIFs. It means that when MOIF is far from the sample surface, there is no impact on it. With decrease of the separation distance stray field from the sample induces a local modification of MOIF response thereby revealing a magnetic pattern. In practice a microscope equipped with polarized light illumination is required to visualize magnetic structure with help of MOIF.

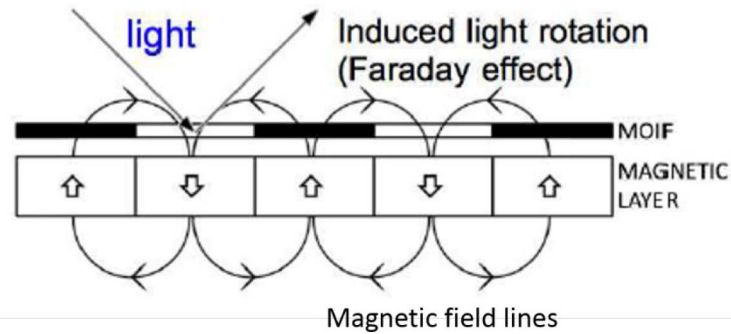


Figure 2.19. Schematic representation of the image obtained with a MOIF, observed by rotation of polarized light [6]. The black and white zones of MOIF reveal the oppositely magnetized (“up” and “down”) zones of magnetic layer.

MOIF technique can be employed for characterization of micromagnet arrays produced by all fabrication procedures described previously. It is a fast and simple approach to verify the quality of obtained magnetic pattern: localization, shape, lateral size and homogeneity (presence/absence of magnetic structure defects like area (1) and (2) in Figure 2.20b).

The achievable spatial resolution is limited by the MOIF-sample distance, the thickness of active magneto optic layer [17] and depends on the domain structure size. The vertical resolution is limited by the film thickness. The demonstrated spatial resolution is $1\ \mu\text{m}$ at best [17], but with MOIFs available during my PhD magnetic features of less than $10\ \mu\text{m}$ were not well resolved. The lateral size of magnetic features studied in this work was about $50\ \mu\text{m}$ or more, thus, the resolution of provided MOIFs was good enough for magnetic pattern visualization.

The uniaxial¹² MOIF (U-MOIF) was used for localization and lateral size measurements of magnetic patterns for TMP and μMI samples, the results are presented in Figures 2.20 and 2.21 respectively[#].

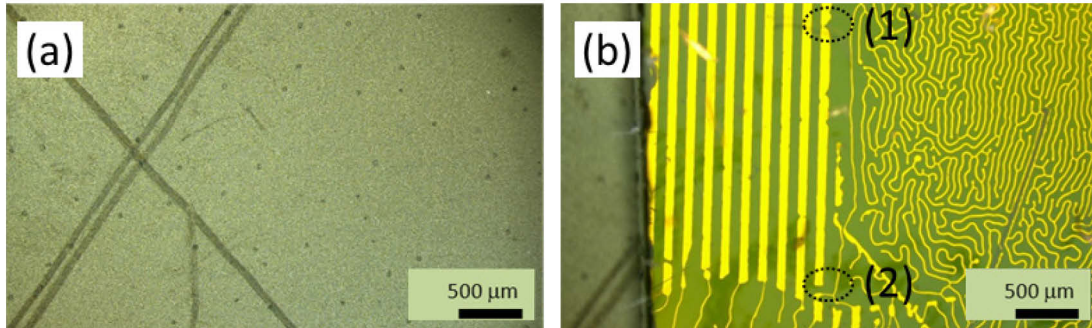


Figure 2.20[#]. Optical images of NdFeB TMP sample with $50\ \mu\text{m}$ stripes pattern (a) without MOIF and (b) with U-MOIF placed on the top of the sample. Yellow stripes correspond to RZs while green stripes to NRZs of magnetic pattern.

Figure 2.20 (a) displays an optical image of TMP sample with $50\ \mu\text{m}$ stripes pattern where the mechanical scratch in the centre is considering as a spatial reference. No magnetic pattern is observed. Figure 2.20 (b) presents the same area with U-MOIF placed on top of the film. On the left side of the image (free of MOIF) mechanical scratch is observed, the centre of the image (with MOIF) reveals magnetic pattern with $50\ \mu\text{m}$ stripes while on the right side (with MOIF) magnetic film free of the pattern in non-saturated state (as the field created by the magnet is restricted to the zones close to the pattern) is revealed. The interface between RZs (yellow stripes) and NRZs (green area) is well-defined, nevertheless some pattern defects are detected. The average width of the RZ is $50\ \mu\text{m}$, but at the edges of the pattern (for example, areas (1) and (2) of the last yellow stripe in Figure 2.20b) the stripe is not well-

¹² U-MOIF has an out-of-plane spontaneous magnetization, thus, a polarized light is rotated even if no field is acting on the film. With U-MOIF placed above a magnetic pattern a binary image can be obtained.

defined, constricted shape is observed. Moreover, the length of the stripes varies from line to line. The appearance of the constricted RZ can be explained by bad contact of MOIF with sample surface (for example due to the sample tilt or surface roughness), mechanical damage of MOIF or sample inhomogeneity due to fabrication process. The difference in the length of RZ from line to line can be caused by bad contact of MOIF with sample surface or the film pattern can have not well-defined structure due to fabrication process.

On the optical image (Figure 2.21a) of μ MI sample with 5 μ m diameter NdFeB microparticles, the pattern of lines formed by microspheres with the separation distance of 50 μ m is presented. Some particles are captured not only along the lines, but also in between as it was shown in experiments in section II.2.2 mainly due to inhomogeneity of the master structure (TMP sample presented in Figure 2.20). Thus, the magnetic pattern revealed by MOIF (Figure 2.21b) is not as well-defined as for TMP sample. There are a number of explanations for this observation. Firstly, it can be due to μ MI sample by itself. Magnetic particles trapped between lines create additional magnetic inhomogeneity. The lines formed by microparticles in polymer matrix are not homogeneous neither: their thickness and depth vary along the same line and from line to line. The improvements in μ MI fabrication process can minimize these effects. Secondly, these features can be explained by the quality of MOIF (mechanical damage, low resolution) and its interaction with the sample (bad contact between MOIF and sample).

Through MOIF characterization of μ MI samples, lack of trapped microparticles or their agglomerates can be detected (restricted or extended stripes revealed by changes in colour).

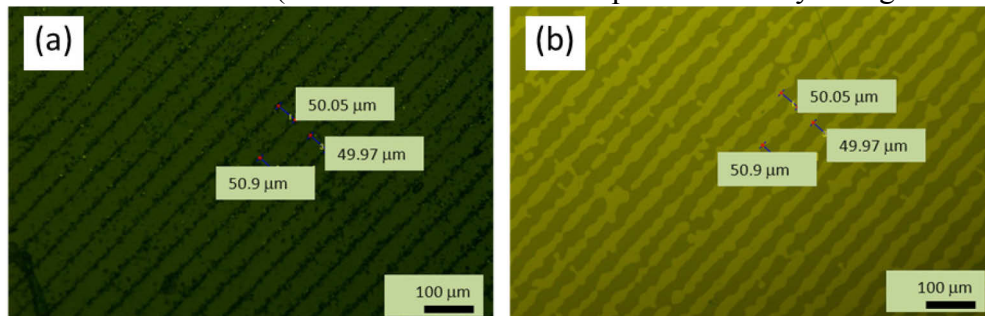


Figure 2.21#. Optical images of μ MI sample with trapped 5 μ m diameter NdFeB microparticles separated by 50 μ m distance: (a) without MOIF and (b) with U-MOIF placed on the top of the sample. Yellow areas localize the position of trapped magnetic microspheres.

Thanks to MOIF, localization of magnetic pattern and its quality for both TMP and μ MI samples were verified: magnetic patterns of 50 μ m stripes formed on TMP and μ MI samples are observed. However, in case of TMP samples more detailed imaging of the pattern is required for detection and measurements of magnetic inhomogeneity of RZ, the so-called “magnetic roughness” [18].

II.2.4 Reverse depth determination of TMP sample

Like lateral dimensions of magnetic pattern, the depth of reversed zone (RZ) has a strong impact on magnetic properties of such samples: an increase of RZ thickness induce a variation in magnetic field intensity (Figure 2.16a) above the magnetic junction (which lead to a higher field gradient) and by the way on the force acting on magnetic objects in its vicinity.

Different approaches have been applied to estimate RZ depth value. The first one is based on the combination of MOIF with Vibrating Sample Magnetometer (VSM) and the second one on the measurements of the stray field by Scanning Hall Probe Microscopy (SHPM).

The main principle of VSM is based on Faraday's law: an electromagnetic force is generated in a coil when there is a change in flux through this coil. Magnetic flux change is induced by sinusoidal motion (mechanical vibrations) of the sample and causes a voltage proportional to the magnetic moment of the sample in the coil.

The reversed zone depth of TMP sample is estimated by the combination of VSM and MOIF measurements. The use of MOIF with image treatment software (for example, ImageJ) provides information about irradiated reversed zone (RZ) surface (S_1) and whole surface of the film (S_2). The volume of RZ is considered to be a parallelepiped with unknown depth h_r .

Magnetization measurements were performed by VSM for both the patterned state, M_{ri} , and the remanent state after saturation in 8 T field, M_{rs} . The reversed thickness value h_r is estimated with the equation (2.1):

$$h_r = 0.5t \cdot (S_1 + S_2) / S_2 \cdot (1 \pm M_{ri} / M_{rs}), \quad (2.1)$$

where t is the whole film thickness.

The results of this macroscopic approach provides a value of $(1.2 \pm 0.3) \mu\text{m}$, the error is associated with the uncertainty in the film thickness estimation and the areas corresponding to the RZ and NRZ [1]. This experimental value of h_r is included in the Models to refine the simulations of the magnetic fields and magnetic force. However to obtain a complete validation of the Models and the associated simulations, direct magnetic field measurements are needed.

II.2.5 Direct measurements of stray field produced by micromagnet array

The experimental set-up for Scanning Hall Probe Microscopy (SHPM) was developed at the Néel Institute by Klaus Hasselbach group. The measurements of the stray magnetic field z-component above the micropatterned films were performed using second-generation quantum-well Hall probe (contains three Hall crosses of active area size 4×4 , 10×10 and $40 \times 40 \mu\text{m}^2$) based on a 2D electron gas. The measured field profiles were used to derive the spatial variation in the field and field gradient values at distances in the range $0.1\text{--}10 \mu\text{m}$ above the micromagnet arrays. Plan-view of the Hall probe and experimental set-up are presented in Figure 2.22.

The Hall probe was fixed on a commercial quartz tuning fork and the sample stage was attached to a piezoactuator regulated by closed-loop proportional-integral-derivative (PID) control, where the amplified amplitude of the signal from the tuning fork was supplied to the input of the PID. After careful definition of the distance between the Hall cross and the surface of the sample, the measurements of magnetic field with the resolution better than $100 \mu\text{T}$ were performed. Further details about the technique and experimental set up can be found in [19].

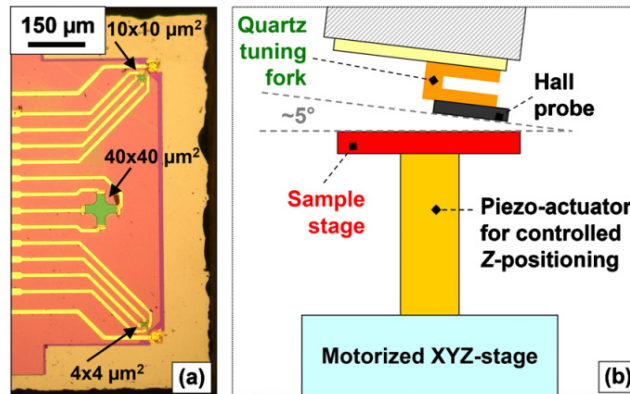


Figure 2.22. (a) Plan-view image of the Hall probe containing three active areas; (b) schematic diagram of the scanning Hall probe microscope set-up [19].

Figure 2.23 (a) displays the results of SHPM on a chessboard TMP sample (z-component of the stray field, B_z). On the associated cross-section, we observe that the maximum of z-component of magnetic field is reached at the centre of each square zone and varies in an abrupt way at the approach of the magnetic junction. Using a model with the same pattern, analytical calculations of B_z were performed varying the reversal depth values: $0.5 \mu\text{m}$ (blue), $1.0 \mu\text{m}$ (red) and $1.5 \mu\text{m}$ (green) (Figure 2.23b). More detailed experiment description and calculations are presented in [1,19]. Based on comparison of experimental data and analytical

calculations a reversal depth of $(1.1 \pm 0.2) \mu\text{m}$ was found, the error is associated with uncertainties on the estimated volume and the sample-probe distance. These values are in agreement with the results of previously described experiments for RZ thickness measurements $(1.2 \pm 0.3) \mu\text{m}$ based on combination of MOIF and VSM (section II.2.4).

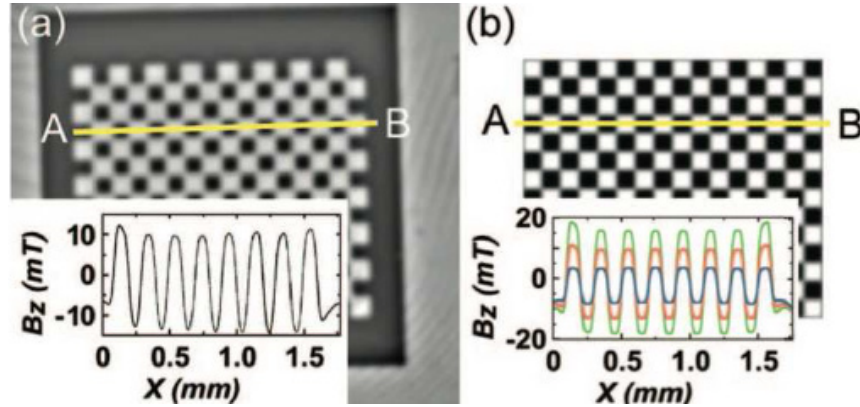


Figure 2.23. (a) Representation of the z-component of the magnetic field B_z as observed by SHPM; inset: B_z profile along the yellow line; (b) Schematic of the magnets considered on the analytical calculations; inset: B_z profiles corresponding to magnets with different reversal depths ($0.5 \mu\text{m}$ - blue; $1.0 \mu\text{m}$ - red; $1.5 \mu\text{m}$ - green). The maximum B_z values are observed above the centre of squares [1].

This experimental set up was applied to characterize the stray magnetic field z-component of μMI samples obtained by trapping $16 \mu\text{m}$ or $5 \mu\text{m}$ size NdFeB microparticles [3]. Measurements were carried out with a micro-Hall probe of active area $2 \times 2 \mu\text{m}^2$ at different heights ($5 \mu\text{m}$, $20 \mu\text{m}$ and $50 \mu\text{m}$) and compared to SHPM results of master TMP samples (Figure 2.24). These images clearly show that μMI samples do not produce a replica of the master structure, but a new structure defined by the master's stray field pattern. Indeed the maximum magnetic field is reached above the particle lines corresponding to the maximum force gradient on the TMP master sample. The intensity of the magnetic field is higher to the TMP master sample by approximately a factor of 3 (B_{max} equal to 10 mT versus 3.5 mT at a height of $50 \mu\text{m}$) that can be explained by a number and total volume of particles trapped to form a pattern on μMI sample.

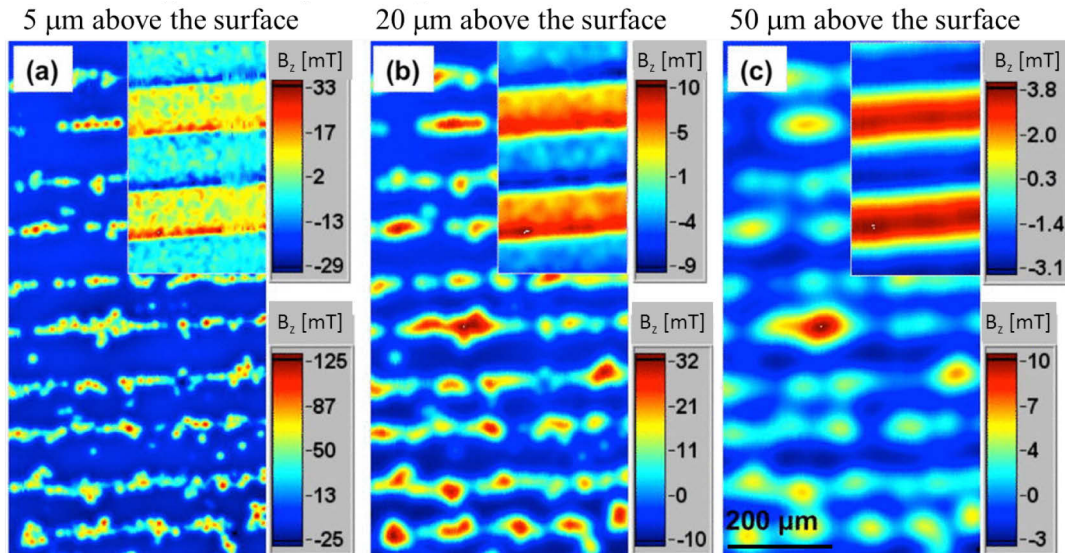


Figure 2.24. Scanning Hall Probe measurements of the stray magnetic field B_z measured at a height of $5 \mu\text{m}$ (a), $20 \mu\text{m}$ (b) and $50 \mu\text{m}$ (c) above a $100 \mu\text{m}$ striped μMI structure made with $16 \mu\text{m}$ spherical gas-atomised NdFeB particles. The inset of each figure corresponds to a measurement of the master thermo-magnetically patterned structure at the same scan height – note the higher range in colour scale for the μMI structures (bottom right of each image) compared to the master structures (top right of each image) [3].

For comparison of experimental results with numerical calculations in Figure 2.25 simulations of the stray field z-component at heights of 5 μm , 20 μm and 50 μm above μMI structures made with spherical powders of average particle size 16 μm or 5 μm are presented. Zero lateral position corresponds to the centre of pattern (centre of a single trapped sphere or spheres agglomerate). Magnetic field z-component B_z strongly depends on the trapped microsphere size (and magnetic volume) and decays fast with increase of the distance (for 16 μm diameter spheres: 110 mT at 5 μm and 0.6 mT at 50 μm ; for 5 μm diameter spheres: 60 mT at 5 μm and 0.12 mT at 50 μm). The width of B_z peak is proportional to the width of microspheres forming a single line of pattern. Moreover, close to surface (distance depends on the sphere size; for 16 μm diameter spheres it is about 5 μm) the shape of the field is affected by the structure of spheres agglomerate. This can explain three maximum peaks in Figure 2.25 for the first and second agglomerates configurations (black and blue curves).

Experimental results were compared with simulations and in agreement: peak-to-peak z-component field value at a scan height of 5 μm above a line of 16 μm particles are 130 mT and 110 mT, respectively. Simulations indicate magnetic field gradients of up to $5 \cdot 10^5$ T/m above the trapped particles at the surface of such μMI structures. For both, μMI and TMP samples fast decay of magnetic field intensity with increase of the probe-sample distance is observed.

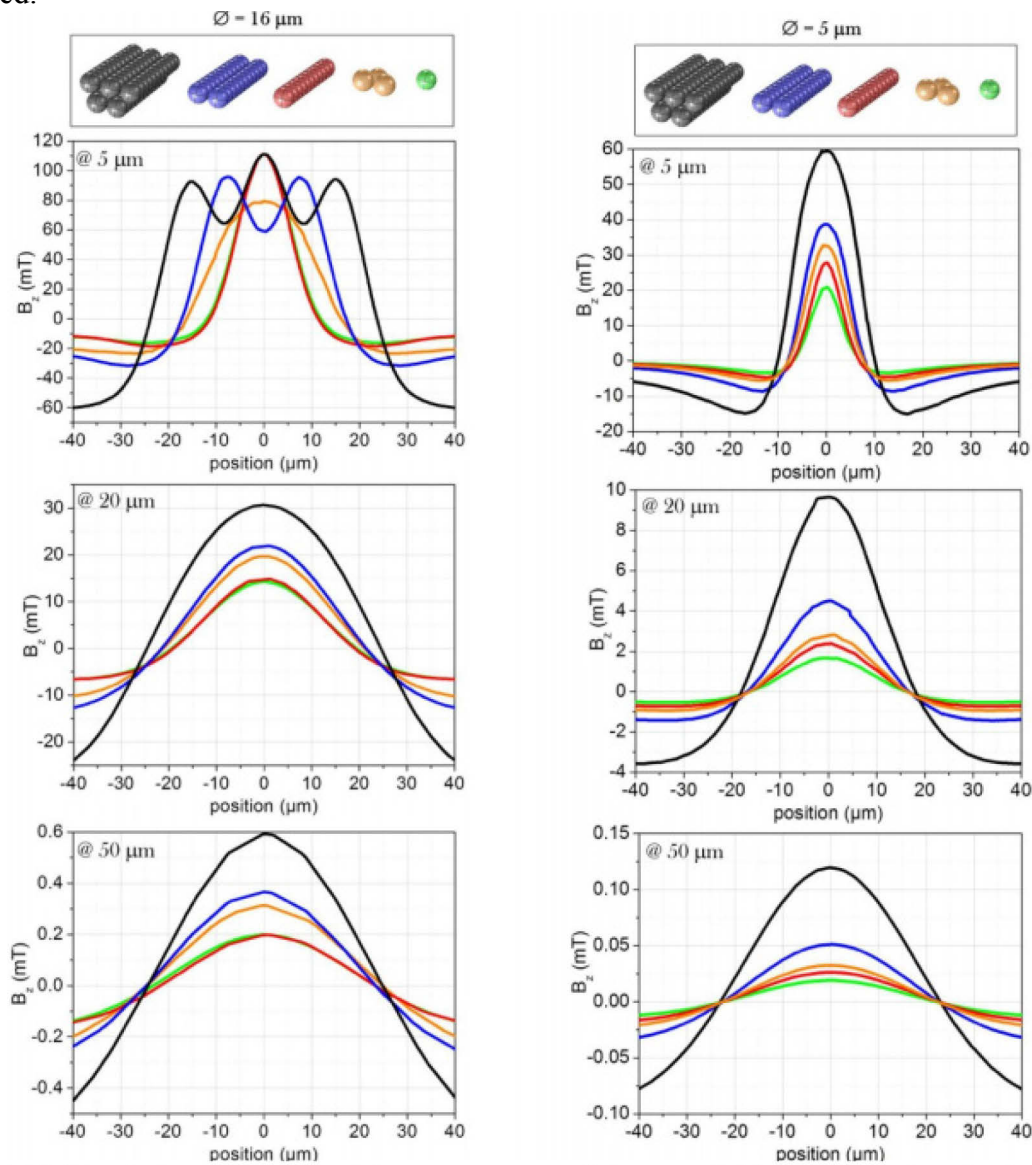


Figure 2.25. Simulations (Comsol) of the z-component of the stray field pattern produced at heights of 5 μm , 20 μm and 50 μm above μMI structures made with spherical powders of average particle size 16 μm (a) and 5 μm (b) [20].

SHPM provides quantitative characterization of stray magnetic field z -component. The main disadvantage of this technique is that the probe due to its construction cannot approach very close to the surface and it leads to a limited lateral resolution (linked to probe-sample distance). This distance affects the image: on inserts in Figure 2.24 magnetic inhomogeneity of TMP samples at probe-sample separation distance of $5\ \mu\text{m}$ is barely observed (a), but disappears when probe is lifted further from the surface (b,c). For μMI samples some magnetic microparticles trapped outside of the pattern are localized in SHPM images at $5\ \mu\text{m}$ above the sample, but the resolution is lost with increase of the distance. This can be explained by fast decay of magnetic stray field with increase of the distance. These experiments combined with simulations demonstrate spatial variation in the field and field gradient above the micromagnet array at micro-scale. To complete this study additional characterization with a technique providing higher spatial resolution is required.

II.2.6 Nano-scale characterization of TMP sample surface morphology and magnetic properties

Scanning Probe Microscopy (including AFM and MFM) can display qualitative and quantitative characterization of micromagnet array topography and its associated magnetic properties with high resolution (up to few tens of nm). AFM measurements are complementary to Scanning Electron Microscopy (SEM) technique for surface imaging with high 3D resolution. MFM technique can be implemented for localization and characterization of magnetic junctions, for identification of magnetic inhomogeneity and for direct force measurements between micromagnet array and a single magnetic micro-object (soft or hard magnetic microsphere). Experimental results and theoretical calculations will be presented in details in next chapters (Chapter III and Chapter IV). Here, the preliminary characterization of TMP samples is provided.

First experiments at the Néel Institute to study thick NdFeB films (patterned and without pattern) using AFM and MFM technique have been conducted during PhD of Georgeta Ciuta [21] and more recent results of this work can be found in [22]. The measurements were performed with different types of MFM (mechanically stiff and soft, with high and low coercivity magnetic coating) probes in dynamic mode. Some results together with associated simulations are presented in Figure 2.26. Experimental MFM signal above a set of $7\ \mu\text{m}$ width micromagnets for 4 different scan heights (0.005 , 0.5 , 1 and $2.5\ \mu\text{m}$) is displayed in Figure 2.26a. For comparison, the calculated z -field (Figure 2.26b), z -field's first derivative (Figure 2.26c) and z -field's second derivative (Figure 2.26d) for the same heights, are shown. For more accurate comparison of experimental and numerical results Ta coating layer of $100\ \text{nm}$ covering TMP micromagnet array was taken into account in simulations; experimental profiles were extracted by averaging 50 scan lines. The measurements have been conducted with "stiff"¹³ MFM probe [22].

Variation of magnetic field intensity along z -axis depends on the distance from the surface: for low tip-sample distances (less than $1\ \mu\text{m}$) its maximum is observed in vicinity of magnetic junctions; with increase of the separation distance (from $1\ \mu\text{m}$) z -field reaches its maximum above the middle of each micromagnet. These experiments are in agreement with the results of SHPM imaging of stray field z -component for TMP samples (Figure 2.23).

¹³ Resonance frequency is $300\ \text{kHz}$, spring constant is $40\ \text{N/m}$, coercivity of magnetic coating is more than $0.5\ \text{T}$.

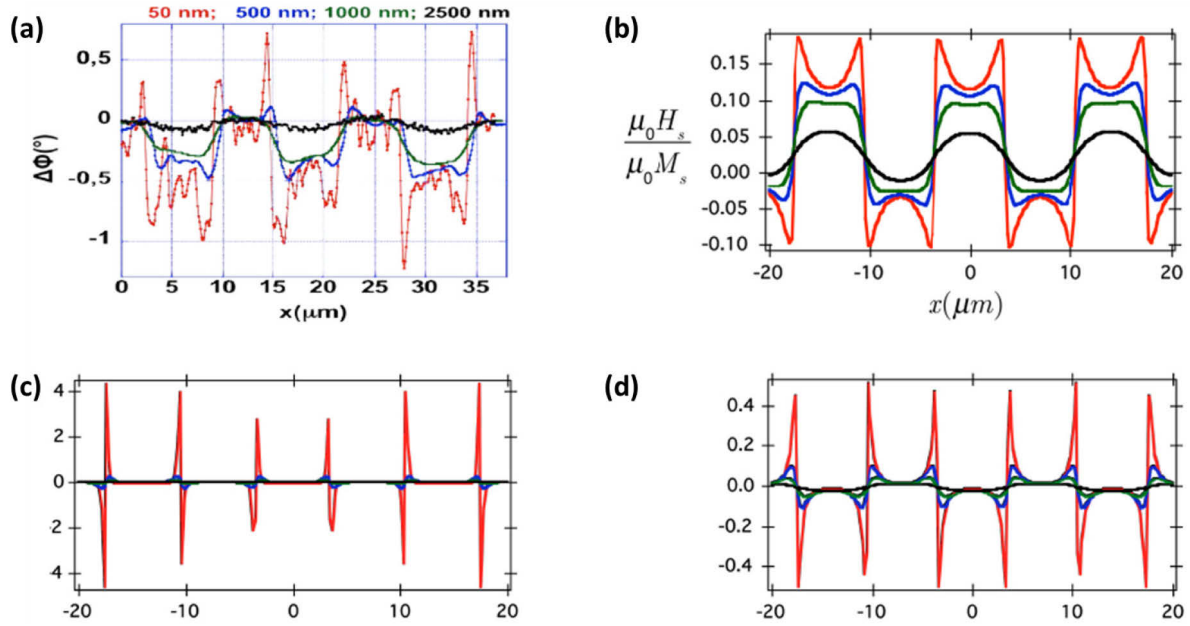


Figure 2.26. (a) Experimental scan lines of the MFM signal (phase shift) at different scan heights (50, 500, 1000 and 2500 nm) compared to (b) calculated vertical field, (c) its first derivative and (d) its second derivative along z [21].

The map of the stray field best reproduces the experimental contrast. The calculated derivatives decay with enlargement of tip-sample distance much faster than the experimental data. The phase shift reflecting the stray field itself, rather than one of its derivatives, is therefore an aspect specific to permanent magnets with potentially long-range stray fields. It was shown that in MFM measurements of TMP magnets the stray field is mapped when coarse magnetic domains with long-range stray fields are imaged, which is usually not the case for standard MFM measurements¹⁴.

In PhD work of Georgeta Ciuta [21] it has been demonstrated that mechanically stiff MFM probes coated with a hard magnetic material are best suited to the study of thick hard magnetic films due to the strong probe-sample interaction. However, the use of these probes has an impact on MFM (phase shift) maps. Dark-light contrast in vicinity of oppositely magnetized micromagnets is observed (Figure 2.27a): the light contrast is much stronger at the bottom of each square while dark contrast appears on the top of squares. The explanation of this behaviour relies on probe or/and sample magnetic properties. Firstly, if micromagnets are not perfectly oriented out-of-plane, in-plane component arising from the sample can cause this contrast. To test this assumption, magnetic sample was rotated by 45 degrees (Figure 2.27b). The direction of alternation in dark-light contrast remains vertical (light contrast is much stronger at the bottom, dark contrast in top) proving that micromagnet array was magnetized vertically (oop). Secondly this effect can be explained by the fact that in vibrating mode oscillation direction makes always an angle with the normal to the sample (Figure 2.27c).

Tilted MFM probe with hard magnetic coating is sensitive to an in-plane component of the sample stray field due to its alignment with a part of magnetic moment of the tip. A good agreement of the experiment with the calculation was observed and confirms that dark/light contrast appears due to in-plane component of the probe magnetization.

¹⁴ Most of the samples measured by MFM produce short-range stray fields. This implies that only a small part of the magnetic tip is active during the imaging and the monopole and/or dipole models are more appropriate to describe magnetic interaction. This effect is amplified by the finite radius of curvature of the tip apex combined with the typically normal incident deposition of magnetic material, resulting in a larger thickness of material at the apex than on the sides of the tip.

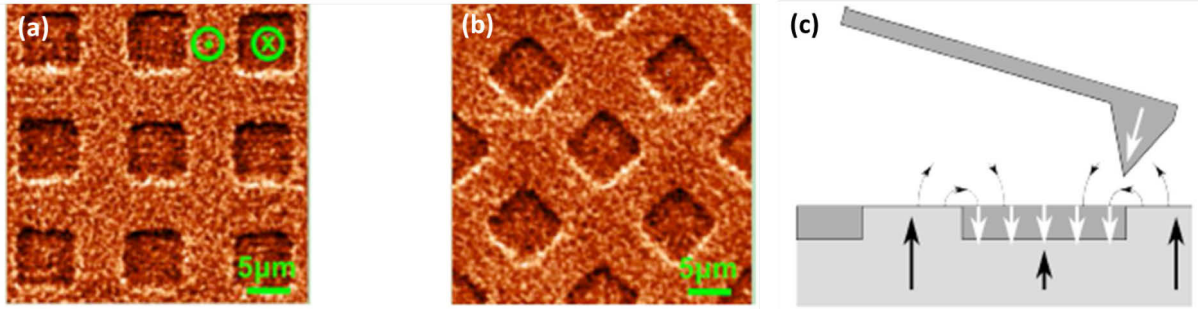


Figure 2.27. MFM (phase) images of TMP sample obtained with hard magnetic coating stiff MFM probe (a) before and (b) after sample rotation by 45 degrees. (c) Schematic of the real tip-sample geometry during scanning [21].

To complete characterization of TMP samples by commercial MFM probes additional experiments have been carried out with standard MFM probe with soft magnetic coating (MagneticMulti-75G, BudgetSensors) during my PhD[#].

In Figure 2.28 the preliminary characterization of TMP sample with 50 μm stripes pattern by soft coating MFM probe together with results of SEM imaging are presented. AFM image of TMP sample (Figure 2.28 a) reveals its topography. The surface has bumpy shape (due to extraction of Nd during annealing step) with the maximum height of 1 μm . Similar results are obtained by SEM (Figure 2.28 c): the surface structure is well observed, the lateral resolution is improved, but it does not provide an access to the height of Nd-rich features. The AFM is complementary for SEM imaging technique in case of surface topography characterization providing unprecedented 3D resolution.

In MFM image (Figure 2.28 b) two dark lines corresponding to interfaces between neighbouring micromagnets (magnetic junctions, MJ) are observed. The absence of dark-light contrast between oppositely magnetized magnets is explained by magnetic properties of the probe coating. The interaction between magnetic tip and sample is always attractive, since the stray field arising from the sample controls magnetization direction of the tip. The area between magnetic junctions exhibits magnetic inhomogeneity or “*magnetic roughness*” [18] allowing us to identify this region as a reversed zone (RZ). Thus, the left magnetic junction corresponds to NRZ/RZ boundary and the right one to RZ/NRZ boundary.

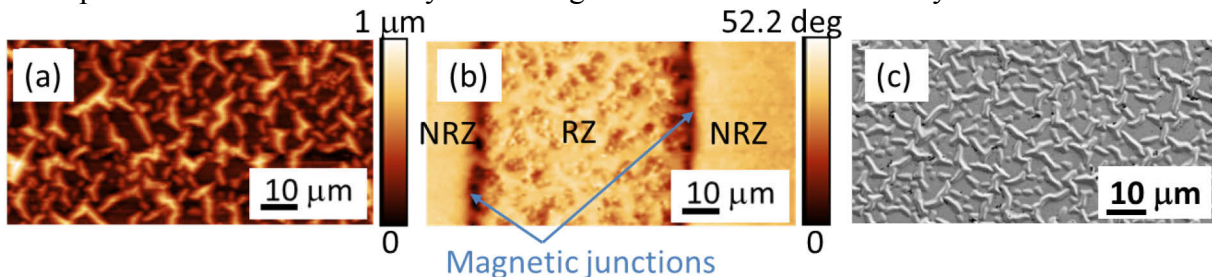


Figure 2.28[#]. (a) AFM image of TMP sample topography and (b) MFM image of TMP magnetic pattern obtained with soft magnetic probe (Multi-75G, BudgetSensors). The measurements are performed in dynamic mode. (c) SEM image of TMP sample.

Compared to the previously described methods (MOIF, SHPM and VSM), Magnetic Force Microscopy is the first technique providing at the same time measurements on topography and magnetic properties of micromagnet array with nanoscale resolution. Magnetic junction localization is performed with precision of few tens of nm and magnetic inhomogeneity can be clearly observed and measured [18]. The maximum phase shift $\Delta\varphi$ above the magnetic junctions corresponds to the regions of the highest field gradient. This confirms the high magnetic field gradient above the magnetic junctions as it was detected and measured by Scanning Hall Probe Microscopy technique.

MFM provides additional information that cannot be detected by MOIF or SHPM. Firstly, the difference in magnetic roughness between NRZ and RZ is clearly highlighted on

MFM image: the RZ is much less homogenous than the NRZ. This observation is in agreement with experimental results on magnetic particles static capture (Figure 2.10) and can explain trapping of the particles far from the magnetic junctions. Secondly, MFM imaging demonstrates the variation of magnetic junction width and its intensity providing higher than MOIF resolution. In addition, with MFM experiments, direct force (static mode) or force gradient (dynamic mode) measurements of magnetic interaction between micromagnet array and magnetic probe can be obtained. More detailed description and experimental results of micromagnet characterization by commercial and custom-made MFM probes will be discussed in Chapters III and IV.

II.2.7 Micromagnet array properties. Summary

A wide number of experiments for study of TMP, TOPO and μ MI magnetic flux sources was carried out; the most general properties of micromagnet arrays are summarized in Table 2.2. Thanks to TMP process different complex patterns can be created on magnetic film by magnetizing it in out-of-plane or in-plane direction. The minimum lateral size of the features and the maximum depth of the reversed part are limited by the thermal diffusion during irradiation (2 μm and 1.3 μm respectively). TMP can be performed on a flat film or on a topographic magnet, but only flat films allow fine control of the magnetic field, which is a crucial point for many applications in biology, especially for positioning of magnetic objects.

Topographic magnets have more simple structure compared to TMP due to the fabrication approach. The minimum lateral size of the features is limited by potential of lithography and cannot exceed few micrometres. Moreover, the ratio thickness-to-width should not be much higher than 1 to avoid possible breakage of the pattern on magnetic films deposition and microelectronic device integration steps. From the other hand, the thickness of TOPO magnet can reach 50 μm that increases a lot the action distance, because the magnetic field gradient is produced by the topographic variations of the film. This is a crucial parameter for devices where long-range action is required.

Micro magnetic imprinting is a very promising, but recently developed technique. Its advantage is a low fabrication and materials cost, short fabrication time. Different types of magnetic powders (magnetically hard and soft, superparamagnetic) can be used depending on application. The choice of a polymer matrix allows producing a transparent flexible or rigid biocompatible magnetic flux source. However, for micromagnets fabrication by μ MI a master magnet with desirable pattern is required. It can be TMP or TOPO magnet: application of an external magnetic field can increase the thickness of the particle agglomerates inside polymer matrix. Very few experiments for cells trapping have been done so far, the on-going work is focused on a deeper study of μ MI magnets and their possible applications.

To sum up: TMP samples have demonstrated highest field/field gradients at short distances and are suitable for particle attraction at the vicinities of the magnets; meanwhile TOPO magnets can produce homogeneous high field/field gradients (due to the high thickness of magnetic layer) further from the sample surface and more adapted for particle attraction at long distances.

	TMP	TOPO	μMI
Shape of the pattern	Stripes, squares, circles	Stripes, squares, circles	Stripes, squares, circles
Lateral size of magnetic features, (μm)	> 2 (limited by thermal diffusion during irradiation)	> 1	Depends on the embedded sphere size

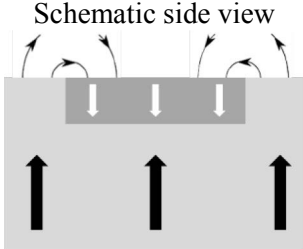
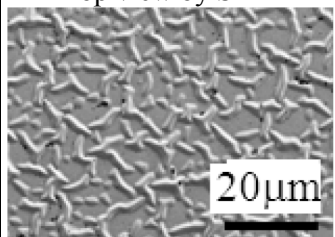
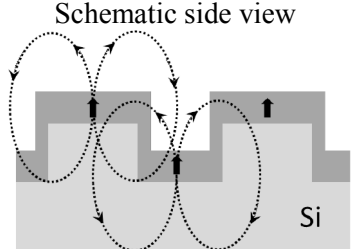
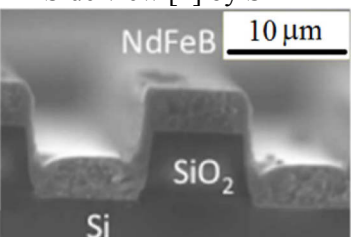
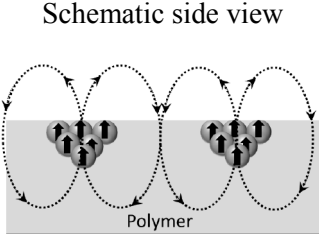
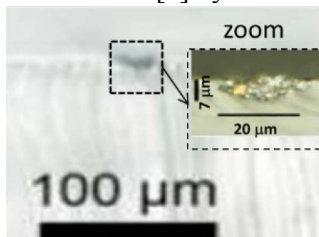
	TMP	TOPO	μ MI
Side/top view	 	 	 
Reversal depth (TMP); Thickness (TOPO; μ MI), (μ m)	< 1.3 (limited by thermal diffusion during irradiation)	< 50	Depends on the embedded sphere size
Sample/substrate	Flat or topographically patterned surface	Flat or topographically patterned surface	Transparent; flexible/rigid; biocompatible
Notes	<ul style="list-style-type: none"> • Multidirectional patterning in flat films; • Only flat film allows fine control of magnetic field; • Magnetic field gradient is max above the magnetic junctions. 	<ul style="list-style-type: none"> • ip or oop magnetization; • Thickness-to-width ratio < 1; • Features lateral size is limited by potential of lithography; • Magnetic field gradient is produced by topographic variations. 	<ul style="list-style-type: none"> • TMP or TOPO “master” magnet is required; • External magnetic field increases the thickness of the particle agglomerates inside polymer matrix; • Z-component of the stray magnetic field at 5 μm from the surface: 150 mT for 16 μm trapped NdFeB particles.
Thickness of magnetic layer/particles agglomeration, (μ m)	4-5 for NRZ; 1.1 \pm 0.2 for RZ	up to 100	Depends on the particles size (from tens of nm up to tens of μ m)
Coercivity $\mu_0 H_c$, (T)	up to 1.9 for NRZ; 0.6-1.9 for RZ	up to 1.5	Depends on the magnetic powder coercivity (up to 0.9 T for NdFeB particles)
Remanence $\mu_0 M_r$, (T)	1.4	up to 1.2	Depends on the density of the magnetic powder (varies from sample to sample)
Magnetic field gradient, (T/m)	up to 10^6 (above the surface) up to $2 \cdot 10^5$ (at 1 μ m above the surface, from simulations)	up to $2 \cdot 10^5$ (for 30 μ m thick magnetic layer at 1 μ m above the surface, from simulations)	up to $5 \cdot 10^5$ (above the surface, from simulations)

 Table 2.2. General parameters of TMP, TOPO and μ MI magnetic flux sources.

II.3 Microfluidic devices for micro-objects handling

Micromagnets as magnetic flux sources have been integrated in various devices dedicated to several applications as positioning, capture and separation of micro-objects in fluid. This section summarizes them and emphasizes the role of the various forces acting on the micro-objects during the handling process.

Microfluidics manipulates small amounts of fluids: liquids or gases. As in solid bodies, in liquids each molecule is surrounded by many others, but they do not have a fixed position in a lattice and thermal oscillations make them able to flow. For the analysis and prediction of fluid properties and behaviour a continuum hypothesis where the fluid is considered to be a continuous entity is used. There are two main types of microfluidic devices: (i) digital microfluidics manipulates isolated amounts of fluid, or droplets and (ii) continuous flow microfluidics where the fluid continuously passes through the microchannel. The second technique is more common nowadays thanks to its simpler device structure.

Microfluidic device for micro-objects handling based on magnets usually consists of polymer-based channels fabricated above polymer pre-covered magnets [6]. On Figure 2.29a an example of microfluidic device based on micromagnet array is schematically presented.

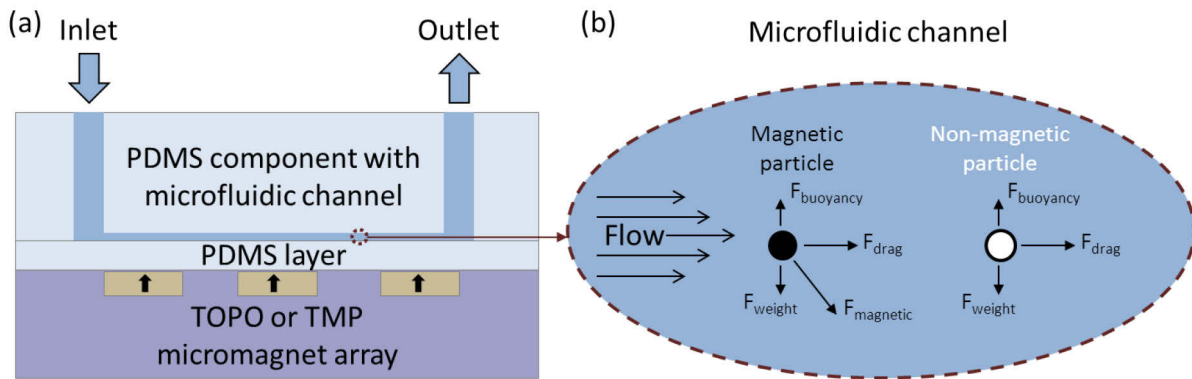


Figure 2.29. (a) Schematics of microfluidic device side-view used for magnetic particles handling. (b) Main forces acting on magnetic and non-magnetic particles inside a microfluidic channel.

The magnetic species within the channels are submitted to several interactions: (a) magnetic force due to all field sources, (b) viscous drag, (c) inertia, (d) gravity, (e) buoyancy, (f) thermal kinetics, (g) particle/fluid interactions (perturbations to the flow field), and (h) inter-particle effects, including (i) magnetic dipole interactions, (ii) electric double-layer interactions, and (iii) van der Waals force [23]. The combination of all forces together and the particle flow characteristics (laminar or turbulent) define the particle trajectory. However, for most magnetophoretic applications involving (sub)micron particles, the buoyancy, drag (viscous) and magnetic forces are dominant and one can ignore all other effects (Figure 2.29b) [23].

The quality of a microfluidic device based on magnetophoretic action depends on the magnetic flux source capability to produce high magnetic field gradients, thus, array of permanent micromagnets is a perfect candidate to fabricate efficient microfluidic device.

II.3.1 Static capture and positioning

In previous section (II 2.2), some examples illustrated magnetic particles trapping and positioning by TMP samples. To improve handling process additional experiments were performed [24] using textured thick ($5\ \mu\text{m}$) NdFeB films with oop magnetization. The choice of magnetic pattern was explained by the future use of micromagnet. Indeed, for capturing of magnetic particles stripes and chessboard magnetic patterns with lateral dimensions about $50\text{--}100\ \mu\text{m}$ were fabricated to avoid the interactions between particles trapped by neighbouring interfaces. Stray magnetic fields produced by micromagnet arrays were characterized by uniaxial MOIFs. The results presented in Figure 2.30 a,b (dark and light contrast on magneto-

optical images) confirm that films were initially magnetized oop, then after TMP procedure in some regions (according to the magnetic pattern) magnetization was reversed. MOIF characterization of TMP film with stripes does not reveal any particularities in the pattern structure, while for 50 μm chess-board pattern a gap between the vertices of squares is observed (Figure 2.30b, inside red dashed circle). This can be explained by the structure of the mask where the apertures through which the laser beam passes (correspond to RZs on patterned film) are physically separated by a distance of about 10 μm along their diagonal axes (Figure 2.30c) [25]. Such mask configuration can affect the trapping process: magnetic particles will be mainly attracted by sides of patterned squares, but not in the regions between square vertices.

Using analytical expressions magnetic field gradient along z-axis ($\partial B/\partial z$) was calculated [24] at the distance of 1 μm (estimated gap between the magnetic film and the active layer of MOIF) above the magnetic film (Figure 2.30 a,b, inserts). For both, stripes and chess-board TMP patterns the magnetic junctions (interfaces between “up” and “down” magnetized micromagnets) reveal the highest magnetic field gradient.

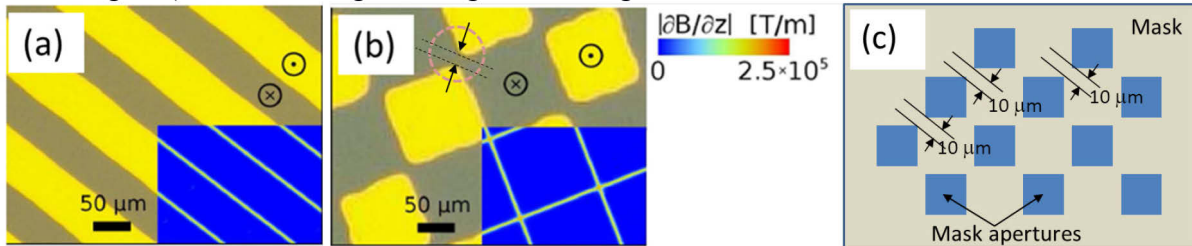


Figure 2.30. U-MOIF images of (a) stripe and (b) chessboard oop patterns in NdFeB (the insets represent the modulus of the magnetic field gradient $\partial B/\partial z$ [24]); (c) schematics of the mask used for chessboard patterning. Red dashed circle represents the area where the gap between RZs due to the TMP mask structure is observed.

These TMP samples have been employed for trapping commercial superparamagnetic fluorescent (sub)microparticles (Chemicell GmbH and MicroParticles GmbH) with diameters ranging from 200 nm up to 4.9 μm . These beads are polystyrene microspheres with embedded nano-sized iron oxide inclusions. Small volume droplets of an aqueous solution containing superparamagnetic particles were poured onto a TMP micromagnet array. Conventional and fluorescence optical microscopy reveal precise positioning of magnetic particles on the interface between oop magnetized magnetic structures, i.e. regions of highest field gradient (Figure 2.31).

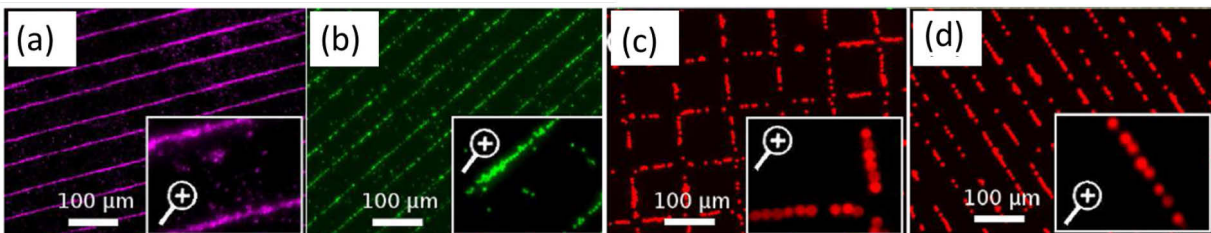


Figure 2.31. Fluorescence images of the superparamagnetic particles trapped by micromagnets [(a): 200 nm above oop magnetized NdFeB; (b): 1.4 μm above oop magnetized NdFeB; (c), (d): 4.9 μm above oop magnetized NdFeB]. The insets present a zoom on the particles positioned above each magnetic configuration [24].

For both, stripes and chess-board TMP patterns magnetic particles are mainly trapped above the magnetic junctions. However, it was noticed that for small particles (200 nm; 1.4 μm) some of them were trapped out of the magnetic junctions (Figure 2.31 a,b) mainly in the RZs. As in the case of previously described experiments it can be explained by inhomogeneity in the magnetic film leading to the local magnetic field gradient variations. This is also proved by the results of much more precise alignment of bigger particles (4.9 μm diameter) (Figure 2.31 c,d): local magnetic roughness in the RZ seems not strong enough to trap them. One can

notice the effect of the gap between RZs vertices for chessboard pattern: the particles are trapped above the magnetic junctions reproducing the square structure, but not in between the square vertices.

Thanks to the variability of TMP patterns, single particle positioning can be achieved when the pattern lateral dimensions are comparable with microparticle diameter: only one bead can be captured by each magnetic feature (above two neighbouring magnetic junctions), and a periodic particle array can be formed. In Figure 2.32, the magnetic pattern consisting of ($7 \times 7 \mu\text{m}^2$) features, separated by a step of $5 \mu\text{m}$ (Figure 2.32a), and an array of superparamagnetic microspheres of $10.3 \mu\text{m}$ diameter trapped by this pattern (Figure 2.32b), are presented. On the MOIF image edges of the pattern appear not squared, but rounded due to the limited spatial resolution of the imaging technique, as well as the MOIF-magnetic film distance.

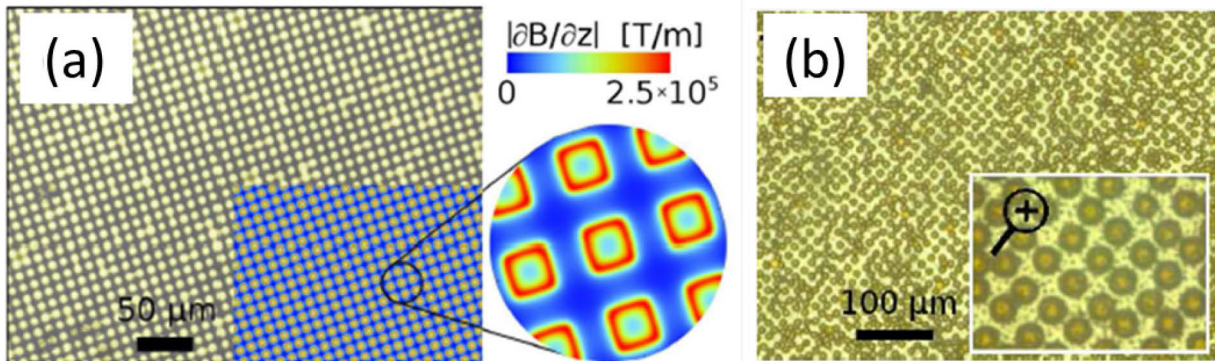


Figure 2.32. (a) U-MOIF image of NdFeB film patterned oop with a mask that consists of square array ($7 \times 7 \mu\text{m}^2$) motifs. The insets represent the modulus of the magnetic field gradient $\partial B/\partial z$. (b) $10.3 \mu\text{m}$ particles individually positioned above this pattern. The insets present a zoom on the particles positioned above each magnetic configuration [24].

These preliminary results demonstrate the possibility of precise positioning of superparamagnetic and hard magnetic microparticles by variation of the particle size and the micromagnet size and orientation. The next step is the trapping experiment on magnetically-labelled biological objects, such as bacteria, cells and proteins.

One of the first experiments on biological applications of TMP magnets was performed in order to position human embryonic kidney cells (HEK293, $\varnothing \sim 10 \mu\text{m}$) magnetically functionalized with 100 nm superparamagnetic particles (Figure 2.33a) by endocytosis [24] and to trap liposomes containing superparamagnetic nanoparticles (Figure 2.33b) [25]. The samples with $50 \mu\text{m}$ chess-board pattern (like in Figure 2.30b) were employed for trapping of biological objects. As in experiments with superparamagnetic microparticles, magnetically-labelled cells were mainly aligned along the magnetic junctions, but not between the square vertices due to the mask configuration. The formation of cell clusters can be explained by biological cellular adhesion. The use of micromagnets for single bacteria trapping was studied as well [26].

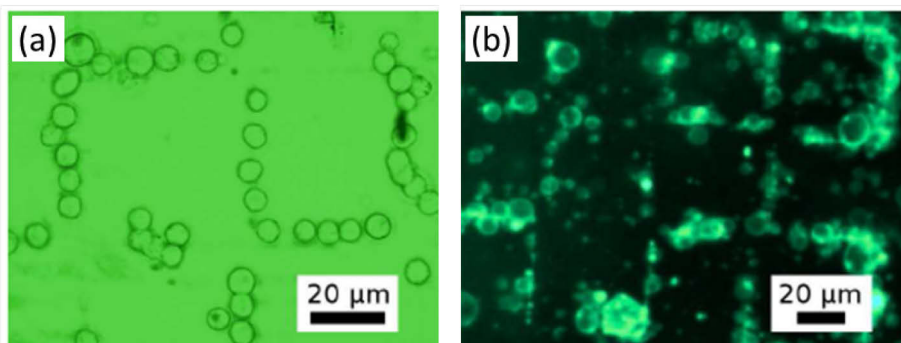


Figure 2.33. (a) HEK293 cells and (b) liposomes trapped on chessboard-like magnetic patterns ($50 \times 50 \mu\text{m}^2$ squares) [24,25].

More detailed study of the endocytosis uptake of 100 nm magnetic nanoparticles by HEK293 cells was performed by Osman et al. [27]. They investigated the influence of the nanoparticle concentration in the extracellular medium and the incubation time by observing cellular distribution above TMP magnets. This work is an important step to the definition of the threshold amount of particles required for magnetic trapping, thus reducing issues related to particle toxicity. For biomedicine and microbiology this study is of prime significance.

Similar tests have been carried out with μ MI structures to demonstrate their potential for trapping of cells functionalised with superparamagnetic beads [3]. In figure 2.34 mouse embryonic fibroblast cells line NIH/3T3 functionalised with red fluorescent polystyrene beads (diameter of 2.8 μm) containing superparamagnetic iron oxide inclusions (MicroParticles GmbH) were used. It was shown that μ MI structures of $100 \times 100 \mu\text{m}^2$ made with 16 μm and 5 μm diameter NdFeB particles trap magnetically functionalised cells at the regions of maximal stray magnetic field.

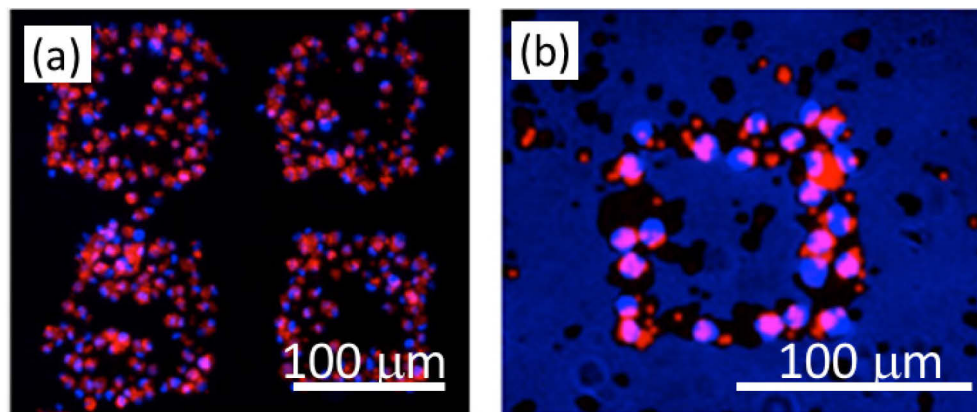


Figure 2.34. (a) fluorescence image of fibroblast cells (nuclei, Hoechst staining, blue) attached to polystyrene microspheres (red), trapped on the μ MI sample; (b) superposition of bright field and fluorescence images of fibroblast cells (nuclei, Hoechst staining, blue) attached to polystyrene microspheres (red), trapped on the μ MI sample [3].

Nevertheless, in all these experiments related to biological species, the exact force and force gradient acting on the object stays not well defined. Indeed, the inside of biological objects is soft, therefore the behaviour of the NPs is not known: depending on the magnetic force intensity they can move or remain homogeneously distributed inside the object. In case of NPs movement or aggregation inside the biological species, the magnetic interaction should be modified due to its variation with the spatial distribution of the magnetic volume.

II.3.2 Dynamic capture and separation

Similar experiments to capture magnetic particles were performed in dynamic configuration, where microfluidic channel was placed above a patterned magnetic film. For preliminary tests, a chessboard TMP micromagnet array was integrated into a microfluidic channel and magnetic microparticles of 1 μm diameter were injected. It was observed that flowing particles firstly pinned on the squares close to the inlet of the channel and then roll over the trapped particles to fill subsequent squares (Figure 2.35). To control the pinning process flow rate and PDMS layer thickness can be adjusted.

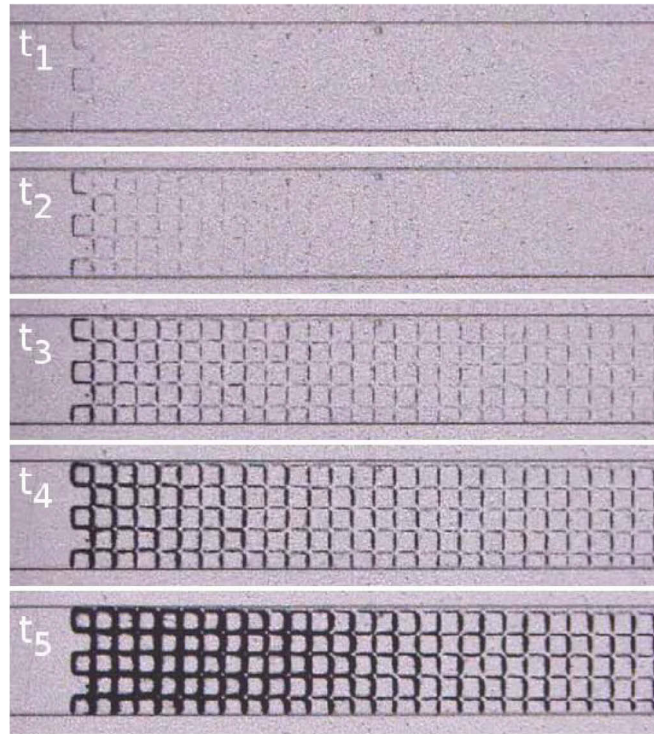


Figure 2.35. Evolution of the capture of 1 μm magnetic microparticles by a chessboard-like magnet array inside a microfluidic channel with flow rate of 15 $\mu\text{l}/\text{min}$ after 20s ($t_5 = 20$ s) [6].

Based on previous results microfluidic devices for magnetic separation by capturing were designed. The main principle of these devices is based on the difference in force acting on: (i) non-magnetic objects submitted to gravity (including buoyancy) and viscous forces (neglecting Brownian motion) and (ii) magnetic objects (e.g., magnetic particles), additionally submitted to a magnetic force (Figure 2.29 b).

After simulations to optimize the design of the separation device [28], its efficiency for magnetic separation was proved by experiments. Two initial solutions containing magnetic and non-magnetic particles of micron size were chosen. At the fixed flow rate (15 $\mu\text{l}/\text{min}$) the solutions passed through the microfluidic channel resulting solutions with trapped and non-trapped particles at the outlet. The high purity of both solutions (not less than 95%) confirms the efficiency of TMP micromagnet arrays for magnetic separation in microfluidic devices. Trapping of non-magnetic particles can be explained by a steric effect, when the trapped magnetic particles may block the movement of the non-magnetic particles along the bottom of the channel.

II.3.3 Continuous guiding

Microfluidic devices based on micromagnet arrays can be applied not only for magnetic particles trapping and separation, but also for dynamic guiding. Magnetic patterns can be used as rails for particles while a microfluidic drag force pushes the particles forward.

There are two main conditions which are necessary to make particles follow the rail: (i) to induce the movement, a component of the drag force should be aligned with the axis of the rail and (ii) the perpendicular drag force component should be weaker than magnetic force along the same axis.

The goal of such an experiment is to attract the particles towards the lines and then, by rolling or sliding, guide them towards the outlet of the channel or to the other part of the channel. The efficiency of particle guiding was confirmed by two types of magnetic rails: (i) parallel-to-flow magnetic rails and (ii) magnetic rails with an angle to the channel. Schematic of microfluidic channel system and experimental results are presented in Figure 2.36.

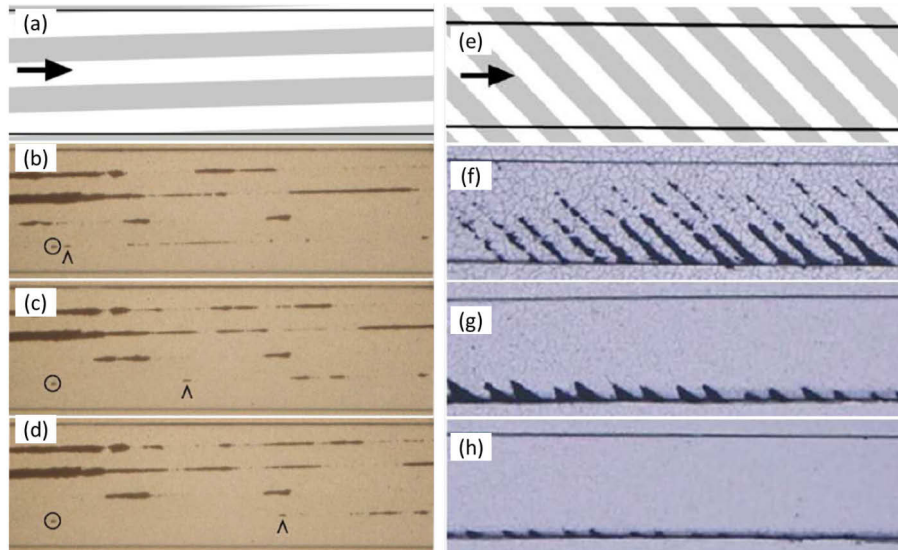


Figure 2.36. (a) Schematic representation of a system in which the guiding rails are parallel to the microfluidic channel and, thus, to the fluid flow. The experimental setup at different times is shown in (b), (c) and (d). Particle agglomerate moves along a magnetic rail, as indicated by the small arrow. The circle indicates agglomerate which is pinned to a zone of high magnetic field gradient. (e) Schematic of the system showing a microfluidic channel limited by the black lines with angled magnetic stripes below. The arrow indicates the direction of fluid flow. Magnetic particles deviated by the rails (f) close to the inlet, (g) in the middle of the channel and (h) close to the outlet. The particles are gradually deviated towards one edge of the channel and follow a thin streamline towards the outlet [6].

This kind of experiments can achieve continuous extraction of particles from a volume (3D) towards a line on a surface (1D). It means that cells in a reactive medium can be aligned in a single line for observations and further manipulations. Moreover using few magnetic rails all the magnetic particles can be concentrated at the one edge of a channel. Based on these experiments a device for continuous particle sorting have been designed: it has two inlets (1st inlet containing mixed solution of magnetic and non-magnetic particles, 2nd inlet with buffer solution) and two outlets, thus, a solution free of magnetic particles can be collected on the one side (1st outlet) and solution containing magnetic particles on the other side (2nd outlet). A schematic of this device and some experimental results are presented in Figure 2.37.

For this kind of devices, both TOPO and TMP micromagnets can be employed [6].

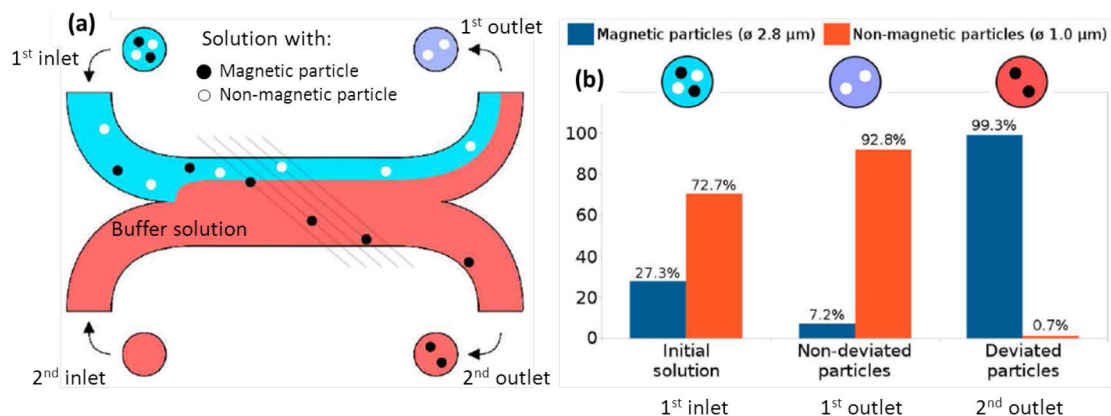


Figure 2.37. (a) Schematic of the system used for continuous magnetic sorting, composed of one channel with two inlets and two outlets. Non-magnetic (white) and magnetic (black) particles are pumped in, concentrated at first on one side of the channel. Magnetic particles are deviated by magnetic rails and collected on the 2nd outlet, while non-magnetic particles follow their initial streamlines and are collected on the 1st outlet. (b) Particle counting performed by flow cytometry in the initial solution (blue) containing both magnetic and non-magnetic particles, the solution containing the non-deviated particles (purple) collected on 1st outlet and the solution containing the deviated particles (red) collected on 2nd outlet [adapted from 6].

References

- 1 “Thermomagnetically patterned micromagnets”, F. Dumas-Bouchiat et al, Applied Physics Letters, Vol. 96, No. 10, 102511 (2010).
- 2 “Micro-patterning of NdFeB and SmCo magnet films for integration into micro-electro-mechanical-systems”, A. Walther et al, Journal of Magnetism and Magnetic Materials, Vol. 321, No. 6, pp. 590–594 (2009).
- 3 “Micro-magnetic imprinting of high field gradient magnetic flux sources” N.M. Dempsey et al, Appl. Phys. Lett. 104, 262401 (2014).
- 4 “Sputtered permanent Nd-Fe-B magnets”, B.A. Kapitanov et al., J. Magn. Magn. Mater. 127, 289 (1993).
- 5 “High performance hard magnetic NdFeB thick films for integration into micro-electro-mechanical systems”, N. M. Dempsey, A. Walther, F. May, and D. Givord, Applied Physics Letters 90, 092509 (2007).
- 6 “Structures magnétiques et microsystèmes pour applications biologiques”, L. Zanini, PhD thesis, Université de Grenoble, France (2013).
- 7 “Evolution of magnetic and microstructural properties of thick sputtered NdFeB films with processing temperature”, A. Walter et al, Journal of Magnetism and Magnetic Materials 316 pp.174–176 (2007).
- 8 “Structural, magnetic, and mechanical properties of thick SmCo films suitable for use in microelectromechanical systems”, A. Walther, D. Givord, N. M. Dempsey, K. Khlopkov and O. Gutfleisch, Journal of Applied Physics 103, 043911 (2008).
- 9 “The influence of buffer/capping-layer-mediated stress on the coercivity of NdFeB films”, Y. Zhang et al, Acta Materialia 60, 9, pp. 3783-3788 (2012).
- 10 “High-coercivity Nd–Fe–B thick films without heavy rare earth additions”, N.M. Dempsey, T.G. Woodcock, H. Sepehri-Amin, Y. Zhang, H. Kennedy, D. Givord, K. Hono, O. Gutfleisch, Acta Materialia 61, pp. 4920-4927 (2013).
- 11 “Coercivity enhancement of HDDR-processed Nd-Fe-B permanent magnet by rapid hot-press consolidation process”, N. Nozawa et al, J Magnet Magnet Mater 323(1), pp.115–121 (2010).
- 12 “Magnetic Micro-Actuators and Systems (MAGMAS)”, O.Cugat et al, IEEE Trans. Mag. 39, p. 3607-3612 (2003).
- 13 “Magnetic Nanostructures in Modern Technology”, O.Gutfleisch et al, Ghidini (Eds.), Springer, Berlin, NewYork, p. 167 (2007).
- 14 “Chemical Mechanical Planarization of Semiconductor Materials”, M. R. Oliver, Springer, New York (2004).
- 15 “Gradient based optimization of semi-numerical models with symbolic sensitivity: Application to a simple ferromagnetic MEMS switch device”, B. Delinchant et al, 10th International Workshop on Optimization and Inverse Problems in Electromagnetism (OIPE 2008), Germany (2008).
- 16 “Magnetic Nanostructures in Modern Technology”, B. Azzarboni et al. (eds.), R. Grechishkin et al, “Magnetic Imaging Films”, pp. 195–224 (2008).
- 17 “Progress in magnetic domain observation by advanced magneto-optical microscopy”, J. McCord, J. Phys. D: Appl. Phys. 48 (2015).
- 18 “Measuring the Force Gradient Acting on a Magnetic Microsphere above a Micro-magnet Array”, S. Ponomareva et al, Advanced Materials Research Vol. 872, pp 167-173 (2014).
- 19 “Magnetic characterization of micropatterned Nd–Fe–B hard magnetic films using scanning Hall probe microscopy”, M. Kustov, Journal of Applied Physics 108, 063914 (2010).
- 20 <http://dx.doi.org/10.1063/1.4886375>, supplementary material for N.M. Dempsey et al, “Micro-magnetic imprinting of high field gradient magnetic flux sources” Appl. Phys. Lett. 104, 262401 (2014).
- 21 “Une etude experimentale de la coercivite des aimants NdFeB”, Georgeta Ciuta, PhD thesis, Universite de Grenoble, France (2013).
- 22 “Some aspects of Magnetic Force Microscopy of Hard Magnetic Films”, G. Ciuta, F. Dumas-Bouchiat, N.M. Dempsey, O. Fruchart, IEEE Transactions on magnets, Vol. 52, No. 9 (2016).
- 23 “Analysis of Particle Transport in a Magnetophoretic Microsystem”, E. P. Furlani, J. Appl. Phys. 99, 024912 (2006).
- 24 “Micromagnet structures for magnetic positioning and alignment”, L. F. Zanini, O. Osman, M.

Frenea-Robin, N. Haddour, N. M. Dempsey et al. *J. Appl. Phys.* 111, 07B312 (2012).

25 “Trapping of magnetically-labeled liposomes on flat micro-patterned hard magnetic films”, J. Pivetal et al, *AIP Conference Proceedings*, Vol. 1311, pp. 192 (2010).

26 “Micro-magnet arrays for specific single bacterial cell positioning”, J. Pivetal et al., *Journal of Magnetism and Magnetic Materials* (2014).

27 “Monitoring the endocytosis of magnetic nanoparticles by cells using permanent micro-flux sources”, O. Osman et al, *Biomedical Microdevices*, Vol. 14, pp. 947–954 (2012).

28 “Autonomous micro-magnet based systems for highly efficient magnetic separation” L. Zanini et al, *Appl. Phys. Lett.* 99, 232504 (2011).

Chapter III: Microsphere Scanning Force Microscopy for quantitative magnetic interaction studies

<u>III. Microsphere Scanning Force Microscopy for quantitative magnetic interaction studies</u>	76
<u>III.1 Scanning Force Microscopy</u>	76
<u>III.1.1 Atomic Force Microscopy probe</u>	78
<u>III.1.2 Tip-sample interaction</u>	80
<u>III.1.3 Force spectroscopy mode</u>	82
<u>III.1.4 Imaging in Static Mode (DC)</u>	85
<u>III.1.5 Imaging in Dynamic Mode (AC)</u>	86
<u>III.2 Magnetic Force Microscopy (MFM)</u>	89
<u>III.2.1 General Operating Mode</u>	89
<u>III.2.2 Our Working conditions</u>	89
<u>III.2.3 Magnetic Force or Force Gradient mapping</u>	90
<u>III.2.4 MFM on micromagnet array using standard MFM probes</u>	91
<u>III.3 Microsphere Scanning Force Microscopy</u>	94
<u>III.3.1 Microsphere probe fabrication using AFM manipulation</u>	95
<u>III.3.2 Force gradient mapping between micromagnet array and a single microsphere</u> ..	96
<u>III.3.3 Toward quantitative mapping: Microsphere probe fabrication by Focused Ion Beam</u>	97
<u>References</u>	101

III. Microsphere Scanning Force Microscopy for quantitative magnetic interaction studies

This chapter describes the main principles of Scanning Force Microscopy (SFM) and its derivative called Microsphere Scanning Force Microscopy (MSFM). After the section dedicated to AFM and MFM, we present our approach for experimental study of magnetic interaction exerted by TMP sample on a single magnetic (superparamagnetic or hard magnetic) microsphere. It is a reliable and reproducible method based on MSFM technique conducted with magnetic microsphere probes. For this purpose, we fabricated smart MFM probes by attaching a single magnetic microsphere to the tip apex of a commercial non-magnetic probe.

The aim of this Chapter is to reveal the possibility of qualitative and quantitative force measurements through the experiments conducted with (i) standard and (ii) smart custom-made magnetic microsphere probes.

III.1 Scanning Force Microscopy

Scanning Probe Microscopy (SPM) is a technology for imaging surfaces and measuring their physical properties such as morphology, conductivity, static charge distribution, localized friction, magnetic fields, and elastic moduli. The main principle of SPM is based on a physical sharp probe that scans the sample surface backward and forward. Computer gathers data of probe-sample interaction and generates an image of the surface. SPM is complementary of surface imaging techniques such as Magneto Optical Indicator Film (MOIF), Optical and Scanning Electron Microscopies, by providing unprecedented 3D resolution in various working environments (Table 3.1). The most common scanning probe microscopes are Scanning Tunnelling Microscope (STM), Scanning/Atomic Force Microscope (SFM or AFM) (Figure 3.1) and Near-field Scanning Optical Microscope (NSOM) [1]. Nowadays, the most widespread technique in fundamental and industrial research is the Scanning Force Microscopy thanks to its versatility about sample type (conductive or not), working environments (ambient conditions, in liquid or vacuum) and commercial availability of the AFM probes with various specificities. SFM is composed of various related techniques based on the same concept (surface force or interaction measurement) but using probes with specific coating or functionalization on tip surface providing additional physical (electric, magnetic, mechanic), chemical or biological information on sample surface properties [2,3,4,5].

In this work, two main SFM techniques will be discussed in details: Atomic Force Microscopy (AFM) and Magnetic Force Microscopy (MFM).

	Probe	Mechanism	Sample preparation	Working environment	Resolution
Optical Microscopy	Light	Waves properties: <ul style="list-style-type: none"> • Diffraction • Reflection • Scattering 	<ul style="list-style-type: none"> • Reflection mode: No specific preparation • Transmission mode: the sample must be transparent 	<ul style="list-style-type: none"> • Ambient conditions • Liquid • Vacuum 	<ul style="list-style-type: none"> • For X-Y lateral imaging: Up to 100 nm [6] • Limitation due to Rayleigh criterion [7]
Magneto-Optic Imaging Film	Light	Waves properties: <ul style="list-style-type: none"> • Diffraction • Reflection • Scattering Magnetic properties: <ul style="list-style-type: none"> • Zeeman exchange splitting • Spin-orbit interaction. 	Depends on the sample: <ul style="list-style-type: none"> • In general no particular sample preparation is required • To improve the resolution, the distance between MOIF and sample should be minimized, thus grinding or polishing might be applied 	<ul style="list-style-type: none"> • Ambient conditions • Vacuum 	<ul style="list-style-type: none"> • X-Y lateral imaging: Up to 1 μm [8] • Lateral resolution: limitation due to MOIF-sample distance and thickness of the active magneto optic layer [9]; • Vertical resolution: limitation due to MOIF thickness [9] • Magnetic field intensity (P-MOIF, calibration is required)
Electron Microscopy	Electron	Waves properties: <ul style="list-style-type: none"> • Diffraction • Reflection • Scattering 	Depends on the sample: <ul style="list-style-type: none"> • Grinding/Polishing; • Chemical or thermal etching • Electrical grounding • Coating with electrically conducting material for insulated samples • Increase of the sample bulk conductivity by impregnation with osmium (usually for biological samples). 	<ul style="list-style-type: none"> • High vacuum chamber • In control atmosphere (Environment SEM). 	<ul style="list-style-type: none"> • X-Y lateral imaging: $\text{\AA} - \mu\text{m}$ • Limitation due to lens aberrations, the brightness of the electron source, the interaction volume [10].
Scanning Probe Microscopy	Tip	Tip/sample interaction: <ul style="list-style-type: none"> • Mechanic • Electrostatic • Magnetic • Chemical • Capillary 	Depends on the sample: <ul style="list-style-type: none"> • Grinding/ Polishing • Chemical or thermal etching. • Electrical grounding of the probe and sample • Sample fixation for measurements in vacuum 	<ul style="list-style-type: none"> • Ambient conditions • In liquid • High vacuum for high imaging resolution 	<ul style="list-style-type: none"> • Z-height measurement: $\text{\AA} - \text{nm}$ • Lateral resolution: limitation due to the tip dimensions: tip apex curvature radius and sidewall angles • Vertical resolution: limitation due to SPM instrument noise (mechanical vibrations induced by Brownian motion)

Table 3.1. Comparison between traditional Optical and Electron microscopies, MOIF and SPM.

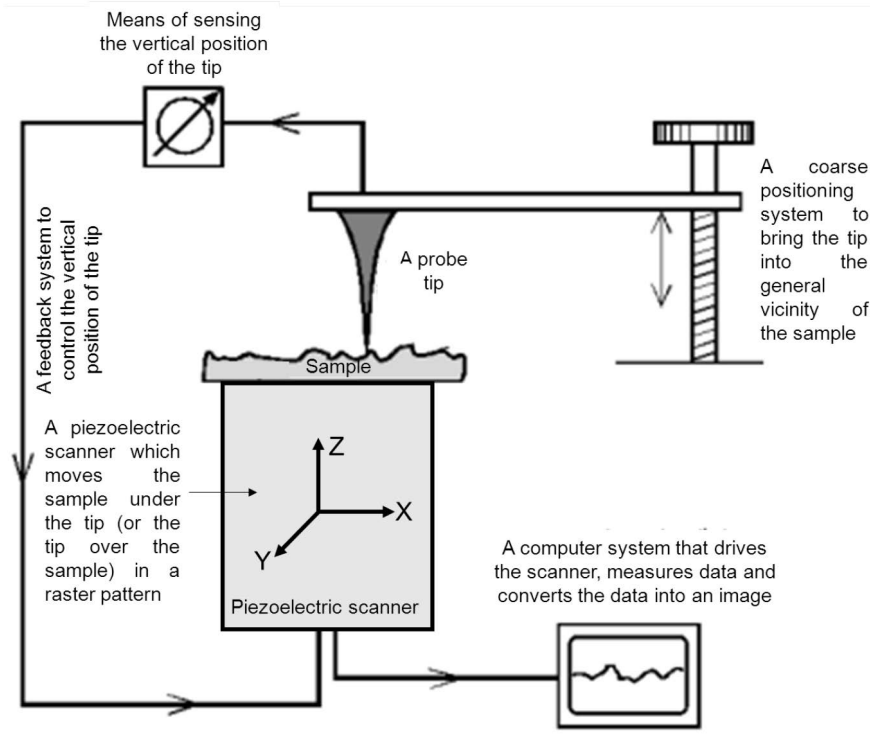


Figure 3.1. Schematic overview of SFM technique (readapted from [1]).

III.1.1 Atomic Force Microscopy probe

The first AFM was introduced by Binnig, Quate and Gerber in 1986 [11]. The main principle of AFM is based on the interaction between probe and surface. A standard AFM probe is an elastic cantilever with a sharp tip on the free end meanwhile the second end is clamped to the silicon holder or chip (Figure 3.2). The main technique to produce AFM probes is a combination of photolithography and etching of silicon, SiO_2 or Si_3N_4 layers deposited onto a silicon wafer [12,13].

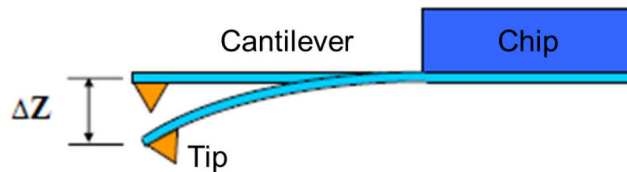


Figure 3.2. Schematic of an AFM probe [14].

Depends on the application, different types of AFM probes are available. The probe characteristics determine the interaction force between tip and sample, the possible lateral resolution and sample properties that can be measured. Usually, the tip has pyramidal, tetrahedral or cone shape those the apex has a radius of curvature in the range between 1-50 nm. The value of the radius of curvature defines the lateral resolution that can be achieved with the probe i.e. the minimum distance between two objects lying on the surface need to be separated. However, in some cases, AFM measurements can be carried out with custom-made probe, where nanowires or micro/nano-objects have been fixed at the tip apex using for example Focused Ion Beam [15].

The mechanical characteristics of an AFM probe are its resonant frequencies ω_i and its associated spring constants k_i that are directly linked with the cantilever material and dimensions (length L ; width W ; and thickness t) [16]. In classical AFM/MFM modes, only the fundamental resonance frequency ω_0 , static (k_s) and fundamental (k_0) spring constants are required. The shape of the cantilever by itself can be varied, but most of them exhibit rectangular or triangular shape. Normally resonant frequency is in the range between 10 and

1000 kHz (can go up to 5 MHz, for example USC-F5-k30 NanoWorld Arrow™ UltraHighFrequency probes).

Resonant frequency can be found by following formula [17]:

$$\omega_0 = \sqrt{\frac{k_0}{m^*}} \quad (3.1)$$

where k_0 is the fundamental cantilever spring constant and m^* is the cantilever effective mass¹. Usually high resonant frequency is required to decrease an impact of external (usually low frequency) vibrations and noise on the AFM measurements. The static and fundamental spring constants k_s and k_0 of the cantilever depend on its shape, dimensions and material properties [18]. For rectangular cantilever, it can be found by formula [19]:

$$k_0 = k_s = E \frac{Wt^3}{4L^3} \quad (3.2)$$

and for triangular cantilever after its approximation by two parallel beams can be found by formula [19]:

$$k_0 = k_s = E \frac{Wt^3}{2L^3} \quad (3.3)$$

Low spring constant provides high sensitivity (but the force resolution remains the same due to the Brownian motion) thanks to high cantilever deflection (ΔZ , Figure 3.2) even when small force is applied. For soft cantilevers (with low spring constant) the cantilever width W and thickness-to-length ratio t/L should be small.

The appropriate material, shape and dimensions of an SFM cantilever should be chosen according to the application; it depends on the sample type, scanning mode, the information that is required from the measurements and etc. In our work, to perform magnetic measurements, we choose AFM probe with magnetic coating or with attached magnetic object to the tip apex.

The mostly used set-up to register cantilever bending was invented by Amer and Meyer [20]: A laser beam is focused at the free end of the cantilever (just above the tip position) and reflected for measurements of the tip displacement. The reflected laser beam is detected with a position-sensitive detector (Figure 3.3 a). Nowadays special four-section detectors measures (i) longitudinal (cantilever bending due to z-component of attractive or repulsive forces (F_z)) and (ii) torsion cantilever bending due to lateral component (F_L) of probe-sample interaction (Figure 3.3 b-e).

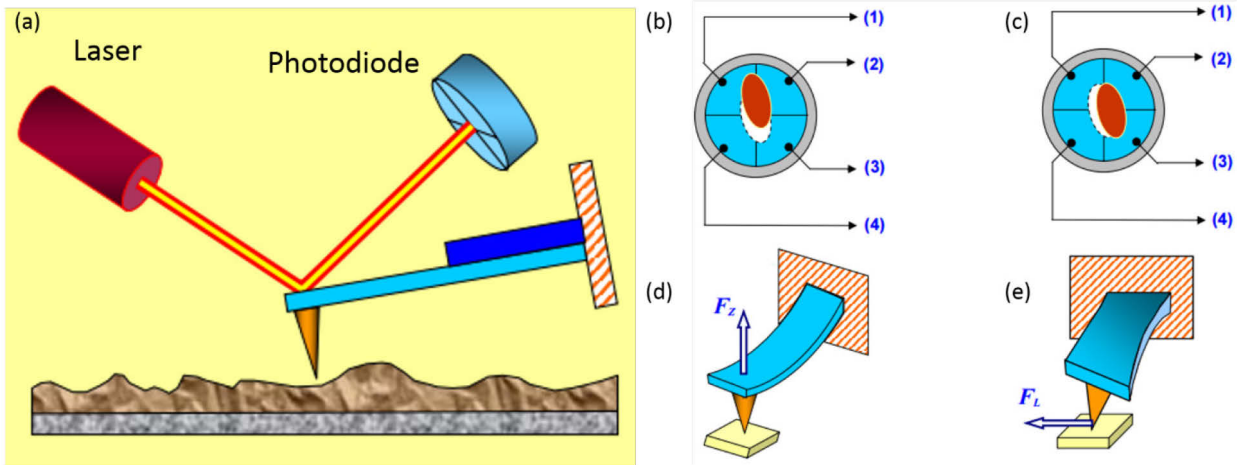


Figure 3.3. (a) Schematic of an optical registration of the AFM cantilever bending. Laser spot displacement on four parts photodiode due to (a) vertical and (b) lateral forces (F_z and F_L) acting on the cantilever and corresponding (d, e) cantilever bending [14].

¹ The cantilever effective mass for the first resonant mode can be written as $m^* = \rho L t W \cdot \frac{3}{(1.875)^4} \approx 0.24 m$, where ρ is the cantilever material density [17].

When the cantilever deflection is equal to zero, the laser beam is positioned at the centre of the photodiode. The cantilever bending leads to a displacement of the laser spot. To track and quantify the cantilever deflection, the light signal received by four parts of photodiode is converted into voltage by current-voltage amplification. The signal of the parts (1+2)-(3+4) is proportional to the cantilever bending due to a normal force and reflects vertical deflection of a cantilever (Figure 3.3 b,d); signal of the parts (1+4)-(2+3) is proportional to the cantilever twist due to lateral forces (Figure 3.3 c,e).

III.1.2 Tip-sample interaction

As it was mentioned above, the main principle of AFM is based on the interaction between probe and surface. During the scanning process, several interactions can take place according to the working environment and the tip coating: capillary, Van der Waals, chemical, electrostatic or/and magnetic (Figure 3.4) interactions; they induce the cantilever deflection. By tracking the cantilever movements, the probe-sample interaction can be measured and controlled.

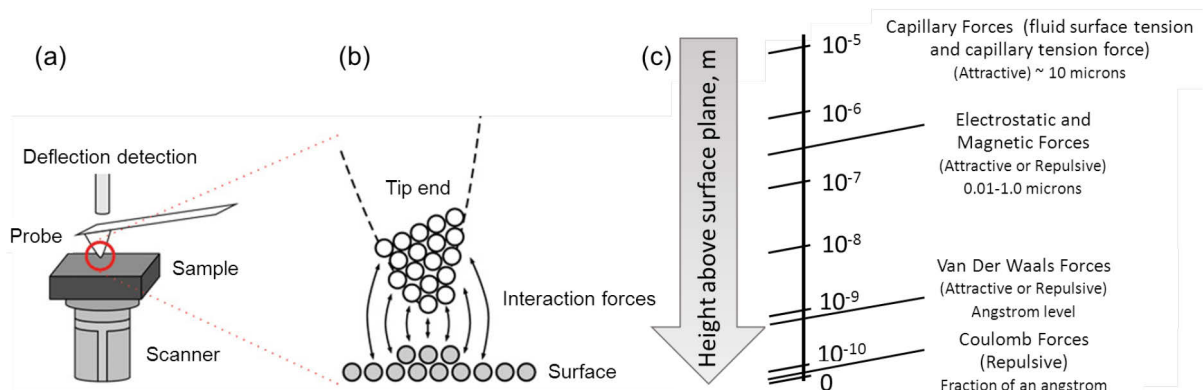


Figure 3.4. (a) Sketch of a macroscopically flat surface probed by a sharp tip. (b) Atomic structure of tip and sample at small separation distance. (c) Forces acting on the cantilever at the micro/nano-scale in air (adapted from [21]).

The following expressions define forces arising between probe modelled as a sphere with radius R (diameter D) and surface modelled as a plane at the distance z between tip and sample [22]:

- *Capillary force* (fluid surface tension force and capillary tension force) after some approximations:

$$F_{cap} = 2\pi R\gamma(\cos\theta_1 + \cos\theta_2)/(1 + D/z), \quad (3.5)$$

where θ_1 is the contact angle between the water meniscus and the surface and θ_2 is the contact angle between the water meniscus and the tip; γ is the liquid's surface tension.

- *Electrostatic force*:

$$F_{el} = \frac{1}{2} \frac{\partial C}{\partial z} U^2, \quad (3.6)$$

where C is the capacitance between the probe and sample, U is the voltage between the tip and the sample.

- *Magnetic force*:

$$\vec{F}_{mag}(r) = \mu_0(\vec{m} \cdot \nabla)\vec{H}(r), \quad (3.7)$$

where μ_0 is the magnetic permeability of free space, \vec{m} is the magnetic moment of the tip approximated as a point dipole, \vec{H} is the magnetic stray field of the sample, r is the space position.

- *Van Der Waals Forces:*

$$F_{vdw} = \frac{H_a R}{6z^2}, \quad (3.8)$$

where H_a is the Hamaker constant.

- *Coulomb forces:*

$$F_{rep} = \frac{A}{z^m}, m > 3, \quad (3.9)$$

where A is the Hamaker constant.

According to the separation distance between probe and sample, different forces dominate. The effect of the tip-sample distance on the force between them (force response curve) is presented in Figure 3.5. For the sake of simplicity the force representing tip-sample interaction $F_{t/s}(z)$ is considered as an interatomic Lennard-Jones force [23,24]:

$$F_{t/s}(z) = -\frac{A}{z^7} + \frac{B}{z^{13}}, \quad (3.10)$$

where z is the actual tip-sample distance, A and B are the coefficients that depend on the type of forces acting between the tip and sample. With equation (3.10) only a simple qualitative description of the tip-sample interaction can be provided. In practice, the attractive force between surfaces actually follows a force law $-z^{-n}$ with $n \leq 3$ (and not $n = 7$) and the repulsive part of the force is much more complex than the one modelled by the Lennard-Jones force. Main forces affecting the probe close to the surface are Van der Waals (red curve) and Coulomb forces (blue curve). The presence of Van der Waals forces is explained by existence of temporary fluctuating dipoles. These are attractive forces contributing the AFM cantilever movements at the separating distance of up to few nanometres. The Coulomb interaction is a strong short-range force caused by electrostatic repulsion of electron clouds of the tip and sample; it increases with decay of the tip-sample distance. When the probe is far from the surface, the resulting force curve (green) as well as curves presenting repulsive and attractive forces is close to zero. As the probe approaches to the surface Van der Waals forces lead to the attraction of the probe towards the surface. This effect increases, as the tip gets closer to the sample (0). However, with the decrease of interatomic separation Coulomb forces arise leading to attractive force weakness (1). When the separating distance is comparable to the length of a chemical bond (few angstroms) the resulting force becomes equal to zero (2) because the repulsive and attractive forces counterbalance. Then Coulomb forces become dominant (3) and the tip and sample atoms are in mechanical “contact”, but remain in the elastic regime (the situation is fully reversible).

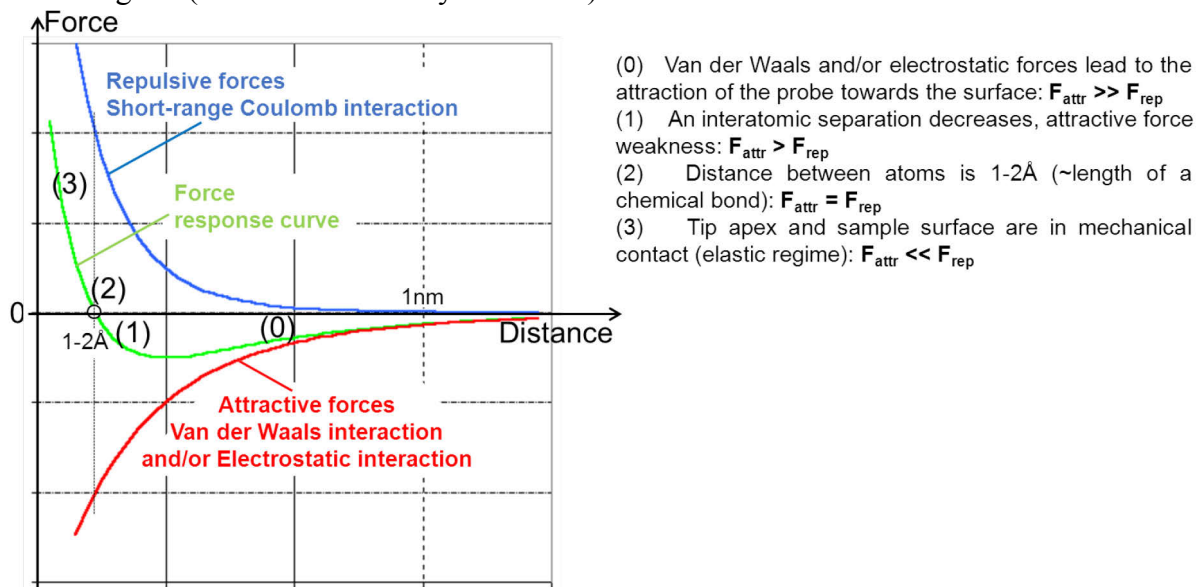


Figure 3.5. Sketch to illustrate the effect of the tip(sphere)-sample (plane) distance on the force between them: short-range repulsive Coulomb interaction (blue), long-range attractive Van der Waals and/or electrostatic interaction (red) and resulting force curve (green).

Long-range interactions as magnetic and electrostatic forces have an influence on the force response curve as well. Detailed calculations of the forces acting between AFM probe with attached magnetic (superparamagnetic) microsphere and micromagnet array are presented in Annex III.1.

III.1.3 Force spectroscopy mode

In spectroscopy mode, direct force measurements between the tip and the sample as a function of distance between them (separating distance) can be carried out. In this mode, the feedback loop is off and the spectroscopy results represent cantilever deflection measured through the photodiode signal versus the extension of the piezoelectric scanner (cantilever vertical displacement). During the force spectroscopy, two forces are acting on the tip: the one between the tip apex and the sample surface $F_{t/s}$ and the one between the cantilever and the tip $F_{c/t}$ (Figure 3.6).

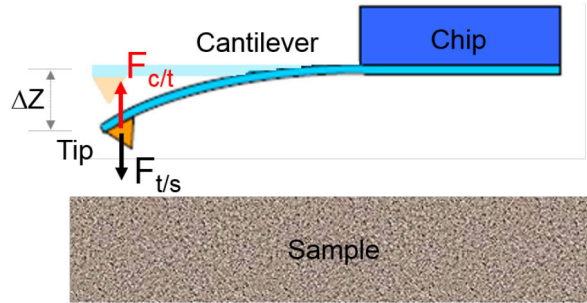


Figure 3.6. Sketch illustrating the two forces acting on the tip: force $F_{t/s}$ between the tip apex and the sample surface and force $F_{c/t}$ between the cantilever and the tip.

Considering that the tip is always in equilibrium, we can write that the sum of the forces acting on the tip is equal to zero:

$$\sum \vec{F}_t = \vec{F}_{t/s} + \vec{F}_{c/t} = \vec{0}, \quad (3.11)$$

where $F_{c/t} = k_s \Delta z$, k_s is the static spring constant of the cantilever and Δz is the cantilever vertical deflection.

This equation holds for all the tip apex-sample distances, which means that by recording the cantilever bending (i.e. $F_{c/t}$), we have an access to the tip apex-sample force $F_{t/s}$.

In order to monitor this cantilever force, the whole system has to be calibrated, especially the photodiode signal. In practice to obtain a force-distance curve in spectroscopy mode, cantilever is approached and pressed towards the surface and subsequently retracted while its bending is recorded. Figure 3.7 displays the generic form of a typical force curve recorded on a flat hard surface. Usually the assumption that there is no deformation of the tip or the surface (hard surface) is done. This allows finding the response of the system to the probe displacement and by the way to calibrate the photodiode to convert the photodiode signal from Volt to nanometres (linear part of curve in Figure 3.7). A typical force-distance curve (Figure 3.7) consists of two curves: approach (blue) and retract (red). Approach curve represents cantilever bending while approaching towards the sample. Firstly, when the separating distance is large the vertical deflection of the cantilever due to its interaction with the sample is equal to nearly zero (1, a); by reducing the tip-surface gap, the force is increasing slowly leading to a bending of the cantilever (b) until the force gradient intensity equals the value of the spring constant of the cantilever. At this point very close to the surface, the cantilever jumps into contact with the surface due to electrostatic and/or adhesion forces (2, c). Further approach towards the surface firstly leads to a decrease of the cantilever bending due to the step-by-step balance between attractive and repulsive interactions (Figure 3.4 c) acting on the tip apex until their perfect equilibrium (no more cantilever bending) at point (d). Beyond this point the repulsive forces become predominant leading to a positive bending (up) of the cantilever proportionally to the change of the piezoelectric scanner height

(3, e). When the deflection set point is reached (4) the cantilever is withdrawn. The cantilever upwards bending decreases (5) reaching zero at a certain moment (d) then changes to the bending towards the surface due to attraction forces, mainly adhesion. Usually this linear part of the retract curve is used for photodiode calibration. The cantilever (6, f) loses the contact with surface and it jumps to the position when the force gradient becomes smaller than the spring constant of the cantilever. This point corresponds to the point of higher negative force on red curve of Figure 3.5. Then the cantilever bending (b) decreases significantly and returns step-by-step to zero deflection (7, a).

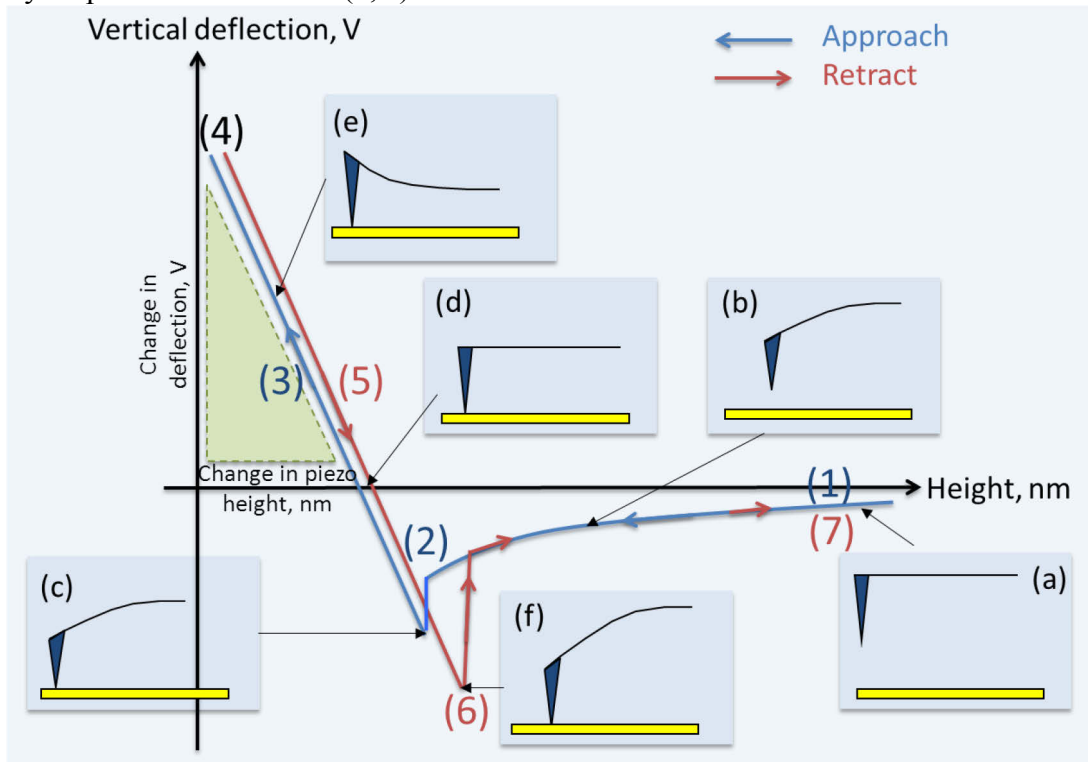


Figure 3.7. Classical approach-retract curves (approach curve is blue, retract curve is red) showing probe-sample interaction and corresponding cantilever bending recorded in air or in vacuum on a 'hard' surface. The gradient chosen for sensitivity measurements (green triangle) to convert photodiode signal from V (change in deflection) to nm (change in piezo height) is presented.

Figure 3.7 presents response of the system to the probe displacement, specifically the force between the tip and the cantilever F_{ct} , while the Figure 3.5 illustrates the forces acting between the tip and the sample F_{ts} . The combination of the forces from Figure 3.5, F_{ts} with the equation (3.10) leads to the curves presented in Figure 3.7, F_{ct} .

Usually force spectroscopy mode is applied to plot approach-retract curves for photodiode calibration, to measure sample properties and different tip-sample interactions [25].

With the correct photodiode calibration thanks to spectroscopy mode, ΔZ can be found precisely. The definition of cantilever spring constant is more complicated. In theory, it can be calculated if cantilever dimensions are well known: for rectangular cantilever formula (3.2) and for triangular cantilever formula (3.3) can be used.

However, these calculations can give an error of up to tens of per cent due to the thickness of the cantilever that is not well known [26]. Even the probes from the same set can have dimensions different from the datasheet indications due to the fabrication technique: deposition and etching. An additional layer to increase the reflectivity (for better detection) or to provide magnetic properties and so on should be taken into account as well. As the thickness of the cantilever cannot be measured easily and quickly with a standard optical microscope (a SEM is required but it is time consuming), the use of formula based on cantilever dimensions can be mainly applied for rough estimation of the spring constant. For

more precise force measurements, more complicated techniques are required. Different approaches can be implemented for determination of the cantilever spring constant: (i) nanoindenter performing load-displacement curve measurements at different positions of the cantilever [27]; (ii) special balance where the cantilever is pushed against a rigid surface and its deflection is monitored optically [28]; (iii) the reference cantilever with known stiffness [18]; (iv) micromanipulations using added mass model and based on the change of resonant frequency [29] and so on. In our experiments cantilever spring constant was calculated by thermal tune method based on cantilever mechanical response to the thermal noise [30,31] that is the standard method implemented in most of commercial AFM instruments. According to the equipartition theorem linking the spring constant of the cantilever with its Brownian motion we have [32]:

$$\frac{1}{2}k_0\langle z^2 \rangle = \frac{1}{2}k_B T, \quad (3.12)$$

where k_0 is the spring constant of the cantilever for the fundamental resonance (for rectangular cantilever, k_s is equal to k_0), $\langle z^2 \rangle$ is the mean-square displacement of the cantilever's thermal motion, k_B is the Boltzmann constant, T is the absolute temperature (in Kelvin).

Here, the left part of equation corresponds to the average kinetic energy of the cantilever vertical motion, and the right part to the thermal energy. The thermal noise spectrum represents cantilever vibrations as a function of frequency, and the highest amplitude is observed around cantilever resonant frequency. The fitting of thermal resonance curve by Lorentzian function provides the cantilever spring constant value [32]. The average error of the spring constant calibration by thermal tune method was estimated in [32] to be around 5%. It is a fast and simple method for cantilever spring constant measurements. Its only disadvantage is that the cantilever should be pressed against hard surface for the photodiode calibration, which can lead to the tip damage. The example of the spring constant measurements by thermal tune method with Asylum microscope is presented in Figure 3.8: blue curve corresponds to the amplitude of cantilever movements due to thermal noise in a function of frequency; purple curve represents the fitting of resonance curve. The area below the peak (calculated by integration of purple curve) provides mean square cantilever deflection $\langle z^2 \rangle$. Using the equation (3.12) cantilever spring constant can be found: $k_0 = k_B T / \langle z^2 \rangle$.

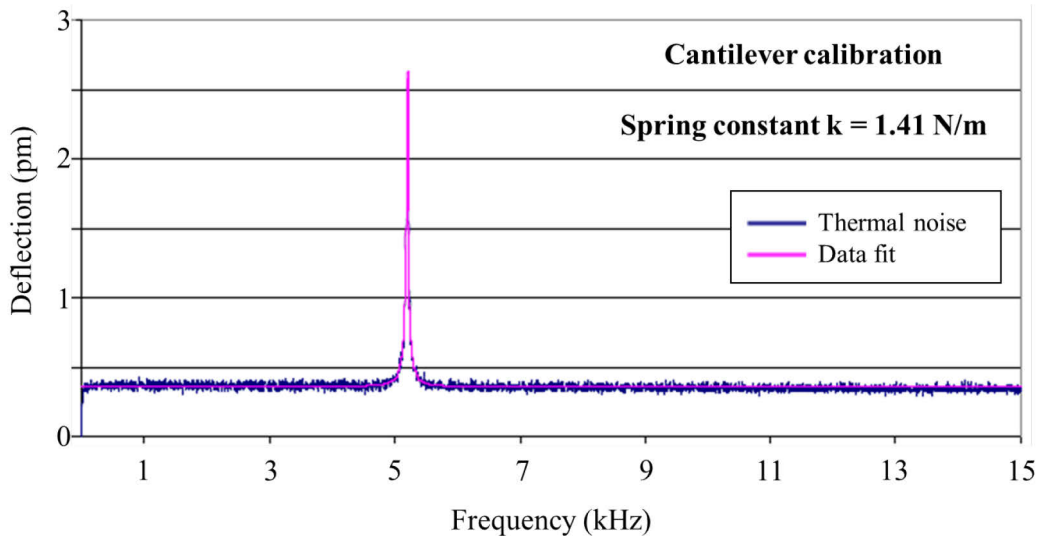


Figure 3.8. Measurements of the cantilever fundamental spring constant k_0 by thermal tune method. Resonance curve due to the thermal/Brownian motion is measured (the amplitude of the cantilever movements in a function of frequency (blue)). Fitting of the resonance curve (purple). The area below the peak provides the mean square cantilever deflection.

III.1.4 Imaging in Static Mode (DC)

All the techniques used in AFM to study sample surface and its properties can be divided in two main groups: static (DC) and dynamic (AC) modes.

In static mode, the monitoring signal is the cantilever deflection when the probe scans the sample in close vicinity of the surface thanks to short-range interaction (linear part of the curve in Figure 3.7). In static mode, the AFM probe can be modelled as a spring-mass system to which only static deformations are applied. The interaction force can be found according to the Hook's law:

$$F = k_s \times \Delta Z, \quad (3.13)$$

where k_s is the static spring constant of the cantilever and ΔZ is the vertical cantilever deflection.

Usually for static mode, soft cantilevers with the spring constants from 0.001 up to few N/m are employed to avoid tip or surface damage caused by high mechanical local pressure.

To perform surface topography image, two main approaches are available in static mode (called also contact mode): (i) constant force or (ii) constant altitude.

In constant force mode (i), the user chooses a reference force called set point and the feedback loop drives the piezoelectric scanner in z direction to keep the tip-sample force constant. By recording for each (X,Y) pixel of the scan, the z displacement of the piezoelectric scanner, a topographic image of the sample surface is displayed (Figure 3.9a). Measurements performed in constant force mode provide high resolution and a possibility to measure sample topography. Contact mode is the fundamental basis of additional modes as Scanning Capacitance Mode (SCM), Scanning Spreading Resistance Mode (SSRM), Lateral Force Microscopy (LFM) and Force Modulation Microscopy (FMF). The main disadvantage of this mode is a probability to damage the sample (especially soft samples like polymers or biological species) due to the permanent contact with surface.

For the very flat samples (usually with an average roughness of less than 1 nm) the measurements are conducted at the constant altitude (Figure 3.9b). The cantilever scans the surface at a fixed distance Z_{avg} and its bending variation ΔZ is recorded at each pixel. Obtained AFM image provides the spatial variation of the tip-sample interaction. If the sample surface is homogenous (same material), the variations of the cantilever bending translate the roughness of the sample. This imaging mode is fast because no feedback loop is needed, but is reserved to flat surface sample and often for small size scan in order to reach the atomic or molecular resolution [33].

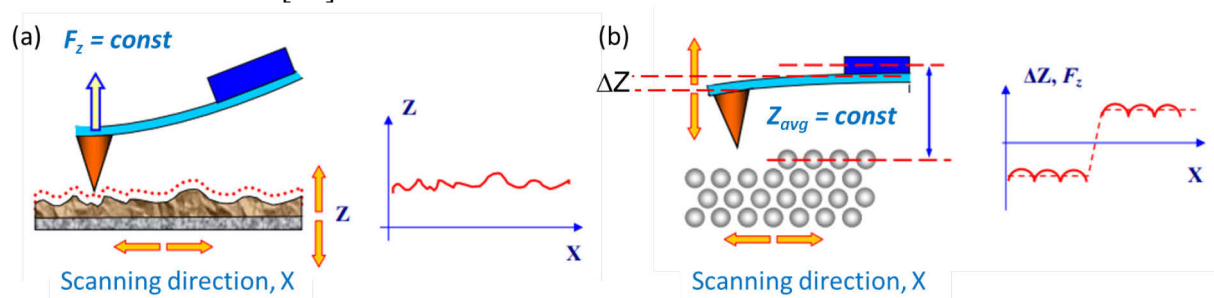


Figure 3.9. AFM image formation (a) with the constant tip-sample interaction and (b) at the constant altitude [14].

The static mode is fast and provides high resolution (in vacuum), but usually it is not suitable for soft (for example, biological or some polymer) samples due to the permanent contact with the surface. This can lead to sample or/and probe damage. Moreover, for the measurements in atmosphere the strong effect of capillary forces due to presence of thin fluid layer on sample surface is observed. To minimize these negative effects the measurements can be conducted in vibrating mode.

III.1.5 Imaging in Dynamic Mode (AC)

AFM measurements in Dynamic Mode are based on the recorded registration of interaction between the vibrating cantilever and the sample surface. To induce cantilever vibrations, an additional piezoelectric element that oscillates up and down is added to the cantilever holder. The cantilever vibrates in free space near or at the resonant frequency ω_0 with an excitation force $F_{exc}(\omega)$. It is a complex mathematical task to describe its oscillations. However, localized mass model [34] can be used for approximation. The cantilever can be considered as an elastic massless beam (with elastic constant k), fixed at one end on the piezoelectric vibrator, with an effective mass m^* localized on the other (free) end of the lever [17] (Figure 3.10).

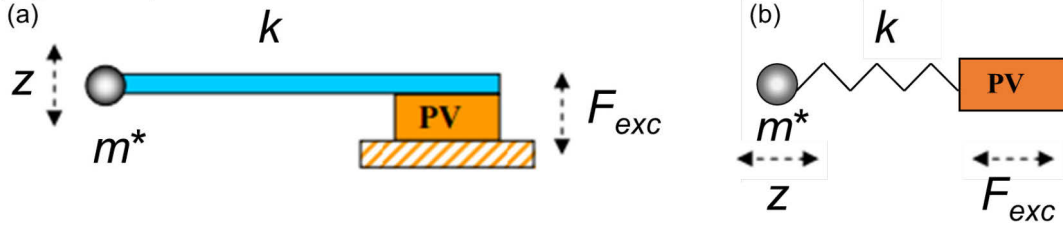


Figure 3.10. (a) Localized mass model for cantilever oscillations modelling, where m^* and k are the effective mass and the spring constant of the cantilever respectively, z is the vertical displacement of the cantilever and F_{exc} is the excitation force of the cantilever vibrations [14]. (b) Sketch representing cantilever beam as a simple spring-mass system.

The cantilever vibrates with frequency ω and the excitation force F_{exc} induced by the piezoelectric vibrator oscillations:

$$F_{exc}(z, t) = F_0 \cos(\omega t) \quad (3.14)$$

When the probe approaching the sample, the probe and the sample start to interact and this additional force $F_I(z)$ (representing all the forces acting between probe and surface at nano-scale distance) should be taken into account. Motion equation of the damped harmonic oscillator can describe the system:

$$\ddot{z} + \gamma \dot{z} + \omega_0 z^2 = \frac{F_{exc}(\omega)}{m^*} + \frac{F_I(z)}{m^*}, \quad (3.15)$$

where the terms \dot{z} and \ddot{z} are the first and the second derivatives with time of the tip-sample distance, respectively and γ is the damping coefficient, $F_I(z)$ is the total force acting on the tip from the surface while approaching towards it.

When the probe is far from the surface the interaction force $F_I(z)$ is negligibly small and the steady state solution of the system is:

$$z(t) = A(\omega) \cos(\omega t - \varphi(\omega)), \quad (3.16)$$

where

$$A(\omega) = \frac{F_0}{m^*} \frac{1}{\sqrt{(\omega_0^2 - \omega^2)^2 + \gamma^2 \omega^2}}, \quad (3.17)$$

is the amplitude of the cantilever vibration and

$$\varphi(\omega) = \arctan\left(\frac{\gamma \omega}{\omega_0^2 - \omega^2}\right), \quad (3.18)$$

is the phase of the cantilever vibration.

To find the solution of the equation (3.14) when the probe is approaching towards the surface and the tip-sample interaction cannot be negligible anymore the knowledge of interaction force $F_I(z)$ is required. In the case of small oscillations and small force gradients, the approximation to the first order of $F_I(z)$ can be done²:

$$F_I(z) \approx F_I(z_0) + \frac{\partial F}{\partial z}(z_0), \quad (3.19)$$

Thus, the equation (3.15) becomes:

² This approximation is not valid for standard tapping mode, but correct for the 2nd pass in Electrostatic and Magnetic Force Microscopy, where the separation distance between the oscillating probe and the sample is much higher than the probe oscillation amplitude.

$$\ddot{z} + \gamma\dot{z} + \left(\omega_0^2 - \frac{1}{m^*} \frac{\partial F}{\partial z}(z_0) \right) z = \frac{F_{exc}(\omega)}{m^*} + \frac{F_1(z_0)}{m^*}, \quad (3.20)$$

where $\frac{F_1(z_0)}{m^*}$ is the constant that displaces the equilibrium position of the system (static cantilever deflection) without influence on the frequency.

The amplitude or the phase of the oscillation while $\frac{\partial F}{\partial z}(z_0)$ induces the variation in the resonance parameters of the system:

$$\omega_m = \omega_0 \left(1 - \frac{1}{2k} \frac{\partial F_1}{\partial z}(z_0) \right) = \sqrt{\frac{k}{m}} \left(1 - \frac{1}{2k} \frac{\partial F_1}{\partial z}(z_0) \right), \quad (3.21)$$

$$\frac{\partial F}{\partial z} = -\Delta\varphi \cdot \frac{k}{Q} \quad (3.22)$$

where $\Delta\varphi$ is the phase shift of the cantilever vibration, k is the cantilever spring constant, $Q = \omega_0/\Delta\omega$ is the vibrating system quality factor³, ω_0 is the resonant frequency, $\Delta\omega$ is the bandwidth.

A typical response curve of a cantilever is shown in Figure 3.11. Attractive force gradient shifts the resonant frequency to a lower value while repulsive force gradient shifts the resonant frequency to a higher value. The change of amplitude (Figure 3.11 a) and phase (Figure 3.11 b) due to small attractive (dash lines) and repulsive (dotted lines) force gradients is presented as well.

Usually the probe vibrates near its resonant frequency and oscillation amplitude can be varied from few up to few hundred nanometres. The electronic part of the microscope controls the height of the cantilever above the sample to keep the amplitude (which is used as a feedback parameter) constant, when the tip goes close to the surface then Van der Waals forces, dipole-dipole interactions, electrostatic forces etc. take place, causing the amplitude of the cantilever's oscillation to change. A tapping AFM image is therefore produced by imaging the force of the intermittent contacts of the tip with the sample surface.

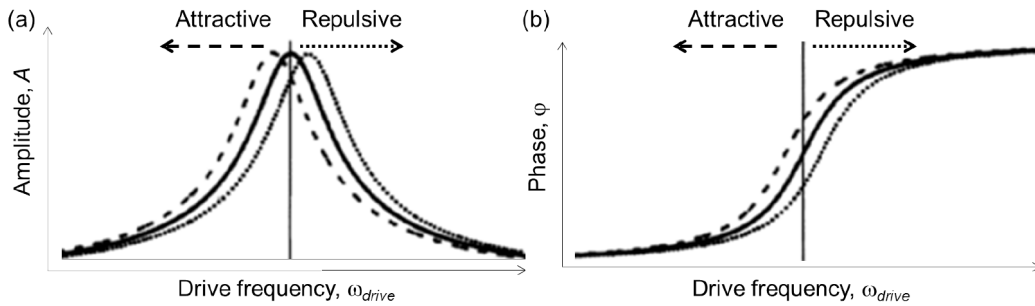


Figure 3.11. The change of amplitude (a) and phase (b) for oscillating cantilever according to the tip-sample interaction. The dash lines correspond to negative force gradient, which leads to decrease of the resonant frequency and dotted lines correspond to positive force gradient, which leads to increase of the resonant frequency.

According to the interaction between the probe and sample, the detected force gradient can have different signs. A negative force gradient ($\frac{\partial F}{\partial z} < 0$) due to attraction between the tip and sample leads to the drop in resonance frequency, ω_0 . Thus, the drive frequency overcomes this value ($\omega_0 < \omega_{drive}$) causing increase of the amplitude and phase shift (dash lines in Figure 3.11). Repulsive interaction leads to a positive force gradient and to a drop in amplitude and phase (dotted lines in Figure 3.11).

³ Quality factor Q is a dimensionless parameter that describes how under-damped an oscillator or resonator is, and characterizes a resonator's bandwidth relative to its center frequency. It can be found as a ratio between resonance frequency and the bandwidth over which the power of vibration is greater than half the power at the resonant frequency (full width at half maximum). For a typical cantilever $Q = 1000-100000$ in vacuum, $Q = 100-1000$ in air and $Q = 1-10$ in liquid.

Referring to the detection mechanisms, dynamic modes can be divided into two groups: Amplitude Modulation AFM (AM-AFM) and Frequency Modulation AFM (FM-AFM). AM-AFM with a lock-in amplifier is mainly used for *Tapping (or Intermittent/Semi-Contact)* mode where the tip actually touches the surface by entering in the repulsive regime of the short-range interaction, and then moves completely away from the sample in each oscillation cycle.

In FM-AFM [35] the cantilever's resonant frequency is tracked with a phase-locked loop. Phase signal is used as an error signal for a feedback loop and the drive frequency is varied to keep phase constant. Absence of friction forces in high vacuum allows AFM measurements with high quality factor Q cantilevers. However, the possibility of FM-AFM measurements in liquids has been demonstrated as well [36]. Measurements of the changes in oscillation frequency provide information about tip-sample interaction and form a topographical image:

$$\frac{\partial F}{\partial z} = -2k \cdot \frac{\Delta\omega}{\omega_0}, \text{ if } \frac{\partial F}{\partial z} \ll k \quad (3.23)$$

The AM-AFM is mainly used in air or liquids. The viscous forces in such environments lower cantilever quality factor Q by damping the cantilever, which in turn leads to faster cantilever stabilization.

In *Non-Contact (Contactless)* AFM mode cantilever oscillates with small oscillation amplitude (few nanometres down to few pedometers) at either its resonant frequency (FM-AFM) or just below (AM-AFM) to stay close to the surface all the time [37]. In more common AM-AFM mode the shift in the oscillation amplitude or phase provides the feedback signal for obtaining the image. In FM-AFM with the help of phase-locked loop, the image is formed as a function of the cantilever resonant frequency shift. Very stiff cantilevers can be used for FM-AFM since the frequency can be measured with very high sensitivity, thus, true atomic resolution in ultra-high vacuum conditions can be achieved [38].

Main advantages and disadvantages of Contact, Non-Contact and Tapping modes are presented in Table 3.2. It should be noticed that in this table general information is provided and cannot be applied straightforward to each particular experiment.

Scanning mode	Advantages	Disadvantages
Static Contact	<ul style="list-style-type: none"> • High scan speeds; • Possible atomic resolution (without point defects); • Measurements of friction forces. 	<ul style="list-style-type: none"> • Heavily influenced by frictional and adhesive forces; • Possible tip/sample damage and image data distortion due to lateral (shear) forces; • In ambient conditions may get strong capillary forces due to adsorbed fluid layer that can reduce the lateral resolution; • Possible reduction of resolution due to combination of lateral and strong normal forces.
Dynamic Semi-Contact/ Intermittent / Tapping	<ul style="list-style-type: none"> • Lateral forces almost eliminated; • Lower forces so less damage to soft samples or tips. 	<ul style="list-style-type: none"> • Slower scan speed than in contact mode.
Dynamic Non-Contact/ Contactless	<ul style="list-style-type: none"> • Both normal and lateral forces are minimized; • Good for measurements of very soft samples thanks to the working point in long-range interaction; • Can get atomic resolution in a UHV (ultrahigh vacuum) environment. 	<ul style="list-style-type: none"> • Work mainly in vacuum where the capillary force is removed.

Table 3.2. Main advantages and disadvantages of Contact, Tapping and Non-Contact modes.

III.2 Magnetic Force Microscopy (MFM)

Magnetic Force Microscopy (MFM) is a derivative of AFM dedicated to the interaction between magnetic probe and magnetic field of the sample. The first publication mentioning MFM technique was presented shortly after AFM development in 1987 [39]. Nowadays it is widely used method for fundamental study of magnetic materials properties, high resolution imaging of magnetic structures and for magnetic recording processes. The main effort of the researches is focused now on resolution improvements, qualitative magnetic measurements, imaging of a single magnetic micro/nano-objects and experiments with application of an external magnetic field [40,41].

III.2.1 General Operating Mode

In order to distinguish magnetic interaction from the short-range ones acting on the tip, several methods have been developed [42,43], but the most common is a double-step (or two pass) procedure. In the first step, topography measurements are performed in a chosen (static or dynamic) standard AFM mode, where several interactions take place (Figure 3.4). In the second step, the probe is lifted away from the surface to separate short-range and long-range interactions. Thus, the probe scans the surface at the distance of usually few tens nanometres above previously recorded topography.

The second pass can be performed in two different ways: (i) Linear Scan (Figure 3.12 a) or (ii) Lift Scan (Figure 3.12 b,c). Linear Scan mainly applied to the samples with small roughness. In this mode, the probe is lifted away from the surface at a certain distance and measurements are conducted at the constant altitude, while amplitude and phase variation is recorded, and the frequency is set to a certain value.

For more rough samples Lift Scan mode is used to prevent possible tip-sample contact and damage of sample or/and probe. In this mode the distance between probe and sample (lift scan height, LSH) remain constant, thus, the probe follows previously (first step) recorded topography.

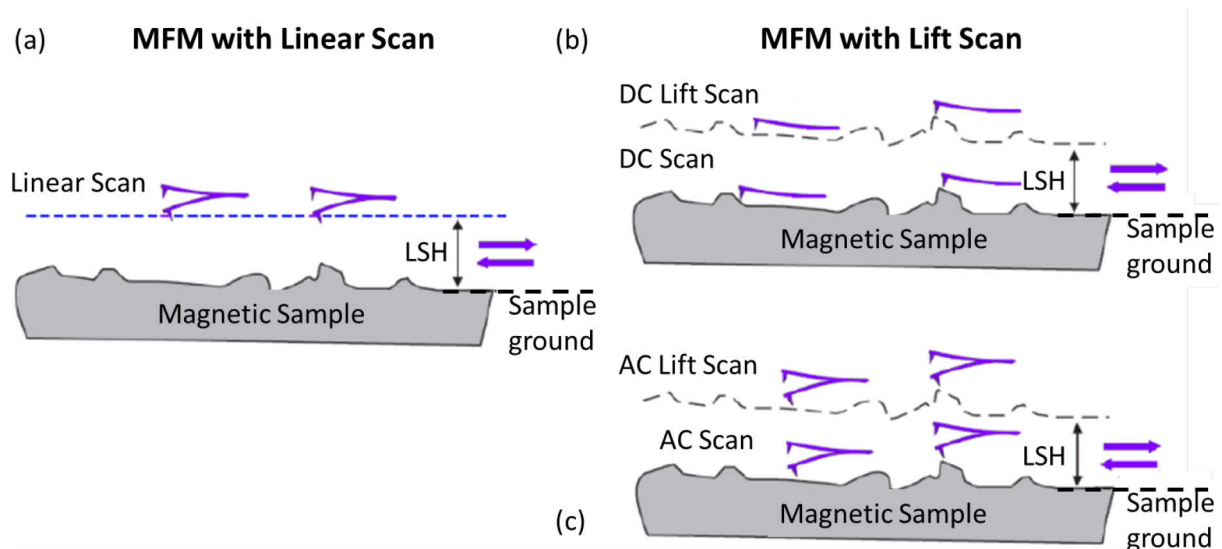


Figure 3.12. MFM procedure of a) Linear or Constant height mode; b) Static or DC MFM/ Lift procedure; c) Dynamic or AC MFM/ Lift procedure; LSH is the lift scan height.

III.2.2 Our Working conditions

In our experiments, all magnetic measurements were performed in ambient conditions. Lift scan mode was chosen to avoid the possible probe/sample damage due to fact that the roughness of studied NdFeB magnetic films is about 2-3 times higher than the minimal lift scan height (up to 1.5 μm and 0.5 μm , respectively).

To reduce the impact of the electrostatic force, the AFM probe and the sample were electrically grounded. The sample was electrically connected to the chuck through the sample puck, so that it was held at ground potential. Since the surface of the sample is conductive (Ta layer) and the base is not (SiO_2/Si), the back side of the sample and the part of the surface were covered with silver paint to ensure that it contacts one edge of the sample surface and one edge of the conductive mount (sample holder) (Figure 3.13).

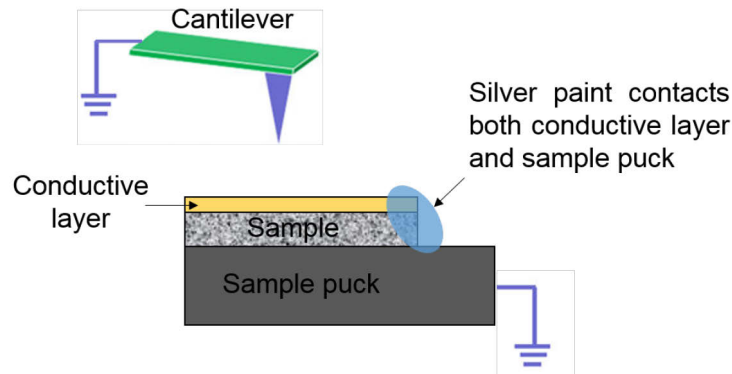


Figure 3.13. Schematic diagram showing electrically grounded cantilever and sample. The sample is connected onto a sample holder (puck) with conductive silver paint.

The lift scan height values range was chosen from 0.5 up to 3.5 μm to ensure that the capillary bridge is removed when the probe is lifted up for the second pass and predominantly magnetic force acts on the tip.

III.2.3 Magnetic Force or Force Gradient mapping

As well as Atomic Force Microscopy, Magnetic Force Microscopy can be performed in Static and Dynamic modes [44], these two modes provide complementary information.

Static mode (DC) for direct magnetic force mapping

In this mode during the first pass, sample topography is recorded in contact mode. During the second pass, the probe-sample magnetic interaction can be measured through Hooke's law according to the equation (3.13). In our experiments the lift heights LSH (Figure 3.12) varies from 0.5 up to 3.5 μm in order to distinguish short-range and long-range forces acting on the probe (Figure 3.4): the Coulomb and Van der Waals forces can be neglected during the second pass where only long-range interaction become effective. In these conditions where short range interaction are annulled, MFM in static mode provides direct measurements of magnetic force acting on the tip according to the equation (3.7). However, for quantitative force measurements the photodiode calibration and precise spring constant measurements have to be performed (as for spectroscopy mode) otherwise only qualitative information is available about force variation and sign of the force.

Dynamic mode (AC) for magnetic force gradient mapping

In this mode, the surface topography is scanned in Tapping mode where the cantilever oscillates close to or at its resonant frequency. The main origin of the oscillation amplitude and phase variations of the probe during the first scan is the short-range interaction. Then the probe is lifted from the sample and the oscillating cantilever follows previously recorded topography (Figure 3.12c).

During the second scan, mainly magnetic forces (attractive or repulsive) take place. An attraction between the magnetic probe and magnetic sample leads to decrease of the resonance frequency (and vice versa for a repulsion), thus changing the oscillation amplitude of the probe and its phase (Figure 3.11). The frequency shift is proportional to the force gradient acting on the tip and can be measured in Dynamic AFM in Amplitude Modulation or Frequency Modulation mode.

Choice of our working conditions

As the micromagnet arrays are mainly used in air at room temperature, our goal was to characterize these samples and their trapping force in these working conditions. By the way, all mapping images were recorded in air at room temperature with commercial AFM microscopes (Dimension 3100 and NT-MDT Solver Pro) using mainly the static mode in order to obtain a direct quantitative magnetic force map for various lift heights. However the first experiments were performed in AM-AFM to map the force gradient at various lift heights.

In practice, due to the sample roughness comparable to the lift heights, direct magnetic force measurements were performed by recording static cantilever deflection in Lift mode (Figure 3.12b and c) to avoid tip crash.

It should be noticed that Static contact measurements are faster than measurements performed in Tapping mode thanks to the instantaneous detection of the cantilever bending. Main advantage of the Contact MFM mode is to provide direct force measurements (equation 3.13) while its drawback compared to Dynamic MFM, is a mechanical contact of the probe with the surface during the first pass that can alter the probe or/and the sample.

A possible solution for non-destructive direct force measurements of magnetic force between probe and sample can be conducting first scan in dynamic mode (to decrease possible tip and sample damage) and second scan in dynamic by recording both the static deflection of the cantilever as the same time as the phase and/or amplitude variation. In this way, both force and force gradient of the magnetic interaction will be recorded at the same time in one slot. This approach should be comprehensive, but it has not been applied during this work because it was not available straightforward on our commercial AFM instruments.

III.2.4 MFM on micromagnet array using standard MFM probes

A standard MFM probe is an AFM probe with a thin magnetic layer deposited on the tip apex, tip-cone and on the lever. Different magnetic coatings are available; the choice of magnetic material layer for MFM probe is crucial for magnetic measurements [45]. Depends on the magnetic properties of the sample and imaging technique (static or dynamic), cantilever with an appropriate stiffness and magnetic coating should be chosen. Since both probe and sample exert magnetic properties, magnetic interaction relies on both of them.

In this subsection, MFM characterization of the NdFeB micromagnet array with an out-of-plane magnetization using different types of standard commercial MFM probes will be discussed. As NdFeB micromagnet array is a permanent magnet with stray field up to 1 T above the surface (for NdFeB TMP films [46]), the probability to reverse magnetic domain structure of the sample by standard low-coercivity commercial MFM tip (with magnetic field in order of mT [47]) is negligible. From the other side, depending on the coercivity of MFM probe magnetic layer, such sample may modify the tip magnetization. To evaluate this hypothesis and to study the micromagnet array action on different types of magnetic material, we performed MFM imaging with three types of MFM probes: two commercial MFM probes and a custom-made one based on AC160TS, Olympus probe that was covered by magnetic layer at the Néel Institute (Table 3.3).

	MagneticMulti75-G, BudgetSensors [48]	PPP-MFMR, Nanosensors [49]	AC160TS, Olympus [50]
Probe type	“soft”	“medium”	“hard”
Length/width/thickness of cantilever (μm)	225/28/3	225/28/3	160/50/4.6
Tip radius, (nm)	< 60	< 30	<50
Coating material	Soft magnetic	Co alloy	CoPt/FePt
Spring constant, (N/m)	3	2.8	42
Resonant frequency, (kHz)	75	75	300
Coercivity μ_0H_c , (T)	-	0.03	0.5

Table 3.3. Comparison of MFM probes characteristics used for experiments.

We should notice that the thickness, the coercivity value or even the chemical composition of the magnetic layer is not always available on the probe datasheets and can vary from one probe to another in the same set.

Before starting experiments, to reach the saturation state each MFM probe was magnetized in a field of 8 T in z direction (perpendicular to the sample surface) using a superconducting coil. The direction of the probe magnetization was chosen according to the studied sample properties. Both, the probe and the sample exhibit an out-of-plane magnetization to optimize the magnetic interaction along the z-axis.

Figure 3.14 displays topography and magnetic phase images (128 lines with 256 pixels per line) and their associated average cross-sections of NdFeB TMP sample scanned with the three types of MFM probes (Table 3.3). The measurements were performed using double-pass technique in Lift mode ($LSH = 500$ nm) in Dynamic (Tapping) regime. Each experimental average cross-section (Figure 3.14 g,h,i) associated to MFM image, was obtained by averaging 128 real scan lines.

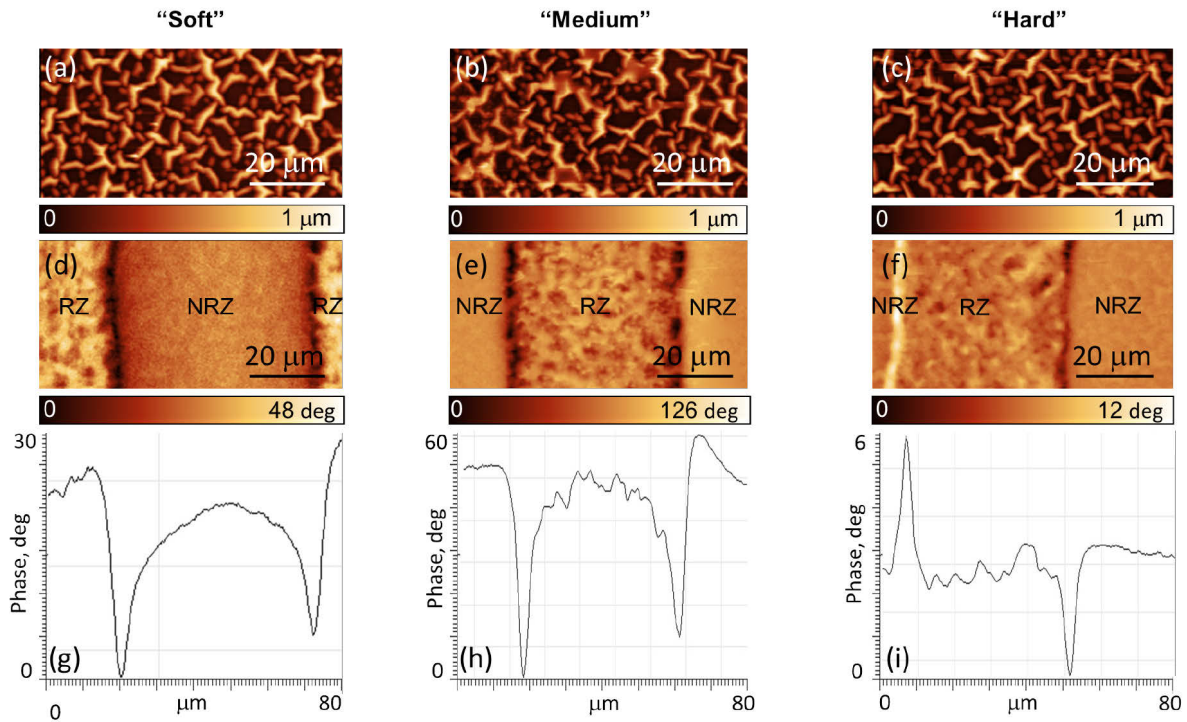


Figure 3.14. Topography (a,b,c), phase (d,e,f) and average cross-section (g,h,i) images of NdFeB TMP sample with 50 μm “stripes” pattern obtained with commercial MFM probes in Dynamic mode: MagneticMulti-75G (a,d,g); PPP-MFMR (b,e,h) and AC160TS (c,f,i) with magnetic coating. Lift scan height is 500 nm.

All the AFM images (Figure 3.14 a,b,c) reveal microstructure features of bumpy shape with height of up to 1 μm . Previous work [51] has shown by SEM and X-ray spectroscopy that these bumps contain Nd-rich material classically considered as non-magnetic. Their formation caused by annealing step of NdFeB films fabrication. On topography measurements no magnetic pattern is detected: it is the proof that the surface forces (Van der Waals, capillary, etc.) are much stronger than magnetic forces at short-range distance (see Annex III.1 and Figure 3.5).

During the second pass magnetic image is formed. The results can be seen from two equivalent points of view: obtained image can be interpreted as (i) the force acting on the probe’s magnetization by magnetic field arising from the sample and (ii) the force exerted on the samples’ magnetization by the field arising from the probe. In our experiments, samples with well-controlled magnetic structure (TMP) were chosen: an array of permanent micromagnets with an out-of-plane (oop) magnetization.

On all MFM phase images (Figure 3.14 d, e, f) three different regions are observed: RZ/NRZ/RZ or NRZ/RZ/NRZ. RZ reveals additional magnetic irregularity (strong light/dark contrast inside RZ) due to inhomogeneity of the irradiated zone during TMP fabrication process [52]. The interface between RZ and NRZ (or vice versa) or so-called *magnetic junction* corresponds to the region of the highest magnetic field/field gradient. The width of magnetic junction measured with described above probes is about few micrometres ($\sim 5 \mu\text{m}$ for “soft” and “medium” MFM probes, and $\sim 3 \mu\text{m}$ for “hard” MFM probe). This value relies on the tip radius curvature and effective tip volume relevant for MFM imaging, V_{eff} [53]:

$$V_{eff} = M_{tip} \cdot m_z, \quad (3.24)$$

where M_{tip} is remanent magnetization of the tip’s magnetic coating material (constant) and m_z is the magnetic dipole moment of the tip along z-axis (changes with the distance between tip and magnetic sample). The effective tip volume V_{eff} equals a particular portion of the thin magnetic coating deposited onto the tip. Figure 3.15a schematically presents pyramidal tip with magnetic coating (grey) of thickness t , the correspondent effective tip volume (grey) relevant for magnetic imaging is presented in Figure 3.15b (grey). It means that not the whole magnetic volume of MFM tip with height h , but only a part of it with height $h_{eff} < h$ (effective magnetic tip volume) will be involved in the magnetic signal.

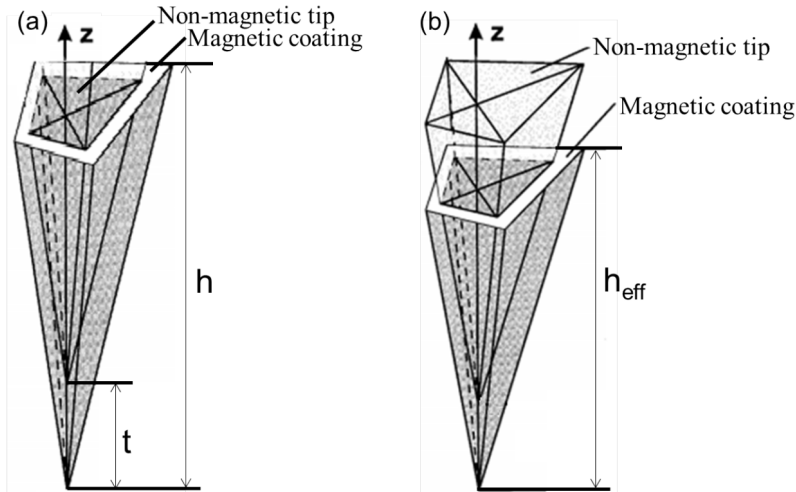


Figure 3.15. (a) Tip of an MFM probe with thin magnetic layer (gray). (b) Part of the magnetic tip relative to MFM imaging (grey). t is the thickness of magnetic coating (constant along z-axis), h is the tip height, h_{eff} is the height of the tip relevant for MFM imaging.

From equation (3.24) follows that increase of tip magnetic moment m_z (as a function of decay distance between tip and magnetic sample) implicates increase of effective tip volume, V_{eff} . Its value should be small to minimize the spatial extent of the long-range magnetic tip-sample interaction and maximize spatial resolution⁴.

Figure 3.14 (g,h,i) presents the average cross-section for corresponding MFM image. The strong increase of the magnetic interaction above the magnetic junctions compared to the other parts of the sample is observed. However, there is a difference in the sign of magnetic interaction (positive or negative) and its intensity for different MFM probes. According to the obtained MFM images, results can be classified depending on magnetic and mechanical properties of the MFM probes:

- “Soft” MFM probe

On MFM phase image obtained with soft magnetic coating probe (Figure 3.14d) the magnetic junction corresponding to the region of the highest magnetic field gradient appears as a dark vertical line. Figure 3.14g presents the average cross-section for the associated

⁴ High coercivity low stray field tips with thin magnetic coating are used to make the influence of the tip on the sample negligible. Reduced magnetization volume lowers the emitted magnetic stray field from the tip.

MFM image, showing the negative phase shift for both magnetic junctions: above both interfaces the magnetic probe undergoes attractive interaction. Strong magnetic field arising from the sample (few hundreds of mT) magnetizes the soft MFM probe, which reveals magnetic pattern shape and localizes magnetic junctions.

- “*Medium*” MFM probe

Similar results are obtained with PPP-MFMR probe (Figure 3.14 e, h). The interaction between the probe and the sample above the magnetic junction is always attractive. This can be caused by low coercivity of the probe (0.03 T) that can be re-magnetized by the field arising from the sample. Though the magnetic signal (phase shift) is stronger for results obtained with “medium” magnetic probe than with the “soft” one by a factor of 2 (phase shift of about 45 and 20 deg, respectively), for both “soft” and “medium” MFM probes, difference in magnetic signal between the first and the second magnetic junctions (up to 20%) remains unchanged with an increase of the Lift height. This effect could be attributed to the variation in sample properties.

- “*Hard*” MFM probe

Magnetic images obtained with AC160TS probe with high-coercivity hard magnetic coating (Figure 3.14 f,i) look different. Magnetic junctions are identified by light and dark contrast between RZ and NRZ corresponding to repulsive (light contrast, positive phase shift) and attractive (dark contrast, negative phase shift) forces between the probe and the sample. High coercivity of this type of probes protects them of a magnetization change due to the magnetic field arising from the sample.

In the MFM images obtained with three different magnetic probes, quantitative measurement of the magnetic force acting on tip is difficult to evaluate. Indeed, for most of commercially available MFM probes the magnetic layer covers the tip apex and cone as well as the lever, thus, the calculation of the effective magnetic volume is not straightforward. The point probe approximation [54] does not provide an adequate model to describe MFM signal quantitatively. One of the possible solutions is the development of more elaborated tip models, such as an analytical ‘pseudo-pole’ model of Häberle [55]. However, the detailed knowledge of commercially available MFM probe properties is required, which cannot be always obtained. An alternative solution is a fabrication of custom-made MFM probes with well-known (desired) magnetic properties and volume as well as localization (tip apex). Several techniques have been implemented for this purpose such as electron beam modification of standard MFM probe with magnetic coating [56] or attachment of a single magnetic object to a non-magnetic AFM probe: iron filled carbon nanotube [57], ferromagnetic-film-coated carbon nanotube [58,59], single nitrogen-vacancy defects in diamond to detect electron spin resonance [60], high-aspect-ratio rare-earth nanomagnets [61] and Nd-Fe-B microspheres [62]. The shape and material of the magnetic object fixed on non-magnetic AFM probe can be varied according to the experiments.

III.3 Microsphere Scanning Force Microscopy

For our experiments, we have attached a single magnetic microsphere to a non-magnetic commercial AFM probe. These microparticle MFM probes can be used for localization of magnetic patterns and also for quantitative studies of the interaction between single magnetic object (attached microsphere) and a micromagnet array (TMP, TOPO and μ MI. Until now, there is no standard technique that can perform directly and easily this kind of measurement.

The value of the cantilever spring constant should be selected according to the magnetic properties and volume of the microsphere in order to provide a reasonable signal over noise ratio in MFM mode: microsphere containing small magnetic volume should be fixed on a very flexible cantilever (low spring constant) and vice versa. Once the microsphere and the cantilever are chosen, the microparticle MFM probe can be fabricated. During this thesis, two

procedures for magnetic microsphere probe fabrication have been developed. The first one is similar to the one described by Yang Gan [63] and based on the imaging and manipulation capabilities of commercial AFM [64]. The second approach is similar to the one described by H. Campanella et al [61,65]. It exploits the capabilities of a dual beam Focused Ion Beam/Scanning Electron Microscopy (FIB/SEM) machine (Zeiss NVision 40 DualBeam) equipped with a micromanipulator and permits accurate microsphere positioning on the tip apex.

III.3.1 Microsphere probe fabrication using AFM manipulation

Commercial superparamagnetic polystyrene microspheres (microParticles GmbH) with a mean diameter of 3 μm functionalized with biocompatible iron oxide nanoparticles are the model objects to mimic the behaviour of biological species with similar size (as bacteria or cells). To study the action of micromagnet array on these model objects, we decided to attach *a single* of these microspheres to a commercial silicon AFM probe [64].

Worn probes (NSC 15⁵, MikroMasch) were chosen for Magnetic Particle Force Microscopy (MPFM) probe fabrication in order to facilitate glue deposition. Firstly, a TMP sample with magnetic stripes pattern where some superparamagnetic microspheres were trapped and a Si substrate with small droplet of glue (silver paint) were mounted on the sample holder and introduced into the AFM. The resonance frequency of a chosen cantilever was measured and its resonance curve was recorded (Figure 3.16 a). Secondly, the Si substrate was moved in x-y direction to align the probe above the silver paint droplet. For deposition of glue on the tip, the probe was approached towards the surface until its amplitude reached zero. The tip approach and the cantilever amplitude and deflection variation were managed by AFM microscope software. Zero amplitude of the probe indicates that the tip is immersed in the glue at a depth where the viscous forces are strong enough to annul the cantilever oscillations. To ensure that glue covers well the tip cone further dipping of the probe was performed until cantilever deflection reaches a positive value (cantilever bending upwards the surface). After a number of experiments, the curing time was found: 30s of probe staying in the droplet is enough to obtain a homogenous and sufficient glue deposition on the tip sides. Thirdly, the probe was removed far from the droplet and its resonant frequency was measured again (Figure 3.16 b). The shift of the resonant frequency to a lower value is due to additional mass at the free end of the lever, this confirms the glue deposition. Based on experimental results an optimal frequency shift for chosen AFM probes was found to be around 100 kHz. The detailed calculations of deposited glue mass ($\sim 10^{-12}$ g) due to the frequency shift are presented in Annex III.2.

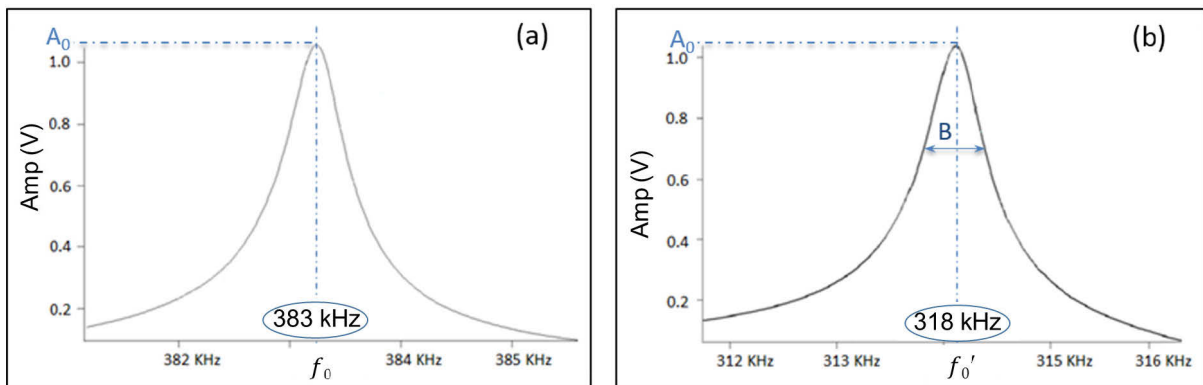


Figure 3.16. Resonance curves of the AFM cantilever: (a) Initial resonance curve, resonant frequency $f_0 = 383$ kHz (without glue); (b) Resonance curve of the cantilever with tip covered by glue, new resonant frequency $f'_0 = 318$ kHz [64].

⁵ According to the data sheet the nominal fundamental frequency is 325 kHz and the spring constant is 40 N/m.

To attach a magnetic microsphere to the tip apex covered with glue a single sphere was localized by optical system of an AFM instrument (Figure 3.17a, inside the red circle). Firstly, its topography was characterized by recording an image in tapping mode with a light tip-sample interaction (imaging amplitude $A_i \approx 0.8 A_0$, where A_0 is the amplitude at the resonance frequency) at a scan rate of 0.5 Hz (Figure 3.17b). Secondly, when the image of the half of the sphere was obtained, the standard scan mode swapped over the scan of the same line in order to glue the imaged microsphere (blue rectangle in Figure 3.17c). During the scan of the same line, we tuned the tip-sample interaction by decreasing the set point value (down to $0.1 A_0$) until the microsphere disappeared from the topography image (straight red line on the bottom in Figure 3.17c). The optical system of the AFM instrument displays that the chosen sphere vanished from its initial position (Figure 3.17d, inside the red circle) and should be glued to the tip apex.

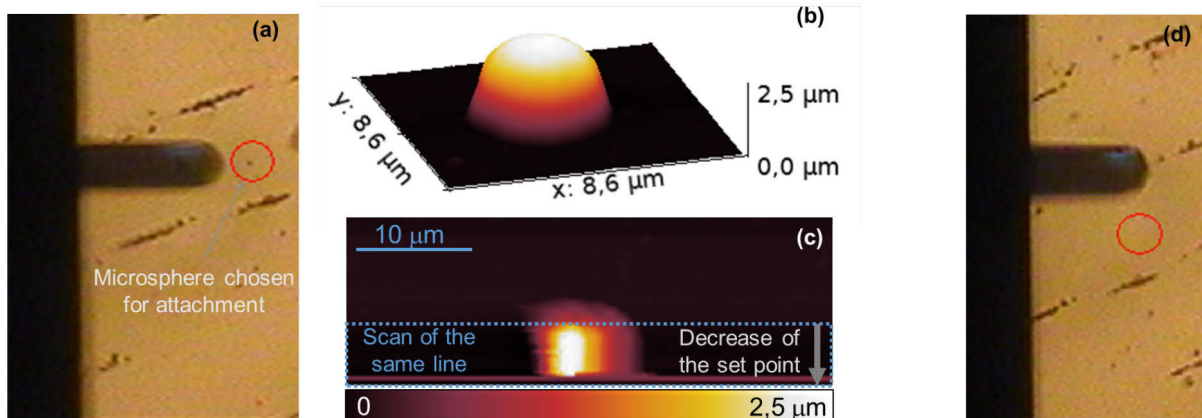


Figure 3.17. Procedure of the microsphere attachment. (a) Optical image of an isolated microsphere (in red circle). (b) 3D topography image of the chosen isolated microsphere performed in tapping mode. (c) Topography image of the microsphere performed in tapping mode. The area in blue rectangle presents the scan of the same line. The straight red line in the bottom of the rectangle corresponds to the moment when the sphere was glued to the tip apex. (d) Optical image of the scanning area. The sphere has disappeared from the surface (red circle) [64].

SEM images (Figure 3.18) confirm the attachment of the microsphere and its localisation on a side of the pyramid closed to the tip apex (around $0.5 \mu\text{m}$ from the worn apex in Figure 3.18a): our first Microsphere probes have been obtained.

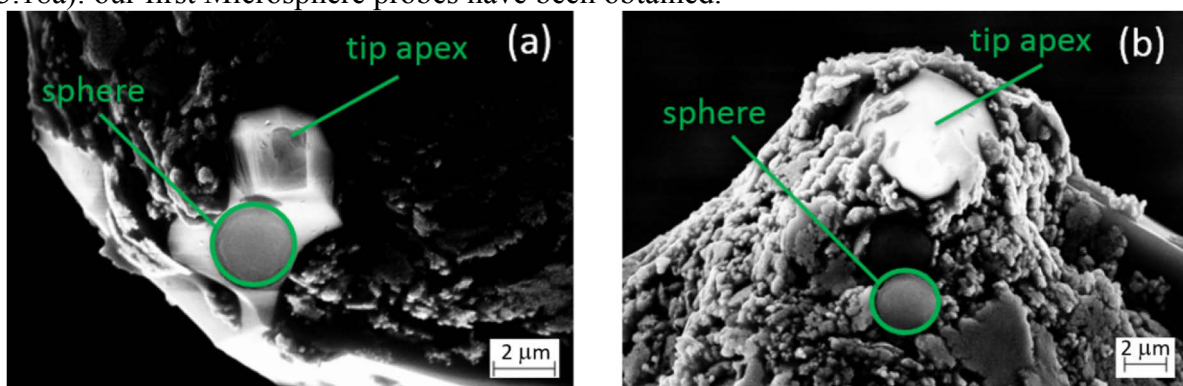


Figure 3.18. SEM images of the worn tip with (a) $2.85 \mu\text{m}$ and (b) $3 \mu\text{m}$ diameter attached superparamagnetic microspheres [64].

III.3.2 Force gradient mapping between micromagnet array and a single microsphere

Fabricated MPFM probes were used to map the action of TMP micromagnet array on a single magnetic micro-object through force gradient measurement. Topographic and magnetic phase images obtained with $2.85 \mu\text{m}$ superparamagnetic microsphere attached to an AFM cantilever (resonant frequency is 200 kHz , spring constant is 50.3 N/m) are presented in

Figure 3.19. Measurements were conducted in dynamic mode with the double-pass technique at $LSH = 800$ nm.

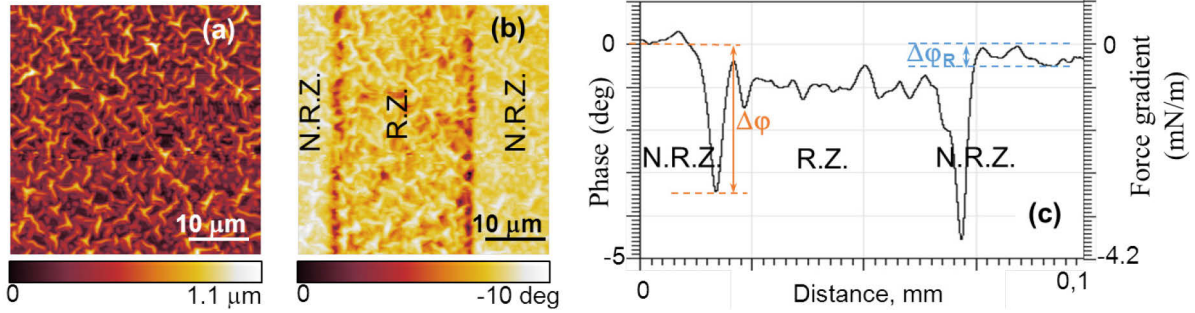


Figure 3.19. AFM image of TMP sample obtained with a $2.85 \mu\text{m}$ MPFM probe. (a) Topography image. (b) MFM (phase) image. (c) The average cross-section from MFM (phase) image: $\Delta\varphi$ is the difference in average phase signal above magnetic junction and non-reversed zone (phase shift), $\Delta\varphi_R$ is the variation in phase signal inside non-reversed or reversed zone (“magnetic roughness”). Lift height is equal to 800 nm.

On topographical image (Figure 3.19 a) we observe despite the “double tip effect” Nd-rich features of bumpy shape on the sample surface without sign of magnetic pattern (magnetic junction).

The MFM phase image (Figure 3.19 b) is similar to these obtained with “soft” and “medium” MFM probes. Three areas corresponding to NRZ, RZ and NRZ are observed, they are separated by two well-defined regular lines (magnetic junctions) that exhibit negative phase shift revealing attractive interaction between the superparamagnetic microsphere and the TMP sample.

Figure 3.19c reveals an average cross-section of corresponding magnetic phase image by averaging 128 real scan lines. One can notice that both RZ and NRZ exhibit some inhomogeneity, the so-called “magnetic roughness” $\Delta\varphi_R$ equal to 0.6 and 0.4 deg (peak-to-peak) respectively. Its presence can be explained by the granular structure of the NdFeB film coupled with local misalignment of individual grains. An increase of $\Delta\varphi_R$ for RZ is attributed to local magnetic inhomogeneity due to magnetization reversal during TMP process [52]. Using equation (3.22) force gradients $\frac{\partial F}{\partial z}$ due to magnetic roughness for NRZ and RZ were calculated: 3.6×10^{-4} N/m and 5.4×10^{-4} N/m respectively. From an experimental point of view, this magnetic roughness fixes the lowest phase shift value $\Delta\varphi_{min}$ that can be distinguished to localize a magnetic junction: $\Delta\varphi_{min} \geq \Delta\varphi_R$

With these MPFM probes, we have demonstrated that the interaction between a single magnetic microsphere attached to a non-magnetic AFM probe and a TMP sample can be detected and first “quantitative” measurements (force gradient) of the interactions exerted by a TMP micromagnet array on a well-define magnetic micro-object were carried out [64]. The results of quantitative force gradient measurements will be discussed in details in Chapter IV.

The next step was to perform direct quantitative measurements of the force exerted by magnetic flux source on a single magnetic microsphere. Since the magnetic force decays fast with the distance between magnetic sample and microsphere, this distance should be well defined. Thus, for reliable quantitative measurements, a better control of the magnetic microsphere positioning on the tip apex is required.

III.3.3 Toward quantitative mapping: Microsphere probe fabrication by Focused Ion Beam

Different types of commercial non-magnetic AFM probes were used for MPFM probes fabrication. Standard AFM cantilevers (NSC14/Al BS, MicroMasch) were shaped with Focused Ion Beam (FIB) to obtain a cavity adapted to the size of the selected microsphere (Figure 3.20 a). To facilitate the fixing process, specific commercial conductive AFM probes (PL2-CONTR and PL2-FMR, Nanosensors) called “plateau” tips that exhibit a flat and

circular apex of 1.8 μm diameter were chosen as well (Figure 3.20 b). Finally, standard AFM probes with a tetragonal tip apex (OMCL-AC240TS, Olympus) (Figure 3.20 c) were also employed for magnetic microsphere attachment.

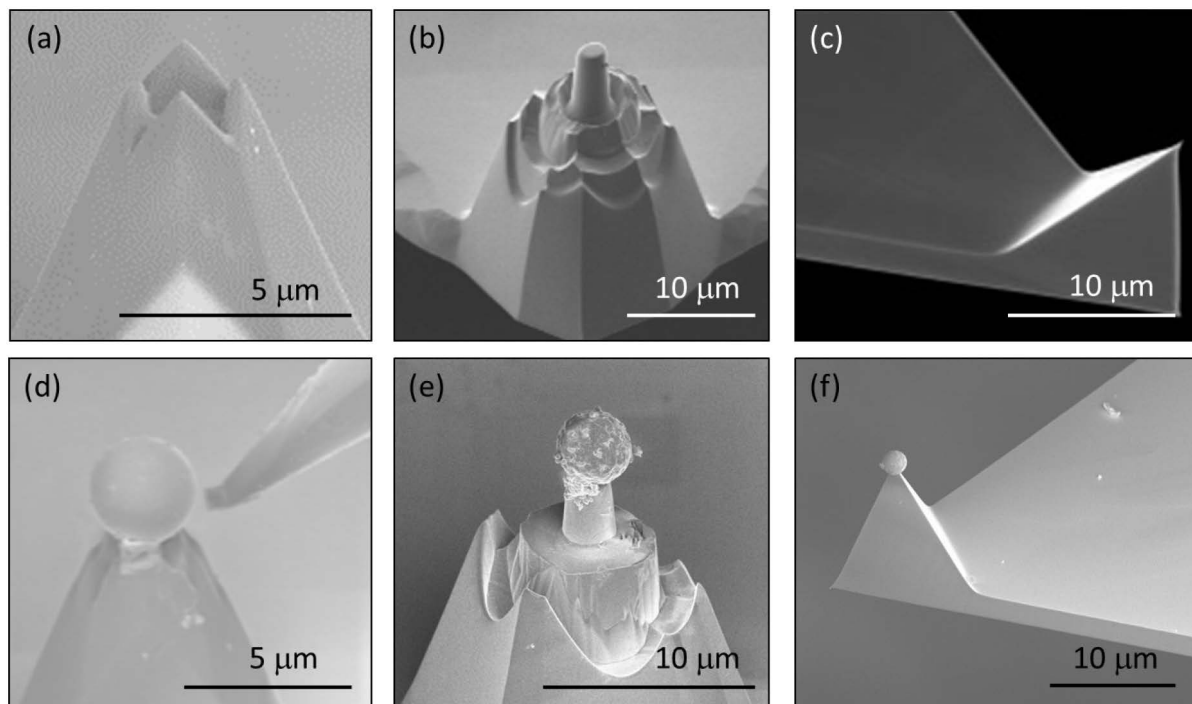


Figure 3.20. Commercial AFM cantilevers used for magnetic microsphere attachment. (a) FIB-shaped tip apex of NSC14/Al BS, MicroMasch probe; (b) tip apex of PL2-CONTR, Nanosensors probe; (c) tip apex of OMCL-AC240TS, Olympus probe; (d) NSC14/Al BS, MicroMasch probe with attached 3 μm NdFeB microsphere; (e) PL2-CONTR, Nanosensors probe with attached 1.5 μm superparamagnetic microsphere; (f) OMCL-AC240TS, Olympus probe with attached 1.8 μm NdFeB microsphere.

Two types of commercially available magnetic microspheres were chosen for attachment: (i) polystyrene microspheres functionalized with iron oxide nanoparticles (NPs), so-called superparamagnetic microspheres (microParticles GmbH), and isotropic NdFeB microspheres (MQP-S-11-9-20001-070, Molycorp Magnequench).

According to the manufacturers' specification iron oxide inclusions in superparamagnetic microspheres consist of a mixture of maghemite Fe_2O_3 and magnetite Fe_3O_4 with the weight of not less than 30% from the total microsphere weight. The size of iron oxide NPs has been estimated in the range of about 3 nm [66]. Detailed calculations concerning volume ratio of magnetic NPs inside superparamagnetic microsphere and its magnetic properties are presented in Annex III.3. The results together with provided by supplier data can be found in Table 3.4.

Sphere type*	Diameter* (μm)	Density* (g/cm^3)	wt.% of magnetic NPs	vol.% of magnetic NPs
PS-MAG-S1850	0.27	2.4	73	35
PS-MAG-S1645	1.33	2.24	67	30
PS-MAG-S2180	3.90	1.62	40	13

Table 3.4. Information about superparamagnetic microspheres used for MPFM probes fabrication. Data marked with * is provided by microParticles GmbH. The weight (volume) of magnetic NPs wt.% (vol.%) was calculated as a ratio between weight (volume) of all magnetic inclusions inside a microsphere and microsphere total weight (volume).

Sphere type	Theoretical/ apparent density ⁶ (g/cm ³)	Residual induction B_r (mT)	Energy product (BH) _{max} (kJ/m ³)	Intrinsic coercivity H_{cl} (kA/m)	Coercive force, H_c (kA/m)
MQP-S-11- 9 20001-070	7.43/3.6-4.2	730-760	80-92	670-750	440

Table 3.5. Information about NdFeB microspheres used for MPFM probes fabrication provided by Molycorp Magnequench.

The MPFM probe fabrication procedure consists of few steps. Firstly, a silicon sample with spread magnetic microspheres on its surface and AFM cantilevers are introduced inside the FIB chamber. Then, using SEM imaging magnetic spheres are localized and their size is measured. Secondly, a micromanipulator (tungsten needle) is approached close to the chosen microsphere and the sphere is soldered to the needle by injection of an organometallic precursor ($((\text{CH}_3)_3\text{Pt}(\text{CH}_3\text{C}_5\text{H}_4))$, methylcyclopentadienyl-trimethyl-platinum) (Figure 3.21a). This process is called Ion Assisted Chemical Vapour Deposition (IACVD).

Thirdly, the microsphere is positioned in the middle of the tip apex by moving the stepper motor of the sample holder and bounded to it by IACVD process (Figure 3.21 b). Ion-beam-assisted milling is used to separate tungsten needle from the sphere by elimination of the tying material between them. Finally, when the micromanipulator stage is released and moved away, the sphere remain attached to the tip (Figure 3.20 d,e,f and Figure 3.21c).

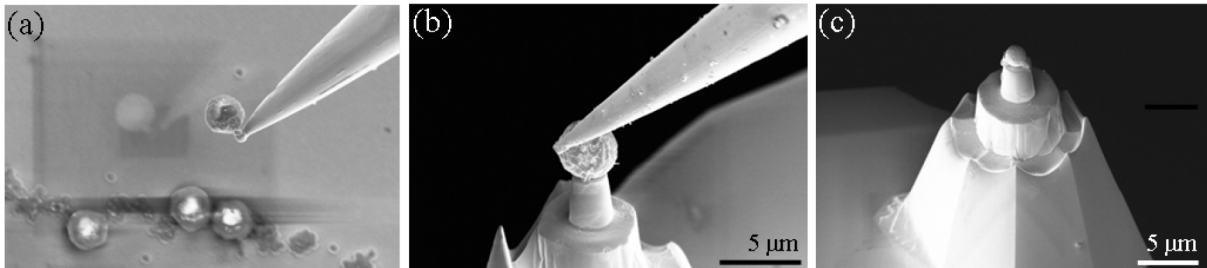


Figure 3.21. SEM images of the probe fabrication procedure: (a) A microsphere is soldered to the micromanipulator by IACVD of Pt gaseous precursor. (b) The selected microsphere is placed onto the plateau tip apex. (c) The microsphere is attached to the tip apex and free from the tungsten needle.

Using this procedure, superparamagnetic and hard magnetic microspheres with a diameter ranging from 0.29 μm up to 3.6 μm have been attached to the non-magnetic AFM probes. The calibration of these probes was performed in air at room temperature using thermal tune method in order to determine precisely the cantilever spring constants. All the MPFM probes with NdFeB particles were submitted to a magnetic field of 7 T in direction perpendicular to the cantilever before starting MFM measurements. List of all fabricated MPFM probes can be found in Annex III.4.

Thanks to these fabricated MPFM probes, quantitative magnetic maps of TMP sample action on a single magnetic microsphere have been recorded using the standard double-pass MFM technique in lift mode. Figure 3.22 displays typical results of TMP sample mapping obtained with superparamagnetic and NdFeB MPFM probes using contact and static lift mode (Lift Scan Height = 500 nm).

For both types of magnetic microsphere, the only magnetic part of the MPFM probe is the microsphere therefore the cantilever bending recorded during the second pass is essentially due to the magnetic force acting on it. Thus, after a careful cantilever and photodiode calibration, the force can be found using Hooke's law (Equation 3.13).

Note that this assumption would not apply for commercial MFM probes, for which a magnetic layer covers the entire probe surface (tip apex, tip cone and cantilever).

⁶ Apparent density is the density of the solid material excluding the volume of any open pores, but including the volume of closed pores.

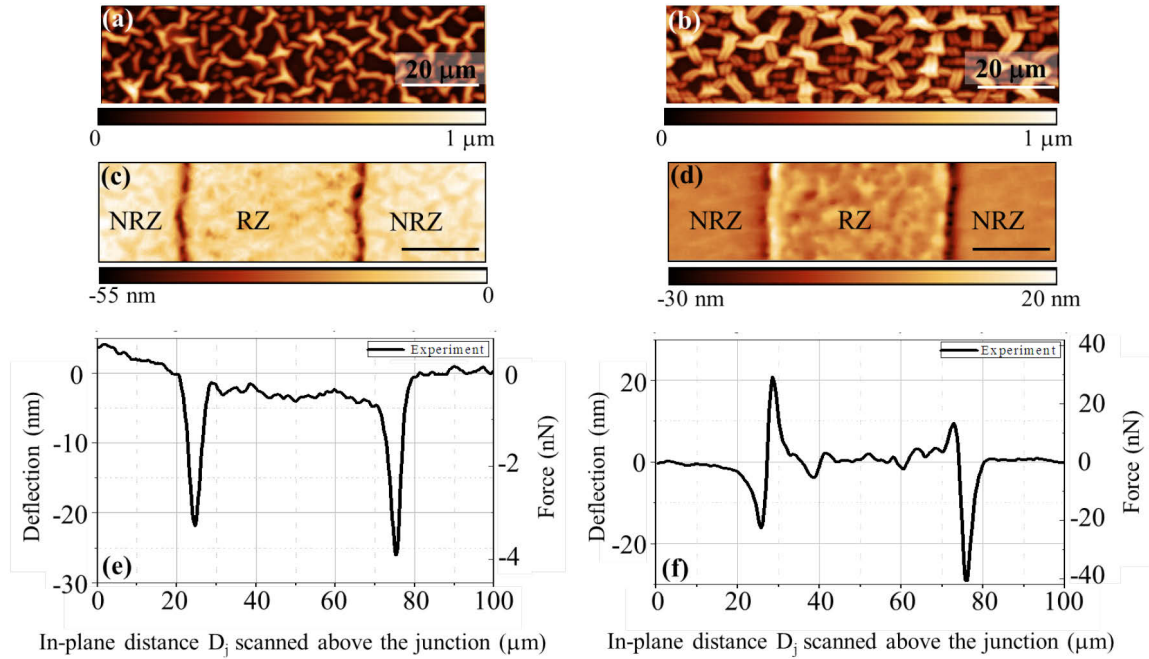


Figure 3.22. Topographical and MFM images of an array of NdFeB micromagnets obtained with 1.5 μm superparamagnetic microsphere (resonance frequency is 12 kHz, spring constant is 0.15 N/m) (a,c) and 1.3 μm NdFeB microsphere (resonance frequency is 52 kHz, spring constant is 1.4 N/m) (b,d) in static mode for $LSH = 500$ nm. Associated mean experimental profiles obtained with 1.5 μm superparamagnetic microsphere (e) and 1.3 μm NdFeB microsphere (f). Lateral scale bar is 20 μm .

For both type of MPFM probes, topographical images (Figure 3.22 a,b) are similar to these obtained with commercial MFM probes and MPFM probes produced by first approach: they reveal surface topography of bumpy shape and no magnetic features.

MFM deflection image and associated mean experimental profile (Figure 3.22 c,e) obtained with 1.5 μm superparamagnetic microsphere probe are similar to these obtained with “soft” or “medium” MFM probes. Three areas (NRZ/RZ/NRZ) are observed and separated by well-define dark line corresponding to magnetic junctions where the attractive force reaches its maximum intensity (4 nN). This result demonstrates that these MPFM probes are suitable for localization of magnetic junctions and precise force measurements between micromagnet array and a single magnetic object (microsphere functionalized with magnetic nanoinclusions).

MFM deflection image and associated mean experimental profile (Figure 3.22 d,f) obtained with 1.3 μm NdFeB microsphere look more similar to the data obtained with “hard” MFM probe. Not only three zones (NRZ/RZ/NRZ) are observed, but also magnetic junctions defined by two lines (dark and light contrast) above the same interface are presented. This corresponds to two peaks: negative and positive and vice versa on average cross-section profile above each of two interfaces (NRZ/RZ and RZ/NRZ). This result demonstrates two points: (1) NdFeB MPFM probes are reliable and well adapted for quantitative magnetic interaction measurements between micromagnet array and a single hard magnetic microsphere and (2) the interaction behaviour between TMP and magnetic microsphere varies with the magnetic object properties.

Based on these results, detailed studies have been carried on TMP sample and single magnetic microsphere and are described in Chapter IV.

References

- 1 "A practical guide to scanning probe microscopy, Authors (first edition)", R. Howland and L. Benatar, (1993).
- 2 "Chemical Force Microscopy: Exploiting Chemically-Modified Tips To Quantify Adhesion, Friction, and Functional Group Distributions in Molecular Assemblies", A. Noy et al, *J. Am. Chem. Soc.*, 117 (30), pp. 7943–7951 (1995).
- 3 "Common Approaches to Tip Functionalization for AFM-Based Molecular Recognition Measurements", <http://www.bruker.co.jp/axs/nano/imgs/pdf/AN130.pdf>
- 4 "Metal-coated carbon nanotube tips for magnetic force microscopy", Z. Deng et al, *Appl. Phys. Lett.* 85, 6263 (2004).
- 5 "Imaging the local electrical properties of metal surfaces by atomic force microscopy with conducting probes", F. Houz   et al, *Appl. Phys. Lett.* 69, 1975 (1996).
- 6 "Scattering Lens Resolves Sub-100 nm Structures with Visible Light" Van Putten et al, *Physical Review Letters* 106 (19) (2011).
- 7 <http://www.olympusmicro.com/primer/digitalimaging/deconvolution/deconresolution.html>
- 8 "Progress in magnetic domain observation by advanced magneto-optical microscopy" J. McCord, *J. Phys. D: Appl. Phys.* 48333001 (2015).
- 9 B. Azzerboni et al. (eds.), "Magnetic Nanostructures in Modern Technology", R. Grechishkin et al, *Magnetic Imaging Films*, pp. 195–224 (2008).
- 10 "A history of scanning electron microscopy developments: Towards "wet-STEM" imaging" A. Bogner et al, *Micron* 38, pp. 390–401 (2007).
- 11 "Atomic force microscope", G. Binnig et al, *Phys. Rev. Lett.*, Vol. 56, No. 9, pp. 930 – 933 (1986).
- 12 "AFM probes with directly fabricated tips", Anja Boisen, Ole Hansen and Siebe Bouwstra, *J. Micromech. Microeng.* 6 pp. 58–62 (1996).
- 13 https://www.agilent.com/cs/library/slidepresentation/Public/AFM%20Probe%20ManufacturingNanoworld_tip_technologyPRussell07.pdf
- 14 "The textbook for students of the senior courses of higher educational institutions", V. L. Mironov, The Russian Academy of Sciences Institute for Physics of Microstructures, Russia, Nizhniy Novgorod, Reviewer: Giacomo Torzo (2004).
- 15 "Ultra-high aspect ratio replaceable AFM tips using deformation-suppressed focused ion beam milling", A. Savenko et al, *Nanotechnology* 24 (2013).
- 16 "Force measurements with the atomic force microscope: Technique, interpretation and applications", H.-J. Butt et al., *Surface Science Reports* 59 pp. 1–152 (2005).
- 17 "Scanning Force Microscopy", D. Sarid, Oxford University Press, Oxford, ISBN 0-19-509204-X, 1991.
- 18 "Spring constant calibration of atomic force microscope cantilevers of arbitrary shape" John E. Sader et al, *Rev. Sci. Instrum.* 83, 103705 (2012).
- 19 "14 MHz micromechanical oscillator", T. Mattila et al, *Sensors Actuators A* 97-98 (2002) 497.
- 20 US Pat. RE37,299 (Reissued Pat. No. 5,144,833).
- 21 <http://www.nanoscience.de/HTML/methods/afm.html>
- 22 "Atomic Force Microscopy", E. Meyer, *Progress in Surface Science*, Vol. 41, pp. 3-49.
- 23 "Force-distance curves by atomic force microscopy", B. Cappella, G. Dietler, *Surface Science Reports* 34 pp. 1-104 (1999).
- 24 "Advances in atomic force microscopy", Franz J. Giessibl, *Reviews of modern physics*, Vol. 75, (2003).
- 25 https://www.google.ru/url?sa=t&ret=j&q=&esrc=s&source=web&cd=1&ved=0ahUKEwjy9X48b3NAhWHfiwKHZq2DIwQFggbMAA&url=http%3A%2F%2Fusa.jpk.com%2Findex.download.c46f64176d66c310620d0c4bdf4be7ef&usq=AFQjCNGLM6zm4MnoeZePYZrvcYVOcm32Fw&sig2=4WvntHQaUbuS5UEkk_RV8g&bvm=bv.125221236,d.bGg&cad=rja
- 26 "Comparison of calibration methods for atomic force microscopy cantilevers", N.A. Burnham et al, *Nanotechnology* 14, pp. 1–6 (2003).
- 27 "The determination of atomic force microscope cantilever spring constants via dimensional methods for nanomechanical analysis", C.A. Clifford et al, *nanotechnology* 16 (9), pp. 1666-1680 (2005).
- 28 "Methods for determining and processing 3D errors and uncertainties for AFM data analysis", A.

- Campbell et al, *Meas. Sci. Technol.*, 22 (2011).
- 29 “Experimental Determination of Spring Constants in Atomic Force Microscopy”, T.J. Senden et al, *Langmuir* 10, p. 1003 (1994).
- 30 <http://www.bruker.co.jp/axs/nano/imgs/pdf/AN090.pdf>
- 31 “Thermal tune method for AFM oscillatory resonant imaging in air and liquid”, S. Belikov et al, 2014 American Control Conference (ACC) June 4-6, 2014. Portland, Oregon, USA
- 32 “Calibration of Atomic Force Microscope Tips” in *Review of Scientific Instruments*, L. Hutter and John Bechhoefer 64(7), p. 1868 (1993).
- 33 “An atomic-resolution atomic-force microscope implemented using an optical lever”, S. Alexander et al, *Journal of Applied Physics*, 65, pp. 164-167 (1989).
- 34 “Exploring Scanning Probe Microscopy”: Mat Publisher: John Wiley & Sons, D. Sarid (1997).
- 35 “Frequency modulation detection using high-Q cantilevers for enhanced force microscope sensitivity”, T.R. Albrecht et al, *T. R. Journal of Applied Physics* 69 (2): p. 668 (1991).
- 36 “Frequency Function in Atomic Force Microscopy Applied to a Liquid Environment”, Po-Jen Shih, *Sensors*, 14, pp. 9369-9379 (2014).
- 37 “The Chemical Structure of a Molecule Resolved by Atomic-Force Microscopy” L. Gross et al, *Science* 325 (5944), pp. 1110–1114 (2009).
- 38 “True atomic resolution by atomic force microscopy through repulsive and attractive forces”, F. Ohnesorge, G. Binnig, *Science* 260(5113), pp. 1451-1456 (1993).
- 39 “Magnetic Imaging by Force Microscopy with 1000Å Resolution”, Y. Martin et al, *Appl. Phys. Lett.* 50 (20), 1455–1457(1987).
- 40 “Quantitative measurement of the magnetic moment of individual magnetic nanoparticles by magnetic force microscopy”, S. Sievers et al, *Small*, 8, No. 17, pp. 2675–2679 (2012).
- 41 “Application of magnetic force microscopy in nanomaterials characterization” Lozanne A., *Microsc Res Tech.* 69(7), pp. 550-562 (2006).
- 42 “Precise force curve detection system with a cantilever controlled by magnetic force feedback”, Sh. Yamamoto et al, *Rev. Sci. Instrum.* 68, 4132 (1997).
- 43 “Probing Intermolecular Forces and Potentials with Magnetic Feedback Chemical Force Microscopy”, D. Ashby et al, *J. Am. Chem. Soc.* 122, pp. 9467-9472 (2000).
- 44 “Scanning Probe Techniques: MFM and SP-STM”, A. Swartz et al, *Universitat Hamburg, Hambur, Germany.*
- 45 “The use of MFM for investigating domain structures in modern permanent magnet materials”, L. Folks and R. C. Woodward, *JMMM* 190, pp. 28-41 (1998).
- 46 “Magnetic characterization of micropatterned Nd–Fe–B hard magnetic films using scanning Hall probe microscopy”, M. Kustov et al, *J. Appl. Phys.* 108, 063914 (2010).
- 47 “Analytical and numerical calculations of the magnetic force microscopy response: A comparison”, R. Engel-Herbert et al, *J. Appl. Phys.* 99, 113905 (2006).
- 48 http://www.budgetsensors.com/downloads/MagneticMulti75-G_Datasheet_EN.pdf
- 49 <http://www.nanosensors.com/Point-Probe-Plus-Magnetic-Force-Microscopy-Reflex-Coating-afm-tip-PPP-MFMR>.
- 50 <http://www.asylumresearch.com/Probe/AC160TS,Olympus>.
- 51 “High-coercivity Nd–Fe–B thick films without heavy rare earth additions”, N.M. Dempsey, T.G. Woodcock, H. Sepehri-Amin, Y. Zhang, H. Kennedy, D. Givord, K. Hono, O. Gutfleisch, *Acta Materialia* 61, pp. 4920-4927 (2013).
- 52 “Thermomagnetically patterned micromagnets”, F. Dumas-Bouchiat et al, *Appl. Phys. Lett.* 96, 102511 (2010)
- 53 “Quantitative determination of effective dipole and monopole moments of magnetic force microscopy tips ” J. Lohau, S. Kirsch, A. Carl, G. Dumpich, and E. F. Wassermann *Journal of Applied Physics* 86, 3410 (1999).
- 54 “The point dipole approximation in magnetic force microscopy”, U. Hartmann, *Phys. Lett. A* 137 pp. 475-478 (1989).
- 55 “Towards quantitative magnetic force microscopy: theory and experiment”, T. Häberle et al, *New J. Phys.* 14 043044 (2012).
- 56 “Fabrication and characterization of advanced probes for magnetic force microscopy”, P. Leinenbach et al, *Appl. Surf. Sci.* 144-145 492 (1999).
- 57 “Magnetic force microscopy sensors using iron-filled carbon nanotubes”, A. Winkler et al, *J. Appl.*

Phys. 99 104905 (2006).

58 “The advantages of the magnetic structure in ferromagnetic-film-coated carbon nanotube probes”, T. Manago et al, *Nanotechnology* 23 (2012).

59 “Optimal ferromagnetically-coated carbon nanotube tips for ultra-high resolution magnetic force microscopy”, Y. Lisunova et al, *Nanotechnology* 24 (2013).

60 “Nanoscale magnetic field mapping with a single spin scanning probe magnetometer”, L. Rondin L et al, *Appl. Phys. Lett.* 100 153118 (2012).

61 “Nanomagnets with high shape anisotropy and strong crystalline anisotropy: perspectives on magnetic force microscopy”, H. Campanella et al, *Nanotechnology* 22 (2011).

62 “Magnetic particle imaging with a cantilever detector”, J. W. Alldredge, J. Moreland, *Journal of Applied Physics* 112, 023905 (2012).

63 “A review of techniques for attaching micro- and nanoparticles to a probe’s tip for surface force and near-field optical measurements”, Y. Gan, *Review of scientific instruments* 78, 081101 (2007).

64 “Measuring the Force Gradient Acting on a Magnetic Microsphere above a Micro-Magnet Array”, S. Ponomareva et al, *Advanced Materials Research*, Vol. 872, pp. 167-173 (2014).

65 “Focused-Ion-Beam-Assisted Magnet Fabrication and Manipulation for Magnetic Field Detection Applications.”, H. Campanella and al, *Applied materials and interfaces*, Vol.1, pp 527-531(2009).

66 “Autonomous micro-magnet based systems for highly efficient magnetic separation”, L. F. Zanini et al, *Appl. Phys. Lett.* 99, 232504 (2011).

Chapter IV: Quantitative study of TMP sample action on a single magnetic (sub)micronic object

<u>IV. Quantitative study of TMP sample action on a single magnetic (sub)micronic object</u>	106
<u>IV.1 Definition of micromagnet array – magnetic microsphere system</u>	106
<u>IV.2 Simulations of magnetic interaction using CADES framework</u>	109
<u>IV.2.1 Modelling of micromagnet array</u>	109
<u>IV.2.2 Modelling of hard magnetic microsphere</u>	110
<u>IV.2.3 Modelling of superparamagnetic microsphere</u>	110
<u>IV.3 Micromagnet array mapping with Superparamagnetic Microsphere Probe</u>	111
<u>IV.3.1 Quantification of Force Gradient variation in <i>lateral</i> direction</u>	113
<u>IV.3.2 Quantification of Force Gradient variation in <i>vertical</i> direction</u>	115
<u>IV.3.3 Quantification of Force variation in <i>lateral</i> direction</u>	117
<u>IV.3.4 Quantification of Force variation in <i>vertical</i> direction</u>	119
<u>IV.3.5 Magnetic force density variation</u>	122
<u>IV.4 Micromagnet array mapping with Hard Magnetic Microsphere probe</u>	124
<u>IV.4.1 Effect of probe magnetization orientation</u>	127
<u>IV.4.2 Experimental prospective to explore non-symmetrical behaviour of MJ</u>	129
<u>IV.4.3 <i>Vertical</i> variation of force intensity above a symmetric MJ</u>	131
<u>IV.4.4 Magnetic force density variation</u>	132
<u>IV.5 Summary</u>	134
<u>References</u>	136

IV. Quantitative study of TMP sample action on a single magnetic (sub)micronic object

This chapter presents our experiments demonstrating direct quantitative measurements of trapping force between a single magnetic microsphere and a TMP micromagnet array using smart custom-made Magnetic Microsphere Probes (superparamagnetic or NdFeB microspheres). To complete the analysis of experimental results, simulations have been performed and their combinations address several objectives:

- To map the intensity variation of magnetic interaction according to the microsphere-magnetic junction (MJ) distance.
- To identify the nature (attractive, repulsive or mixed) of the force exerted by TMP sample on the microsphere according to their magnetic properties.
- To identify the origin of the difference between the MJ widths measured by Microsphere Scanning Force Microscopy (MSFM) and previous measurements [1].
- To identify and to quantify the magnetic roughness on reverse zone (RZ) and non-reversed zone (NRZ).
- To study the effect of the microsphere magnetic volume on trapping force.
- To study the non-symmetrical signals measured above two neighbouring (RZ/NRZ and NRZ/RZ) interfaces with hard magnetic microsphere probe.

Through this study, specific information has been deduced about TMP sample properties that were not observed before. This will be discussed throughout this chapter composed in five main sections.

IV.1 Definition of micromagnet array – magnetic microsphere system

In the previous chapters it was demonstrated that magnetic field and field gradient produced by TMP micromagnet array decay fast with the distance (see the results of SHPM in section II.2.5 and simulations in Annex II.3). Thus, the distance between magnetic sample and bottom of magnetic microsphere probe, $D_{s/m}$ should be defined precisely. For thermomagnetically patterned NdFeB films used in our experiments it is not that straightforward due to the surface roughness (non-magnetic Nd-rich bumps). The separating distance $D_{s/m}$ for contact/lift mode measurements is composed by several parameters that are not constant during the mapping process (Figure 4.1).

Firstly, deflection of the cantilever during the first pass, Δz_{sp} should be considered. It can be positive, negative or equal to zero according to the value set by an AFM operator: negative cantilever deflection corresponds to an attractive interaction between probe and sample; positive deflection corresponds to a repulsive interaction. For our experiments we have chosen $\Delta z_{sp} = 0$ corresponding to zero cantilever bending to simplify the calculations of separation distance $D_{s/m}$. Figure 3.7 illustrates cantilever vertical deflection Δz_{sp} according to the distance from the sample surface.

Secondly, cantilever deflection measured during the second MFM pass, Δz should be taken into account: negative cantilever deflection corresponds to an attractive magnetic interaction between probe and sample ($\Delta z < 0$ for F_{attr}); positive deflection corresponds to a repulsive magnetic interaction ($\Delta z > 0$ for F_{rep}). The sign and the value of Δz will vary during the second pass according to the magnetic interaction.

Thirdly, the Lift Scan Height (*LSH*) distance should be considered. With the commercial microscopes *LSH* can varies from tens of nanometres up to few microns. This value is fixed for an MFM image but can vary from one image to another.

Fourthly, the non-magnetic Nd-rich bumps (appearing on the annealing step of the film fabrication) with the height comparable to LSH , h_{Nd} up to $1\ \mu\text{m}$ enlarge the distance $D_{s/m}$. This value depends on scanned area.

Finally, the non-magnetic capping layer of Ta, h_{Ta} (usually about $100\ \text{nm}$) has to be included in the distance $D_{s/m}$.

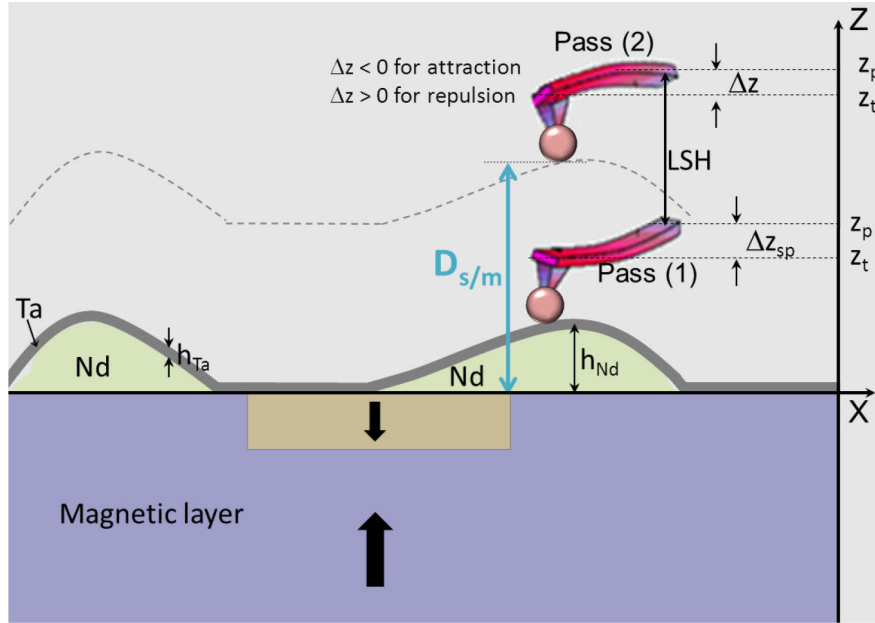


Figure 4.1. Micromagnet array – magnetic microsphere probe system: $D_{s/m}$ is the distance between bottom of magnetic sphere and top of magnetic layer; Δz_{sp} is the vertical cantilever deflection due to set point chosen for the first pass; Δz is the vertical cantilever deflection recorded during the second MFM pass, LSH is the lift scan height used for the MFM pass, h_{Nd} is the height of Nd-rich bumps and h_{Ta} is the thickness of the Ta capping layer.

Taking into account the foregoing, the separation distance $D_{s/m}$ was considered as a distance between top of TMP magnetic layer and bottom of magnetic microsphere attached to the probe:

$$D_{s/m} = LSH + \Delta \bar{z}_{sp} + \Delta \bar{z} + h_{Nd} + h_{Ta} \quad (4.1)$$

Equation (4.1) holds for superparamagnetic and NdFeB microsphere probes and the variables can be found as follows: LSH is set by an AFM operator (in our experiments in static mode LSH varies from 0.5 up to $2.8\ \mu\text{m}$), $\Delta \bar{z}_{sp}$ is set by an AFM operator (in our experiments in static mode $\Delta \bar{z}_{sp} = 0$), $\Delta \bar{z}$ is measured during the second MFM pass (depends on the magnetic volume and properties of the attached microsphere), h_{Ta} is defined by the sample fabrication procedure ($100\ \text{nm}$ for NdFeB TMP films) and the height of Nd-rich features h_{Nd} (up to $1\ \mu\text{m}$) can be measured during the first topography pass in MFM mode.

Due to TMP sample roughness, the separation distance $D_{s/m}$ is different for each point of measurements: $D_{s/m}$ above a bump is much higher (up to a factor of 10) than above a flat part of the sample. Thus, the magnetic interaction measured at the fixed LSH corresponds to different separation distances in different points of the scanned area. To avoid this problem specific data treatment process has been applied to all MFM maps in order to keep only the zones free of bumps ($h_{Nd} \approx 0$).

Figure 4.2 presents main steps of the data processing for topography and MFM images obtained with $3.5\ \mu\text{m}$ superparamagnetic microsphere probe at $LSH = 700\ \text{nm}$. Firstly, for topography image (Figure 4.2a) obtained during the first MFM pass the height distribution graph is plotted (Figure 4.2b). It exhibits bimodal distribution: first high narrow peak corresponds to the flat part of the sample, while second, large peak corresponds to the regions with Nd-rich bumps. Secondly, using commercial software for AFM image treatment (for example, Gwyddion) a special mask (green area in Figure 4.2c) is applied on the topography

image to keep only the part of the sample free of Nd-rich features. Thirdly, thanks to a custom-made dedicated program, the same mask is applied to MFM image (Figure 4.2d,e) and the average deflection profile for regions free of bumps is calculated (Figure 4.2f). The detailed procedure of the data treatment is described in Annex IV.1.

In Figure 4.2f cantilever deflection Δz_{raw} is calculated as a difference between deflection above the MJ (where its intensity is maximal) and above the NRZ (where magnetic roughness is minimal). The increase of the cantilever deflection after the data treatment, Δz_{corr} is about 15% compared to the raw data Δz_{raw} above the magnetic junction. The explanation relies on the fact that the corrected profile was calculated only for regions where $h_{Nd} \approx 0$, thus, the separation distance is constant and lower than for non-treated image, where $h_{Nd} > 0$. The shape of the corrected deflection curve is similar to the raw data one, but less smooth because the points corresponding to Nd-rich bumps were removed after the mask application. One can notice that increase of magnetic roughness is mainly observed above the RZ (left part in Figure 4.2f). A possible explanation relies on the fact that Nd-rich features increase the separation distance thus, diminishing the influence of RZ magnetic roughness appearing during TMP fabrication step (magnetization reversal). Thereby, removal of Nd-rich bumps (classically considered as non-magnetic) leads to a stronger signal of magnetic inhomogeneity above the RZ.

The procedure of data treatment has been applied to all MFM maps obtained with magnetic microsphere probes. The force versus distance $D_{s/m}$ curves for both types of spheres above a magnetic junction were plotted using the mean deflection cross section (Figure 4.2f) obtained from each corrected MFM map. They will be presented after detailed discussion of the associated simulations.

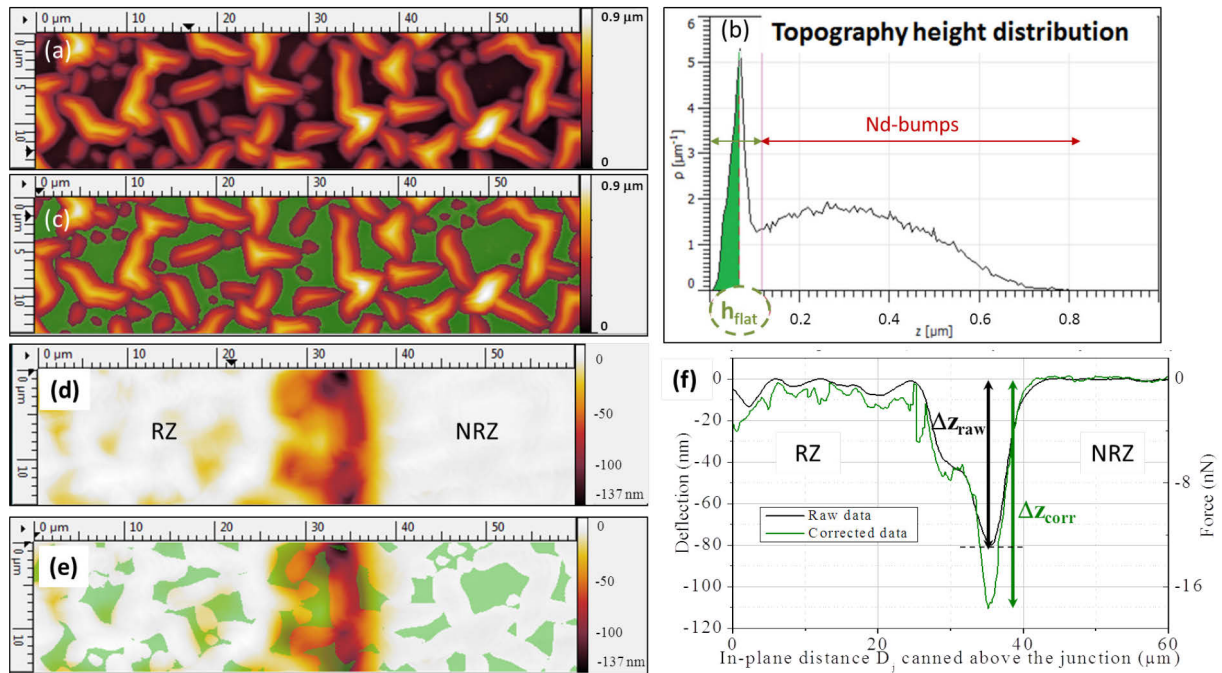


Figure 4.2. Data processing: (a) Topography image; (b) Topography height distribution: first peak corresponds to the flat part of the sample, second peak to the Nd-rich bumps; (c) Mask application on the topography image: green area corresponds to the part of the sample free of Nd-rich bumps; (d) Raw MFM deflection image; (e) Mask application on the MFM deflection image to remove the bumps. Green areas correspond to the data used for the corrected deflection profile plot. (f) Mean deflection profiles for raw (black line) and corrected (green line) experimental data obtained with 3.5 μm superparamagnetic probe at $LSH = 700$ nm in static MFM mode.

IV.2 Simulations of magnetic interaction using CADES framework

There are three main approaches to calculate a field from a magnet:

- to apply the Amperian approach (bound currents) where the magnetization is replaced by an equivalent distribution of current density;
- to apply the Coulombian approach (equivalent charges) where the magnetization is replaced by an equivalent distribution of magnetic charge;
- to calculate the dipole field by integrating over the volume distribution of magnetization.

These approaches are detailed in Annex II.2. From the computation point of view the choice of an approach depends on the sample geometry. Usually for the solid of revolution (for example, cylinder) magnets Amperian approach is used while Coulombian approach is applied for modelling of solid bodies of parallelepiped shape.

In our experiments, only parallelepiped TMP magnets were used. Thus, for calculations of magnetic field/force produced by micromagnet array Coulombian equivalent surface charge approach using pure analytical formulas was implemented.

The next section describes the main aspects and parameters range¹ taken into account in the simulations of the TMP micromagnet array, the hard magnetic microsphere and the superparamagnetic microsphere.

IV.2.1 Modelling of micromagnet array

The micromagnet array was modelled as a set of 20 regular lines (RZs) of 1 cm length and 50 μm width located in the middle of the film (NRZ). The whole film was assumed to have the shape of a parallelepiped of width and length equal to 2 cm with thickness t of 5 μm . Taking into account that magnetization of the irradiated zone cannot overcome the initial film magnetization, the magnetization $\mu_0 M_d$ of RZ and $\mu_0 M_{up}$ of NRZ were varied respectively from 0.6 to 1.2 T and from 1 to 1.2 T; the thickness h_r of RZ was varying from 0.9 to 1.3 μm according to the previous characterization (Section II.2.5).

Magnetic field arising from the micromagnet sample has been computed by applying Coulombian equivalent surface charge approach using pure algebra equations, based on sample geometry [2,3]. To underline the effect of separation distance $D_{s/m}$ on magnetic interaction, the graphical representation of magnetic field z-component, B_z above the magnetic junction is presented in Figure 4.3. On this graph, we can notice that due to non-linearity of the curve, when the distance increases by a factor of 10 (from 0.1 to 1 μm), the magnetic field intensity decreases by a factor of 6.

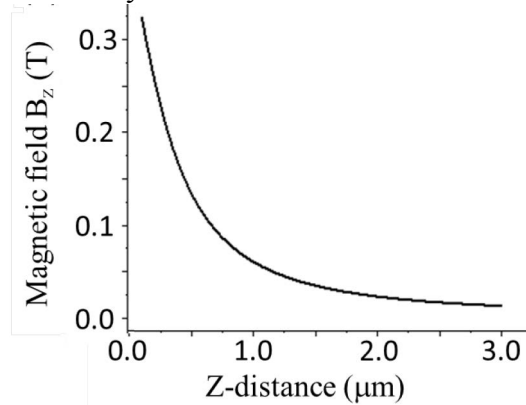


Figure 4.3. Z-component of magnetic field above the magnetic junction in a function of distance $D_{s/m}$ calculated with Model 2.

¹ Unless otherwise stated, the average values to model TMP sample have been used: NRZ magnetization $\mu_0 M_{up} = 1.1$ T, RZ magnetization $\mu_0 M_d = 0.9$ T, RZ thickness $h_r = 1.1$ μm .

IV.2.2 Modelling of hard magnetic microsphere

To match with CADES capabilities, NdFeB microsphere is modelled as a cubic permanent magnet of equal volume. For a sphere of radius R a cube with the side $a = 1.6 R$ was chosen (Figure 4.4a).

The microsphere magnetization $\mu_0 M_{sph}$ was taken as uniform and fixed in direction, it varies from 0.73 T up to 0.76 T according to the manufacture' specification [4]. Initially the direction of magnetization is assumed antiparallel to NRZ magnetization, but can be tilted by an angle, θ . This angle option is required to simulate the experimental tilt inherent to the AFM probe holder setup or sample.

Magnetic field arising from the microsphere has been computed by applying Coulombian equivalent surface charge approach using pure algebra equations, based on cubic geometry.

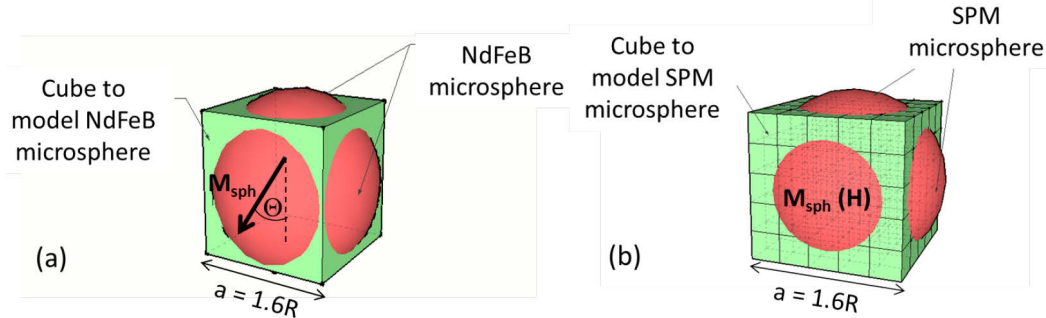


Figure 4.4. Modelling of (a) NdFeB microsphere and (b) superparamagnetic microsphere in CADES framework.

IV.2.3 Modelling of superparamagnetic microsphere

To model the behaviour of superparamagnetic microsphere, it was considered that:

- (1) iron oxide nanoparticles (NPs) are not free to move inside the polystyrene matrix (their distribution remains homogenous during all the experiments, Annex III.3);
- (2) field $B \approx 0.1$ T is enough to saturate the magnetization of the NPs along the direction of applied magnetic field.

For our simulations superparamagnetic sphere was modelled as a cube of equal volume. For a sphere of radius R a cube with the side $a = 1.6 \times R$ was chosen. With this approach sphere material is discretized along the X, Y and Z axes, then the Method of Moments (MoM) is applied to compute a uniform induced magnetization in each elementary block [5,6] (Figure 4.4b). When the magnetization for each element is calculated by Coulombian approach, the total magnetic field produced by the whole volume can be found as a superposition of magnetic fields produced by each elementary unit (Figure 4.5).

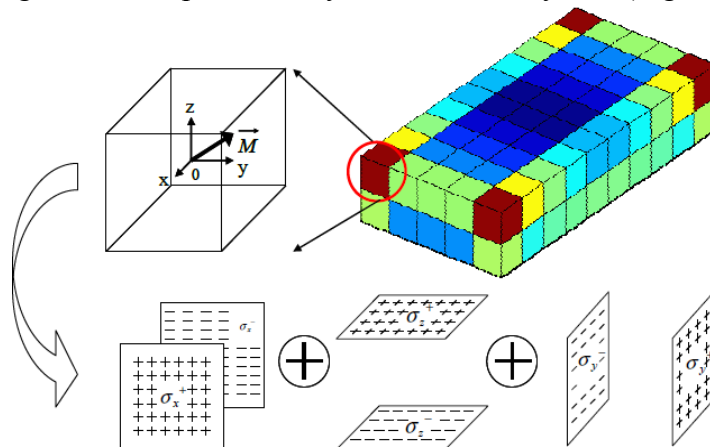


Figure 4.5. Modelling of ferromagnetic material (discretized) by Coulombian approach when the magnetization of each elementary block is calculated [6].

We discretized the cube volume by N^3 elementary cubes with uniform induced magnetization for each one (Figure 4.4b). In practice, we chose N equals to 5 because this value provides force intensity value close to the one obtained with higher N , but does not lead to dramatic increase of the computation time (the computation time increases from 7 min for $N = 5$ up to 45 min for $N = 6$ with the changes in the force by less than 1% for a sphere of 1.5 μm diameter). In order to take into account the distribution of the superparamagnetic inclusions in the microsphere (magnetic volume of all the inclusion inside a superparamagnetic microsphere, V_m , see Table 4.1 and Annex III.3), the force obtained by the simulation has to be reduced to percentage of the volume V_m of the calculated value.

With this program, magnetic field arising from the sample and microsphere, as well as the force intensity between them can be calculated. Detailed manual explaining how to use the program for simulation of systems with superparamagnetic and NdFeB microspheres above a TMP micromagnet array is presented in Annexes II.4 and II.5.

IV.3 Micromagnet array mapping with Superparamagnetic Microsphere Probe

Table 4.1 resumes the experimental characteristics of superparamagnetic microsphere probes used to perform force and force gradient mapping of TMP micromagnet array. For each superparamagnetic sphere the magnetic volume (vol.%) and total weight of magnetic nanoinclusions (wt.%) were calculated based on the sphere diameter (measured by SEM) and average density (measured by supplier for a number of spheres from the same set by pycnometry and sedimentation experiments) (Annex III.3). In practice the magnetic volume and weight can vary for the spheres of the same type, but in our experiments we consider the fixed values presented in Table 4.1. According to our calculations (based on the data provided by supplier, Annex III.3) fast decrease of magnetic weight and volume is observed with increase of the sphere diameter.

Figure 4.6 illustrates topography, MFM (phase and deflection) images and associated mean (phase and deflection) profiles of TMP micromagnet array (out-of-plane magnetization) with 50 μm width stripes pattern scanned with *superparamagnetic microsphere probes*. Measurements presented in Figure 4.6 (a,c,e) were carried out in dynamic mode with 2.85 μm microsphere probe, while results displayed in Figure 4.6 (b,d,f) were obtained in static mode with 1.5 μm microsphere probe. The MFM images and associated mean profiles (phase and deflection) are similar to those obtained with commercial probes with magnetically soft coating: two dark lines corresponding to negative phase shift or deflection (Figure 4.6 e,f) are observed above the magnetic junctions (MJ_1 and MJ_2 in Figure 4.6 c,d).

Cantilever type	Fabrication	Sphere diameter ² (μm)	Cantilever spring constant ³ (N/m)	Magnetic NPs ⁴		Sphere volume (μm^3)		Resonance frequency ² (kHz)	Quality factor ²
				wt. %	vol. %	total	magnetic		
NSC 15, MikroMasch	AFM	2.85	50.3	40	13	12.08	1.57	200	1051
PL2-CONTR, Nanosensors	FIB	0.29	0.167	73	35	0.013	0.005	12	56.4
PL2-CONTR, Nanosensors	FIB	1.5	0.15	67	30	1.77	0.53	12.02	53.5
PL2-CONTR, Nanosensors	FIB	3.5	0.16	40	13	22.46	2.92	12.21	58.1

Table 4.1. List of superparamagnetic microsphere probes.

² Microspheres diameter was measured by Scanning Electron Microscopy.

³ Cantilever spring constant, resonance frequency and quality factor were measured by thermal tune method.

⁴ The information about magnetic NPs volume and weight is derived from the data provided by supplier.

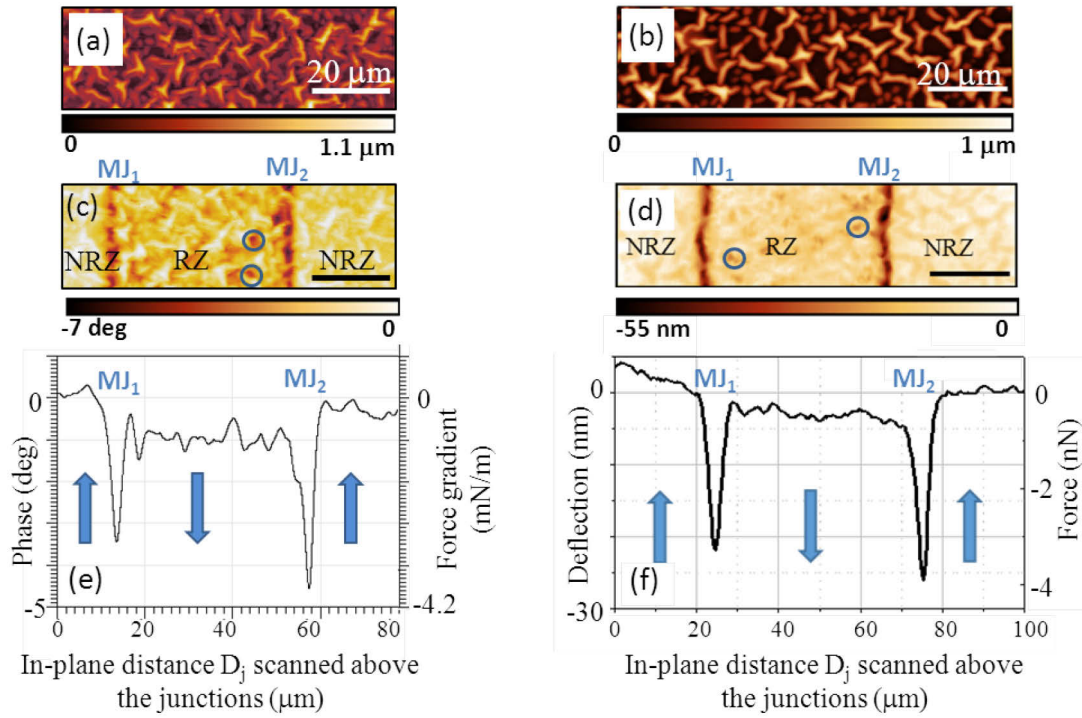


Figure 4.6. Topographical (a, b), MFM (c,d) images and associated mean phase/deflection profiles (e,f) of the NdFeB micromagnet array scanned with 2.85 and 1.5 μm superparamagnetic microsphere probes respectively at $LHS = 600$ nm. MJ_1 is the magnetic junction between NRZ and RZ; MJ_2 is the magnetic junction between RZ and NRZ. Some examples of local variation in magnetic signal inside the RZ (c, d) are marked with blue circles. Lateral scale bar is 20 μm .

On MFM images and associated mean profiles (Figure 4.6c,e phase, Figure 4.6d,f deflection) NRZ and RZ can be distinguished due to higher magnetic roughness for RZ.

For experiments carried out with 2.85 μm microsphere probe in dynamic mode the RZ exhibits magnetic inhomogeneity of about 2 times higher than NRZ (1.1 deg and 0.5 deg, respectively). The local variations of magnetic signal in RZ (inside blue circles in Figure 4.6c) are so strong that can overcome the average phase shift above the MJ (6.65 deg and 4.3 deg, respectively).

On the MFM maps obtained in static mode with 1.5 μm microsphere probe the RZ exhibits magnetic inhomogeneity higher than NRZ by a factor of 1.5 (3.5 nm and 2.3 nm, respectively). Similar results are observed for 3.5 μm microsphere: the ratio between magnetic roughness for NRZ and RZ is 1.3 (16.9 nm and 13.5 nm, respectively). The local variation of magnetic signal inside RZ (inside blue circles in Figure 4.6d for 1.5 μm microsphere) is comparable to the average deflection shift above the MJ (21 nm and 23.5 nm for 1.5 μm microsphere; 56.2 nm and 63.1 nm for 3.5 μm microsphere, respectively).

The information about magnetic roughness and phase/deflection shift above the MJ is summarized in Table 4.2.

These results demonstrate that the force and its gradient exerted by micromagnet array are always respectively attractive and positive. This behaviour is the signature that the stray field arising from a micromagnet sample magnetizes the probe material and its magnetization is matching the magnetic field lines of the sample.

	2.85 μm superparamagnetic microsphere probe		1.5 μm superparamagnetic microsphere probe		3.5 μm superparamagnetic microsphere probe	
	NRZ	RZ	NRZ	RZ	NRZ	RZ
Average magnetic roughness⁵ \pm RMS	0.5 \pm 0.5 deg (0.4 \pm 0.4 mN/m)	1.1 \pm 1 deg (0.88 \pm 0.8 mN/m)	2.3 \pm 2 nm (0.35 \pm 0.3 nN)	3.5 \pm 3 nm (0.53 \pm 0.45 nN)	13.6 \pm 2.1 nm (2.2 \pm 0.3 nN)	16.9 \pm 10.4 nm (2.7 \pm 1.7 nN)
Max value⁶	3.3 deg (2.64 mN/m)	6.65 deg (5.32 mN/m)	13.2 nm (2 nN)	21 nm (3.2 nN)	14.6 nm (2.3 nN)	56.2 nm (9 nN)
Shift above MJ₁	3.3 deg (2.64 mN/m)		23.5 nm (3.5 nN)		63.1 nm (10.1 nN)	
Shift above MJ₂	4.3 deg (3.44 mN/m)		25.3 nm (3.8 nN)		79.8 nm (12.8 nN)	

Table 4.2. Characteristics of a TMP sample mapped with 2.85 μm , 1.5 μm and 3.5 μm superparamagnetic microsphere probes at $LHS = 600$ nm.

Relevant information about the sample properties and the sorting process:

Based on this first set of results we can conclude that the TMP process leads to inhomogeneity in magnetic properties of reversed zones (the local variations of magnetic signal are in the same range as the average phase (deflection) shift observed above the magnetic junctions). These local variations are detectable with all our custom-made AFM magnetic sphere probes.

Thus, some points inside RZs can act as additional isolated magnetic traps: this explains why during object trapping/sorting experiments (Figure 2.16 of Chapter II), some particles are trapped out of the MJs. To minimize this effect TMP fabrication procedure should be improved and/or the microfluidic device has to be adjusted through various parameters: fluid flow, height of the channel and so on. Nevertheless, the average magnetic roughness inside the RZs is less strong than the average signal above the MJs (7 times less for static mode MFM); this is why an increase of the liquid flux can remove most the microspheres captured outside the MJs (Figure 2.17 of Chapter II).

IV.3.1 Quantification of Force Gradient variation in *lateral* direction

Figure 4.7 presents two experimental phase profiles obtained with 0.29 μm (blue) and 2.85 μm (red) superparamagnetic spheres at fixed $LSH = 300$ nm in vicinity of MJ. The MJ widths at the half-height (Figure 4.8a) for 2.85 μm and 0.29 μm are respectively 3.65 μm and 2.1 μm . The ratio between these values ($3.65/2.1 = 1.7$) remains unchanged with increase of LSH , confirming that this ratio is sphere-size dependent.

⁵ Average magnetic roughness is the difference between the maximum positive and negative values for the average phase (or deflection) profile.

⁶ The maximum was found for the whole RZ or NRZ area (not for an average profile) while the minimum was set to zero.

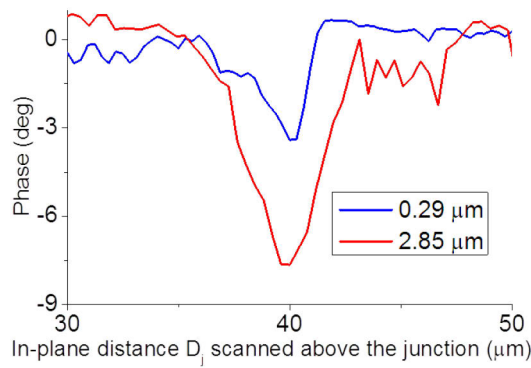


Figure 4.7. MFM phase profiles obtained with 0.29 μm (blue) and 2.85 μm (red) superparamagnetic microsphere probes at $LSH = 300 \text{ nm}$.

In previous studies [1] it was demonstrated that the effective width of magnetic junction is given by the grain size (few hundred nanometres). Enlargement of MJ width observed with microparticle probe can be explained by the tip-sample convolution effect: the lateral resolution of an MFM image is determined by the combination of finite size of the tip apex and the local physical (morphological and magnetic) properties of the sample surface. The “effective” part of the tip could vary between the topographic and magnetic maps: the topographic resolution is directly link with the size of the sphere while the magnetic one is linked with the size of the sphere and distribution of magnetic NPs inside it (i.e. the magnetic volume).

The graphical representation of the magnetic junction width measurements and tip-sample convolution effect are presented in Figure 4.8. The phase shift $\Delta\varphi$ (the difference between $\Delta\varphi = 0$ and $\Delta\varphi = \text{max}$) was measured above the centre of magnetic junction (vertical dashed blue line) and the width of magnetic junction at half-height was measured at distance $\Delta\varphi/2$. Figure 4.8b illustrates the effect of the magnetic microsphere diameter on the width of magnetic junction. As soon as a part of the sphere containing magnetic NPs is affected by z-component of magnetic field in vicinity of magnetic junction (sphere position (1)) cantilever phase shift is induced by attractive magnetic forces. It reaches its maximum ($\Delta\varphi = \text{max}$) when the centres of the sphere and the MJ are aligned (vertical dashed blue line, sphere position (2)); following displacement of the sphere (position (3)) drops down cantilever phase shift. It means that for a fixed magnetic distribution of NPs inside a sphere (magnetic density) MFM phase measurements with a microsphere of bigger size display higher magnetic junction width at the half-height.

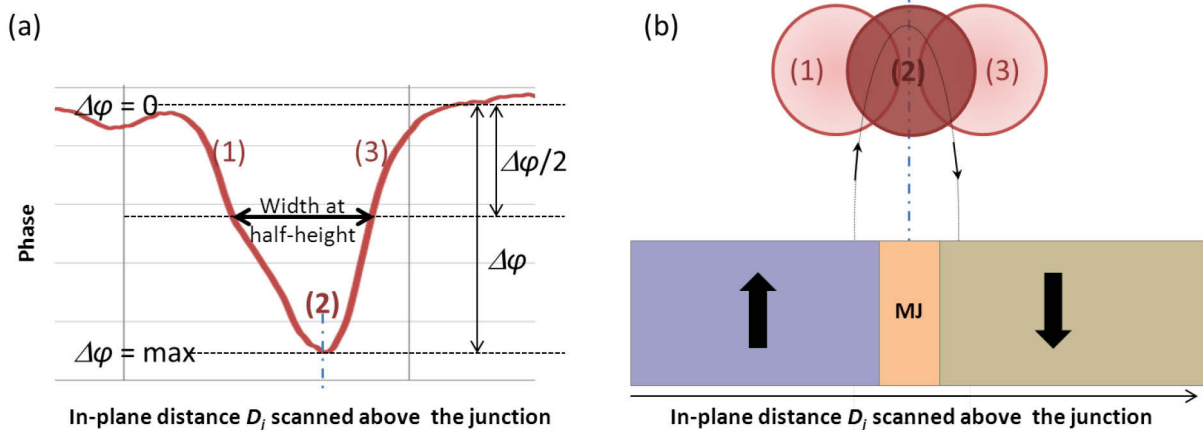


Figure 4.8. (a) The measurements of magnetic junction width at the half-height from MFM phase image. (b) Schematics of an effect of magnetic microsphere diameter on the width of magnetic junction: (1) magnetic microsphere is in vicinity of magnetic junction (MJ) and starts to be affected by z-component of magnetic field; (2) centres of magnetic microsphere and MJ are aligned; (3) magnetic microsphere is moving away from MJ.

IV.3.2 Quantification of Force Gradient variation in vertical direction

To quantify the interaction between superparamagnetic microsphere and TMP micromagnet array, MFM maps were collected for different LSH in dynamic mode. The measurements have been conducted with two different sizes of superparamagnetic probes: $0.29\ \mu\text{m}$ and $2.85\ \mu\text{m}$. For both probes, phase images in dynamic mode have been recorded for LSH ranging from $0.2\ \mu\text{m}$ up to $0.8\ \mu\text{m}$ with a step of $0.1\ \mu\text{m}$. Figure 4.9 displays three average cross-sections deduced from MFM phase images obtained with $0.29\ \mu\text{m}$ (a) and $2.85\ \mu\text{m}$ (b) superparamagnetic probes for three LSH (300, 600 and 800 nm).

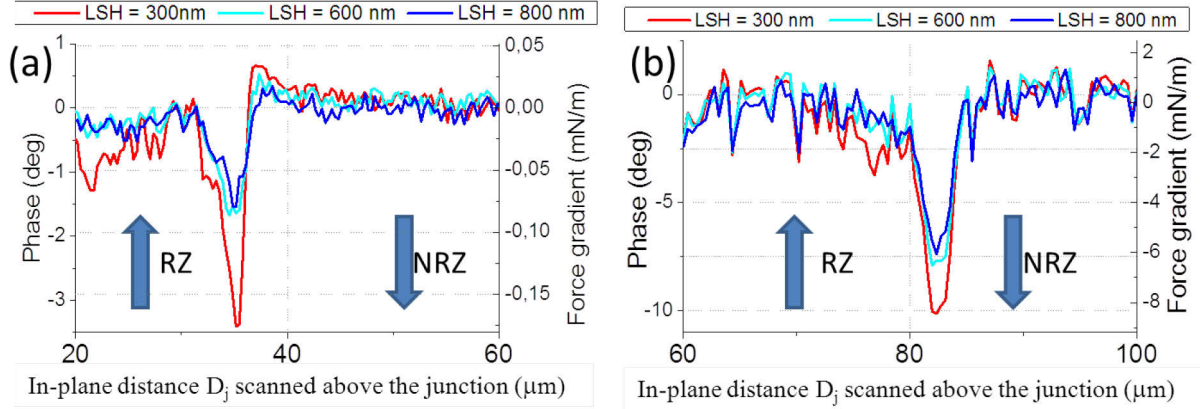


Figure 4.9. The average cross-sections of MFM (phase) images for LSH of 300, 600 and 800 nm obtained with (a) $0.29\ \mu\text{m}$ and (a) $2.85\ \mu\text{m}$ superparamagnetic microsphere probes in dynamic mode.

From the experimental MFM phase profiles force gradient can be found according to the equation:

$$\frac{\partial F}{\partial z} = -\Delta\varphi \frac{k}{Q}, \quad (4.2)$$

where $\Delta\varphi$ is the phase shift of the cantilever vibration, k and Q are the cantilever spring constant and quality factor, respectively. For both microspheres the decrease of the measured MFM phase shift with increase of LSH (and therefore the separation distance $D_{s/m}$) demonstrates the drop of force gradient above the MJ. The phase shift intensity increases with the sphere size ($\Delta\varphi(2.85\ \mu\text{m})/\Delta\varphi(0.29\ \mu\text{m}) = 2.9$ for $LSH = 300\ \text{nm}$) as well as the average magnetic roughness (for NRZ $\Delta\varphi_R(2.85\ \mu\text{m})/\Delta\varphi_R(0.29\ \mu\text{m}) = 1.5$; for RZ $\Delta\varphi_R(2.85\ \mu\text{m})/\Delta\varphi_R(0.29\ \mu\text{m}) = 1.25$). These two observations demonstrate that the phase shift and magnetic roughness signals are sphere dependent (depend on the sphere diameter and magnetic NPs distribution) and linked with the magnetic properties of the sample.

To characterize magnetic interaction between TMP sample and superparamagnetic microsphere as a function of distance, the MFM maps have been recorded for different LSH ranging from 0.2 up to $0.8\ \mu\text{m}$ with a step of $0.1\ \mu\text{m}$. Based on experimental data, the curve of magnetic force gradient versus the distance⁷ between top of magnetic layer above the magnetic junction and centre of superparamagnetic microsphere was plotted for $2.85\ \mu\text{m}$ and $0.29\ \mu\text{m}$ superparamagnetic probes (Figures 4.10a and 4.10b respectively, black line with circles). For $2.85\ \mu\text{m}$ sphere two numerical curves (obtained using Model 1) corresponding to the calculation considering the location of the microsphere exactly at the tip apex (red dash line) and considering a gap of $0.5\ \mu\text{m}$ between the tip apex and microsphere centre (blue dash line) along the z direction are presented. This assumption of the gap between tip apex and microsphere was done after noticing by SEM images that for all microparticle probes fabricated by the first approach (using AFM instrument) tip apex is free of glue and magnetic

⁷ The measurements have been conducted in dynamic mode, thus the average position of the sphere center during the oscillations was chosen. This assumption can be applied because the oscillation amplitude is much lower than the separation distance due to LSH .

Chapter IV: Quantitative study of TMP sample action on a single magnetic (sub)micronic object
 microsphere is in its vicinity (Figure 4.11). The fitting of experimental curve for 0.29 μm microsphere does not require the consideration of a gap. Unlike the 2.85 μm microsphere probe, this one was produced by FIB technique allowing precise sphere positioning at the tip apex (Annex III.4).

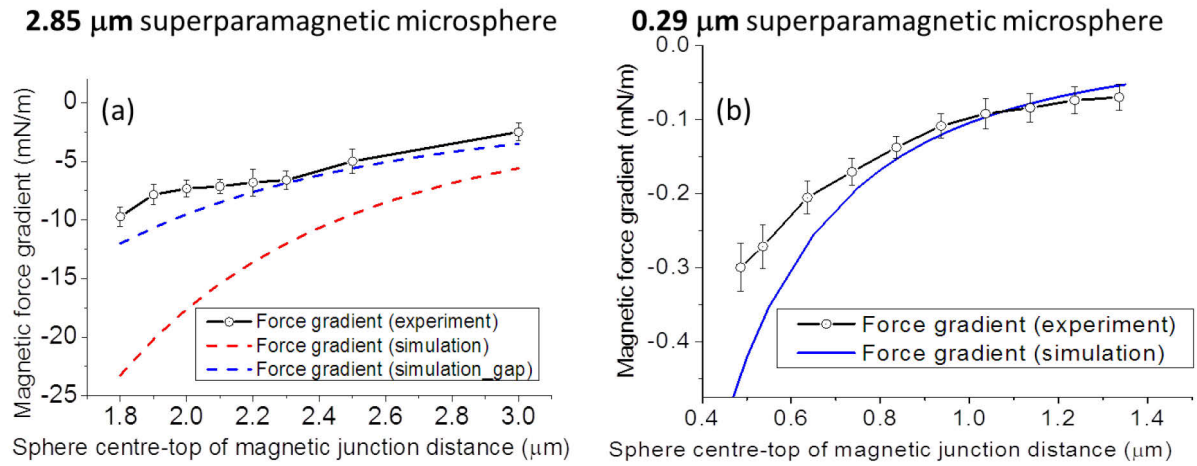


Figure 4.10. Magnetic force gradient versus distance between top of magnetic junction and centre of (a) 2.85 μm and (b) 0.29 μm superparamagnetic microsphere. Black solid lines with circles correspond to the experimental data. In (a) red dash line corresponds to the simulation for a magnetic microsphere located at the tip apex while blue dash curve corresponds to the simulation with a gap of 0.5 μm between the tip apex and the microsphere. In (b) blue line corresponds to the simulation where the magnetic microsphere is located at the tip apex. Theoretical curves are calculated with $\mu_0 M_{up} = 1.1 \text{ T}$, $\mu_0 M_d = 0.9 \text{ T}$, $h_r = t = 1.1 \mu\text{m}$.

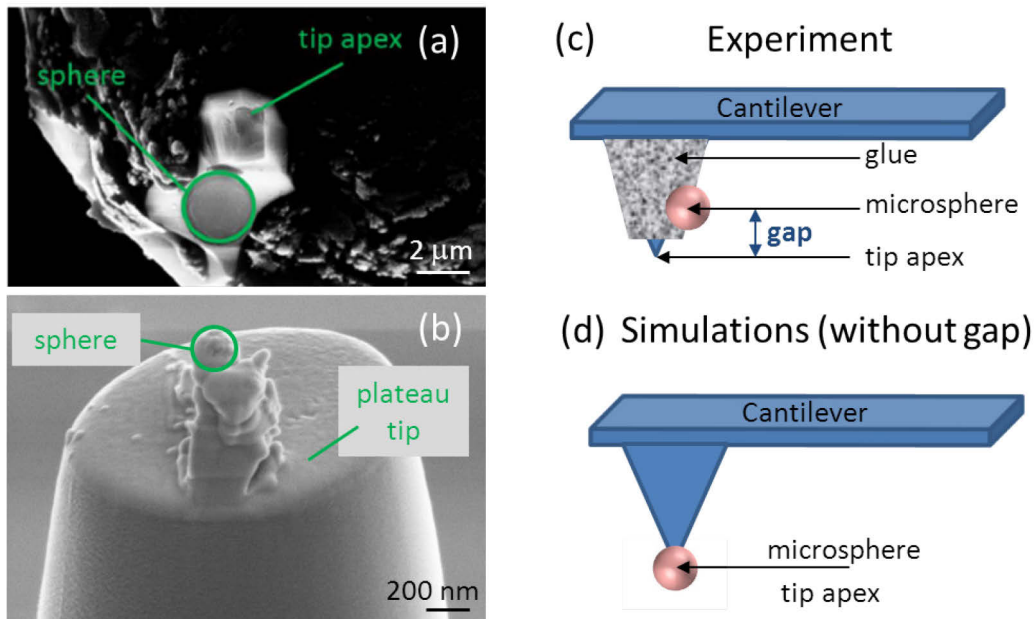


Figure 4.11. (a) SEM image of an AFM probe with glued 2.5 μm superparamagnetic microsphere: tip apex is free of glue and sphere is located in its vicinity. (b) SEM image of an AFM plateau tip with fixed 0.29 μm superparamagnetic microsphere thanks to FIB capability. (c) Sketch of the microsphere positioning for the probe used in experiments: the distance between tip apex and centre of the sphere is the so-called gap. (d) Sketch of the model used for simulations without taking into account the gap (red dash line in Figure 4.10a).

Force Gradient measurements with Superparamagnetic Microsphere Probe: Summary

The conducted MFM experiments demonstrate the possibility to characterize quantitatively the interaction between magnetic sample and a single (sub)micron-size magnetic object using smart microparticle probes. The first quantitative measurements (force

Chapter IV: Quantitative study of TMP sample action on a single magnetic (sub)micronic object gradient) of the interaction exerted by TMP micromagnet array on a superparamagnetic microsphere are summarized in Table 4.3.

	2.85 μm microsphere	0.29 μm microsphere
Separation distance ⁸ (μm)	From 1.8 up to 3	From 0.5 up to 1.1
Force gradient (mN/m)	From 9.7 down to 2.5	From 0.3 down to 0.07

Table 4.3. Force gradient measurements with 2.85 μm and 0.29 μm superparamagnetic microsphere probes.

Based on experimental results, we can conclude that the force gradient measured with superparamagnetic probe is always positive and varies significantly near the MJ in both lateral and vertical directions. It depends on the sphere size and distribution of magnetic nanoinclusions inside it. The detected width of MJ varies due to the tip(sphere)-sample convolution effect (for 2.85 μm superparamagnetic microsphere probe the MJ width is about 2 times higher than for 0.29 μm microsphere probe). The vertical variation of the force gradient changes significantly with increase of the sphere-MJ gap and has a correct matching with the simulation model.

Comparison of experimental and numerical results underlines the importance of precise sphere positioning to define correctly the sphere-sample distance.

To complete the information about interaction between superparamagnetic micro-object and TMP sample, MFM maps in static mode should be recorded to reveal the trapping force exerted by TMP sample on a single magnetic object.

IV.3.3 Quantification of Force variation in *lateral* direction

Magnetic force (as well as magnetic force gradient) intensity detected by superparamagnetic microsphere probe is stronger in the vicinity of magnetic junction; this corresponds to the domain wall where magnetic field gradient $\nabla\vec{H}$ is maximal and it leads to a higher magnetic force \vec{F}_m acting on a microsphere according to the equation (4.3) (Annex IV.2):

$$\vec{F}_m(r) = \mu_0 V_{sph} (\vec{M}_{sph} \nabla) \vec{H}_{MMA}(r), \quad (4.3)$$

where μ_0 is the permeability of the free space, \vec{M}_{sph} is the magnetization of the microsphere, V_{sph} is the magnetic volume of the microsphere; \vec{H}_{MMA} is the external field induced by micromagnet array and r is the space position.

To determine the effect of the sphere size on magnetic force measurements in static mode we recorded cantilever deflection at the fixed distance ($LSH = 700$ nm) above the magnetic junction with 1.5 and 3.5 μm superparamagnetic microspheres (Figure 4.12).

The dash profiles represent experimental measurements of the cantilever deflection translated into the force for 1.5 μm (blue) and 3.5 μm (red) superparamagnetic microsphere probes while solid lines correspond to the simulation performed in CADES framework. For simulations following parameters to describe micromagnet array properties were chosen (section IV.2.1): magnetization of NRZ is $\mu_0 M_{up} = 1.1$ T, magnetization of RZ is $\mu_0 M_d = 0.9$ T and thickness of RZ is $h_r = 1.1$ μm . Both simulated and experimental (raw data) curves exhibit similar behaviour and impact of the microsphere size on magnetic junction width is observed. Indeed, for 3.5 μm microsphere the width at the half height is 1.7 times bigger than for 1.5 μm one for experimental data (6.1 and 3.7 μm , respectively) and 1.6 times bigger for simulated data (4.5 and 2.9 μm , respectively). Increase of the MJ width with increase of the sphere size can be explained by the tip-sample convolution effect (Figure 4.8).

⁸ Separation distance is the distance between top of magnetic layer and center of the sphere.

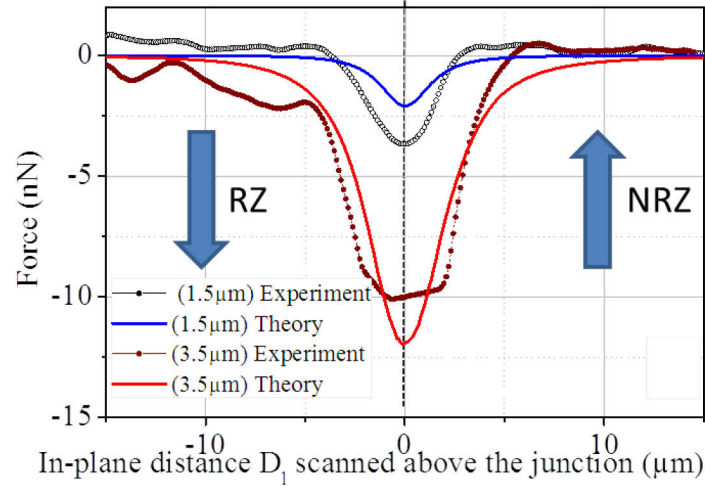


Figure 4.12. Mean experimental (dash lines) and simulated (solid lines) force profiles obtained with 1.5 μm (blue lines) and 3.5 μm (red lines) superparamagnetic microsphere probes at $LSH = 0.7 \mu\text{m}$. Parameters used for simulations: magnetization of NRZ is $\mu_0 M_{up} = 1.1 \text{ T}$, magnetization of RZ is $\mu_0 M_d = 0.9 \text{ T}$ and thickness of RZ is $h_r = 1.1 \mu\text{m}$.

One can notice that the ratio between MJ widths measured with two different spheres in dynamic mode (2.85 μm and 0.29 μm) and in static mode (3.5 μm and 1.5 μm) is the same (1.7), despite the ratio between the sphere diameters used for the same measurements (force gradient or force) is different ($3.5/1.5 = 2.3$ and $2.85/0.29 = 9.8$). It drives us to the conclusion that the width of MJ measured with superparamagnetic microsphere probe depends on the size of the sphere, distribution of magnetic NPs inside it, and on the type of measurements. Increase of the sphere size leads to enlargement of the MJ width. Indeed, according to the simulation results (Annex IV.3) growth of a sphere diameter by a factor of 2 (from 1.5 μm up to 3 μm) for a fixed magnetic volume (30 vol.%) leads to increase of MJ width by a factor of 1.4; while increase of magnetic volume (from 15 vol.% up to 30 vol.%) for a fixed sphere diameter (3 μm) does not change MJ width.

For a fixed sphere size and magnetic volume, we can expect higher MJ width from the experiments conducted in static mode rather than in dynamic mode since the force gradient decays faster with the distance. This hypothesis is confirmed by experimental results for 3.5 and 2.85 μm superparamagnetic spheres. Both spheres contain 13 vol.% of magnetic inclusions, while the ratio between MJ widths at the half height for 3.5 and 2.85 superparamagnetic spheres is higher ($6.1/3.65 = 1.7$) than the ratio between their diameters ($3.5/2.85 = 1.2$).

Table 4.4 summarizes the results of force and force gradient variations in lateral direction confirming that increase of the sphere diameter and magnetic volume leads to increase of MJ width.

Sphere diameter (μm)	vol.% of magnetic nanoparticles	wt.% of magnetic nanoparticles	Type of measurements	Experimental width of MJ at the half-height (μm)
3.5	13	40	Force measurements	6.1
2.85	13	40	Force gradient measurements	3.65
1.5	30	67	Force measurements	3.7
0.29	35	73	Force gradient measurements	2.1

Table 4.4. Width of MJs at the half height measured with superparamagnetic microsphere probes in static and dynamic mode for $LSH = 700 \text{ nm}$.

IV.3.4 Quantification of Force variation in vertical direction

Deflection profiles above the same scan area were recorded with 1.5 μm superparamagnetic probe in static mode for LSH varying from 0.5 up to 2.8 μm with a step of 0.1 μm or 0.2 μm . Figure 4.13 presents mean deflection profiles obtained with this probe at LSH of 0.6 μm , 1 μm and 2.2 μm above one of magnetic junctions.

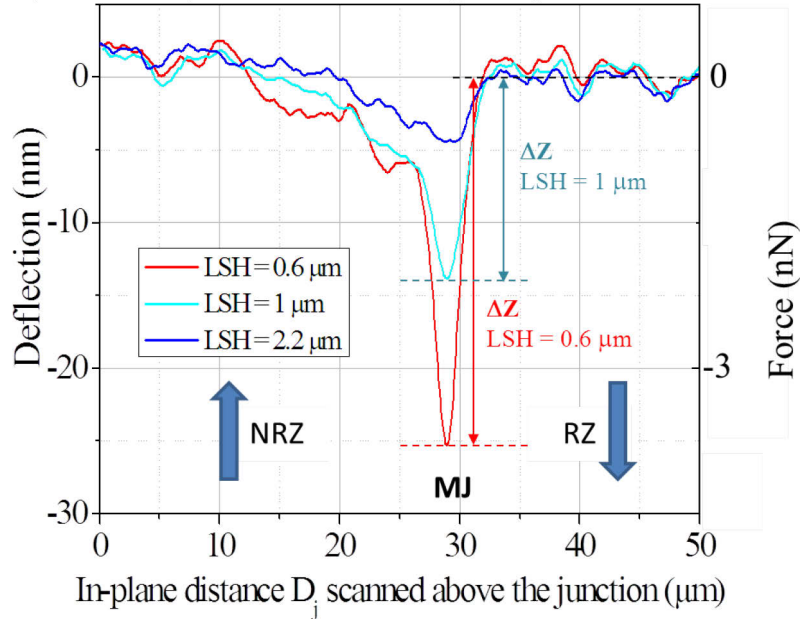


Figure 4.13. Mean deflection profiles obtained from raw data with a 1.5 μm superparamagnetic microsphere probe for three different LSH (0.6; 1; and 2.2 μm).

Force can be found according to the Hooke's law by measuring the cantilever vertical deflection for each LSH :

$$F = k_s \times \Delta Z, \quad (4.4)$$

where k_s is the static spring constant and ΔZ is the vertical deflection of the cantilever. Thus, the drop of cantilever deflection measured in static mode displays decay of the magnetic force acting between superparamagnetic microsphere and TMP sample.

Figure 4.14 presents magnetic force exerted on the superparamagnetic microspheres of (a) 1.5 μm and (b) 3.5 μm diameter as a function of distance between the top of magnetic junction and the sphere bottom part, $D_{j/s}$. In order to quantify the force between microparticle probe and magnetic junction, mean cantilever deflection has been computed from all MFM maps recorded in static mode at various LSH (from 0.5 μm up to 2.8 μm with a step of 0.1 or 0.2 μm). For associated simulations, the following parameters have been chosen: the initial film magnetization $\mu_0 M_{up}$ (1 T; 1.2 T); the magnetization of the reversed part $\mu_0 M_d$ (0.6 T; 1.2 T); the thickness of the reversed part h_r (0.9 μm ; 1.3 μm).

The experimental values have been derived from MFM maps (like Figure 4.6d) recorded for different LSH . Firstly, for all deflection images the data correction procedure has been applied. Secondly, the average deflection value above the magnetic junction has been calculated. Thirdly, for each LSH sphere-sample separation distance has been found by formula (4.1) and corresponding force has been calculated from deflection value by formula (4.4). It should be noticed that $D_{j/s}$ is the separation distance $D_{s/m}$ above the magnetic junction.

The theoretical values have been computed using CADES software. Minimal and maximal parameters to describe TMP sample and superparamagnetic microsphere were used. However, for the force calculation sphere-sample distance has been slightly changed (Figure 4.15). As it was noticed above, due to limitations of CADES, spherical objects could not be modelled. Thus, a cube of equal to magnetic microsphere volume was used for simulations.

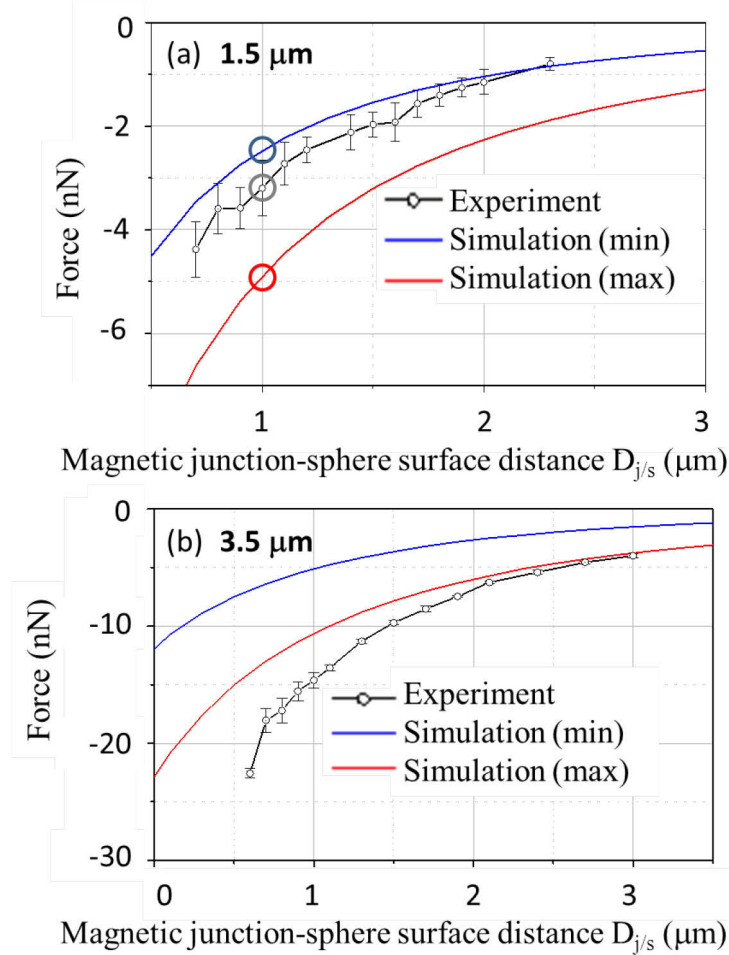


Figure 4.14. Magnetic force versus distance between magnetic junction and (a) 1.5 μm , (b) 3.5 μm superparamagnetic microsphere. Minimal (absolute values) theoretical curves are calculated with $\mu_0 M_{up} = 1 \text{ T}$, $\mu_0 M_d = 0.6 \text{ T}$, $h_r = 0.9 \mu\text{m}$ (blue solid lines) and maximal (absolute values) theoretical curves are calculated with $\mu_0 M_{up} = 1.2 \text{ T}$, $\mu_0 M_d = 1.2 \text{ T}$, $h_r = 1.3 \mu\text{m}$ (red solid lines) taking into account the magnetic volume for each sphere size (Table 4.1).

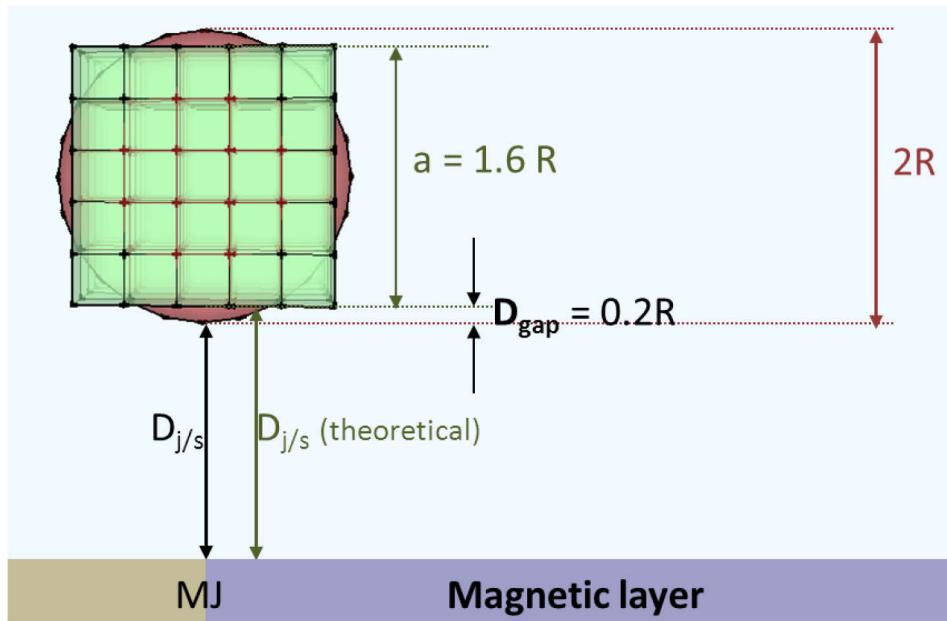


Figure 4.15. Definition of microsphere-magnetic layer distance above the magnetic junction (MJ) for experimental measurements $D_{j/s}$ and for simulations $D_{j/s}$ (theoretical). For simulations microsphere of radius R is modelled as a cube of equal volume with a side $a = 1.6 \times R$. Centres of cube and sphere are aligned.

Indeed, in our model we place the centre of the cube at the point where the centre of the sphere was during the measurements. It means that for each experimental separation distance $D_{j/s}$ associated theoretical distance $D_{j/s}(\textit{theoretical})$ is found as:

$$D_{j/s}(\textit{theoretical}) = D_{j/s} + D_{gap} \quad (4.5)$$

where D_{gap} is equal to $0.2 R$, R is the sphere radius. And for each experimental force value $F_{exp}(D_{j/s})$ associated numerical value is found $F_{num}(D_{j/s}(\textit{theoretical}))$.

For example, for a superparamagnetic microsphere with $1.5 \mu\text{m}$ diameter for a fixed separation distance $D_{j/s} = 1 \mu\text{m}$ experimental force F_{exp} was measured at $D_{j/s} = 1 \mu\text{m}$ (value inside grey circle in Figure 4.14a), but simulated force F_{num} for the same separation distance of $1 \mu\text{m}$ was calculated using $D_{j/s}(\textit{theoretical}) = 1.15 \mu\text{m}$ (value inside blue and red circles in Figure 4.14a for minimal and maximal numerical curves respectively).

To avoid the effect of the “gap” between experimental and theoretical distance several solutions could be proposed, for example:

- (1) to align the bottom parts of the sphere and cube (cube volume is equal to sphere volume);
- (2) to align the sphere top and bottom with the cube ones (cube volume is bigger than sphere volume).

In both cases $D_{j/s}$ and $D_{j/s}(\textit{theoretical})$ would be equal. However, in the case (1) the bottom edges of the cube will strongly affect the magnetic signal between cube and sample leading to overestimated numerical force values (Figure 4.16). And in the case (2) not only the cube edges, but also an increase of the total cube volume will causes growth of calculated force intensity.

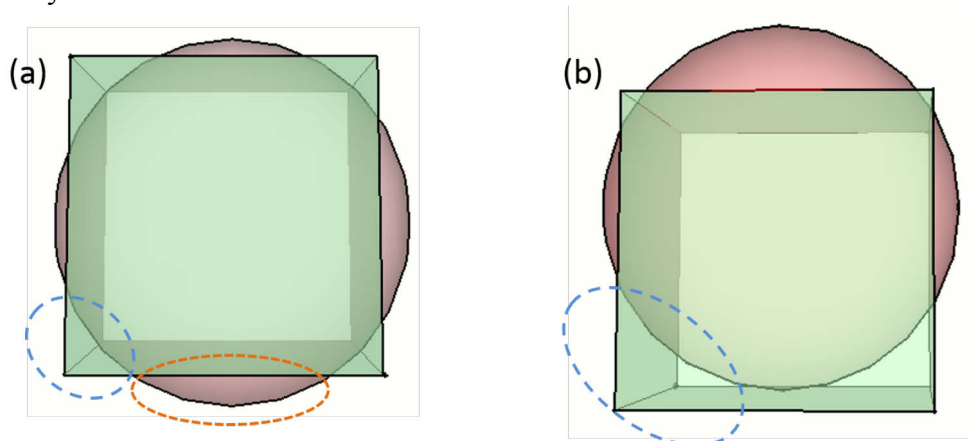


Figure 4.16. (a) Centres of the sphere and cube used to model it are aligned. The bottom edges of the cube extended beyond the sphere (inside blue dashed circle) compensate the sphere part that is out of the cube (inside orange dash circle). (b) The bottoms of sphere and cube used to model it are aligned. The bottom edges of the cube extended beyond the sphere (inside blue dashed circle) lead to overestimated magnetic signal.

Simulated curves taking into account D_{gap} distance demonstrate better matching with experimental data. Experimental and numerical force curves exhibit similar shape and their intensity decays fast with the drop of separating distance between microsphere and magnetic junction. This is in a good agreement with equation (4.3) in which a strong dependence of the magnetic field gradient on the magnetic force is expected.

However, the fitting for $3.5 \mu\text{m}$ superparamagnetic microsphere is not so precise. Possible explanation relies on the definition of separation distance: for simulations this value is higher than for experiments (Equation 4.5). Indeed, for $1.5 \mu\text{m}$ superparamagnetic sphere D_{gap} value is 150 nm (corresponds to the value of the minimum experimental step between two *LSH* measurements) while for $3.5 \mu\text{m}$ superparamagnetic microsphere this value is about two times higher: 350 nm (corresponds to three times the minimal experimental step). As the magnetic field decays fast with the separation distance, simulated results can represent lower

values than the measured ones, in particular for spheres of big diameter. Additionally, the mismatch between experimental and numerical values can be explained by variation in the magnetic volume of the sphere (data from the Table 4.1 represents the average values for the spheres of a certain type).

Comparing the force curves in Figure 4.14a and b one can notice that measured magnetic interaction is higher for microspheres of bigger diameter by a factor of 5 (for experimental data close to surface, $D_{j/s} = 1 \mu\text{m}$). These experimental results are in agreement with the equation (4.3) where magnetic volume of the particle increases the force intensity. Nevertheless, in order to compare the attractive action of the MJ according to the sphere properties, we should consider the force density D_F , i.e. ratio between the force and the magnetic volume of the sphere.

IV.3.5 Magnetic force density variation

From experiments we found that the maximum force exerted on the $3.5 \mu\text{m}$ superparamagnetic microsphere is much higher than the one exerted on the $1.5 \mu\text{m}$. To study the impact of the sphere properties on the trapping process, the force density D_F (ratio between the force and magnetic volume of the sphere) above the magnetic junction was calculated for both superparamagnetic microspheres (Figure 4.17):

$$D_F = F(LSH)/V_{mag}, \quad (4.6)$$

where $F(LSH)$ is the force acting on a magnetic microsphere at fixed LSH and V_{mag} is the microsphere magnetic volume.

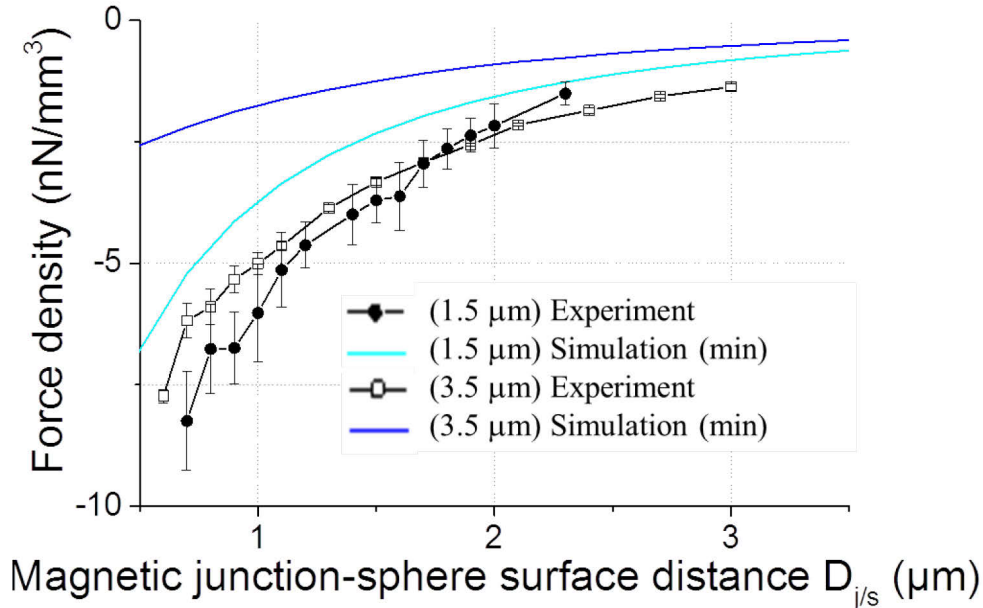


Figure 4.17. Force density for 1.5 and 3.5 μm superparamagnetic microspheres above a magnetic junction as a function of distance $D_{j/s}$. Parameters used for min simulations: magnetization of NRZ is $\mu_0 M_{up} = 1 \text{ T}$, magnetization of RZ is $\mu_0 M_d = 0.6 \text{ T}$, thickness of RZ is $h_r = 0.9 \mu\text{m}$.

For simulated data at small separation distances $D_{j/s}$, theoretical (absolute) values of the force density for superparamagnetic microspheres are higher for 1.5 μm sphere (light blue curve) than for 3.5 μm one (dark blue curve) by a factor of 3, then with increase of $D_{j/s}$ the difference is almost disappeared due to the fast decay of magnetic interaction.

For experimental data we observe similar behaviour: at short sphere-gap distances, the force density is higher for 1.5 μm than 3.5 μm sphere, however the intensity difference is lower compared to the theoretical curves.

In the previous studies [7] it was shown that for the same ratio between magnetic weight and total weight of the particle (wt.%), with a homogenous distribution of magnetic inclusions inside and at a given flying altitude, bigger magnetic objects experience stronger deviation. In our case according to the manufacture specification (Annex III.3) magnetic inclusions are estimated to be 40 wt.% for 3.5 μm microsphere and 67 wt.% for 1.5 μm microsphere. The difference in magnetic volume explains why the measured trapping force normalized by magnetic volume (force density D_F) is not lower for a smaller particle than for a bigger one as it was expected from previous studies. Increase of magnetic weight compared to the total microsphere weight can compensate smaller particle size.

For a fixed magnetic volume the force density for a big magnetic microsphere ($R \gg$ few micrometres) should be lower than for a small one ($R \sim$ few microns) due to the strong decay of magnetic interaction with increase of the distance (defined by sphere diameter). Indeed it was shown before that the magnetic field and its gradient decay fast in Z direction (Figure 2.13, Annex II.3), that means that the magnetic force acting on the bottom of the sphere is maximal and decreases with the distance (Figure 4.18).

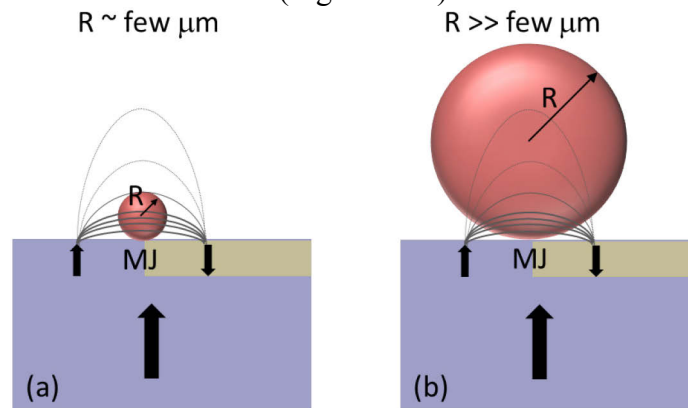


Figure 4.18. The effect of the sphere size on the force density D_F : (a) field variation in Z direction at the bottom and the top of the sphere is high; (b) field variation in Z direction at the bottom of the sphere is high, but close to zero at the top of the sphere.

Contribution of the MFM measurements in static mode about the TMP sample properties and its action on a superparamagnetic object

For all superparamagnetic microsphere probes only attractive interaction was measured. This confirms that once magnetic particles inside polystyrene sphere are magnetized by the field arising from the sample their magnetizations follow the magnetic field lines and switch from “up” to “down” when the probes passes from NRZ to NZ or vice versa.

The MJ position can be localized precisely: it corresponds to the position where the microsphere and MJ centres are aligned, so the microsphere experiences the maximum attraction. As for MFM phase measurements in dynamic mode, the width of magnetic junction is sphere size dependent.

The forces versus distance curves demonstrate trapping force exerted by TMP samples on a single magnetic object in the range of few nN for 1.5 μm sphere and few tens of nN for 3.5 μm microsphere. These values could be used to improve the model used for calculation of forces and sphere trajectories in microfluidic devices [8].

Through the definition of force density it was shown that not only the sphere size, but also the magnetic weight of the sphere (total weight of all magnetic nanoinclusions) has strong impact on the trapping force. For a constant wt.%, of magnetic inclusions homogeneously distributed inside a sphere and at a given distance, bigger magnetic objects experience stronger trapping while the increase of magnetic weight compared to the total microsphere weight for smaller particles leads to increase of the magnetic interaction. This observation should be taken into account while choosing magnetic microspheres for trapping applications.

IV.4 Micromagnet array mapping with Hard Magnetic Microsphere probe

To study the impact of the sphere magnetic material on the trapping process, MFM characterization of TMP samples with hard magnetic (NdFeB) microsphere probes (Table 4.5) will be discussed in the next sections. The first two types of probes (PL2-FMR, Nanosensors) were used for force-distance curves, while the third one (Olympus AC240TS) for additional sample characterizations (by changing scan angle and sample rotation). These three probes were fabricated using FIB capability as described in Chapter III.

Cantilever type	Microsphere material	Microsphere diameter, (μm)	Cantilever spring constant, (N/m)	Cantilever resonance frequency, (kHz)	Cantilever quality factor
PL2-FMR, Nanosensors	NdFeB	1.3	1.4	52.3	194
PL2-FMR, Nanosensors	NdFeB	1.7	1.9	54.7	182
Olympus AC240TS	NdFeB	2	1.9	66	196

Table 4.5. List of NdFeB microparticle probes used for Microsphere Scanning Force Microscopy.

Figure 4.19 presents MFM deflection image and the associated mean deflection (force) profile of TMP micromagnet array scanned with $1.3 \mu\text{m}$ NdFeB microsphere probe in static MFM mode. On this image three different zones separated by two vertical dark/light lines corresponding to MJ₁ and MJ₂ can be observed. This behaviour holds for the all NdFeB microsphere probes and the dissymmetrical response between MJ₁ and MJ₂ is reproducible (this point will be discuss in detail in this chapter).

As for the MFM maps obtained with superparamagnetic probes, the RZ on the deflection image is identified by higher magnetic roughness.

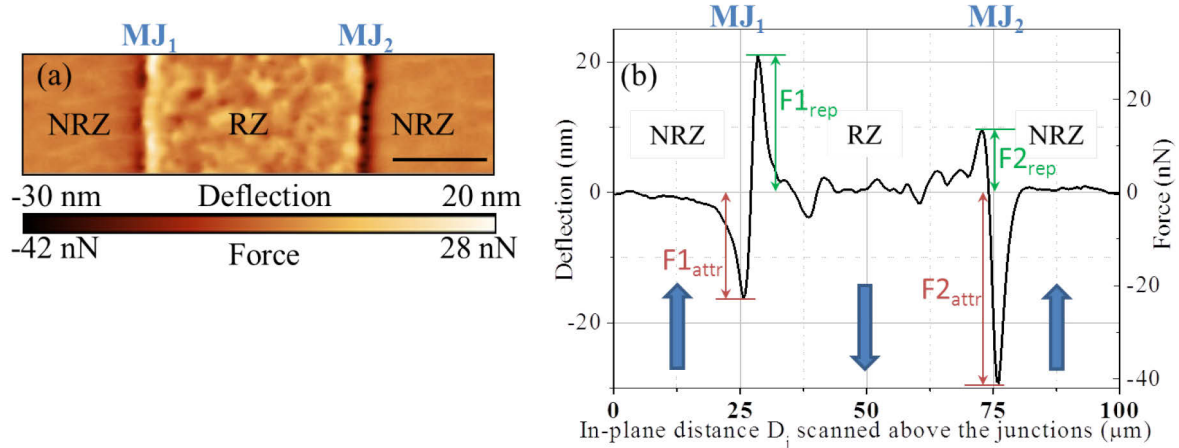


Figure 4.19. (a) MFM image of TMP array of NdFeB micromagnets obtained with $1.3 \mu\text{m}$ NdFeB microsphere in static mode for $LSH = 500 \text{ nm}$. (b) Associated mean experimental profile, where the blue arrows indicate the orientation of magnetic pattern. MJ₁ is the magnetic junction between NRZ and RZ; MJ₂ is the magnetic junction between RZ and NRZ. $F1_{attr}$ and $F1_{rep}$ are the attractive and repulsive forces above MJ₁; $F2_{attr}$ and $F2_{rep}$ are the attractive and repulsive forces above MJ₂. Lateral scale bar is $20 \mu\text{m}$.

The results of magnetic roughness measurements for MFM deflection maps recorded with $1.3 \mu\text{m}$ and $1.7 \mu\text{m}$ NdFeB microspheres in static mode at $LSH = 600 \text{ nm}$ are summarized in Table 4.6.

	1.3 μm NdFeB microsphere probe		1.7 μm NdFeB microsphere probe	
	NRZ	RZ	NRZ	RZ
Average magnetic roughness⁹ + RMS	1.4 \pm 1.3 nm (2.0 \pm 1.8 nN)	6.7 \pm 6.3 nm (9.4 \pm 8.8 nN)	1.7 \pm 1.4 nm (3.2 \pm 2.7 nN)	7.8 \pm 5 nm (14.8 \pm 9.5 nN)
Max value¹⁰	8.3 nm (11.6 nN)	21.8 nm (30.5 nN)	9.8 nm (18.6 nN)	36.9 nm (70.1 nN)
Deflection shift¹¹ above MJ₁ for attraction	18.5 nm (25.9 nN)		20 nm (38 nN)	
Deflection shift¹⁰ above MJ₁ for repulsion	22.9 nm (32.1 nN)		26 nm (49.4 nN)	

Table 4.6. Characteristics of a TMP sample mapped with 1.3 μm and 1.7 μm NdFeB microsphere probes at $LHS = 600$ nm.

The magnetic roughness measured in contact/lift mode with 1.3 μm *hard* magnetic microsphere probe is much higher (by a factor of 20) than the one measured with 1.5 μm *superparamagnetic* probe.

With the NdFeB microsphere probe, attractive and repulsive forces are sensed, and their intensity is much higher compared to experimental results obtained with superparamagnetic microsphere probe. Indeed, the measurements performed with similar microsphere diameters (1.5 μm for superparamagnetic and 1.3 μm for NdFeB) at fixed LSH show the force intensity about 7 times higher for NdFeB microsphere.

The strengthening of magnetic force and magnetic roughness for measurements conducted with hard magnetic microsphere probe compared to superparamagnetic one is mainly caused by different magnetic properties of attached spheres (NdFeB and FeO) and increase of magnetic volume (from 13-35 vol.% for superparamagnetic microspheres up to 100 vol.% for NdFeB microspheres) affected by the sample stray field.

Concerning the characterization of TMP sample with magnetic microsphere probes there are several common observations that are independent of the magnetic nature of the probe:

- the average magnetic roughness above the RZ is always higher than above NRZ (by a factor of 5 for NdFeB sphere and by a factor of 2 for superparamagnetic sphere);
- the local maximum of magnetic roughness above the RZ is the same order of magnitude as the average deflection shift above the magnetic junction;
- the average value and its associated RMS of the magnetic roughness depend on the magnetic microsphere size.

These factors confirm the high magnetic inhomogeneity of RZs that can affect the trapping process. It means that as in case of superparamagnetic particles, some points inside RZs can act as additional isolated magnetic traps. Combination of basic experiments on impact of the fluid flow with magnetic roughness measurements (average magnetic roughness inside the RZs is 7 times less strong than the average signal above the MJJs) confirms that increase of the liquid flux can remove most of the microspheres captured outside of MJJs, but with less efficiency inside RZs due to the strong local magnetic traps.

Thanks to the equation (4.4) cantilever vertical deflection was transformed into magnetic force acting between sample and microsphere. Unlike the force measured with superparamagnetic probe, the force sensed by hard magnetic microsphere probe changes its sign. Such behaviour proves that NdFeB probe magnetization is not flipped to match the

⁹ Peak-to-peak value is the difference between the maximum positive and the maximum negative values for the average phase (or deflection) profile.

¹⁰ The maximum was found for the whole RZ or NRZ area (not for average profile) while the minimum was set to zero.

¹¹ The deflection shift is calculated above more symmetrical magnetic junction.

magnetic field lines in proximity of TMP sample. Dramatic increase of force intensity is observed in vicinity of magnetic junction: for MJ_1 (magnetic junction corresponding to NRZ/RZ interface in Figure 4.19) firstly it becomes attractive (negative cantilever deflection, dark line on MFM image) and then switches to repulsive (positive cantilever deflection, bright line on MFM image) and vice versa for MJ_2 (RZ/NRZ interface in Figure 4.19). Such behaviour can be explained by the nature of magnetic interaction between the probe and the sample.

Let us assume that NdFeB microsphere and micromagnet array magnetizations are parallel (Figure 4.20a). For example, initially film is magnetized in out-of-plane direction (magnetization of NRZ is “up”, M_{up}). Magnetization of RZ is antiparallel to the initial one (magnetization of RZ is “down”, M_d). NdFeB microsphere is magnetized parallel to NRZ magnetization (magnetization of sphere is “up”, M_{sph}). The results of modelling this system with CADES software are presented in Figure 4.20b. It should be noticed that for all simulations only z-component of the force was plotted (x and y-components were modelled and taken into account) because in our MFM experiments only z-component of the force was measured through the vertical cantilever deflection.

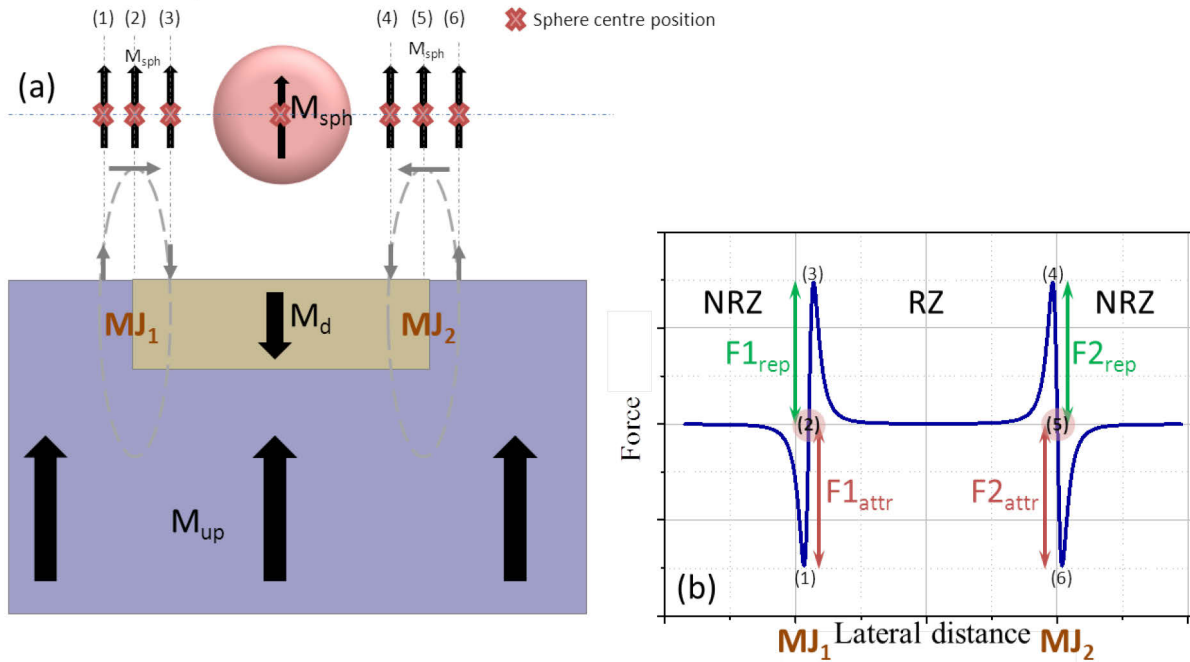


Figure 4.20. (a) Schematic of magnetic interaction between hard magnetic microsphere and micromagnet array when the sphere magnetization, M_{sph} is parallel to initial magnetization of patterned film, M_{up} . Red cross is the centre of the sphere, while positions (1) and (6) correspond to the configuration where sphere magnetization is parallel to the sample stray field lines; positions (3) and (4) correspond to the configuration where sphere magnetization is antiparallel to the sample stray field lines; positions (2) and (5) correspond to the configuration where sphere magnetization is perpendicular to the sample stray field lines. (b) Associated force profile. M_{up} is the NRZ magnetization, M_d is the RZ magnetization, M_{sph} is the sphere magnetization; $F1_{attr}$ and $F1_{rep}$ are the attractive and repulsive forces above MJ_1 ; $F2_{attr}$ and $F2_{rep}$ are the attractive and repulsive forces above MJ_2 .

When the probe with attached hard magnetic microsphere passes close to the first magnetic junction MJ_1 (NRZ/RZ) M_{up} and M_{sph} are close to be parallel (position (1)), thus strong attraction $F1_{attr}$ between them appears leading to the first negative peak in Figure 4.20b. As soon as the centre of probe overcomes magnetic junction MJ_1 sample magnetization M_d is close to be antiparallel (position (3)) to M_{sph} inducing strong repulsive force $F1_{rep}$ corresponding to the first positive peak in Figure 4.20b.

In the middle of NRZ or RZ magnetic interaction (along z-axis) between probe and sample is close to zero due to a low field gradient in these zones compared to MJ. When the

sphere passes above the second magnetic junction MJ_2 (RZ/NRZ), firstly repulsion and then attraction takes place. The zero force corresponds to the configuration where the directions of sample magnetization and microsphere are perpendicular (positions (2, 5) or in the middle of NRZ or RZ) while its absolute maximum intensity is reached when they are parallel (positions (1, 6)) or antiparallel (positions (3, 4)).

The lateral distance between two deflection peaks (attractive and repulsive one, positions (1) and (3) in Figure 4.20b) above the same magnetic junction is about few micrometres and depends on the sphere size. Numerical simulations performed in CADES framework confirm this observation. For measurements conducted with $1.3 \mu\text{m}$ NdFeB sphere probe this distance according to the experimental ($L_{SH} = 600 \text{ nm}$) and simulation results is $2.8 \mu\text{m}$ and $1.9 \mu\text{m}$ respectively (Figure 4.21); for measurements conducted with $1.7 \mu\text{m}$ NdFeB sphere probe this distance according to the experimental ($L_{SH} = 600 \text{ nm}$) and simulation results is $3 \mu\text{m}$ and $2.1 \mu\text{m}$ respectively.

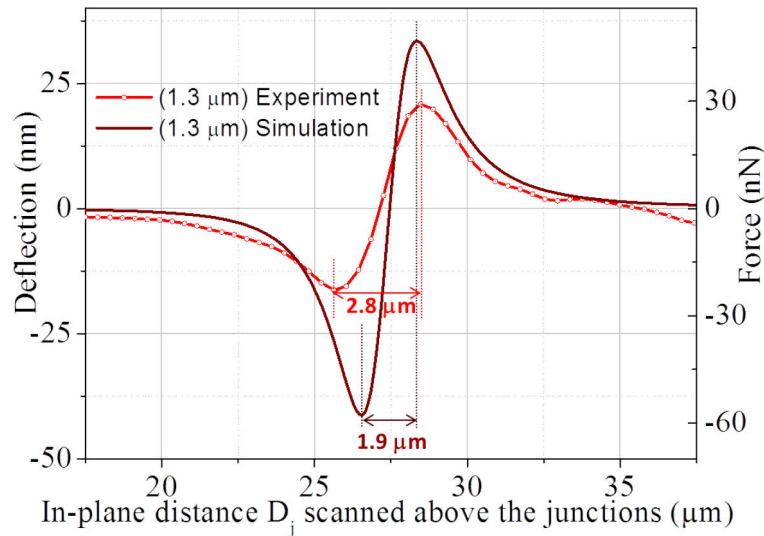


Figure 4.21. Measurements of the distance between attractive and repulsive peaks above one MJ for mean deflection/force profile obtained with $1.3 \mu\text{m}$ NdFeB microsphere probe at $L_{SH} = 600 \text{ nm}$ and associated numerical profile.

In the perfect case when both, micromagnet sample and microsphere are magnetized vertically (along z axis) and the sample does not exhibit magnetic inhomogeneity attractive and repulsive forces above both interfaces should be equal: $F1_{attr} = F1_{rep} = F2_{rep} = F2_{attr}$.

However, for experimental data mismatch between positive and negative peaks above the same magnetic junction and between two neighbouring junctions is observed (Figure 4.19b). Possible explanations of the discrepancy between experimental data and CADES simulations can be due to: (1) misalignment between the magnetization orientation of the microsphere and micromagnet array leading to an in-plane component of magnetization; (2) magnetic inhomogeneity of the sample properties.

To explore and to identify the origin of this behaviour several experiments and analyses have been performed and are described in the next sections: the impact of in-plane probe magnetization component and magnetic inhomogeneity of reversed zone.

IV.4.1 Effect of probe magnetization orientation

On all MFM maps obtained with NdFeB microsphere probes, we can observe that the maximum intensity of the attractive interaction is not equal to the repulsive one above the same magnetic junction. In Figure 4.19b for the first magnetic junction MJ_1 , $F1_{attr}$ is about 25% less than $F1_{rep}$ and for the second magnetic junction MJ_2 the dissymmetrical behaviour is much stronger, where $F2_{attr}$ is about 3 times higher than $F2_{rep}$.

This difference can be a signature of misalignment between magnetization orientation of

the microsphere and micromagnet array introducing an angle between them leading to appearance of an in-plane component. A part of this misalignment is caused by the in-plane component of the sphere magnetization (Figure 4.22a) induced by mechanical tilt Θ of the cantilever (usually between 7° and 20° instead of the horizontal case due to the probe holder geometry) [8]. This tilt is required for the cantilever displacement detection system based on a laser and a photodiode.

Indeed, NdFeB microsphere probe is preliminary magnetized along the z-axis, but due to the probe holder construction, the cantilever is tilted by 10 degrees. It leads to appearance of in-plane component of NdFeB microsphere magnetization, which can be parallel or antiparallel to an in-plane component of micromagnet array stray field [9]. Considering a tilt of 10 degrees, the effect of the in-plane (ip) and out-of-plane (oop) sphere magnetization components on the total force is presented in Figure 4.22 b,c.

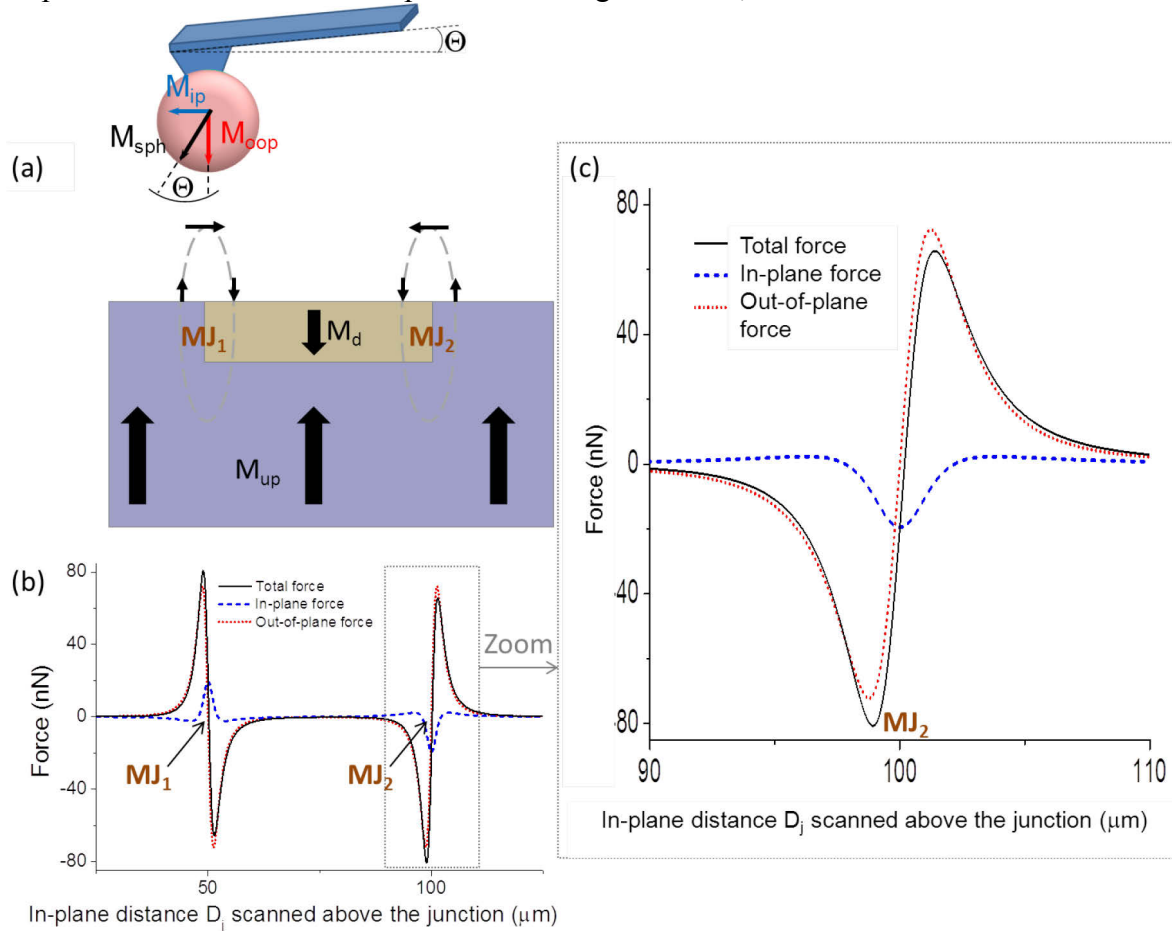


Figure 4.22. (a) Sketch in 2D of the experimental set-up: tilt Θ of the probe holder leads to appearance of in-plane (M_{ip}) and out-of-plane (M_{oop}) magnetization components of NdFeB microsphere. (b, c) Simulations of the ip and oop components of the force acting in z-direction on $1.7 \mu\text{m}$ NdFeB microsphere above the micromagnet array with the tilt of the probe Θ equals to 10 degrees.

For a given geometry, the tip in-plane force component increases repulsive interaction and decreases attractive one for the first magnetic junction MJ_1 (NRZ/RZ) and vice versa for the second junction MJ_2 . This in-plane magnetization induces an additional positive or negative force in Z direction leading to dissymmetrical force intensity between attractive and repulsive forces above the same magnetic junction (around 10% according to CADES simulation).

This additional in-plane force component slightly changes the lateral position of attractive and repulsive peaks above the same MJ (less than 100 nm) compared to the force profile calculated without taking into account the 10 degrees tilt in probe magnetization. This change is caused by superposition of in-plane and out-of-plane magnetization components of

Chapter IV: Quantitative study of TMP sample action on a single magnetic (sub)micronic object sphere and sample that can be parallel or antiparallel. This angle can explain the difference in attractive and repulsive experimental force signals above the MJ_1 but not the difference in force signals above the MJ_2 (Figure 4.19).

IV.4.2 Experimental prospective to explore non-symmetrical behaviour of MJ

Taking into account the in-plane magnetization of NdFeB microsphere due to the probe holder set up, mirror symmetry between two neighbouring junctions is expected. It means that the attractive force above MJ_1 should be equal to the repulsive force above MJ_2 and vice versa: $F1_{attr} = F2_{rep}$ and $F2_{attr} = F1_{rep}$ (in terms of Figure 4.20b). This mirror symmetry is confirmed by simulations (Figure 4.22b), but not observed in experimental maps (Figure 4.19): $F1_{attr} > F2_{rep}$ while $F1_{rep} < F2_{attr}$.

This experimental behaviour could have several origins: (1) an artefact due to the experimental procedure; (2) sample magnetic properties variations as a non-homogeneity of RZ thickness or/and in-plane field components associated with local variations in the alignment of individual grains that can be sensed with hard magnetic microsphere probe; (3) probe magnetization modification.

To choose between these statements, additional experiments have been carried out to test the effect of the scan direction or sample position. AFM and MFM characterization in static mode has been performed using $2\ \mu\text{m}$ NdFeB microsphere probe on new NdFeB TMP sample with small surface roughness (less than 50 nm in average) due to lower content of Nd. Figure 4.23 presents topographical image and the schematics of scanning process. Figure 4.24 displays MFM deflection maps (a,b,c) and associated mean deflection profiles (d,e,f).

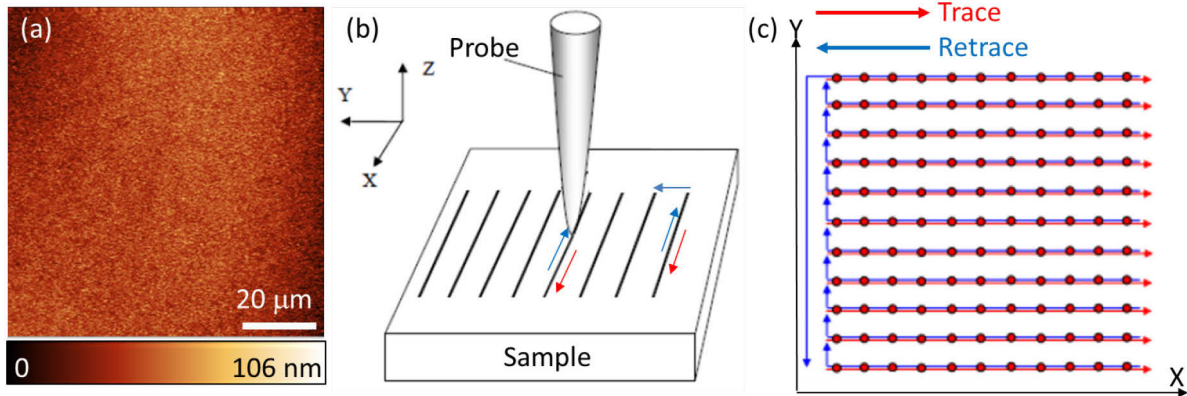


Figure 4.23. (a) Topographical image of a TMP sample obtained in contact mode during the double pass MFM procedure at $LSH = 500\ \text{nm}$ with $2\ \mu\text{m}$ NdFeB microsphere probe. (b, c) Schematic of tip movements to form an image: red arrow corresponds to cantilever motion forward (trace) and blue arrow corresponds to cantilever motion backward (retrace).

To form an AFM (or MFM) image the tip moves forward and backward (trace, red arrows and retrace, blue arrows in Figure 4.23 b,c). Initially (scan angle is 0°) the fast scan axis¹² is parallel to the X-axis of scanner. With an introduction of the scan angle, the fast scan axis changes its direction: parallel to y-axis in case of scan angle of 90° and antiparallel to x-axis for scan angle of 180° .

In our experiments the same area was scanned, but the scan angle was changed by 180° (Figure 4.24 a,b). It means that the *trace* recorded for 0° scan angle ($RZ_1/NRZ/RZ_2$) coincides with the *retrace* ($RZ_1/NRZ/RZ_2$) for 180° scan angle.

¹² The axis that the probe scans along is referred to the fast scan axis, whereas the axis that the probe slowly creeps along is referred to the slow scan axis.

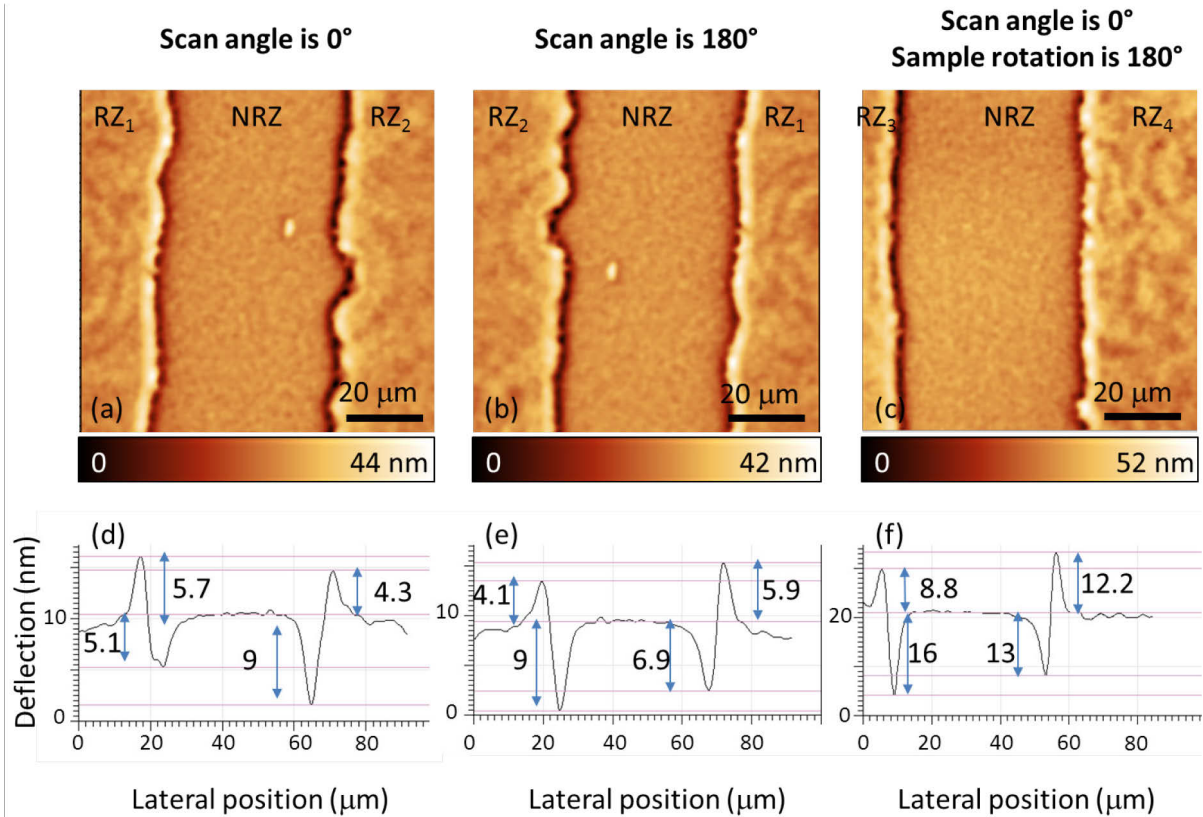


Figure 4.24. MFM deflection (a,b,c) and associated mean deflection profiles (d,e,f) obtained in static MFM mode at $LSH = 500$ nm with $2 \mu\text{m}$ NdFeB microsphere probe.

From both associated mean deflection profiles (Figure 4.24 d,e) magnetic force can be calculated according to the equation (4.4). It can be noticed that for NRZ/RZ₂ interface attractive force is more than two times higher than the repulsive one: 9 nm (17.1 nN) and 4.3 nm (8.17 nN) respectively (for Figure 4.24b); 9 nm (17.1 nN) and 4.1 nm (7.8 nN) respectively (for Figure 4.24c). It means that such a strong dissymmetry above the same junction compared to the predicted by simulation value of 10% cannot be explained by the change of scan angle.

Additional experiment was performed with the same sample rotated manually by 180° (Figure 4.24 c,f). This manual rotation leads to probing of an area close to the previous one but not exactly the same one. Again attractive force is two times higher than the repulsive one above the RZ₃/NRZ interface (16 nm (30.4 nN) and 8.8 nm (16.7 nN) respectively). From the other hand, the difference between attractive and repulsive forces above the second interface for all MFM maps does not exceed 10% as numerical simulations taking into account 10 degrees probe tilt predicted.

Based on these experimental results, we can conclude that no artefact due to the experimental AFM/MFM procedure can be at the origin of the different behaviour between RZ/NRZ and NRZ/RZ interfaces. It is also confirmed that such behaviour does not depend on the TMP film preparation procedure: dissymmetrical signal above the interfaces is observed for both types of samples: “flat” one and with Nd-rich bumps.

The structural and magnetic inhomogeneity of the patterned sample, in particular of RZ can explain this behaviour (Figure 4.25):

- (a) the model applied for TMP sample;
- (b) the variation of reversed zone depth leads to magnetic signal variation above the RZ and MJ changing shape and intensity of measured magnetic force profile (magnetic roughness);

(c) the variation of reversed zone shape changes the width of RZ and MJ, leading to dissymmetrical behaviour of magnetic force signal above the MJ;

(d) tilt in RZ magnetization leads to dissymmetrical behaviour of magnetic force signal above the MJ.

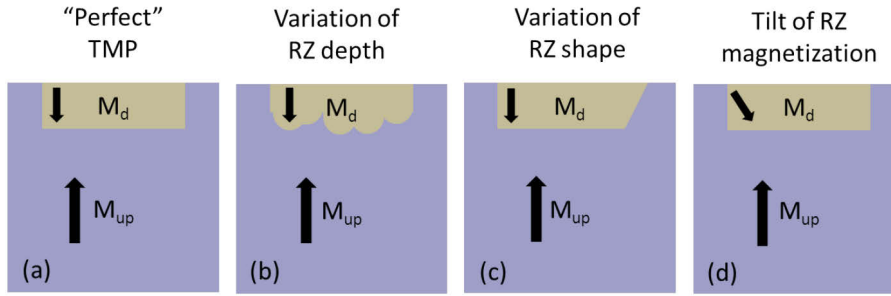


Figure 4.25. TMP model (a) and examples of the structural and magnetic inhomogeneity of TMP sample (b,c,d,) that can affect MFM image leading to increase of magnetic roughness inside RZ, different artefacts such as dissymmetrical response between two neighbouring magnetic junctions, and so on.

Based on the experimental observations confirmed by simulations we can assume that TMP samples used in our experiments can be described as a combination of the structures presented in Figure 4.25 (b,c,d). To identify which of these three structures is the most relevant, additional simulations will have to be performed.

IV.4.3 Vertical variation of force intensity above a symmetric MJ

To illustrate the vertical variation of the force intensity above more symmetric magnetic junction, Figure 4.26 presents cantilever deflection/force above a magnetic junction (first magnetic junction in Figure 4.19) for three different *LSH* (0.6 μm , 1 μm and 2.2 μm) recorded with a 1.3 μm NdFeB microsphere.

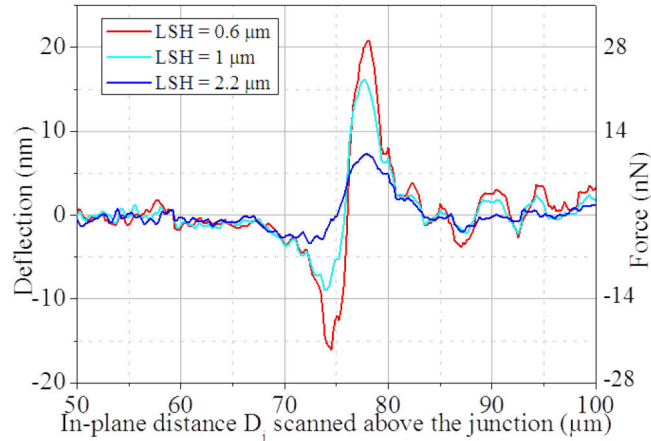


Figure 4.26. Mean profiles obtained from raw data with a 1.3 μm NdFeB microsphere probe for three different *LSH* (0.6; 1; and 2.2 μm).

In order to quantify the interaction intensity, cantilever deflection images have been recorded in static mode for *LSH* varying from 0.5 μm up to 2.8 μm with a step of 0.1 or 0.2 μm with two sizes of hard magnetic microspheres. Figure 4.27 displays attractive and repulsive forces measured between (a) 1.3 μm and (b) 1.7 μm NdFeB microspheres and TMP micromagnet array above the magnetic junction. For associated simulations, the following parameters have been set to minimal and maximal values: the initial film magnetization $\mu_0 M_{up}$ (1 T; 1.2 T); the magnetization of the reversed part $\mu_0 M_d$ (0.6 T; 1.2 T); the thickness of the reversed part h_r (0.9 μm ; 1.3 μm) and the sphere remanent magnetization $\mu_0 M_{sph}$ (0.73 T; 0.76 T). The angle θ induced by the probe holder construction (10 degrees) was taken into account for calculation of numerical curves.

As for superparamagnetic microsphere probes, data correction procedure has been applied on all the deflection images before the calculation of the average deflection value from more symmetrical profile above the magnetic junction. For each LSH , sphere-sample separation distance has been determined by equation (4.1) and corresponding force has been calculated from deflection maps according to equation (4.4).

The associated numerical values have been computed with minimal and maximal parameters to describe TMP sample and NdFeB sphere. The sphere-sample distance defined by equation (4.5) was used in simulations.

Good matching between experimental and numerical curves is observed for both attractive and repulsive interactions: they exhibit similar shape (fast decay of intensity with increase of $D_{j/s}$) and force intensities are in between the minimum and maximum associated numerical curves.

The intensity of the force acting on $1.7 \mu\text{m}$ NdFeB microsphere is about 2 times stronger than the one exerts on $1.3 \mu\text{m}$ NdFeB microsphere for small separation distances (less than $2 \mu\text{m}$). This difference can be explained by sphere volumes. For detailed comparison of magnetic volume impact on the trapping force the force density D_F for NdFeB microspheres was calculated.

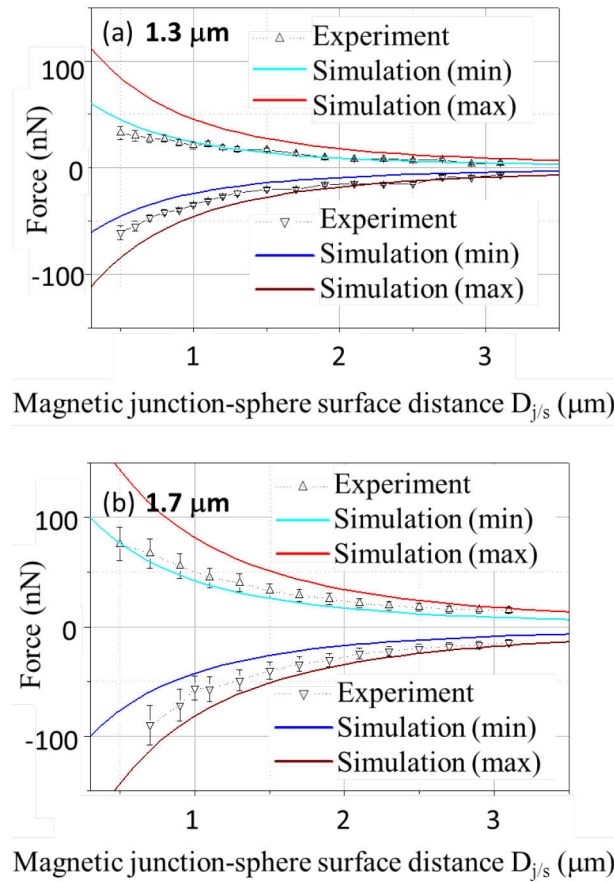


Figure 4.27. Magnetic force versus distance between magnetic junction and (a) $1.3 \mu\text{m}$ and (b) $1.7 \mu\text{m}$ NdFeB microspheres. Minimal (absolute values) theoretical curves are calculated with $\mu_0 M_{up} = 1 \text{ T}$, $\mu_0 M_d = 0.6 \text{ T}$, $h_r = 0.9 \mu\text{m}$ and $\mu_0 M_{sph} = 0.73 \text{ T}$ (blue solid lines) and maximal (absolute values) theoretical curves are calculated with $\mu_0 M_{up} = 1.2 \text{ T}$, $\mu_0 M_d = 1.2 \text{ T}$, $h_r = 1.3 \mu\text{m}$ and $\mu_0 M_{sph} = 0.76 \text{ T}$ (red solid lines). Sphere magnetization angle Θ of 10° is applied.

IV.4.4 Magnetic force density variation

The force density D_F (see equation (4.6)) for $1.3 \mu\text{m}$ and $1.7 \mu\text{m}$ NdFeB microspheres above more symmetric magnetic junction was calculated. Figure 4.28 presents the impact of

hard magnetic microsphere size on the trapping force exerted by TMP micromagnet array. Only minimal values were used to plot simulated curves to avoid overfilling of graphic area.

Despite the volume of 1.7 μm sphere is about 2 times higher than the volume of 1.3 μm sphere the force density values (experimental and numerical) are very close to each other. Slightly lower absolute values (about 10%) are observed for a sphere of 1.7 μm . It means that for microspheres with magnetic volume equal to total volume (100 vol.%) decrease of magnetic field with a distance leads to a lower magnetic action on the top of a bigger sphere as illustrated in Figure 4.18.

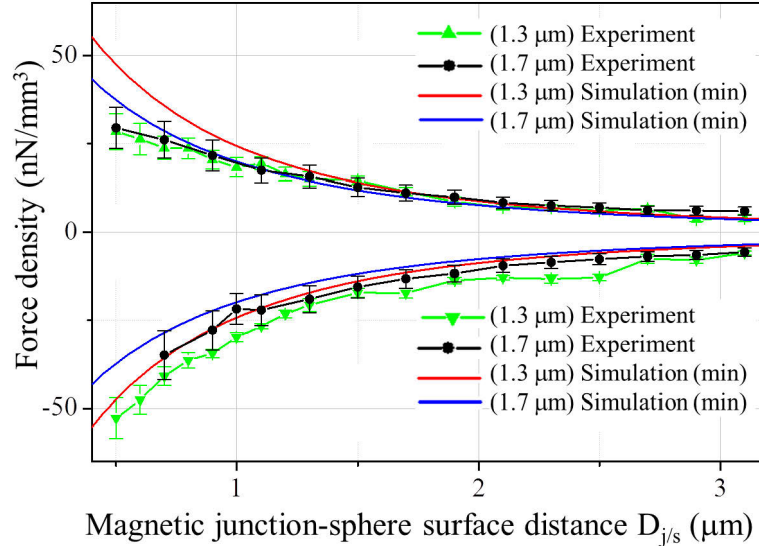


Figure 4.28. Force density for 1.3 and 1.7 μm NdFeB microspheres above a magnetic junction as a function of distance $D_{j/s}$. Parameters used for min simulations: magnetization of NRZ is $\mu_0 M_{up} = 1$ T, magnetization of RZ is $\mu_0 M_d = 0.6$ T, thickness of RZ is $h_r = 0.9$ μm , sphere magnetization $\mu_0 M_{sph} = 0.73$ T, $\Theta = 10^\circ$ is the angle of sphere magnetization.

Contribution of the MFM measurements in static mode about the TMP sample properties and its action on a hard magnetic (NdFeB) object

For all NdFeB microsphere probes attractive and repulsive interactions were measured. This confirms that once magnetic microsphere is magnetized (in a field of ~ 7 T, before MFM measurements) its magnetization does not flip due to the field arising from the sample. Indeed, according to the manufacture' specification a magnetizing field to reach $> 95\%$ saturation for NdFeB microparticles is about 2 T while the field produced by TMP samples over the surface does not overcome 1 T [10]. It means that when the probe with NdFeB microsphere passes from NRZ to NZ or vice versa, depends on the alignment of sample and probe magnetizations attractive or repulsive interaction will be sensed. Unlike the measurements conducted with superparamagnetic microparticle probes, for NdFeB microsphere probes two maximum peaks (absolute value) are observed in vicinity of each magnetic junction: the distance between them and MJ depends on the microsphere diameter and tilt in sphere magnetization. In our experiments the negative deflection peak located 1-1.5 μm from the MJ corresponds to attractive interaction, while the positive deflection peak located on the same distance from the MJ but on the other side corresponds to repulsive interaction.

Based on the experiments carried out with NdFeB microsphere probes, the width of magnetic junction and the force intensity are sphere size dependent. The forces versus distance curves demonstrate trapping force exerted by TMP samples on a single NdFeB microsphere (1.3-1.7 μm in diameter) in the range from few nN up to hundred of nN.

IV.5 Summary

The present approach completes the usual magnetic field and field gradient characterization techniques (e.g. MOIF and Scanning Hall Probe Microscopy or MFM with standard probe), with the specific advantage of providing direct force measurements with high resolution (limited by magnetic roughness). For both types of magnetic spheres, the force and its gradient measurements are in agreement with numerical simulations.

Smart MFM probes have been employed to scan at various distances a NdFeB TMP micromagnet array in order to obtain 3D force/force gradient maps. Both types of magnetic microsphere probes exhibit similar behaviours:

- (1) Magnetic interaction varies significantly when the microsphere is in vicinity or above a magnetic junction and decreases when the microsphere-magnetic junction distance increases. It has to be noticed that the force gradient (the force derivative of the distance) decays faster than the force. For superparamagnetic microsphere probes enlargement of the distance by 1 μm leads to lowering of magnetic force by a factor of 2.5 while magnetic force gradient drops down by a factor of 3.5.
- (2) The width of magnetic junction measured with microsphere probes is about few micrometres and increases with the sphere diameter (sphere-size dependent). This can be explained by the tip-sample convolution effect. Thus, microparticle probes cannot be used for direct measurements of magnetic junction width, but can be employed for definition of the domain wall localization.
- (3) Variation of magnetic signal inside the reversed zone is about few times higher than variation inside the non-reversed zone. Magnetic roughness of RZ is caused by magnetic inhomogeneity of TMP samples appearing during the fabrication process. For trapping applications it means that some single particles could be captured outside of magnetic junctions. However, the increase of the liquid flux can remove most of the microspheres trapped outside of MJs due to the fact that the average magnetic roughness inside the RZs is about 10 times weaker than the average signal above the MJs.
- (4) Magnetic force depends on the sphere size and magnetic volume: its maximum intensity increases with increase of the sphere diameter and magnetic content.

For superparamagnetic microsphere probe:

- (1) Magnetic interaction is always attractive and reaches its maximum when the microsphere centre and the magnetic junction are aligned.
- (2) Magnetic force depends on the sphere size and magnetic volume: its maximum intensity increases with the magnetic volume. However, the experimental force density for 1.5 μm and 3.5 μm microspheres displays similar values. It demonstrates that both, microsphere diameter and total number of superparamagnetic nanoparticles (i.e. the magnetic volume) contained in the sphere affect trapping process.
- (3) For the same magnetic weight, bigger particles should experience stronger deviation, but increase of magnetic volume leads to more efficient capturing of smaller particles.
- (4) Quantitative measurements of magnetic interaction between superparamagnetic microsphere and TMP sample can be used for validation and optimization of the model used for calculations of the microspheres trajectory in microfluidic applications.

For NdFeB microsphere probe:

- (1) Force profile in the vicinity of a magnetic junction is complex: a repulsive interaction following by an attractive one (or the reverse according to the magnetic junction configuration) is recorded. This behaviour demonstrates that the magnetization of the sphere does not flip during the experiments.
- (2) The maximum force intensity of each phase (attractive or repulsive) is microsphere size dependent: it increases with the microsphere diameter and therefore magnetic volume.
- (3) The maximum force intensity for repulsive and attractive phases above the same magnetic junction or two neighbouring junctions can be dissymmetric due to (i) the angle between the sphere and the micromagnet array magnetizations and (ii) the magnetic inhomogeneity of the sample (for example, the variation of reversed zone depth or shape and local variations of magnetic properties).
- (4) The qualitative characterization revealing the asymmetry of magnetic junctions can be employed for estimation of TMP sample quality.
- (5) Direct measurements of trapping force exerted by magnetic junctions can explain stronger deviation of magnetic particles towards some interfaces (exhibiting stronger forces) explaining the formation of additional magnetic patterns.

References

- 1 “High performance hard magnetic NdFeB thick films for integration into micro-electro-mechanical systems”, N. M. Dempsey, A. Walther, F. May, and D. Givord, *Applied Physics Letters* 90, 092509 (2007).
- 2 “Methode et util de generation automatique de modele pour l’optimisation fortement contrainte des microsystemes magnetiques”, H. L. Rakotoarison, PhD thesis, Grenoble, France (2007).
- 3 “Analytical Calculation of Cuboidal Magnet Interactions in 3D”, J.P. Yonnet, H. Allag, The 7th International Symposium on Linear Drives for Industry Applications (LDIA 2009), Incheon, Korea, pp. 162-165 (2009).
- 4 http://www.mqitechnology.com/downloads/powder_datasheet_PDF/MQP-S-11-9-20001-070-pds.pdf
- 5 “Gradient based optimization of semi-numerical models with symbolic sensitivity: Application to a simple ferromagnetic MEMS switch device”, B. Delinchant et al, 10th International Workshop on Optimization and Inverse Problems in Electromagnetism (OIPE 2008), Germany (2008).
- 6 “Formal Sensitivity Computation of Magnetic Moment Method”, H. L. Rakotoarison, V. Ardon, O. Chadebec, B. Delinchant, S. Guerin, and J.-L. Coulomb, *IEEE Transaction on magnets*, Vol. 44, No. 6 (2008).
- 7 “Autonomous micro-magnet based systems for highly efficient magnetic separation”, L. F. Zanini, N. M. Dempsey, D. Givord, G. Reyne, and F. Dumas-Bouchiat, *Appl. Phys. Lett.* 99, 232504 (2011).
- 8 “Tilt of atomic force microscope cantilevers: effect on spring constant and adhesion measurements”, L. O. Heim, M. Kappl, and H. J. Butt, *Langmuir*, Vol. 20, No.7, pp. 2760-2764 (2004).
- 9 “Some aspects of Magnetic Force Microscopy of Hard Magnetic Films”, G. Ciuta, F. Dumas-Bouchiat, N.M. Dempsey, O. Fruchart, *IEEE Transactions on magnets*, Vol. 52, No. 9 (2016).
- 10 “Magnetic characterization of micropatterned Nd–Fe–B hard magnetic films using scanning Hall probe microscopy”, M. Kustov,, P. Laczkowski, D. Hykel, K. Hasselbach, F. Dumas-Bouchiat, D. O’Brien, P. Kauffmann, R. Grechishkin, D. Givord, G. Reyne, O. Cugat, and N. M. Dempsey, *J. Appl. Phys.* 108 (2010).

Chapter V: Conclusions and prospects

- V. Conclusions and prospects 139**
- V.1 Conclusions..... 139
- V.2 Prospects 141
- References 143

V. Conclusions and prospects

V.1 Conclusions

The work performed during my PhD led to a deeper understanding of the interaction between an individual (sub)micronic sphere and a NdFeB micromagnet array fabricated by TMP process. As a result of this study we obtained 3D quantitative force maps and deduced specific force-curves above the MJs where the trapping of magnetic particles takes place. Based on these results, we have quantified magnetic interaction and demonstrated its variation in a function of distance according to the dimensions and magnetic properties of sphere and sample. During this study complementary information about micromagnet array arose: it allows quantification of TMP sample magnetic inhomogeneity. Additionally in the framework of this thesis a number of μ MI samples with NdFeB and SmFeN particles were fabricated and their basic characterization has been performed.

Study of magnetic interaction between magnetic microsphere and TMP sample

Our original approach permits quantitative measurements of trapping force between a single magnetic (sub)microsphere and a TMP sample for any lateral position of the sphere (above the MJ, inside RZ or NRZ) at a fixed distance (up to 3 μ m). It is based on the use of *Micro Particle Scanning Force Microscopy* (MPSFM) with *smart* probes and provides the magnetic 3D force maps. A numerical approach was developed to support this experimental work.

For *smart* probe fabrication a single magnetic (sub)microsphere was placed on the tip apex of a non-magnetic AFM cantilever by one of the developed approaches: 1st approach is based on the imaging and manipulation capabilities of commercial AFM; 2nd approach is based on the capabilities of a dual beam FIB/SEM machine equipped with a micromanipulator and permits accurate microsphere positioning on the tip apex. We have succeeded to fabricate magnetic microsphere probes with the superparamagnetic and NdFeB microspheres ranging from 0.3 μ m up to 3.5 μ m diameter.

MPSFM conducted with smart microparticle probes, or the so-called *Microsphere Scanning Force Microscopy* (MSFM) is based on the standard double pass MFM technique and allows quantification of interaction between magnetic microsphere and TMP sample. The precise force/force gradient measurements are achieved via (i) calibration of microparticle probe spring constant by thermal tune method, (ii) SEM measurement of microsphere diameter and calculation of its magnetic volume and (iii) careful definition of the distance between microsphere and magnetic layer of TMP sample. A key feature of MSFM is that dimensions and magnetic properties of the attached sphere are well known thus, the effective tip volume relevant for magnetic imaging can be determined.

For superparamagnetic microsphere probe the force acting on it from TMP micromagnet array is always attractive and reaches its maximum when the microsphere centre and the magnetic junction are aligned. It means that MSFM probe with superparamagnetic microsphere can be employed for precise localization of maximum magnetic field gradient corresponding to the position of the domain wall. The strength of the attraction between TMP sample and superparamagnetic microsphere depends on the sample properties and sphere diameter and total number of magnetic nanoparticles distributed inside it (i.e. the magnetic volume). Previously conducted experiments have shown that for a fixed ratio between magnetic volume and total microsphere volume, bigger particles experience stronger deviation. Indeed additionally performed simulations demonstrated that increase of the sphere diameter (for a fixed magnetic volume) influence magnetic interaction stronger than the change of magnetic volume (for a fixed diameter). Nevertheless from the experimental force density curves we have deduced that increase of magnetic volume in smaller particles leads to more efficient capturing of them: increase of magnetic weight compared to the total

microsphere weight can compensate smaller particle size. These observations drive us to the conclusion that the most relevant parameter in the trapping processes is the sphere size, though the increase of magnetic volume enhances magnetic interaction as well.

Though the main aim of this work was to measure magnetic interaction between sphere and TMP sample from obtained force maps we have deduced new relevant information about TMP sample structure. Indeed, we have demonstrated that TMP fabrication process leads to high magnetic inhomogeneity of RZ: average variation in magnetic signal sensed with MSFM probe (magnetic roughness) is up to five times higher for RZs than for NRZs; the local variation in magnetic signal inside RZs is in the same order of magnitude as the magnetic signal above the MJs. Taking into account the quantitative characterization of RZ magnetic roughness and the fact that magnetic microparticles are attracted to the regions where the magnitude of magnetic field gradient is maximal we can assume that some magnetic microparticles would be trapped not only above the MJs, but also inside the RZs. Indeed, this assumption is confirmed by additional trapping experiments.

In contradiction to superparamagnetic microsphere, force acting between NdFeB microsphere and TMP micromagnet array can be attractive or repulsive according to the sample and magnetic microsphere magnetization directions. Thereby additional information about TMP sample can be deduced from the MFM maps. We have observed the dissymmetrical behaviour in vicinity of MJs: (i) attractive force is at least 10% different from the repulsive one above the same MJ; (ii) attractive (repulsive) force above one MJ is at least 10% different from the repulsive (attractive) force above the second (neighbouring) MJ. The 10% difference can be explained by the probe holder construction that leads to the tilt of the probe of about 10 degrees introducing an in-plane component of the sphere magnetization sensitive to the sample stray field. However, in the most of our experiments much stronger dissymmetry was observed. Taking into account the foregoing, we have conducted additional experiments to test the assumptions about impact of the experimental parameters (like scan direction and angle) and tilt in magnetization of TMP sample. These hypotheses were excluded which drives us to the conclusion about local sample inhomogeneity, in particular inside the RZ: local variations in alignment of individual grains or tilt in magnetization of the RZ combined with the variation of its depth and shape could explain dissymmetrical magnetic signal in vicinity of MJ.

For both, superparamagnetic and NdFeB microspheres, we have shown that the diameter and magnetic volume of the sphere play important role in the interaction. Decrease of magnetic field with the distance leads to a lower magnetic action on the top of a bigger sphere, while it should be equal for the bottom of both, smaller and bigger spheres.

We have shown that for implemented MSFM procedure in case of micromagnet array with surface roughness comparable to *LSH* we should take into account the height of Nd-rich bumps in the definition of separation distance. Increase of the gap between sphere and top of magnetic layer due to Nd features affects the force sensed with microparticle probe decreasing its value by $\sim 15\%$. To minimize the effect of Nd-rich bumps on the force measurements we have developed an algorithm to exclude them from the MFM maps.

Taking into account the foregoing (different nature of magnetic interaction between superparamagnetic or hard magnetic microsphere and TMP sample; dissymmetry of magnetic response above the MJs, effect of the Nd-rich bumps) the adequate force-distance curves were deduced leading to magnetic interaction in nN range (from few nN up to hundred nN) between a single magnetic microsphere and a TMP sample for the separation distance up to 3 μm with the step of 0.1 μm .

The examination of experimental results conducted according to the same protocol, but with different types of microsphere probes (superparamagnetic or hard magnetic) underlines the flexibility of MSFM method and provides complementary information about sphere-sample interaction.

Simulations have been performed to improve the analysis of experimental results. The

validity of the force-distance curves was supported by comparison with numerical calculations. The obtained analytical results are in agreement with experiments confirming that in trapping applications the magnetic particles should be captured along the MJs due to the strongest force gradient observed above the interface between NRZ and RZ. Nevertheless, the difference between predicted by modelling and experimental results underlines the effect of magnetic roughness revealed and quantitatively measured with Microsphere Scanning Force Microscopy.

Different nature of magnetic microspheres (superparamagnetic or hard magnetic) allows modelling of various processes. Thus, polystyrene microspheres functionalized with iron oxide nanoparticles can serve as a reasonable model for biological species tagged with magnetic nano-inclusions due to their similarity in diameter, density, magnetic particles distribution, Young's modulus and so on. Hard magnetic microspheres due to their excellent magnetic characteristics and fixed direction of magnetization can be employed for quantitative magnetic characterization.

V.2 Prospects

Based on the recent progress made by a number of groups with micromagnet arrays fabrication, there is much potential to further microfluidic applications for magnetic particles trapping, positioning, sorting and so on. The developed quantitative MFM imaging based on *Magnetic Particle Force Microscopy* with probes of known magnetic volume and magnetization is of prime interest.

Micro Particle Force Microscopy probes

The two approaches developed for microparticle probe fabrication can be implemented to make the probes with attached magnetic or non-magnetic (sub)micron size objects of different shape and nature. The approach based on FIB/SEM machine capabilities provides higher precision in sphere positioning. The use of such *smart* probes could minimize or avoid several issues arising in MFM measurements as well as to open the new prospects for AFM and MFM measurements:

- Cantilevers with attached hard magnetic sphere can be magnetized in any direction (for magnetically isotropic sphere) in order to be sensible to the field produced by samples with in-plane, out-of-plane and partially rotated magnetization.
- Probes with diamagnetic particle attached to the tip apex can be employed for diamagnetic levitation force measurements. For this purpose the numerical model developed in this thesis could be adapted (diamagnetic material can be introduced in CADES framework) to estimate diamagnetic force. Based on this value, the cantilever with correct spring constant can be chosen to quantify experimentally the diamagnetic force. The protocol similar to the one used for measurements of interaction between NdFeB sphere and TMP sample can be employed.
- Finally, magnetic microsphere probes could act as a motive micromagnet and force sensor, to localize, identify and quantify the presence of magnetic micro/nano-particles inside a (micro)system [1] dedicated to biological trapping of single species.

Direct measurement of magnetic interaction for improvement of microfluidic devices

The results obtained with superparamagnetic microsphere probes could improve the design of future microfluidic devices:

- The knowledge of the trapping force at a certain distance can help (i) to adjust the height of microfluidic channel and microsphere flying altitude; (ii) to calculate the trajectories of magnetic microspheres attracted by micromagnets in microfluidic devices.
- The force density curves define the quantity required to functionalize biological cells according to their size. The knowledge of minimal magnetic volume enough for trapping biological object of interest allows diminishing the risk of toxicity.

Additional experiments

Despite a wide range of experiments carried out for characterization of TMP micromagnet array and measurements of its interaction with magnetic (sub)micro-object some additional test could be performed.

- The force-distance curves for measurements carried out in liquid could be obtained. This should help to reproduce the conditions in microfluidic devices. The comparison with experiments conducted in air may reveal the presence of additional long-range forces acting on the probe in liquids, for example the electrostatic double-layer force. The protocol established for MSFM measurements could be adjusted for experiments in solutions [2].
- The basic trapping experiments could be performed with “flat” TMP samples to exclude the hypothesis that the particles captured out of magnetic junctions are trapped mainly due to morphological structure of the sample (between Nd-rich bumps).
- To measure the interaction between magnetic microsphere probe and micromagnet sample at longer distances (for $LSH > 3 \mu\text{m}$), additional piezo scanner can be attached to the sample holder. This can be especially attractive for big diameter hard magnetic microspheres that are sensitive to the sample stray field at larger distances.
- A possible solution for non-destructive direct force measurements between magnetic microparticle probe and sample is to conduct the first scan in dynamic mode (to decrease possible tip and sample damage) and to perform the second scan in dynamic mode by recording both the static deflection of the cantilever at the same time as the phase and/or amplitude variation. In this way, both force and force gradient of the magnetic interaction could be recorded in one slot.

Additional simulations

- Additional simulations could be performed to validate the assumptions about RZ magnetic inhomogeneity. Thus, small inclusions with higher or lower magnetization can be included in RZ; variation of the reversed zone depth, shape and magnetization direction can be introduced into the model for further comparison with experimental results.
- To exclude the “edge” effect of the cube used to model magnetic microspheres (due to limitations of CADES) the sphere could be modelled as a set of parallelepipeds of different dimensions or variation of the mesh shape could be used.
- Superparamagnetic microsphere could be modelled as a cube of smaller than the sphere volume (inside the sphere), but with equal magnetic volume.

As since the beginning of the work, the MPSFM has been extended to characterize other micromagnet arrays [3] at Neel Institute or in collaboration with other institutes to study trapping devices [1] it is of prime interest to carry out the experimental and numerical studies in order to improve the future applications where magnetic action on individual objects at micro- and nano- scale is involved.

References

- 1 “Detection of a magnetic bead by hybrid nanodevices using scanning gate microscopy”, H. Corte-León, P. Krzysteczko, F. Marchi, J.-F. Motte, A. Manzin, H. W. Schumacher, V. Antonov, O. Kazakova *AIP Advances*, No. **6**, 056502 (2016).
- 2 “Magnetic force microscopy in liquids”, P. Ares, M. Jaafar, A. Gil, J. Gomez-Herrero, A. Asenjo, *Small*, Vol. 11, No. 36, pp. 4731-4736 (2015).
- 3 “Mechanotransductive cascade of Myo-II-dependent mesoderm and endoderm invaginations in embryo gastrulation”, D. Mitrossilis, J.-C. Roper, D. Le Roy, B. Driquez, A. Michel, C. Menager, G. Shaw, S. Le Denmat, L. Ranno, F. Dumas-Bouchiat, N. M. Dempsey, E.I Farge, *Nature Communications*, 8 (2017).

Annex II.1. TMP mask fabrication procedure

Mask production consists of few steps:

Step 1: 5 nm of Ta or Cr deposited on the substrate as an adhesion layer by sputtering;

Step 2: 100 nm of copper deposited by sputtering;

Step 3: 2 μm of a negative photoresist (ma-N 420) deposited by spin-coating, then lithography is used to create a required for TMP pattern;

Step 4: up to 2 μm of copper is electrodeposited on the sputtered copper layer;

Step 5: photoresist is removed with acetone exposing the copper surface, which is then wet etched using Chrome Etch 18.

Annex II.2. Main approaches to magnetic field calculations

There are three main approaches to calculate a field from a magnet with magnetization M [1]:

- to calculate the dipole field by integrating over the volume distribution of magnetization;
- to apply the Amperian approach (bound currents) where the magnetization is replaced by an equivalent distribution of current density;
- to apply the Coulombian approach (equivalent charges) where the magnetization is replaced by an equivalent distribution of magnetic charge.

Schematics of these models are presented in Figure 1 for a cylinder with uniform magnetization M .

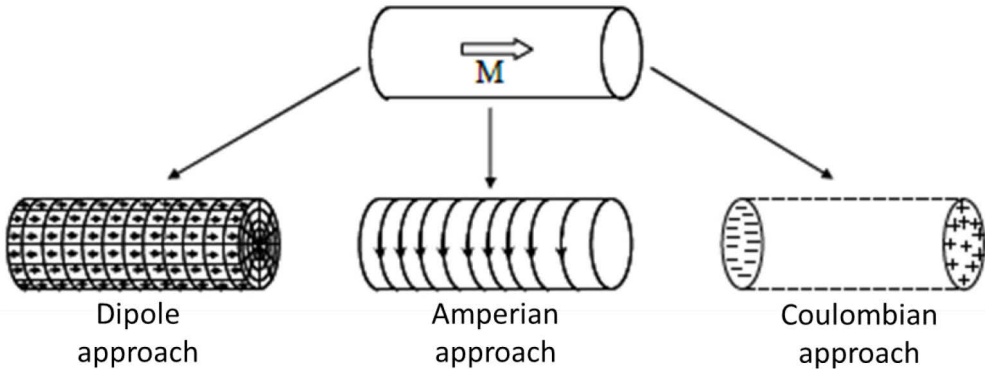


Figure 1. Schematics of Dipole, Amperian and Coulombian approaches for modelization of cylinder magnet with uniform along its axis magnetization M .

The three approaches briefly described above provide identical results for the field in free space outside the magnetized material but not within it. Dipole approach is time-consuming method that systematically requires the volume integrations. The Amperian approach is more suitable for calculation of magnetic field for solid of revolution and the Coulombian approach is better from the computation point of view for solid bodies of parallelepiped shape (Figure 2).

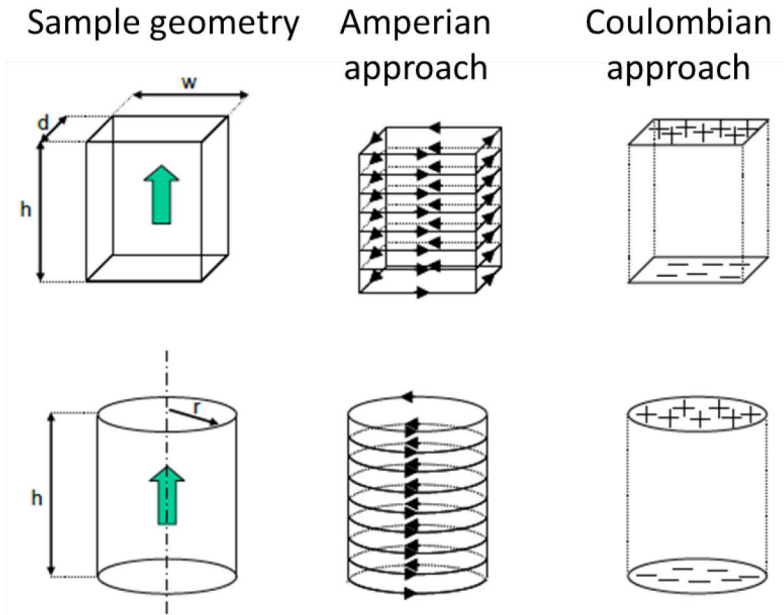


Figure 2. Schematics of the Amperian and Coulombian approaches for magnetic field modelization of cylinder and parallelepiped [2].

Indeed, applying Amperian approach for modelling of parallelepiped the calculation of the field created by currents from four side surfaces is necessary; while with Coulombian approach the calculation of the charges from two (upper and lower) surfaces is required decreasing the computation time by a factor of two. From the other hand, for solid of revolution (cylinder) magnet Amperian approach is used for integration of the current only on the lateral surface of the cylinder; while with Coulombian approach the surface charges should be integrated twice: for upper and lower circular ends.

Thus Coulombian equivalent surface charge approach was used in our model. The geometry of the micromagnet array is simple (in our case only parallelepipeds) and pure analytical formula could be used.

The magnetic field arising from the micromagnet sample and the one from the magnetic microsphere were computed. In the present experimental setup, the cantilever deflection gives access to the magnetic force acting on the microsphere along the Z direction only. Thus, all the components of the magnetic field were considered, but only the Z-component of the force was computed in the calculations.

References

-
- 1 “Magnetism: Materials and Applications”, Trémolet de Lacheisserie, Volume 2 E // Springer Science & Business Media. – Science, p. 517 (2005).
 - 2 “Methode et outil de generation automatique de modele pour l’optimisation fortement contrainte des microsystemes magnetiques”, H. L. Rakotoarison, PhD thesis, Grenoble, France (2007).

Annex II.3 Magnetic field and field gradient simulations for TMP magnets

The total magnetic field B produced by TMP samples with stripes of different width ($w = 50, 100$ and $200 \mu\text{m}$) and corresponding field gradient profiles $\partial B/\partial z$ were calculated with Model 1 [1]. Red curves correspond to the sample with stripes width $w = 50 \mu\text{m}$, green curves to the one with $w = 100 \mu\text{m}$ and blue curves to the one with $w = 200 \mu\text{m}$. It should be noticed that red curves sometimes are partially covered by green and blue ones, and green curves are partially superposed by blue ones. Zero lateral position corresponds to the first magnetic junction for all three modelled samples.

Figure 1 presents simulated results for B and $\partial B/\partial z$ at distance of 1 (a,b), 10 (c,d) and 50 (e,f) μm from the top of modelled TMP sample. Detailed analysis of Figure 1(a,b) is presented in Chapter II (section II.2.1 Modelling of TMP micromagnet array properties). Here the field and field gradient at distances of 10 and 50 μm will be discussed.

Decrease of the field intensity B by a factor of 8 (from 0.35 T to 0.045 T) is observed with enlargement of distance above the surface from 1 μm to 10 μm , and by a factor of 100 (from few hundreds of mT to few mT) with the change of distance from 1 μm up to 50 μm . This indicates strong dependence of the magnetic field intensity with the distance. Magnetic field gradient $\partial B/\partial z$ is more sensitive to the change of distance and decays faster than the field B (by a factor of ~ 10).

The impact of the feature width with increase of the distance from 1 μm to 10 μm is not negligible anymore. At 10 μm from the surface wider magnetic stripes (100 and 200 μm) produces slightly higher magnetic field above the magnetic junctions (8.5%) than the narrow features (50 μm) while the field in the middle of pattern remain nearly zero. This is not the case for narrow (50 μm) magnetic stripes pattern, where magnetic field remains positive all over the pattern (0.027 T above the middle of the pattern and 0.045 T above the magnetic junctions).

Similar behaviour exhibit magnetic field gradients at 10 μm from the surface: for all stripes width the maximum (absolute value) is observed above the magnetic junctions; for wide features (200 and 100 μm) $\partial B/\partial z$ drops to zero in the middle of the pattern while for narrow stripes (50 μm) it remains slightly negative.

When the distance above the sample reaches 50 μm , both field and field gradient are very close to zero (few mT and hundred of T/m, respectively). For narrow features (50 μm) the changes in intensity of B and $\partial B/\partial z$ above magnetic junctions and in the middle of pattern are barely noticeable. With increase of the features width (up to 200 μm) the ratio between field B (field gradient $\partial B/\partial z$) above the magnetic junction and in the middle of pattern reaches 1.5 (3).

To sum up:

- magnetic field B and field gradient $\partial B/\partial z$ reach the maximum above the magnetic junctions;
- for distance of 1 μm above the surface magnetic field and field gradient for all stripes widths are equal to 0 in the middle of the pattern;
- for distance of 10 μm above the surface magnetic field/field gradients are close to 0 in the middle of the pattern for wide features (200 and 100 μm) and remain positive (negative for field gradient) for narrow features (50 μm);
- for the distance of 50 μm above the surface magnetic field/field gradients are close to 0.
- magnetic field B and field gradient $\partial B/\partial z$ decay fast with increase of the distance, but the field gradient drops down faster (by a factor of ~ 10).

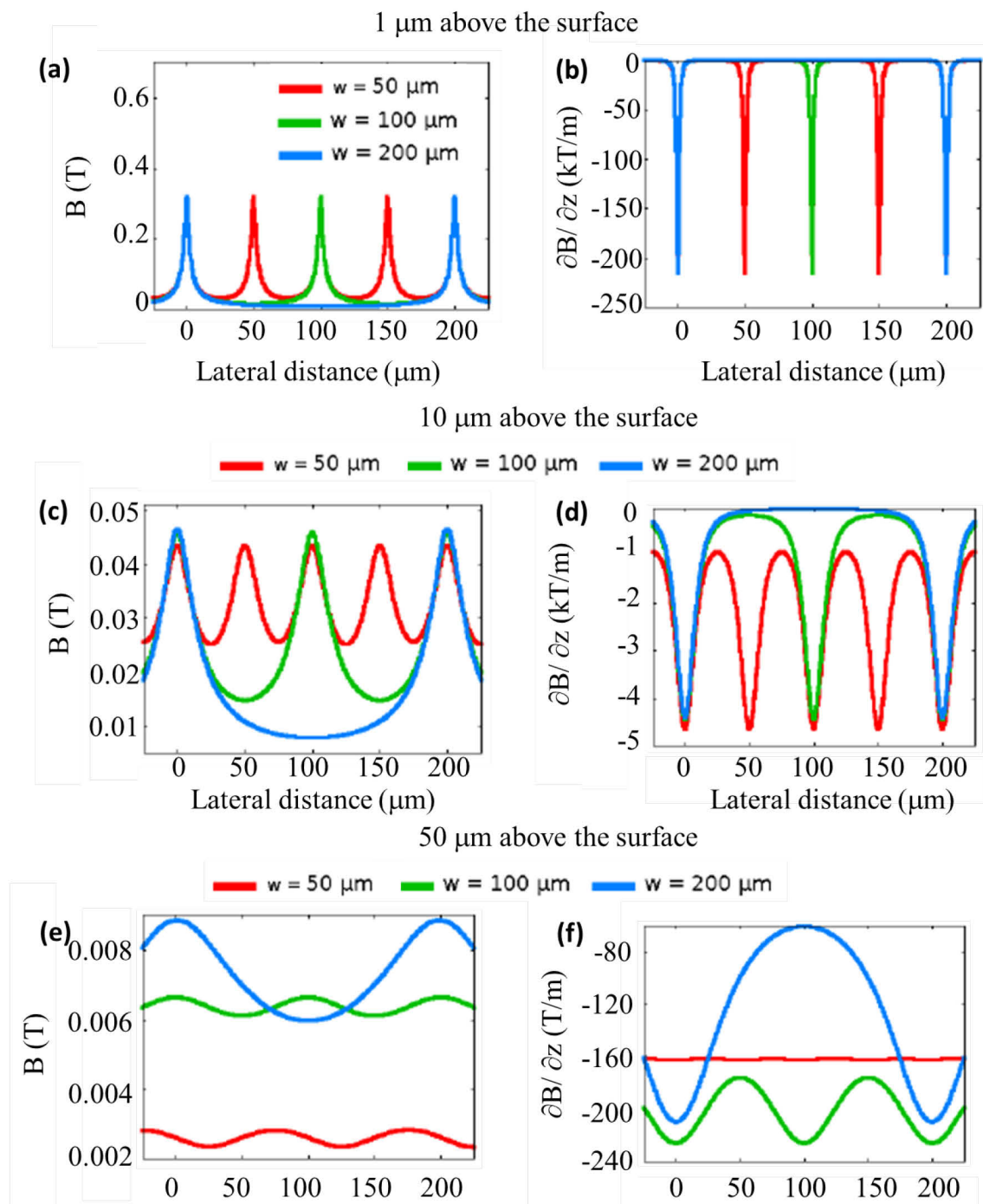


Figure 1. Magnetic field B and field gradient $\partial B/\partial z$ calculated with Model 1 for TMP magnet with stripes of 50 (red), 100 (green) and 200 (blue) μm width at distance of 1 μm (a,b), 10 μm (c,d) and 50 μm (e,f) from the surface [1].

References

- 1 “Une etude experimentale de la coercivite des aimants NdFeB”, G. Ciuta, PhD thesis, Grenoble, France (2013). <NNT : 2013GRENY014>. <tel-00952842>

Annex II.4. Simulation of magnetic field and magnetic force acting on a superparamagnetic microsphere above the “stripes-like” TMP sample with CADES framework

1. To run the simulation open “Calculator” shortcut by double click.

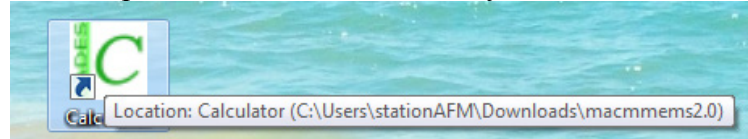


Figure 1. Shortcut to run CADES simulation.

2. Load the file with a model representing superparamagnetic microsphere above the “stripe-like” NdFeB patterned film (Figure 2). Microsphere is presented as a cube of equal volume and placed in the middle of the film.

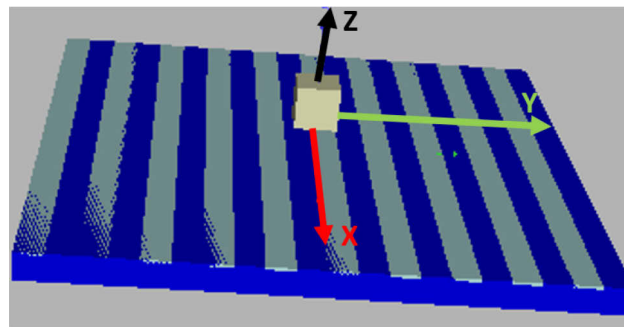


Figure 2. Schematic view of the model used for simulations.

Load the file to set up default values for the simulations (blue area in Figure 3).

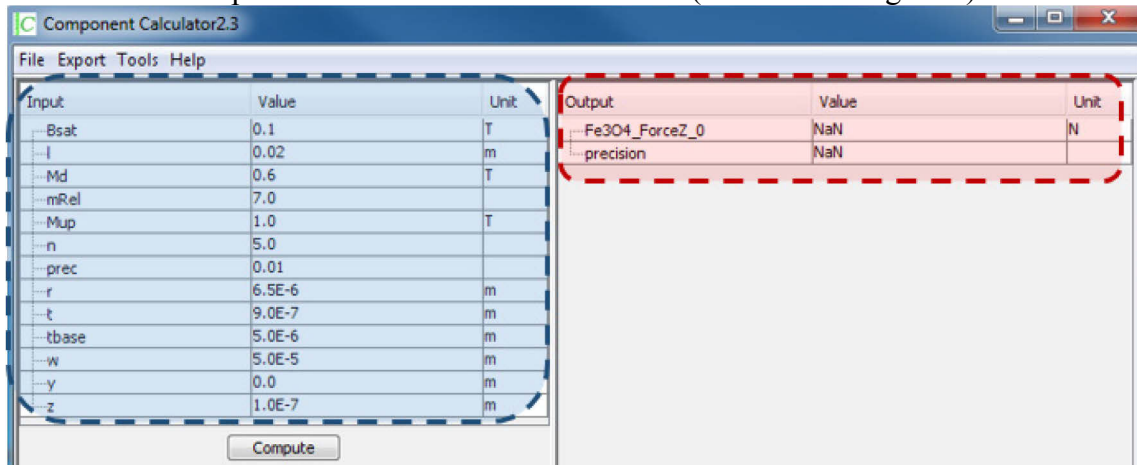


Figure 3. Set up of input values. Input area is marked by blue and output area is marked by red.

3. Input: set up the values (Figure 4):
 - a. $B_{sat} = 0.1\text{T}$ (saturation magnetization, [T])
 - b. $l = 0.02\text{ m}$ (sample width and length, [m])
 - c. $M_d = (0.6; 1.2)\text{T}$ (magnetization of the reversed part, [T])
 - d. $m_{Rel} = 7$ (relative permeability)
 - e. $M_{up} = (1; 1.2)\text{T}$ (initial film magnetization, [T])
 - f. $n = 5$ (number of mesh elements)
 - g. $prec = 0.01$ (precision)
 - h. $r =$ (sphere radius, [m])
 - i. $t = (0.9; 1.3)\text{ }\mu\text{m}$ (reversed part thickness, [m])
 - j. $t_{base} = 5\text{ }\mu\text{m}$ (film thickness, [m])

- k. $w = 50 \mu\text{m}$ (width of the pattern for one line, [m])
- l. y = (lateral position of the sphere above the sample, [m])
- m. z = (distance between bottom of the cube and top of magnetic layer, [m])

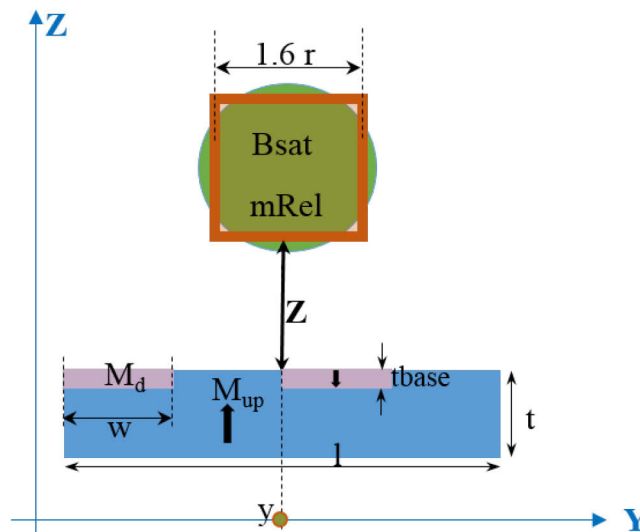


Figure 4. Schematic diagram for the input parameters.

4. Choose **input** (blue area in Figure 3) and **output** (red area in Figure 3) by clicking on the parameters (Figure 5, top):

Output parameters:

Fe3O4_ForceZ_0 (z-component of the force acting on NdFeB microsphere at lateral position y).

5. Set up start, end and step if necessary to compute force/field in several points (green area in Figure 5).

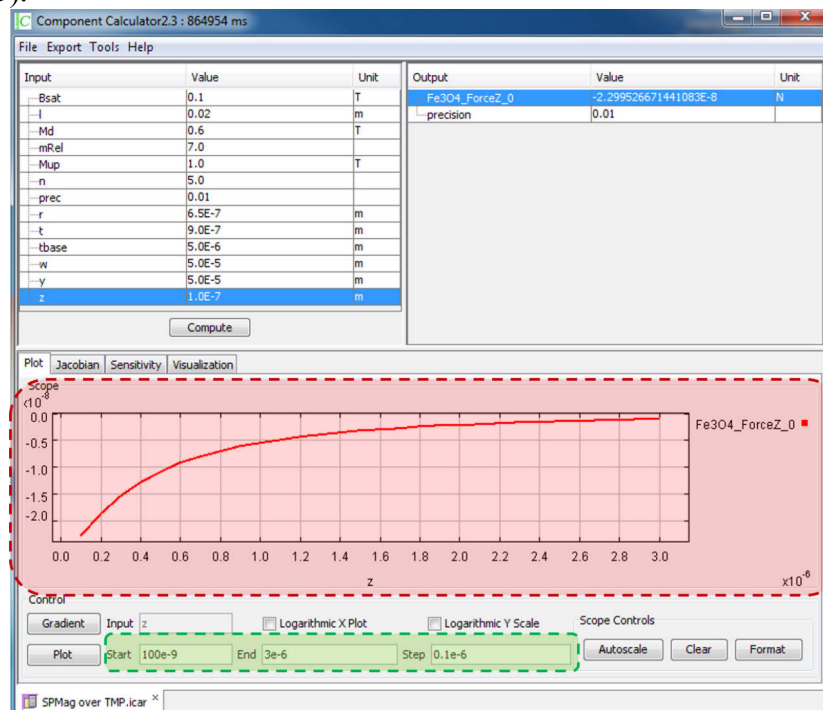


Figure 5. Simulation of the force as a function of the distance z . Top: distance between edge of the cube and top of magnetic layer is chosen as an input. Magnetic force acting on it in z -direction is chosen as an output. Bottom: **Plot of magnetic force as a function of the vertical distance z** (red area) with **the step of $0.1 \mu\text{m}$** (green area).

6. Click **Plot**.

7. To save the data click **Export -> Plot -> choose directory** (Figure 6). File will be saved in ***.dat format**.

Note: numbers will be saved in format **1.234** (not 1,234), therefore for the French software “.” should be replaced by “,”.

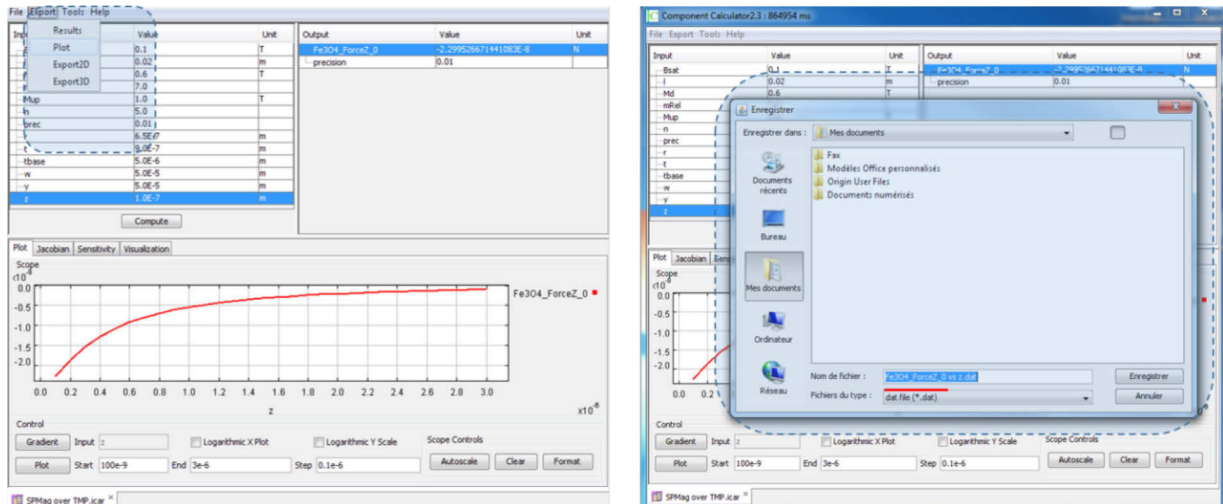


Figure 6. Saving the results of simulation.

8. Multiply obtained force values by the ratio between magnetic and total microsphere volume.

Annex II.5. Simulation of magnetic field and magnetic force acting on a NdFeB microsphere above the “stripes-like” TMP sample with CADES framework

1. To run the simulation open “Calculator” shortcut by double click.

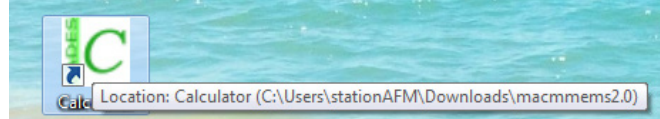


Figure 1. Shortcut to run CADES simulation.

2. Load the file with a model for a NdFeB sphere above the “stripe-like” NdFeB patterned film (Figure 2). Microsphere is presented as a cube of equal volume and placed in the middle of the film.

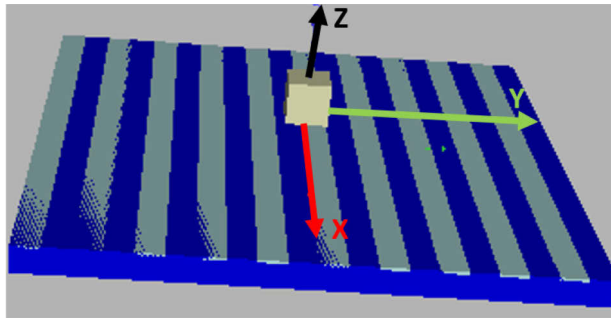


Figure 2. Schematic view of the model used for simulations.

3. Load the file to set up default values for the simulations (blue area in Figure 3).

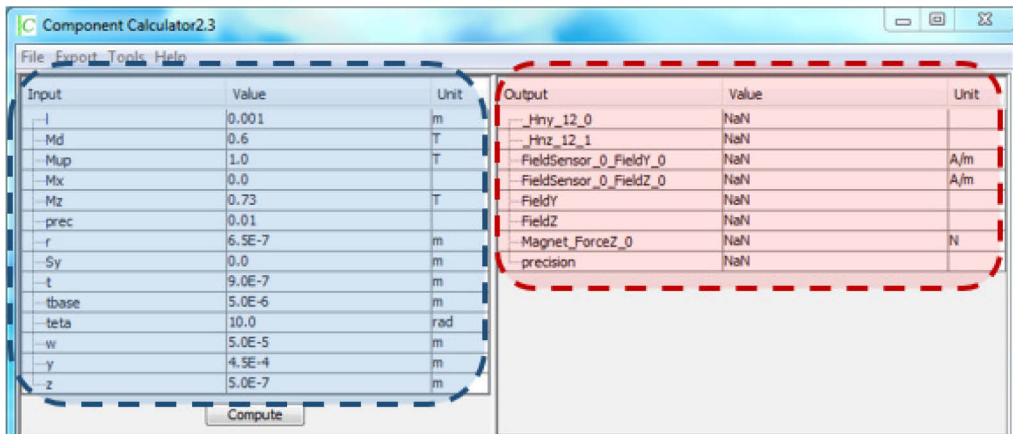


Figure 3. Set up of input values. Input area is marked by blue and output area is marked by red.

4. Input: set up the values (Figure 4):
 - a. $l = 0.02$ m (sample width and length, [m])
 - b. $Md = (0.6; 1.2)$ T (magnetization of the reversed part, [T])
 - c. $Mup = (1; 1.2)$ T (initial film magnetization, [T])
 - d. $Mx = 0$ (probe magnetization along X axis is 0 due to the length of stripe which is \gg than width of the stripe, [T])
 - e. $Mz = (-0.73; -0.76)$ T (sphere magnetization along the Z axis, “-” is to set the direction antiparallel to the initial film magnetization Mup, [T])
 - f. $prec = 0.01$ (precision)
 - g. $r =$ (sphere radius, [m])
 - h. $Sy =$ (lateral position to calculate the field, [m])

- i. $t = (0.9; 1.3) \mu\text{m}$ (reversed part thickness, [m])
- j. $t_{\text{base}} = 5 \mu\text{m}$ (film thickness, [m])
- k. $teta = 10 \text{ deg}$ (tilt of sphere magnetization, [deg])
- l. $w = 50 \mu\text{m}$ (width of the pattern for one line, [m])
- m. $y =$ (lateral position of the sphere above the sample, [m])
- n. $z =$ (distance between sphere and top of magnetic layer, [m])

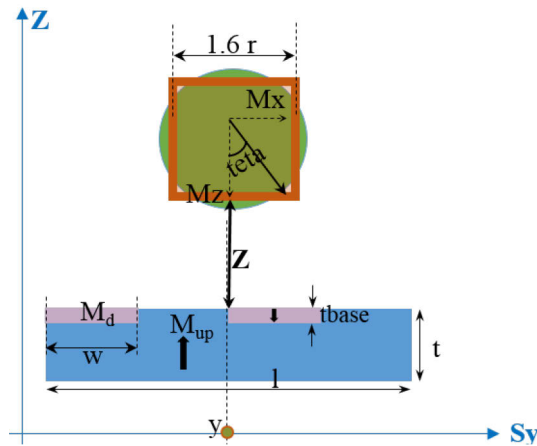


Figure 4. Schematic diagram for the input parameters.

5. Choose **input** (blue area in Figure 3) and **output** (red area in Figure 3) by clicking on the parameters (Figure 5, top):

Output parameters:

- a. FieldSensor_0_FieldY_0 (y-component of the field, A/m)
- b. FieldSensor_0_FieldZ_0 (z-component of the field, A/m)
- c. FieldY (y-component of the field, T)
- d. FieldZ (z-component of the field, T)
- e. Magnet-ForceZ_0 (z-component of the force acting on NdFeB microsphere at lateral position y).

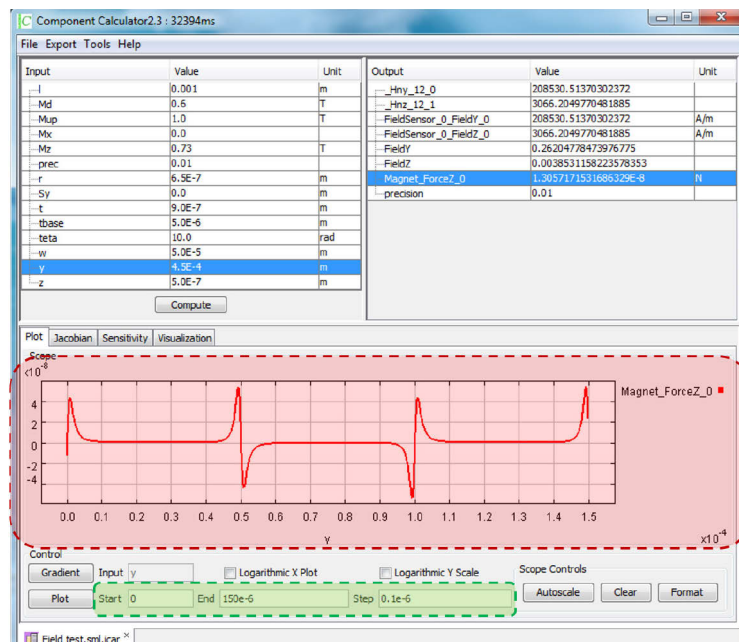


Figure 5. Simulation of the force as a function of microsphere lateral positioning. Top: lateral positioning of microsphere is chosen as an input. Magnetic force acting on it in z-direction is chosen as an output. Bottom: Plot of magnetic force as a function of microsphere lateral positioning (red area) with the step of $0.1 \mu\text{m}$ (green area).

6. Set up start, end and step if necessary to compute force/field in several points (green area in Figure 5).

7. Click **Plot**.
8. To save the data click **Export -> Plot -> choose directory** (Figure 6). File will be saved in ***.dat format**.

Note: numbers will be saved in format **1.234** (not 1,234), therefore for the French software “.” should be replaced by “,”

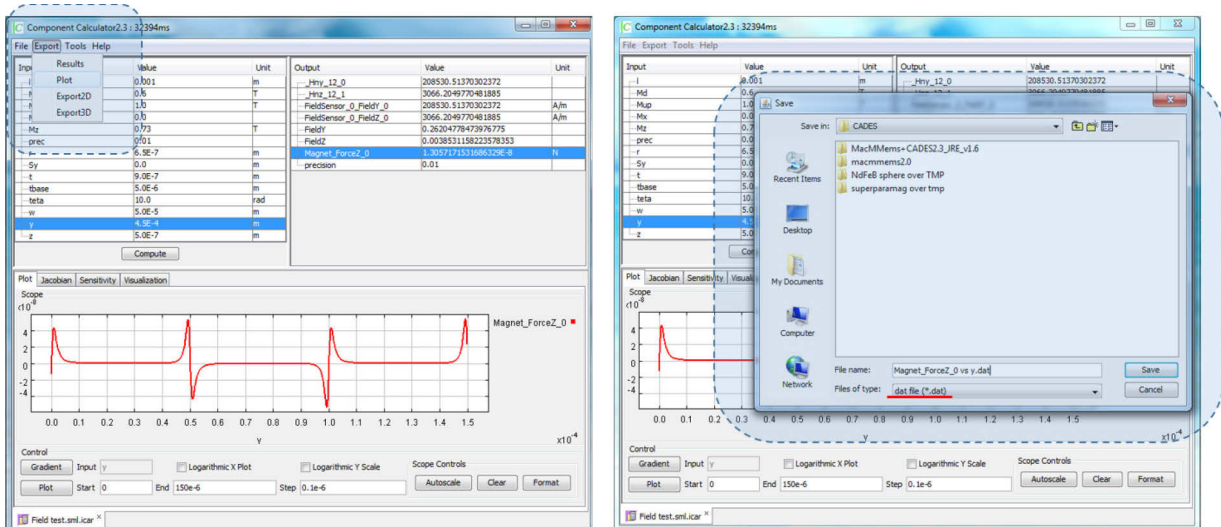


Figure 6. Saving the results of simulation.

Annex III.1. Calculation of the forces arising between the probe and the sample at micro/nano-scale distance

The use of atomic force microscopy to probe the distance dependent forces between various materials separated by air, vacuum or liquids is of prime interest. Figure 1 presents several interactions taking place during scanning process between probe and sample according to the working environment and the tip coating.

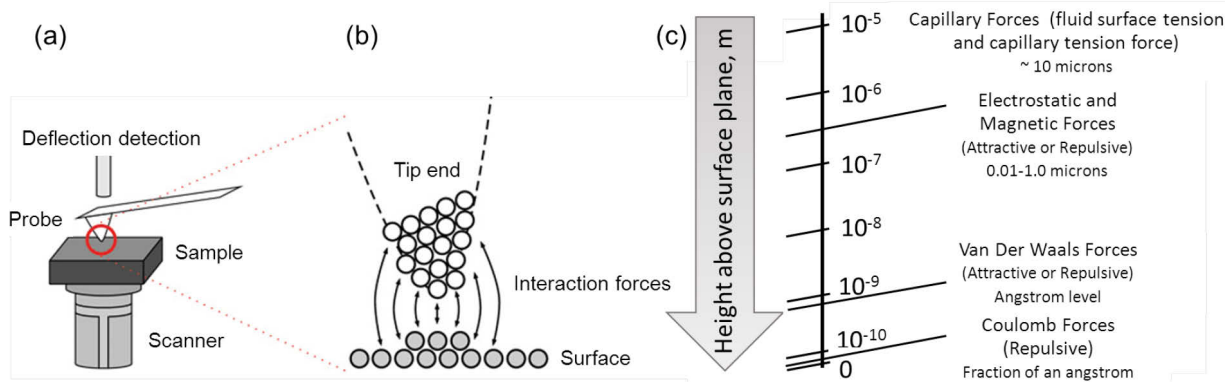


Figure 1. (a) Sketch of a macroscopically flat surface probed by a sharp tip. (b) Atomic structure of tip and sample at small separation distance. (c) Forces acting on the cantilever at the micro/nano-scale in air (adapted from [1]).

For the sake of simplicity the force representing tip-sample interaction $F_{t/s}(z)$ can be considered as an interatomic Lennard-Jones force [2]:

$$F_{t/s}(z) = -A/z^7 + B/z^{13} \quad (1)$$

where z is the actual tip-sample distance, A and B are the coefficients that depend on the type of forces acting between the tip and sample. With the equation (1) only a simple qualitative description of the tip-sample interaction can be provided (Figure 2).

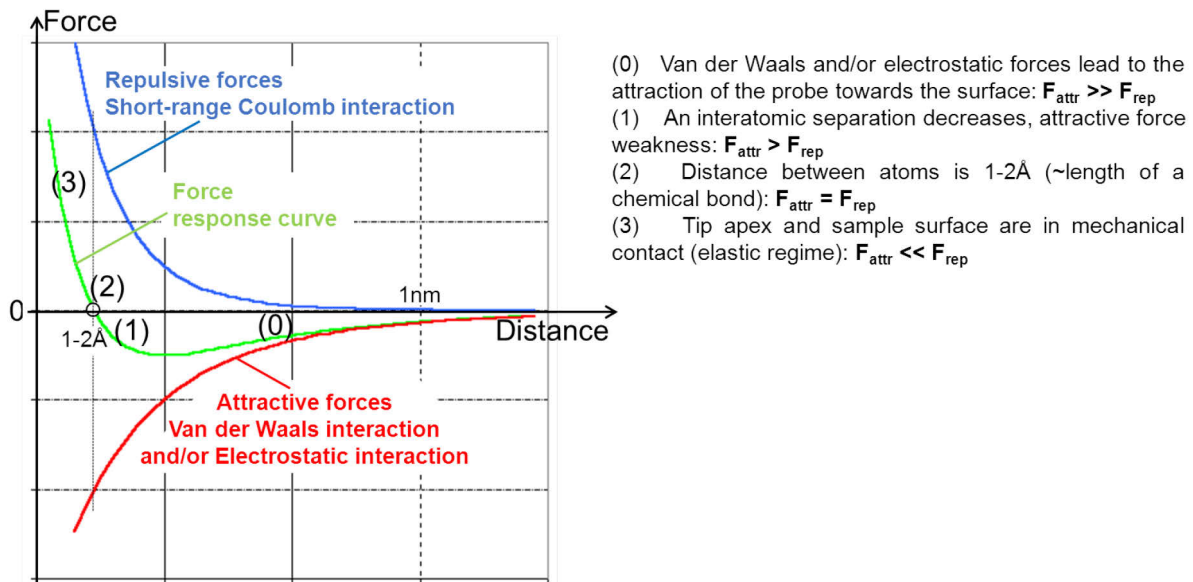


Figure 2. Sketch to illustrate the effect of the distance between tip and sample (modelled as sphere-plane system) on the force between them: short-range repulsive Coulomb interaction (blue), long-range attractive Van der Waals and/or electrostatic interaction (red) and resulting force curve (green).

In practise, the attractive force between surfaces actually follows a force law $-D^{-n}$ with $n \leq 3$ (and not $n = 7$) and the repulsive part of the force is much more complex than the one modelled by the Lennard-Jones force [2].

To estimate the interaction between the probe for Microsphere Scanning Force Microscopy with attached superparamagnetic microsphere and TMP micromagnet array, the probe was modelled as a sphere with diameter $D = 2R = 1 \cdot 10^{-6}$ m and sample surface was modelled as a plane (Figure 3).

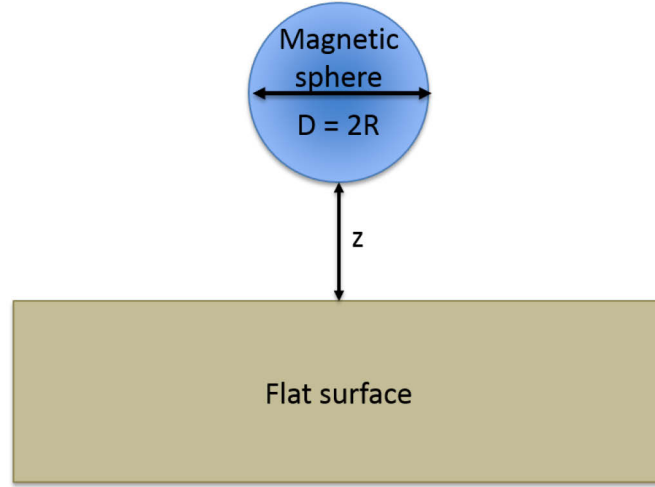


Figure 3. System used for calculation of interactions between probe and micromagnet array: the probe is modelled as a sphere with radius $R = D/2$ and sample surface is modelled as a plane.

For small z values (less than few nm) Van der Waals and Coulomb forces have the strongest impact on the tip-sample interaction. For a chosen tip-sample geometry (Figure 3) Van der Waals forces F_{vdw} can be found as:

$$F_{vdw} = \frac{H_a R}{6z^2}, \quad (2)$$

where H_a is the Hamaker constant (order of magnitude is $10^{-20} \dots 10^{-19}$ J) and R is the tip radius ($0.5 \cdot 10^{-6}$ m).

As it was mentioned above, it is a complex task to describe repulsive Coulomb forces [2]. However, with the knowledge that attractive and repulsive forces are counterbalanced (position (2) in Figure 2) at the distance comparable with the length of a chemical bond ($\sim 1-2$ Å) we can make an approximation:

$$\begin{aligned} F_{rep} &< F_{vdw} \text{ for } z > 1\text{Å} \\ F_{rep} &= F_{vdw} \sim 10^{-6} \text{N for } z = 1\text{Å} \\ F_{rep} &> F_{vdw} \text{ for } z < 1\text{Å} \end{aligned}$$

With increase of the tip-sample distance z (from few nm up to few μm) electrostatic, magnetic and capillary forces take place.

The capillary force F_{cap} is formed due to a thin layer (its thickness depends on humidity) of water vapours adsorbed on the sample surface. Such a layer barely affects attractive forces, whereas it prevents the tip from pulling off from the surface due to its high surface energy. After approximation capillary forces F_{cap} (fluid surface tension force and capillary tension force) can be estimated:

$$F_{cap} = 2\pi R\gamma(\cos \theta_1 + \cos \theta_2) \sim 10^{-7} \text{N}, \text{ for } z \text{ up to few } \mu\text{m}, \quad (3)$$

where $\theta_1 = 52^\circ$ is the contact angle between the water meniscus and the surface and $\theta_2 = 85^\circ$ is the contact angle between the water meniscus and the tip; $\gamma = 73$ mN/m is the liquid's surface tension.

The magnetic force acting on the tip from the sample can be found by

$$\vec{F}_{mag}(r) = \mu_0(\vec{m} \cdot \nabla)\vec{H}(r), \quad (4)$$

where $\mu_0 = 4\pi \cdot 10^{-7}$ N/A² is the magnetic permeability of free space, \vec{m} is the magnetic moment of the tip approximated as a point dipole, \vec{H} is the magnetic stray field of the sample,

r is the space position.

To calculate the interaction between superparamagnetic microsphere and TMP sample Model 2 (Chapter II, II.2.1 Modelling of TMP micromagnet array properties) was implemented. The magnetic force $F_{mag} \sim 10^{-9}N$: varies from 5 nN close to surface ($z = 0.5 \mu\text{m}$) to 1 nN ($z = 3 \mu\text{m}$).

To minimize the effect of electrostatic force F_{el} , both sample and probe were electrically grounded in our experiments. However, with the knowledge of potential difference between the tip and the sample electrostatic force F_{el} can be found:

$$F_{el} = \frac{1}{2} \frac{\partial C}{\partial z} U^2 = \pi \epsilon_0 \left(\frac{R}{z + \frac{z^2}{R}} \right) U^2, \quad (5)$$

where C is the capacitance between the probe and sample, U is the potential difference between the tip and the sample, $\epsilon_0 = 8.854 \cdot 10^{-12} \text{ F/m}$ is the electric constant. For $U = 1 \text{ V}$ and $z = 1 \mu\text{m}$, $F_{el} \sim 10^{-12}N$.

References

-
- 1 <http://www.nanoscience.de/HTML/methods/afm.html>
 - 2 "Force-distance curves by atomic force microscopy", B. Cappella, G. Dietler, Surface Science Reports No. 34 pp. 1-104 (1999).

Annex III.2 Calculations of the cantilever frequency shift due to added mass

An original approach based on AFM manipulation capability was developed (see Chapter III section III.3.1) for Microsphere Scanning Force Microscopy probe fabrication. Worn probes (NSC 15, MikroMasch) and commercial superparamagnetic polystyrene microspheres (microParticles GmbH) functionalized with iron oxide nanoparticles were chosen (Tables 1, 2). More detailed information about probes can be found in [1] and about superparamagnetic microspheres in Annex III.3.

During the fabrication procedure the tip end is plunged into a glue droplet; the glue covers tip sides and adds some mass on the tip end leading to a measurable change in the resonance frequency. The aim of this annex is to estimate the glue mass, m_{glue} .

Cantilever	Resonance Frequency, kHz			Force Constant, N/m			Length $L \pm 5$, μm	Width $W \pm 3$, μm	Thickness $t \pm 0.5$, μm
	min	typ	max	min	typ	max			
NCS 15	265	325	410	20	40	80	125	30	4.0

Table 1. NSC 15, MikroMasch cantilever properties.

Sphere type	Diameter, μm	Density, g/cm ³	wt.% of magnetic NPs	vol.% of magnetic NPs
PS-MAG-S2180	3.90	1.62	40	13

Table 2. Information about superparamagnetic microspheres used for microsphere probe fabrication.

For the first bending mode of a cantilever its resonant frequency is given by [2]:

$$f_0 = \frac{1}{2\pi} \sqrt{k_s/m^*}, \quad (1)$$

where k_s and m^* are the static spring constant and the effective mass. For the first bending mode of a cantilever the effective mass and the spring constant (nearly equal to k_s) are given by:

$$m^* = 0.24 m_0, \quad m_0 = \rho L W t, \quad (2)$$

$$k_s = \frac{E t^3 W}{4L}, \quad (3)$$

where L , W and t are the cantilever dimensions (length, width and thickness, respectively), E is the Young's modulus and ρ is the density of the cantilever.

The deposition of a small mass Δm comparable to that of the cantilever causes the change in the cantilever frequency, Δf :

$$\Delta m = m_{sph} + m_{glue}, \quad (4)$$

where m_{glue} is the mass of deposited glue and m_{sph} is the mass of attached sphere.

As the spring constant k_s remains unchanged, the new resonant frequency f_0' is given by:

$$f_0' = \frac{1}{2\pi} \sqrt{\frac{k_s}{m^* + \Delta m}}, \quad (5)$$

And

$$\Delta f = f_0 - f_0' \quad (6)$$

$$\Delta f = \frac{1}{2\pi} \sqrt{\frac{k_s}{m^*}} - \frac{1}{2\pi} \sqrt{\frac{k_s}{m^* + \Delta m}}$$

$$\Delta m = \frac{k_s m^*}{(2\Delta f \sqrt{m^*} - \sqrt{k_s})^2} - m^*$$

Or using equation (2):

$$\Delta m = \frac{0.24 \frac{Et^3W}{4L} \rho LWt}{(2\Delta f \sqrt{0.24\rho LWt} - \sqrt{\frac{Et^3W}{4L}})^2} - 0.24\rho LWt$$

Taking into account that $\Delta f=100$ kHz (experimental results), $k_s= 40$ N/m (datasheet value) and $\rho = 2329$ kg/m³:

$$\Delta m = 1.77 \cdot 10^{-12} \text{ kg}$$

The mass of the attached sphere m_{sph} is:

$$m_{sph} = \frac{4}{3} \pi R^3 \rho_{sph}$$

$R = 1.95 \cdot 10^{-6}$ m is the sphere radius, $\rho_{sph} = 1620$ kg/m³ is the sphere density

$$m_{sph} = 5 \cdot 10^{-14} \text{ kg} = 0.05 \text{ pg}$$

The mass of the deposited glue m_{glue} is:

$$m_{glue} = \Delta m - m_{sph} = 1.72 \cdot 10^{-12} \text{ kg} = 1.72 \text{ pg}$$

The glue mass is two order of magnitude higher than the sphere mass, therefore the frequency shift is mainly due to the glue deposited on the tip side.

References

1 <http://www.spmtips.com/afm-tip-hq-nsc15-al-bs>

2 “Single microparticles mass measurement using an AFM cantilever resonator”, M. Mauro, R. Battaglia, G. Ferrini, R. Puglisi, D. Balduzzi and A. Galli, Instrumentation and Detectors (2014).

Annex III.3 Superparamagnetic microspheres (microParticles GmbH)

Superparamagnetic beads provided by microParticles GmbH are polystyrene microspheres with iron oxide nanoinclusions randomly dispersed inside. The size of magnetic nanoinclusions is in the range between 1 and 15 nm according to the manufacture's specification. The average diameter was found experimentally [1] equal to 3.3 ± 3 nm. Due to such a small diameter, iron oxide inclusions exhibit superparamagnetic behaviour [2].

According to the manufacture's specification:

- $p_{sph} = (2.4; 2.24; 1.62) \text{ g/cm}^3$ is the density of superparamagnetic microsphere of diameter (0.27; 1.33; 3.9 μm) (Table 1);
- $p_{ps} = 1.0 \text{ g/cm}^3$ is the density of polystyrene;
- $p_{mag} = 5.0 \text{ g/cm}^3$ is the density of magnetic inclusions.
- Iron oxide weight is not less than 30% of the microsphere weight.
- The density of supplied microspheres p_{sph} was measured by pycnometry and confirmed by sedimentation experiments by recording the time of particle settlement.

The total mass of a single magnetic microsphere m_{sph} is equal to:

$$m_{sph} = m_{ps} + m_{mag}, \quad (1)$$

where m_{ps} is the mass of a polystyrene matrix and m_{mag} is the mass of all magnetic inclusions.

Or

$$p_{sph}V_{sph} = p_{ps}V_{ps} + p_{mag}V_{mag}, \quad (2)$$

where V_{ps} is the volume of a polystyrene matrix and V_{mag} is the volume of all magnetic inclusions.

Thus,

$$\frac{V_{mag}}{V_{sph}} = \frac{p_{sph} - p_{ps}}{p_{mag} - p_{ps}} \quad (3)$$

And

$$\frac{m_{mag}}{m_{sph}} = \frac{V_{mag}}{V_{sph}} \cdot \frac{p_{mag}}{p_{sph}} \quad (4)$$

The results of calculations are summarized in Table 1. The volume of magnetic NPs vol.% was calculated as a ratio between volume of all magnetic inclusions inside a microsphere and microsphere total volume according to the equation (3). The weight of magnetic NPs wt.% was calculated as a ratio between weight of all magnetic inclusions inside a microsphere and microsphere total weight according to the equation (4).

Sphere type*	Diameter* (μm)	Density* (g/cm^3)	wt.% of magnetic NPs	vol.% of magnetic NPs
PS-MAG-S1850	0.27	2.4	73	35
PS-MAG-S1645	1.33	2.24	67	30
PS-MAG-S2180	3.90	1.62	40	13

Table 1. Information about superparamagnetic microspheres used for microparticle probe fabrication. Data marked with * is provided by microParticles GmbH.

In the presence of a magnetic field, described above superparamagnetic microsphere is submitted to the magnetic force due to the action of the field on each of iron oxide nanoinclusions. Thus, for the whole microsphere the average magnetization can be obtained

by summing magnetic moments of all nanoinclusions and normalizing with respect to the total volume. The calculations of the force acting on a single magnetic inclusion as well as on the whole microsphere are presented in [3]. The normalized magnetization curves for 2.8 and 1 μm superparamagnetic microspheres and their fitting with Langevin function are presented in Figure 1. For a given size microparticles an average magnetization of 460 kA/m was found.

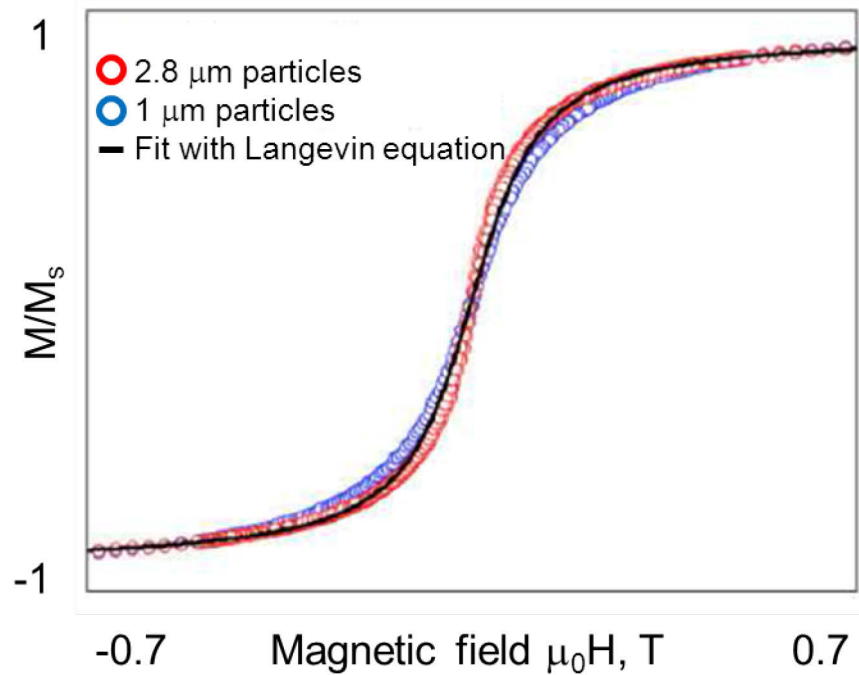
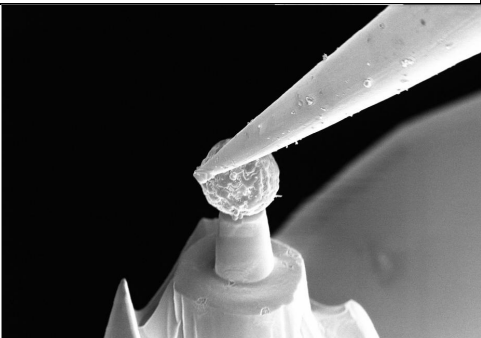
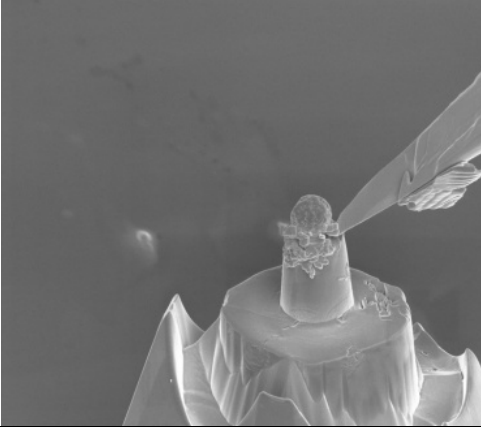
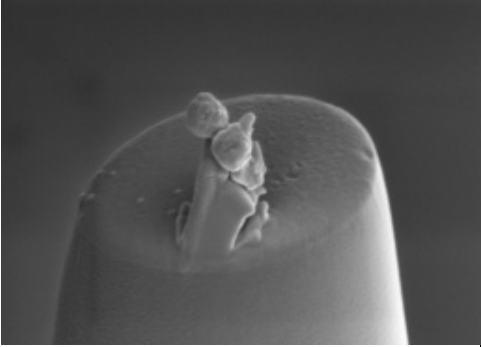
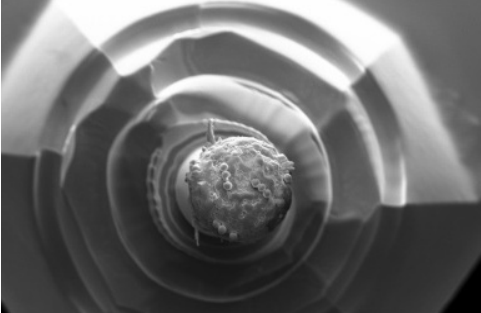


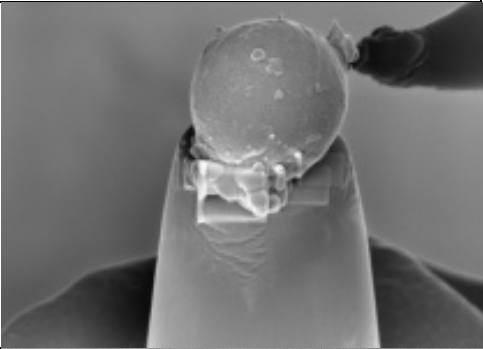
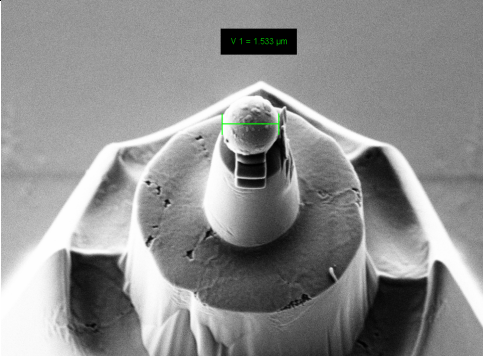
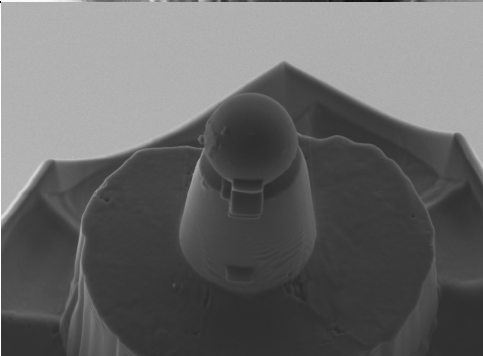
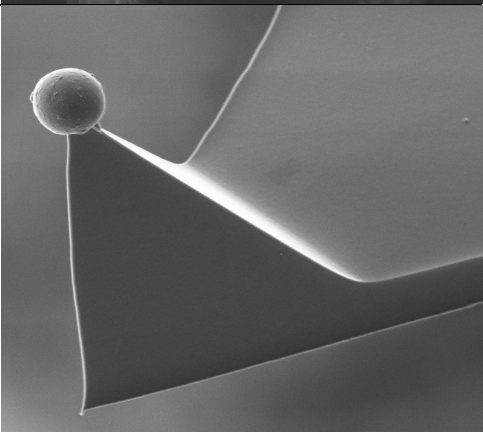
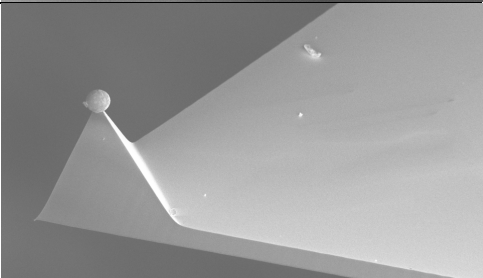
Figure 1. Magnetization curves of superparamagnetic microspheres of 2.8 μm diameter (red) and 1 μm diameter (blue) and fitting with Langevin equation [3].

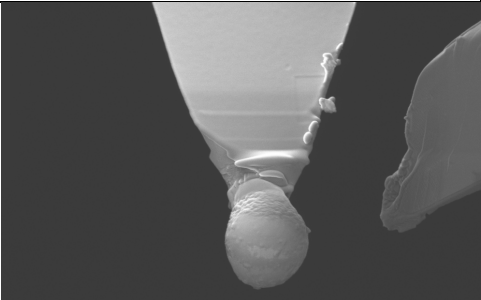
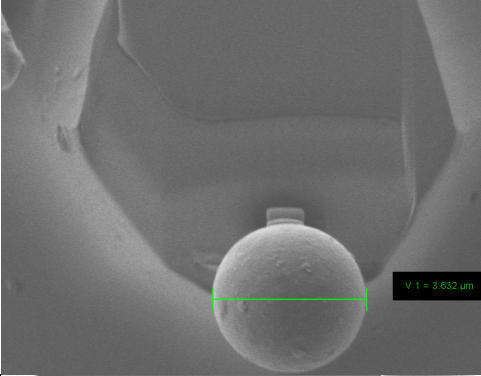
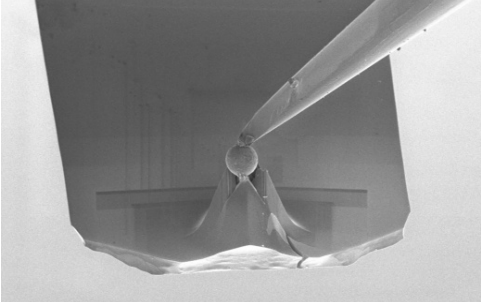
References

- 1 “Autonomous micro-magnet based systems for highly efficient magnetic separation”, L. F. Zanini et al, *Appl. Phys. Lett.* 99, 232504 (2011).
- 2 “Magnetic properties of variable-sized Fe_3O_4 nanoparticles synthesized from non-aqueous homogeneous solutions of polyols”, D. Caruntu et al, *J. Phys. D: Appl. Phys.* 40, pp. 5801–5809 (2007).
- 3 “Structures magnetiques et micro-systemes pour applications biologiques”, L. Zanini, PhD thesis, Grenoble, France (2013).

Annex III.4. List of the non-magnetic AFM probes with attached magnetic microspheres

Probe type	Resonance frequency, (KHz)	Spring const, (N/m)	Diameter of attached sphere (μm)	Material of attached sphere	Image
PL2-CONTR	12.15	0.147	1.48	Superpara magnetic	
PL2-CONTR	12.02	0.149	1.45	Superpara magnetic	
PL2-CONTR	12	0.167	0.29	Superpara magnetic	
PL2-CONTR	12.213	0.1614	3.5	Superpara magnetic	

Probe type	Resonance frequency, (KHz)	Spring const, (N/m)	Diameter of attached sphere (μm)	Material of attached sphere	Image
PL2-FMR	54.67	1.88	1.73	NdFeB	
PL2-FMR	52.3	1.41	1.313	NdFeB	
PL2-FMR	50.68	1.51	1.84	NdFeB	
Olympus AC240TS	69.75	1.97	2.3	NdFeB	
Olympus AC240TS	68.46	2.01	1.778	NdFeB	

Probe type	Resonance frequency, (KHz)	Spring const, (N/m)	Diameter of attached sphere (μm)	Material of attached sphere	Image
Olympus AC240TS	66.38	1.9	2	NdFeB	
NCSC14	108.73	3.51	3.63	NdFeB	
NSC14/ AIBS	109.23	2.93	3.46	NdFeB	

Annex IV.1 Influence of topographic features on MFM imaging: protocol and data treatment for quantitative measurements

The definition of the magnetic microsphere – top of magnetic film distance plays crucial role in the direct force measurements since magnetic interaction is strongly dependent on the distance. As it was mentioned before, most of TMP samples with high magnetic properties have Nd-rich bumpy features on the surface due to annealing step of the sample fabrication. These features do not exhibit magnetic properties and should be taken into account in the separation distance definition. We have decided to apply a special data treatment procedure in order to remove these features from the MFM maps before calculating the average deflection profile.

The protocol of the data treatment consists of four main steps and described below:

Step 1. The average height of non-magnetic Nd-rich features and the sample roughness between the bumps can be found with commercial software for AFM images treatment (for example, Gwyddion).

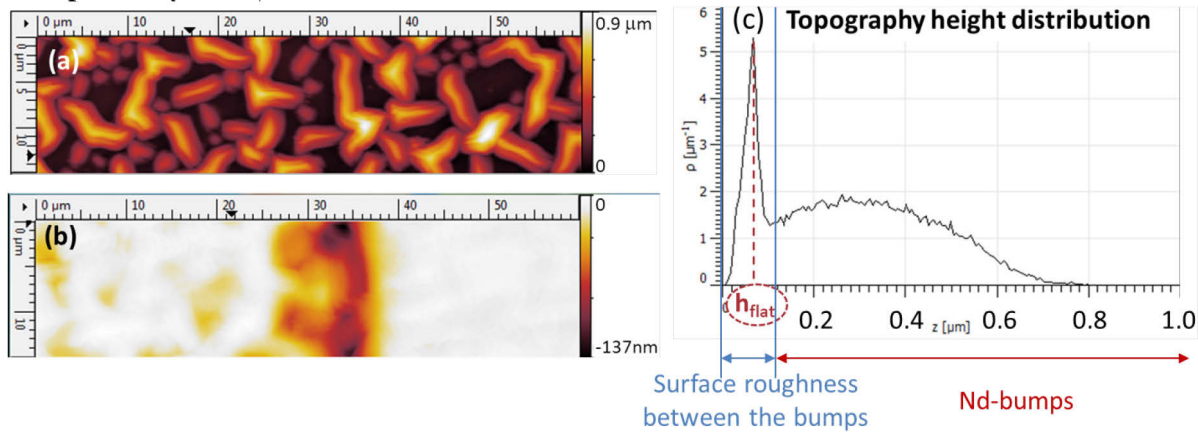


Figure 1. (a) Topography and (b) MFM deflection images obtained in static MFM mode. (c) Topography height distribution.

AFM and MFM maps obtained with MFM probe are presented respectively in Figure 1a and b. In Figure 1c the histogram plotted in Gwyddion of topography height is presented. This distribution exhibit bimodal behaviour, the first intense narrow peak correspond to the “flat” part of the sample between the bumps, meanwhile the second wide peak represents the Nd-rich features. It means that all the pixels on MFM image corresponding to the associated AFM image pixels with height of more than h_{flat} value shouldn't be used to plot mean deflection profile.

Step 2. Thanks to the possibilities of Gwyddion software a mask was applied to all the regions of the AFM image with height of less than h_{flat} (Figure 2).

In Figure 2 the initial AFM image (a) and the one with applied mask (b) (green regions) are presented. The peak corresponding to the surface roughness between the Nd-rich bumps is identified and all the pixels on the topography image with the height more than h_{flat} (out of green region on topography histogram) will be excluded on the associated MFM image.

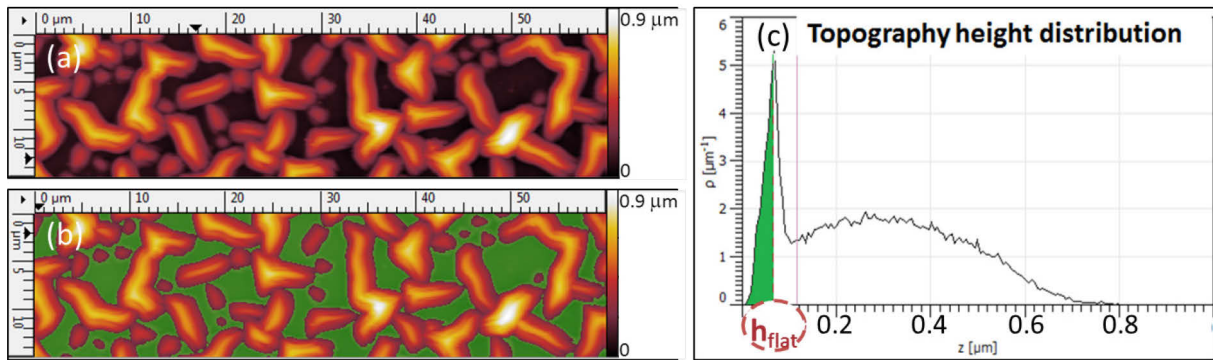


Figure 2. (a) Initial topography image. (b) Mask is applied to mark all the pixels of topography image with the height of less than h_{flat} (green area). (c) On the topography height distribution graph the topography height h_{flat} corresponding to the first peak is identified.

Step 3. The mask is extracted and saved in txt format as matrix of “0” and “1” (Figure 3). “0” value corresponds to the pixel on MFM image that should be removed due to presence of Nd-bump on associated AFM image; “1” value corresponds to the pixel that will be used to plot average deflection profile.

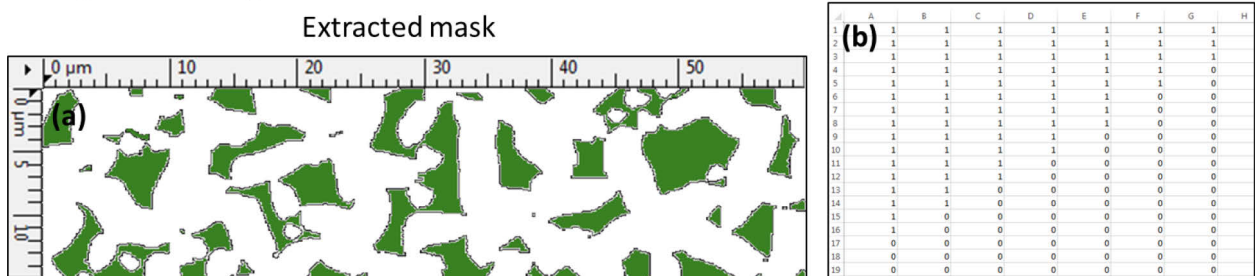


Figure 3. (a) Extracted by Gwyddion software mask. (b) Mask consisting of “0” and “1” in txt format.

Step 4. The matrices for MFM image and for the mask we compared element by element. All the values from MFM matrix corresponding to “0” from the mask matrix were deleted and then for each column of MFM matrix average value was calculated. As a result, an array of values corresponding to the mean profile of MFM image for the regions which were covered by mask is calculated. Figure 4 presents MFM image with applied mask (a) and a line of the code in python (b) that was used for mask and MFM images comparison in order to keep the right pixels.

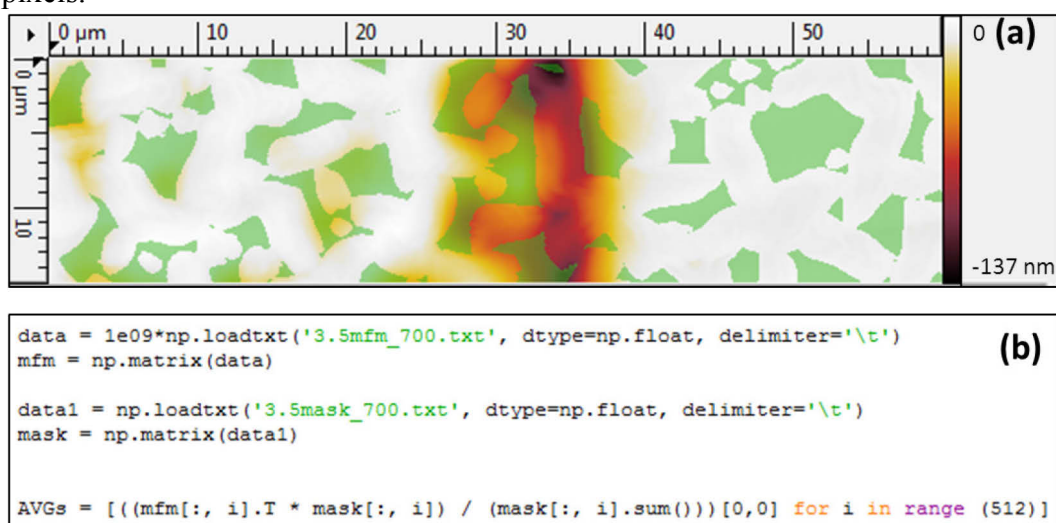


Figure 4. MFM image with an applied mask (green regions). (b) A line from the code written in python for comparison of MFM image and mask in order to keep the right pixels.

The results of the data processing are presented in Chapter IV.

Annex IV.2. Calculation of magnetic force acting on a single magnetic micro/nano particle.

The magnetic force acting on a point-like dipole or magnetic moment \vec{m} , in an applied magnetic field \vec{B} , can be written as the gradient of the magnetic energy¹ [1]:

$$\vec{F}_m = \nabla(\vec{m} \cdot \vec{B}) \approx (\vec{m} \cdot \nabla)\vec{B} \quad (1)$$

From a geometrical view, this force is the differentiation of magnetic induction \vec{B} with respect to the direction of magnetic dipole \vec{m} .

In the case of a *superparamagnetic* particle suspended in a weakly diamagnetic medium such as water, the total moment on the particle can be written:

$$\vec{m} = V\vec{M}, \quad (2)$$

where V is the volume of the particle and \vec{M} is the volumetric magnetization.

For the case of a dilute suspension of nanoparticles in pure water, we can approximate the overall response of the particles by:

$$\vec{B} = \mu_0\vec{H}, \quad (3)$$

So that, equation (1.1) for superparamagnetic nanoparticle becomes:

$$\vec{F} = \mu_0 V (\vec{M} \cdot \nabla)\vec{H} \quad (4)$$

The expressions for diamagnetic particles as well as further calculations for superparamagnetic particles suspended in liquid medium can be found in [2,3].

References

-
- 1 “Electromagnetic Fields and Interactions”, R. Becker, Dover, New York (1982).
 - 2 “Effects of high-gradient magnetic fields on living cell machinery”, V. Zablotkii, O. Lunov, S. Kubinova, T. Polyakova, E. Sykova and A. Dejneka, J. Phys. D: Appl. Phys. 49 (2016).
 - 3 “Applications of magnetic nanoparticles in biomedicine”, Q. A. Pankhurst, J. Connolly, S. K. Jones and J. Dobson, J. Phys. D: Appl. Phys. 36 (2003).

¹ It has to be noticed that the second part of equation holds when the magnetic moment of the particle is not varying in space ($\nabla \cdot \vec{m} = 0$). This assumption is correct only when the moment is permanent or the magnetic particle is in such large field that its magnetization is completely saturated.

Annex IV.3 Effect of sphere diameter and magnetic volume on the width of magnetic junction and force intensity

In our experiments superparamagnetic microspheres of different diameter and magnetic volume have been used. To estimate the effect of these two parameters separately we have conducted additional simulations. Figure 1a presents the force profiles calculated with Model 2 for superparamagnetic microspheres of 1.5 μm diameter with 15 vol.% (red) and 30 vol.% (blue) of magnetic nanoinclusions. For both curves the width of MJ at the half-height is 2.6 μm , while the force intensity for bigger sphere is 2 times higher than for smaller one. Indeed according to the Model 2 for force calculations we model entire magnetic sphere. Then in order to take into account the distribution of superparamagnetic inclusions, the force obtained by the simulation is reduced to percentage of magnetic volume.

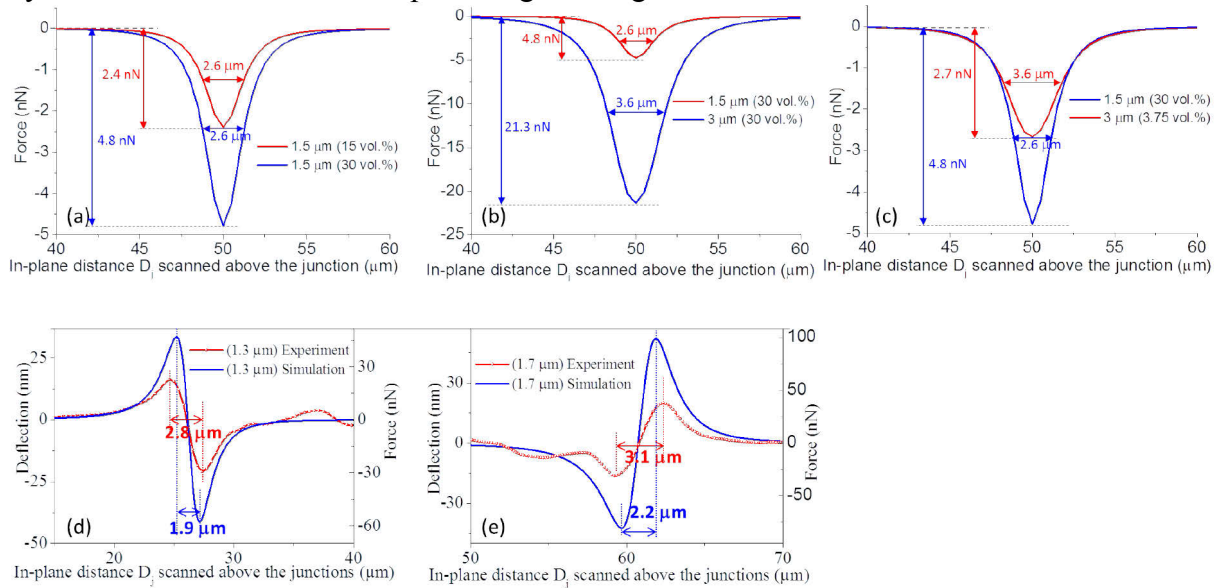


Figure 1. (a,b,c) The measurements of MJ width at the half-height from calculated with Model 2 force profiles: (a) for 1.5 μm diameter superparamagnetic microspheres with 15 vol.% (red) and 30 vol.% (blue) of magnetic nanoinclusions. (b) for 1.5 μm (red) and 3 μm (blue) superparamagnetic microspheres with 30 vol.% of magnetic nanoinclusions. (c) for 1.5 μm (blue) and 3 μm (red) superparamagnetic microspheres with fixed magnetic volume of $0.53 \mu\text{m}^3$ of magnetic nanoinclusions (it corresponds to 30 vol.% for 1.5 μm sphere and 3.75 vol.% for 3 μm sphere). (d,e) The measurements of the distance between negative and positive peaks above the same MJ from experimental (red) and calculated with Model 2 (blue) force profiles: (d) for 1.3 μm NdFeB microsphere; (e) for 1.7 μm NdFeB microsphere. All the experimental and simulated results were obtained for $LSH = 600 \text{ nm}$.

Figure 1b presents the force profiles calculated with Model 2 for superparamagnetic microspheres of 1.5 μm (red) and 3 μm (blue) diameter with 30 vol.% of magnetic nanoinclusions. For a fixed magnetic volume density (30 vol.%) we can observe an increase of magnetic junction width (by a factor of 1.4) and force intensity (by a factor of 4.4) with increase of the sphere diameter (by a factor of 2).

Figure 1c presents the force profiles calculated with Model 2 for superparamagnetic microspheres of 1.5 μm (blue) and 3 μm (red) diameters with a fixed volume of magnetic nanoinclusions ($0.53 \mu\text{m}^3$). This value corresponds to 30 vol.% for 1.5 μm superparamagnetic microsphere and 3.75 vol.% for 3 μm superparamagnetic microsphere.

Based on the results presented in Figure 1 (a,b,c) we can conclude that:

- (1) For a fixed sphere diameter (Figure 1a), the value of magnetic volume density (percentage) increases the force intensity above the MJ;

- (2) The *width (at half height)* of magnetic junction varies with the sphere diameter (Figure 1b), but not with the magnetic volume density (percentage of magnetic volume for a fixed diameter);
- (3) For a fixed magnetic volume (Figure 1c) we can observe decrease of the force intensity (by a factor of 8) above the MJ with the sphere diameter increase.

To complete this analysis we studied the effect of NdFeB spheres diameter on the distance between two peaks above the same MJ. Figure 1d presents the raw (without data treatment) experimental (red) and simulated (blue) deflection/force profiles for 1.3 μm NdFeB sphere. With enlargement of NdFeB sphere diameter (Figure 1e) up to 1.7 μm (by a factor of 1.3) we can observe the increase of the distance between negative and positive peaks (by a factor of 1.1 for experimental profile and by a factor 1.2 for simulated profile) and force intensity (by a factor of ~ 1.5).

According to these results, the magnetic volume density (percentage) influences the force intensity, but not the width of magnetic junction measured at the half height. It means that the spheres with the same diameters, but with different magnetic volumes will produce similar lateral extension of the magnetic force signal above a MJ; while for a fixed magnetic volume density (percentage), the lateral extension of the magnetic force signal above a MJ will increase with the sphere diameter. This last effect is known as the “tip-sample convolution effect”, where the lateral size of the measured signal varies with the size of the *effective* tip (i.e. Figure 4.9 in chapter IV). In this context, the effective tip corresponds to the sphere part containing magnetic material therefore the distribution of nano-inclusions in the sphere will impact the magnetic signal intensity and lateral extension (MJ width at half height).

List of figures

Figure 1.1. (a) Magnetic field B and (b) field gradient $\partial B/\partial z$ calculated for out-of-plane (oop) magnetized NdFeB micromagnet array with stripes of 50 μm width (c) at distance of 1 μm from the surface with Model 2 (Section II.2.1). (d) Fluorescence image of superparamagnetic particles of 1.4 μm diameter trapped by oop magnetized NdFeB micromagnet.....	12
Figure 1.2. Selected Rare Earth Oxide Prices, 2008-2013 (US \$/kg)	14
Figure 1.3. Development of permanent magnets.....	22
Figure 1.4. Magnetic moments behaviour for ferromagnetic, paramagnetic and diamagnetic materials with and without external magnetic field H	23
Figure 1.5. (a) A qualitative sketch of magnetic domains in a polycrystalline material. The dashed lines show demarcation between different magnetic domains; the dark blue curves show the grain boundaries. (b) The magnetic moment in adjoining atoms changes its direction continuously across the boundary between domains.	25
Figure 1.6. $M(H)$ hysteresis loop of ferromagnetic material.....	25
Figure 1.7. Typical $M(H)$ hysteresis loops of (a) <i>hard</i> and (b) <i>soft</i> ferromagnetic material. (c) $B(H)$ hysteresis loop with the energy product $(BH)_{max}$ related to the power or energy required to demagnetize the magnet.	26
Figure 1.8. (a) Side-view schematic of microfluidic channel based on micromagnet array. (b) Zoom of transition area (magnetic junction, MJ) between two neighbouring oppositely magnetized magnets. (c) Numerical simulations of total magnetic field B above the magnetic junction.....	28
Figure 1.9. Fourth quadrant of $B(H)$ hysteresis loop for NdFeB microspheres at different temperatures (-40, 25, 75, 125, 175°C) (datasheet provided by Molycorp Magnequench).....	29
Figure 1.10. (a) A single domain particle has a net magnetic moment; (b) Net magnetic moment of multidomain particle is cancelled by the orientation of different domains.	29
Figure 1.11. Experimental magnetization curves of superparamagnetic microspheres of 2.8 μm diameter (red) and 1 μm diameter (blue) and fitting with Langevin equation.	30
Figure 1.12. (a) Superparamagnetic particles under the influence of an external magnetic field form “chain” structure. (b) Superparamagnetic particles in absence of an external magnetic field with monodispersed particle distribution. (c) Ferromagnetic particles under the influence of an external magnetic field form “chain” structure. (d) Ferromagnetic particles in absence of an external magnetic field form aggregates.....	31
Figure 1.13. (a) A schematic illustrating the fluidic cell used in a TASA process. The template hole depth is indicated by H , the diameter of the template is D , and the diameter of the colloidal spheres is d . The possible forces that may be exerted on a colloidal sphere next to the rear edge of the liquid slug are the capillary force (F_c), gravitational force (F_g) and electrostatic force (F_e) and are illustrated above. (b) SEM image of an example of TASA where a two-dimensional array of trimmers was formed from 0.9 μm polystyrene beads.....	32
Figure 1.14. Three different methods for depositing nanoparticles on a surface patterned with electric charge: (a) The charged chip is immersed into nanoparticle powder. (b) The charged chip is exposed to nanoparticles that are suspended in the gas phase. (c) The silicon chip is immersed into a solution that contains nanoparticles that are agitated using an ultrasonic bath.....	33
Figure 1.15. Schematic representation of a specific attraction of magnetically labelled bacteria onto a 100×100 μm^2 micromagnet arrays.	34
Figure 2.1. Schematic of the triode sputtering apparatus.	41
Figure 2.2. SEM fracture views of NdFeB films microstructure showing (a) equiaxed grains and (b) columnar grains.....	41

Figure 2.3. The structure of a hard magnetic film deposited on a silicon substrate: (a) NdFeB; (b) SmCo.....	43
Figure 2.4. (a) [#] AFM image of NdFeB film surface with bumps. (b) [#] 3D AFM image of NdFeB film surface with bumps. (c) SEM image of a fracture cross-section of NdFeB film: Ta coating layer, Nd-rich bump and NdFeB film with columnar structure are observed.	43
Figure 2.5. Schematic of Thermo Magnetic Patterning principle.	44
Figure 2.6 [#] . Optical images of (a) Quartz mask for TMP fabrication: green lines are the apertures of the mask; (b) TMP sample with trapped 5 μm NdFeB particles: horizontal stripes pattern is observed; (c) TMP sample with trapped 5 μm NdFeB particles: horizontal stripes pattern (dark green arrows) and stripes pattern of 45° tilt to the initial one (blue dotted arrows) are observed.	45
Figure 2.7. (a) Simplified steps to produce topographically patterned micromagnets: substrate patterning; deposition of a magnetic layer; planarization by removal of the upper magnets. The last step is optional, depending on the application. (b) SEM image (side-view) of a TOPO patterned magnet.	46
Figure 2.8. Schematic representation of topographic patterning by the wet etching method.	46
Figure 2.9. Schematic diagram of the micro magnetic imprinting process: (0) master structure; (1) hard magnetic particles sprinkled onto master structure and magnetophoretically concentrated at the interfaces between neighbouring micromagnets; (2) polymer binder poured over the trapped magnetic particles; (3) the solid composite is peeled off the master structure.....	47
Figure 2.10 [#] . (a) Optical plane-view for 5 μm diameter NdFeB trapped particles. (b) Optical plane-view for 3 μm diameter SmFeN trapped particles. Magnetic particles are separated by a pitch of about 50 μm, which corresponds to the width of the micromagnets in the master TMP structure.	48
Figure 2.11. Schematic of Model 1 (a) and Model 2 (b). Points (1), (2) and (3) correspond to the different position of magnetic microsphere: (1) – the sphere is located at the edge of the pattern above the last stripe; (2) – the sphere is located above the last stripe in the middle; (3) – the sphere is located in the middle of the pattern (centre of the film).	49
Figure 2.12. Magnetic microsphere (red) is modelled as a cube of equal volume (green) in Model 2: (a) Superparamagnetic (SPM) microsphere discretized along the X, Y and Z axes; (b) NdFeB microsphere modelled as a permanent magnet cube with magnetization M_{sph} that can be oriented with an angle θ	50
Figure 2.13 [#] . Graphical representation in 2D of magnetic field B above the magnetic junction simulated with Model 1.....	51
Figure 2.14. Magnetic field B and field gradient $\partial B/\partial z$ calculated with Model 1 for TMP magnet with stripes of 50 (red), 100 (green) and 200 (blue) μm widths at distance of 1 μm from the surface.....	51
Figure 2.15. Results of magnetic field simulations with Model1 and Model2: (a) B_z component of magnetic induction; (b) B_y component of magnetic induction. (c) Interface of the program used for simulation of magnetic field and magnetic force acting on a NdFeB microsphere above the “stripe-like” TMP sample by CADES framework. Input area is marked by blue and output area is marked by red. Top: lateral positioning of microsphere y is chosen as an input. Magnetic force acting on it in z -direction Magnet_ForceZ_0 is chosen as an output. Bottom: Plot of magnetic force as a function of microsphere lateral positioning (red area) with the step of 0.1 μm (green area).....	52
Figure 2.16 [#] . Z -component of magnetic field for TMP sample with 50 μm stripes calculated at 1 μm above the MJ: (a) the effect of RZ depth for a fixed film thickness; (b) the effect of the total film thickness. (c), (d) Schematics of TMP configuration corresponding to positions (1) and (2) on the graph (a). (e), (f) Schematics of TMP configuration corresponding to positions (1) and (2) on the graph (b).	53
Figure 2.17. Magnetic microparticles trapped by NdFeB TMP film: (a) 3 μm in diameter SPM particles trapped by chess-board pattern; (b) 3 μm in diameter SPM particles trapped by stripes pattern; (c) [#] 5 μm in diameter NdFeB particles trapped by stripes pattern.....	54
Figure 2.18. (a) A large amount of 3 μm in diameter SPM particles is captured above an array of	

magnetic squares. (b) The drag force removed most of the particles once a strong fluid flow is induced. Particles that remain trapped inside RZ are marked with red circles and inside NRZ are marked with blue circles.....	55
Figure 2.19. Schematic representation of the image obtained with a MOIF, observed by rotation of polarized light. The black and white zones of MOIF reveal the oppositely magnetized (“up” and “down”) zones of magnetic layer.	56
Figure 2.20 [#] . Optical images of NdFeB TMP sample with 50 μm stripes pattern (a) without MOIF and (b) with U-MOIF placed on the top of the sample. Yellow stripes correspond to RZs while green stripes to NRZs of magnetic pattern.....	56
Figure 2.21 [#] . Optical images of μMI sample with trapped 5 μm diameter NdFeB microparticles separated by 50 μm distance: (a) without MOIF and (b) with U-MOIF placed on the top of the sample. Yellow areas localize the position of trapped magnetic microspheres.....	57
Figure 2.22. (a) Plan-view image of the Hall probe containing three active areas; (b) schematic diagram of the scanning Hall probe microscope set-up.	58
Figure 2.23. (a) Representation of the z-component of the magnetic field B_z as observed by SHPM; inset: B_z profile along the yellow line; (b) Schematic of the magnets considered on the analytical calculations; inset: B_z profiles corresponding to magnets with different reversal depths (0.5 μm - blue; 1.0 μm – red; 1.5 μm – green).The maximum B_z values are observed above the centre of squares.....	59
Figure 2.24. Scanning Hall Probe measurements of the stray magnetic field B_z measured at a height of 5 μm (a), 20 μm (b) and 50 μm (c) above a 100 μm striped μMI structure made with 16 μm spherical gas-atomised NdFeB particles. The inset of each figure corresponds to a measurement of the master thermo-magnetically patterned structure at the same scan height – note the higher range in colour scale for the μMI structures (bottom right of each image) compared to the master structures (top right of each image).	59
Figure 2.25. Simulations (Comsol) of the z-component of the stray field pattern produced at heights of 5 μm , 20 μm and 50 μm above μMI structures made with spherical powders of average particle size 16 μm (a) and 5 μm (b).	60
Figure 2.26. (a) Experimental scan lines of the MFM signal (phase shift) at different scan heights (50, 500, 1000 and 2500 nm) compared to (b) calculated vertical field, (c) its first derivative and (d) its second derivative along z.	62
Figure 2.27. MFM (phase) images of TMP sample obtained with hard magnetic coating stiff MFM probe (a) before and (b) after sample rotation by 45 degrees. (c) Schematic of the real tip-sample geometry during scanning.	63
Figure 2.28 [#] . (a) AFM image of TMP sample topography and (b) MFM image of TMP magnetic pattern obtained with soft magnetic probe (Multi-75G, BudgetSensors). The measurements are performed in dynamic mode. (c) SEM image of TMP sample.....	63
Figure 2.29. (a) Schematics of microfluidic device side-view used for magnetic particles handling. (b) Main forces acting on magnetic and non-magnetic particles inside a microfluidic channel.....	66
Figure 2.30. U-MOIF images of (a) stripe and (b) chessboard oop patterns in NdFeB (the insets represent the modulus of the magnetic field gradient $\partial B/\partial z$); (c) schematics of the mask used for chessboard patterning. Red dashed circle represents the area where the gap between RZs due to the TMP mask structure is observed.	67
Figure 2.31. Fluorescence images of the superparamagnetic particles trapped by micromagnets [(a): 200 nm above oop magnetized NdFeB; (b): 1.4 μm above oop magnetized NdFeB; (c), (d): 4.9 μm above oop magnetized NdFeB]. The insets present a zoom on the particles positioned above each magnetic configuration.....	67
Figure 2.32. (a) U-MOIF image of NdFeB film patterned oop with a mask that consists of square array (7 \times 7 μm^2) motifs. The insets represent the modulus of the magnetic field gradient $\partial B/\partial z$. (b) 10.3 μm particles individually positioned above this pattern. The insets present a zoom on the particles positioned above each magnetic configuration.	68

Figure 2.33. (a) HEK293 cells and (b) liposomes trapped on chessboard-like magnetic patterns ($50 \times 50 \mu\text{m}^2$ squares).....	68
Figure 2.34. (a) fluorescence image of fibroblast cells (nuclei, Hoechst staining, blue) attached to polystyrene microspheres (red), trapped on the μMI sample; (b) superposition of bright field and fluorescence images of fibroblast cells (nuclei, Hoechst staining, blue) attached to polystyrene microspheres (red), trapped on the μMI sample.....	69
Figure 2.35. Evolution of the capture of $1 \mu\text{m}$ magnetic microparticles by a chessboard-like magnet array inside a microfluidic channel with flow rate of $15 \mu\text{l}/\text{min}$ after 20s ($t_5 = 20 \text{s}$).	70
Figure 2.36. (a) Schematic representation of a system in which the guiding rails are parallel to the microfluidic channel and, thus, to the fluid flow. The experimental setup at different times is shown in (b), (c) and (d). Particle agglomerate moves along a magnetic rail, as indicated by the small arrow. The circle indicates agglomerate which is pinned to a zone of high magnetic field gradient. (e) Schematic of the system showing a microfluidic channel limited by the black lines with angled magnetic stripes below. The arrow indicates the direction of fluid flow. Magnetic particles deviated by the rails (f) close to the inlet, (g) in the middle of the channel and (h) close to the outlet. The particles are gradually deviated towards one edge of the channel and follow a thin streamline towards the outlet.....	71
Figure 2.37. (a) Schematic of the system used for continuous magnetic sorting, composed of one channel with two inlets and two outlets. Non-magnetic (white) and magnetic (black) particles are pumped in, concentrated at first on one side of the channel. Magnetic particles are deviated by magnetic rails and collected on the 2 nd outlet, while non-magnetic particles follow their initial streamlines and are collected on the 1 st outlet. (b) Particle counting performed by flow cytometry in the initial solution (blue) containing both magnetic and non-magnetic particles, the solution containing the non-deviated particles (purple) collected on 1 st outlet and the solution containing the deviated particles (red) collected on 2 nd outlet.....	71
Figure 3.1. Schematic overview of SFM technique.	78
Figure 3.2. Schematic of an AFM probe	78
Figure 3.3. (a) Schematic of an optical registration of the AFM cantilever bending. Laser spot displacement on four parts photodiode due to (a) vertical and (b) lateral forces (F_z and F_L) acting on the cantilever and corresponding (d, e) cantilever bending.....	79
Figure 3.4. (a) Sketch of a macroscopically flat surface probed by a sharp tip. (b) Atomic structure of tip and sample at small separation distance. (c) Forces acting on the cantilever at the micro/nano-scale in air.....	80
Figure 3.5. Sketch to illustrate the effect of the tip(sphere)-sample (plane) distance on the force between them: short-range repulsive Coulomb interaction (blue), long-range attractive Van der Waals and/or electrostatic interaction (red) and resulting force curve (green).	81
Figure 3.6. Sketch illustrating the two forces acting on the tip: force $F_{t/s}$ between the tip apex and the sample surface and force $F_{c/t}$ between the cantilever and the tip.	82
Figure 3.7. Classical approach-retract curves (approach curve is blue, retract curve is red) showing probe-sample interaction and corresponding cantilever bending recorded in air or in vacuum on a 'hard' surface. The gradient chosen for sensitivity measurements (green triangle) to convert photodiode signal from V (change in deflection) to nm (change in piezo height) is presented.	83
Figure 3.8. Measurements of the cantilever fundamental spring constant k_0 by thermal tune method. Resonance curve due to the thermal/Brownian motion is measured (the amplitude of the cantilever movements in a function of frequency (blue)). Fitting of the resonance curve (purple). The area below the peak provides the mean square cantilever deflection.	84
Figure 3.9. AFM image formation (a) with the constant tip-sample interaction and (b) at the constant altitude.....	85
Figure 3.10. (a) Localized mass model for cantilever oscillations modelling, where m^* and k are the effective mass and the spring constant of the cantilever respectively, z is the vertical displacement of the cantilever and F_{exc} is the excitation force of the cantilever vibrations. (b) Sketch representing cantilever beam as a simple spring-mass system.	86

Figure 3.11. The change of amplitude (a) and phase (b) for oscillating cantilever according to the tip-sample interaction. The dash lines correspond to negative force gradient, which leads to decrease of the resonant frequency and dotted lines correspond to positive force gradient, which leads to increase of the resonant frequency.	87
Figure 3.12. MFM procedure of a) Linear or Constant height mode; b) Static or DC MFM/ Lift procedure; c) Dynamic or AC MFM/ Lift procedure; LSH is the lift scan height.....	89
Figure 3.13. Schematic diagram showing electrically grounded cantilever and sample. The sample is connected onto a sample holder (puck) with conductive silver paint.....	90
Figure 3.14. Topography (a,b,c), phase (d,e,f) and average cross-section (g,h,i) images of NdFeB TMP sample with 50 μm “stripes” pattern obtained with commercial MFM probes in Dynamic mode: MagneticMulti-75G (a,d,g); PPP-MFMR (b,e,h) and AC160TS (c,f,i) with magnetic coating. Lift scan height is 500 nm.	92
Figure 3.15. (a) Tip of an MFM probe with thin magnetic layer (gravy). (b) Part of the magnetic tip relative to MFM imaging (grey). t is the thickness of magnetic coating (constant along z-axis), h is the tip height, h_{eff} is the height of the tip relevant for MFM imaging.	93
Figure 3.16. Resonance curves of the AFM cantilever: (a) Initial resonance curve, resonant frequency $f_0 = 383$ kHz (without glue); (b) Resonance curve of the cantilever with tip covered by glue, new resonant frequency $f_0' = 318$ kHz.	95
Figure 3.17. Procedure of the microsphere attachment. (a) Optical image of an isolated microsphere (in red circle). (b) 3D topography image of the chosen isolated microsphere performed in tapping mode. (c) Topography image of the microsphere performed in tapping mode. The area in blue rectangle presents the scan of the same line. The straight red line in the bottom of the rectangle corresponds to the moment when the sphere was glued to the tip apex. (d) Optical image of the scanning area. The sphere has disappeared from the surface (red circle).	96
Figure 3.18. SEM images of the worn tip with (a) 2.85 μm and (b) 3 μm diameter attached superparamagnetic microspheres.	96
Figure 3.19. AFM image of TMP sample obtained with a 2.85 μm MPFM probe. (a) Topography image. (b) MFM (phase) image. (c) The average cross-section from MFM (phase) image: $\Delta\varphi$ is the difference in average phase signal above magnetic junction and non-reversed zone (phase shift), $\Delta\varphi_R$ is the variation in phase signal inside non-reversed or reversed zone (“magnetic roughness”). Lift height is equal to 800 nm.	97
Figure 3.20. Commercial AFM cantilevers used for magnetic microsphere attachment. (a) FIB-shaped tip apex of NSC14/Al BS, MicroMasch probe; (b) tip apex of PL2-CONTR, Nanosensors probe; (c) tip apex of OMCL-AC240TS, Olympus probe; (d) NSC14/Al BS, MicroMasch probe with attached 3 μm NdFeB microsphere; (e) PL2-CONTR, Nanosensors probe with attached 1.5 μm superparamagnetic microsphere; (f) OMCL-AC240TS, Olympus probe with attached 1.8 μm NdFeB microsphere.	98
Figure 3.21. SEM images of the probe fabrication procedure: (a) A microsphere is soldered to the micromanipulator by IACVD of Pt gaseous precursor. (b) The selected microsphere is placed onto the plateau tip apex. (c) The microsphere is attached to the tip apex and free from the tungsten needle. ...	99
Figure 3.22. Topographical and MFM images of an array of NdFeB micromagnets obtained with 1.5 μm superparamagnetic microsphere (resonance frequency is 12 kHz, spring constant is 0.15 N/m) (a,c) and 1.3 μm NdFeB microsphere (resonance frequency is 52 kHz, spring constant is 1.4 N/m) (b,d) in static mode for $LSH = 500$ nm. Associated mean experimental profiles obtained with 1.5 μm superparamagnetic microsphere (e) and 1.3 μm NdFeB microsphere (f). Lateral scale bar is 20 μm . 100	
Figure 4.1. Micromagnet array – magnetic microsphere probe system: $D_{s/m}$ is the distance between bottom of magnetic sphere and top of magnetic layer; Δz_{sp} is the vertical cantilever deflection due to set point chosen for the first pass; Δz is the vertical cantilever deflection recorded during the second MFM pass, LSH is the lift scan height used for the MFM pass, h_{Nd} is the height of Nd-rich bumps and h_{Ta} is the thickness of the Ta capping layer.....	107
Figure 4.2. Data processing: (a) Topography image; (b) Topography height distribution: first peak	

corresponds to the flat part of the sample, second peak to the Nd-rich bumps; (c) Mask application on the topography image: green area corresponds to the part of the sample free of Nd-rich bumps; (d) Raw MFM deflection image; (e) Mask application on the MFM deflection image to remove the bumps. Green areas correspond to the data used for the corrected deflection profile plot. (f) Mean deflection profiles for raw (black line) and corrected (green line) experimental data obtained with 3.5 μm superparamagnetic probe at $LSH = 700$ nm in static MFM mode.	108
Figure 4.3. Z-component of magnetic field above the magnetic junction in a function of distance $D_{s/m}$ calculated with Model 2.	109
Figure 4.4. Modelling of (a) NdFeB microsphere and (b) superparamagnetic microsphere in CADES framework.	110
Figure 4.5. Modelling of ferromagnetic material (discretized) by Coulombian approach when the magnetization of each elementary block is calculated.	110
Figure 4.6. Topographical (a, b), MFM (c,d) images and associated mean phase/deflection profiles (e,f) of the NdFeB micromagnet array scanned with 2.85 and 1.5 μm superparamagnetic microsphere probes respectively at $LHS = 600$ nm. MJ_1 is the magnetic junction between NRZ and RZ; MJ_2 is the magnetic junction between RZ and NRZ. Some examples of local variation in magnetic signal inside the RZ (c, d) are marked with blue circles. Lateral scale bar is 20 μm	112
Figure 4.7. MFM phase profiles obtained with 0.29 μm (blue) and 2.85 μm (red) superparamagnetic microsphere probes at $LSH = 300$ nm.	114
Figure 4.8. (a) The measurements of magnetic junction width at the half-height from MFM phase image. (b) Schematics of an effect of magnetic microsphere diameter on the width of magnetic junction: (1) magnetic microsphere is in vicinity of magnetic junction (MJ) and starts to be affected by z-component of magnetic field; (2) centres of magnetic microsphere and MJ are aligned; (3) magnetic microsphere is moving away from MJ.	114
Figure 4.9. The average cross-sections of MFM (phase) images for LSH of 300, 600 and 800 nm obtained with (a) 0.29 μm and (a) 2.85 μm superparamagnetic microsphere probes in dynamic mode.	115
Figure 4.10. Magnetic force gradient versus distance between top of magnetic junction and centre of (a) 2.85 μm and (b) 0.29 μm superparamagnetic microsphere. Black solid lines with circles correspond to the experimental data. In (a) red dash line corresponds to the simulation for a magnetic microsphere located at the tip apex while blue dash curve corresponds to the simulation with a gap of 0.5 μm between the tip apex and the microsphere. In (b) blue line corresponds to the simulation where the magnetic microsphere is located at the tip apex. Theoretical curves are calculated with $\mu_0 M_{up} = 1.1$ T, $\mu_0 M_d = 0.9$ T, $h_r = t = 1.1$ μm	116
Figure 4.11. (a) SEM image of an AFM probe with glued 2.5 μm superparamagnetic microsphere: tip apex is free of glue and sphere is located in its vicinity. (b) SEM image of an AFM plateau tip with fixed 0.29 μm superparamagnetic microsphere thanks to FIB capability. (c) Sketch of the microsphere positioning for the probe used in experiments: the distance between tip apex and centre of the sphere is the so-called gap. (d) Sketch of the model used for simulations without taking into account the gap (red dash line in Figure 4.10a).....	116
Figure 4.12. Mean experimental (dash lines) and simulated (solid lines) force profiles obtained with 1.5 μm (blue lines) and 3.5 μm (red lines) superparamagnetic microsphere probes at $LSH = 0.7$ μm . Parameters used for simulations: magnetization of NRZ is $\mu_0 M_{up} = 1.1$ T, magnetization of RZ is $\mu_0 M_d = 0.9$ T and thickness of RZ is $h_r = 1.1$ μm	118
Figure 4.13. Mean deflection profiles obtained from raw data with a 1.5 μm superparamagnetic microsphere probe for three different LSH (0.6; 1; and 2.2 μm).	119
Figure 4.14. Magnetic force versus distance between magnetic junction and (a) 1.5 μm , (b) 3.5 μm superparamagnetic microsphere. Minimal (absolute values) theoretical curves are calculated with $\mu_0 M_{up} = 1$ T, $\mu_0 M_d = 0.6$ T, $h_r = 0.9$ μm (blue solid lines) and maximal (absolute values) theoretical curves are calculated with $\mu_0 M_{up} = 1.2$ T, $\mu_0 M_d = 1.2$ T, $h_r = 1.3$ μm (red solid lines) taking into account the magnetic volume for each sphere size (Table 4.1).	120

Figure 4.15. Definition of microsphere-magnetic layer distance above the magnetic junction (MJ) for experimental measurements $D_{j/s}$ and for simulations $D_{j/s}$ (<i>theoretical</i>). For simulations microsphere of radius R is modelled as a cube of equal volume with a side $a = 1.6 \times R$. Centres of cube and sphere are aligned.....	120
Figure 4.16. (a) Centres of the sphere and cube used to model it are aligned. The bottom edges of the cube extended beyond the sphere (inside blue dashed circle) compensate the sphere part that is out of the cube (inside orange dash circle). (b) The bottoms of sphere and cube used to model it are aligned. The bottom edges of the cube extended beyond the sphere (inside blue dashed circle) lead to overestimated magnetic signal.....	121
Figure 4.17. Force density for 1.5 and 3.5 μm superparamagnetic microspheres above a magnetic junction as a function of distance $D_{j/s}$. Parameters used for min simulations: magnetization of NRZ is $\mu_0 M_{up} = 1$ T, magnetization of RZ is $\mu_0 M_d = 0.6$ T, thickness of RZ is $h_r = 0.9$ μm	122
Figure 4.18. The effect of the sphere size on the force density D_F : (a) field variation in Z direction at the bottom and the top of the sphere is high; (b) field variation in Z direction at the bottom of the sphere is high, but close to zero at the top of the sphere.....	123
Figure 4.19. (a) MFM image of TMP array of NdFeB micromagnets obtained with 1.3 μm NdFeB microsphere in static mode for $LSH = 500$ nm. (b) Associated mean experimental profile, where the blue arrows indicate the orientation of magnetic pattern. MJ ₁ is the magnetic junction between NRZ and RZ; MJ ₂ is the magnetic junction between RZ and NRZ. $F_{I_{attr}}$ and $F_{I_{rep}}$ are the attractive and repulsive forces above MJ ₁ ; $F_{2_{attr}}$ and $F_{2_{rep}}$ are the attractive and repulsive forces above MJ ₂ . Lateral scale bar is 20 μm	124
Figure 4.20. (a) Schematic of magnetic interaction between hard magnetic microsphere and micromagnet array when the sphere magnetization, M_{sph} is parallel to initial magnetization of patterned film, M_{up} . Red cross is the centre of the sphere, while positions (1) and (6) correspond to the configuration where sphere magnetization is parallel to the sample stray field lines; positions (3) and (4) correspond to the configuration where sphere magnetization is antiparallel to the sample stray field lines; positions (2) and (5) correspond to the configuration where sphere magnetization is perpendicular to the sample stray field lines. (b) Associated force profile. M_{up} is the NRZ magnetization, M_d is the RZ magnetization, M_{sph} is the sphere magnetization; $F_{I_{attr}}$ and $F_{I_{rep}}$ are the attractive and repulsive forces above MJ ₁ ; $F_{2_{attr}}$ and $F_{2_{rep}}$ are the attractive and repulsive forces above MJ ₂	126
Figure 4.21. Measurements of the distance between attractive and repulsive peaks above one MJ for mean deflection/force profile obtained with 1.3 μm NdFeB microsphere probe at $LHS = 600$ nm and associated numerical profile.....	127
Figure 4.22. (a) Sketch in 2D of the experimental set-up: tilt θ of the probe holder leads to appearance of in-plane (M_{ip}) and out-of-plane (M_{oop}) magnetization components of NdFeB microsphere. (b, c) Simulations of the ip and oop components of the force acting in z-direction on 1.7 μm NdFeB microsphere above the micromagnet array with the tilt of the probe θ equals to 10 degrees.....	128
Figure 4.23. (a) Topographical image of a TMP sample obtained in contact mode during the double pass MFM procedure at $LSH = 500$ nm with 2 μm NdFeB microsphere probe. (b, c) Schematic of tip movements to form an image: red arrow corresponds to cantilever motion forward (trace) and blue arrow corresponds to cantilever motion backward (retrace).....	129
Figure 4.24. MFM deflection (a,b,c) and associated mean deflection profiles (d,e,f) obtained in static MFM mode at $LSH = 500$ nm with 2 μm NdFeB microsphere probe.....	130
Figure 4.25. TMP model (a) and examples of the structural and magnetic inhomogeneity of TMP sample (b,c,d,) that can affect MFM image leading to different artefacts such as dissymmetrical response between two neighbouring magnetic junctions, increase of magnetic roughness inside RZ and so on.....	131
Figure 4.26. Mean profiles obtained from raw data with a 1.3 μm NdFeB microsphere probe for three different LSH (0.6; 1; and 2.2 μm).....	131
Figure 4.27. Magnetic force versus distance between magnetic junction and (a) 1.3 μm and (b) 1.7 μm	

NdFeB microspheres. Minimal (absolute values) theoretical curves are calculated with $\mu_0 M_{up} = 1$ T, $\mu_0 M_d = 0.6$ T, $h_r = 0.9$ μm and $\mu_0 M_{sph} = 0.73$ T (blue solid lines) and maximal (absolute values) theoretical curves are calculated with $\mu_0 M_{up} = 1.2$ T, $\mu_0 M_d = 1.2$ T, $h_r = 1.3$ μm and $\mu_0 M_{sph} = 0.76$ T (red solid lines). Sphere magnetization angle Θ of 10° is applied..... 132

Figure 4.28. Force density for 1.3 and 1.7 μm NdFeB microspheres above a magnetic junction as a function of distance $D_{j/s}$. Parameters used for min simulations: magnetization of NRZ is $\mu_0 M_{up} = 1$ T, magnetization of RZ is $\mu_0 M_d = 0.6$ T, thickness of RZ is $h_r = 0.9$ μm , sphere magnetization $\mu_0 M_{sph} = 0.73$ T, $\Theta = 10^\circ$ is the angle of sphere magnetization..... 133

List of scientific papers

1. “Microcharacterization of magnetic flux sources used for cell manipulation”, S. Ponomareva, A. Lemiti, H. Marelli, B. Royer, L. Zanini, G. Ciuta, J.F. Motte, D. Givord, F. Dumas-Bouchiat, N.M. Dempsey and F. Marchi, Russian-German Forum on Nanotechnology, 22-23 May 2013, Tomsk Polytechnic University (TPU), Tomsk, Russia, abstract and poster.
2. “Local force mapping of an array of NdFeB micromagnets using a custom-made sphere MFM probe”, S. Ponomareva, B. Royer, H. Marelli, L. Zanini, J.F. Motte, D. Givord, F. Dumas-Bouchiat, N.M. Dempsey and F. Marchi, Réunion annuelle des utilisateurs de Microscopies à Force Atomique (AFM) de Bruker, 20-21 November 2013, Institut des Nanotechnologies de Lyon (INL), Lyon, France, abstract and oral presentation.
3. “Local force mapping of an array of NdFeB micromagnets using magnetic particle force microscopy”, S. Ponomareva, B. Royer, H. Marelli, L. Zanini, J.F. Motte, D. Givord, F. Dumas-Bouchiat, N.M. Dempsey and F. Marchi, IEEE International Magnetism Conference (INTERMAG Europe 2014), 4-8 May 2014, Dresden, Germany, abstract and poster.
4. “Measuring the Force Gradient Acting on a Magnetic Microsphere above a Micro-magnet Array”, S. Ponomareva, L. Zanini, F. Dumas-Bouchiat, N.M. Dempsey, D. Givord, and F. Marchi, *Advanced Materials Research* Vol. 872 (2014) pp. 167-173.
5. “Fabrication of SmFeN-based magnets by spark-plasma sintering technology”, S.A. Ponomareva, O.L. Khasanov, D.K. Yazykov, VI Russian Conference of Young Scientists "Materials science, technology and the environment in the third millennium", Institute of Strength Physics and Materials Science of the Siberian Branch of the Russian Academy of Sciences (ISPMS SB RAS), Tomsk, Russia, 11-13 May 2016, abstract and oral presentation.
6. “Micro-structure and magnetic properties of Zn-doped SmFeN magnets produced by Spark Plasma Sintering”, J.P. Loison, S.A. Ponomareva, V.V. An and O.L. Khasanov, *Proceeding of 7th International Conference “Nanoparticles, nanostructured coatings and microcontainers: technology, properties, applications”*, p.45, Tomsk, Russia, 12-15 May 2016, abstract and oral presentation.
7. “Fabrication of SmFeN-based magnetic materials by Spark Plasma Sintering method”, S.A. Ponomareva, O.L. Khasanov, F. Marchi, N.M. Dempsey, V.V. An, A.O. Khasanov, *Fundamental research*, No. 10(3), pp. 548-554 (2016).
8. “Study of micro-magnet array by magnetic micro-particle scanning force microscopy”, S. Ponomareva, A. Dias, B. Royer, H. Marelli, J.F. Motte, D. Givord, F. Dumas-Bouchiat, N.M. Dempsey and F. Marchi (in progress).

Acknowledgements

In this section I would like to acknowledge everybody who helped me from a personal, scientific and/or financial point of view.

First of all I would like to express my profound gratitude to the members of my graduation committee. I would like to thank Dr. Olga Kazakova for agreeing to be a reviewer of the manuscript, and for corrections, detailed remarks and valuable suggestions on every section of the manuscript. I would like to thank Dr. Michael Gauthier for agreeing to be a reviewer of the manuscript, and for the valuable remarks and comments that he made on my PhD manuscript. I truly appreciate the work that has been done on reviewing the manuscript. I would like to thank Dr. Nora Dempsey and Prof. Rostislav Grechishkin for agreeing to be examiners at my defense and for the interesting discussions that we had. I would like to thank Prof. Hervé Courtois for agreeing to be the president of the jury, and for the valuable remarks and comments that he made on my PhD manuscript.

I would like to express my profound gratitude to my supervisors, Prof. Florence Marchi, Prof. Oleg Khasanov and Dr. Vladimir An, who always supported and encouraged me.

Florence, thank you for the opportunity to do my PhD in Grenoble. Also thanks for your help concerning versatile aspects of my PhD and my life. You were the first person I met when I have arrived to France for the first time in 2012. Since that day you always managed to find time for regular meetings concerning my work and other aspects of my life. All these meetings were very important for me. I would like to say a special thank you for your help with this manuscript. You had so much patience to read and correct it again and again. Thanks a lot for everything.

I would like to express my deep gratitude to Prof. Oleg Khasanov, who has been a mentor to me for many years. Thank you for the comprehensive help with my studies, both in Grenoble and in Tomsk. And thank you that you managed to come for my defence.

I would like to say thanks to Dr. Vladimir An. I truly appreciate your help with countless aspects of this work and other aspects of my life. You always supported me and kept me motivated. Thank you!

Dear Nora, I would like to say a special thanks to you. First of all, thank you for integrating me into your team. I really appreciate the help and support that you offered to me at different stages of my life. Thank you for all the discussions that we had concerning soft and hard magnets, interpretation of MFM and VSM results. I truly appreciate that you involved me in different projects and activities. Your help and support during all these years is truly invaluable.

I would like to express my deep gratitude to Fabio Comin for the opportunity to conduct the experiments at the European Synchrotron Radiation Facility at the Surface Science laboratory. The experience I have got there led to this PhD work. I would like to thank all the SSL members and trainees: Luca1 and Luca2, David, Anthony, Mario, Toshi, Antoine, Nicolas, Baptiste, Brice, Heidi, Jeremy, Berta and Alain. It was a pleasure not only to work with you, but also to go out and hike together. And trust me I improved my carting skills a lot 😊

I would also like to thank Jean Francois Motte for the FIB sessions. Thanks for such beautiful microparticle probes and for your patience to fabricate them. And I really appreciate your effort to speak English with me.

I would like to thank Simon Le Denmat for his help with AFM and MFM measurements, for preparation and magnetization of my probes.

I would like to thank Frédéric Dumas-Bouchiat and Damien Le Roy for the thermomagnetically patterned magnets that I could investigate in this work.

Andre, I would like to say a special thanks to you. You are not only my colleague and officemate, but also my friend. I truly appreciate our discussions about magnetism, simulations and many other things. Thanks for your help in my studies and your support in other aspects of my life. I enjoyed the time we spent in Shakesbeer and JustBeer, skiing in

Chamrousse and playing frisbee in Paul Mistrale (sorry I wasn't born for it ☺).

I would like to thank all the members of NOF and MNM groups of Neel Institute. Thank you for being so friendly with me. I enjoyed the time we spent together in and outside of the lab.

I am thankful to the administrative staff of Institut Néel, Université Grenoble Alpes and Tomsk Polytechnic University who helped me with all the numerous documents.

I would like to thank Campus France and Embassy of France in Moscow for the financial support.

The work was partially supported by the Ministry of Education and Science of the Russian Federation (state assignment "Science", ГЗ № 11.7700.2017/БЧ).

Again I want to thank everybody who helped me and supported me during all these years! I am sorry if I forgot to mention somebody personally!